Data-Based Modeling of Electrochemical Energy and Thermal Systems: Fuel Cell and Lithium-Ion Battery

by
Adithya Legala

A thesis
presented to the University of Waterloo
in fulfillment of the
thesis requirement for the degree of
Doctor of Philosophy
in
Mechanical and Mechatronics Engineering

Waterloo, Ontario, Canada, 2025
© Adithya Legala 2025

Examining Committee Membership

The following served on the Examining Committee for this thesis. The Committee's decisions are made by majority vote.

External Examiner:	Dr. Marc Secanell Professor, Department of Mechanical Engineering, University of Alberta
Supervisor	Dr. Xianguo Li Professor, Department of Mechanical and Mechatronics Engineering, University of Waterloo
Internal Member	Dr. Sushanta Mitra Professor, Department of Mechanical and Mechatronics Engineering, University of Waterloo
Internal Member	Dr. Xiaoyu Wu Assistant Professor, Department of Mechanical and Mechatronics Engineering, University of Waterloo
Internal-External Member	Dr. Satyam Panchal Adjunct Assistant Professor, Department of Chemical Engineering, University of Waterloo

Author's Declaration

This thesis consists of material all of which I authored or co-authored: see Statement of Contributions included in the thesis. This is a true copy of the thesis, including any required final revisions, as accepted by my examiners.

I understand that my thesis may be made electronically available to the public.

Statement of Contribution

I, Adithya Legala, am the sole author of Chapters 1, 3, 8, and 9, which were written under the direct supervision of Dr. Xianguo Li for the sole purpose of this thesis and were not published prior to this. Chapters 2, 4, 5, 6, 7, and 8 were adapted from manuscripts published in peer-reviewed journals written by the author during the doctoral program.

Chapter 2 & Chapter 4: Legala, Adithya et al. "*Machine learning modeling for proton exchange membrane fuel cell performance*." Energy and AI, vol. 10, Nov. 2022, p. 100183, https://doi.org/10.1016/j.egyai.2022.100183.

Chapter 5: Legala, Adithya, et al. "*Data-based modelling of proton exchange membrane fuel cell performance and degradation dynamics*." Energy Conversion and Management, vol. 296, Sept. 2023, p. 117668, https://doi.org/10.1016/j.enconman.2023.117668.

Chapter 6: Legala, Adithya, et al. "*Hybrid data-based modeling for the prediction and diagnostics of Li-ion battery thermal behaviors*." Energy and AI, vol. 10, Aug. 2022, p. 100194, https://doi.org/10.1016/j.egyai.2022.100194.

Chapter 7: Legala, Adithya, et al. "*Modeling of diesel particulate filter temperature dynamics during exotherm using neural networks*." Frontiers in Thermal Engineering, vol. 3, Oct. 2023, https://doi.org/10.3389/fther.2023.1265490.

Chapter 8: Legala, Adithya, et al. "*Machine Learning Modelling for Fuel Cell-Battery Hybrid Power System Dynamics in a Toyota Mirai 2 Vehicle Under Various Drive Cycles*." Energy and AI, Aug. 2024, p. 100415, https://doi.org/10.1016/j.egyai.2024.100415.

For Chapter 4, the author and Dr. Jian Zhao developed semi-empirical and computational fluid dynamics models, respectively, to serve as the data source for the surrogate data-based model. The author conceptualized the work, compiled the data, implemented the neural network and support vector machine regressor algorithm, and trained and validated the data-based model against the simulated data sets. For Chapters 5, 6, 7, and 8, the author has conceptualized the work, formulated the regression problem, compiled the data, implemented the machine learning algorithms, trained and validated the data-based model against the experimental data sets, and summarized the insights into the dataset and final prediction results.

Abstract

As a solution to combat climate change and environmental pollution, electrochemical energy systems such as Proton Exchange Membrane Fuel Cell (PEMFC) and Lithium-Ion Battery (LIB) are being developed as the replacement for fossil fuel-powered combustion engines, especially for ground transportation and aviation applications. These electrochemical energy systems must be able to operate independently and in conjunction with each other by complementing their advantages and limitations, such as efficiency, range, thermal behavior, aging, and operating environment. This interoperability requires accurate real-time computational models to control, diagnose, and adapt according to field requirements. A typical electrochemical energy system model needs to incorporate effects related to reactant concentrations, system overpotentials, thermodynamics, porous media mechanics, membrane dynamics, gas diffusion, electrode degradation, electrolyte status, ion transport, and chemical kinetics across various operating conditions, all of which result in complex interactions affecting the accuracy and reliability of the system.

Today, both PEMFC and LIB use complex computational physics-based fluid dynamics models in the product development phase, which requires enormous computational power and long lead times for iterative prototype improvements. On the other hand, both PEMFC and LIB rely on simple lookup tables and semi-empirical equations as plant models that require intensive calibration activity to determine the mode of control and diagnosis for automotive applications. However, considering the present-day automotive propulsion systems, which operate in widely varied applications and geographic locations and have short product development cycles, these approaches are not able to comprehend the complexities, hindering the ability of these systems to operate at their full potential and leading to catastrophic failures (e.g., Thermal runaway). Data-based modeling techniques are one of the potential solutions, which is quite in contrast with other empirical or physics-based models where the entire input-output relations of the model are established primarily based on the data. Data-based models use aspects of statistics, probability, and network architecture, avoiding the complexities of physics-based models and intensive calibration, providing better accuracy in most cases, primarily where the complex mechanisms can’t be modeled using specific governing equations, and fast, efficient computation with much less computational resource requirement.

This thesis focuses on data acquisition (identifying and collecting the relevant data) and data-based model development by incorporating machine learning algorithms and regressors to predict the system's performance, thermal behavior, aging, and faults in real-time (on-board diagnostics). Data for these models is acquired through two approaches, the first approach being experimentation by utilizing the facilities of Fuel Cell and Green Energy Lab such as the Automated Battery Test Station (ABTS), G20 fuel cell automated test station, and by partnering with the relevant industry. In the second approach, data is generated by simulation of physics-based models (CFD, Semi-empirical, equivalent circuit models) that are experimentally validated in the literature and developed within the research groups of UWaterloo. Development of a data-based model includes the identification of feature vectors (inputs), prediction attributes (outputs), state estimates (internal parameters), non-linearity of the systems, correlation factors of various system entities, and application of machine learning techniques such as feed-forward artificial neural network, support vector machine classifier - regressor, along with their respective adaptations and calibration processes. The primary objectives of this study are to develop data-based models for three main application areas: (i) Prediction of PEMFC performance, internal states of the membrane, cell voltage degradation, and system outputs. (ii) Prediction of LIB heat release rate during discharge and thermal dynamics of an open system during an exothermic reaction. (iii) Prediction of fuel cell battery hybrid electric vehicle’s system dynamics and thermal behavior.

During this study, various data-based models were developed to tackle the problems encountered in fuel cell-battery hybrid systems, such as predicting the fuel cell performance, fuel cell voltage degradation, PEMFC membrane dynamics, lithium-ion battery thermal dynamics, thermal behavior during exothermic reactions and dynamics of fuel-cell battery hybrid system. The results presented in this study proved the data-based model’s applicability in surrogate modeling, real-time system monitoring, controls, and diagnostics of electrochemical energy systems both at the component level and system level. Additionally, the results implicate that the data-based model can serve as a complement and alternative to the traditional computational fluid dynamics models as well as complex physics-based and empirical models to predict thermal gradients and system internal states during multifaceted reactions.

Acknowledgments

"Guru Brahma:Guru Vishnu: |Guru Devo Maheshwaraha:|

Guru Saakshat Para Brahma: |Tasmai Sree Gurave Namaha: ||"

- Guru Stotram (Sanskrit Verse)

First, I would like to express my heartfelt gratitude to my advisor, Dr.Xianguo Li, for his constant support and guidance in every aspect of my doctoral journey. Dr Li was an exceptional role model for me in terms of work ethic, long-term vision, determination, and research methods. I am always thankful to him for his availability and approachability, which helped me to advance quickly throughout my research. His constant words of encouragement and optimism helped me continue my research with enthusiasm at times. I am quite fortunate and always grateful for his guidance and care during my academic journey and personal development.

I would also like to thank my committee members, Dr. Sushanta Mitra, Dr. Xiaoyu Wu, and Dr. Satyam Panchal, for providing me with valuable suggestions during my research. I would also like to thank Dr. Samaneh Shahgaldi and Dr. Jian Zhao for their guidance on several aspects of research, which enlarged the scope of my research. I want to thank my mentor, Phillip Weber, from the Southwest Research Institute, for his support and guidance on various engineering aspects and for facilitating research opportunities.

I have always loved and cherished the constant support from my colleagues and group members, especially Pramoth Varsan Madhavan, Amirhossein Amirsoleymani, Abhishek Mishra, Yasmin Shabeer, Matthew Kubesh, Dr. Prasad Arkhat, Dr. Venkata Rajesh Chundru, Dr. Bapi Raju Surampudi (Late), to name a few. Without their help, encouragement, and fruitful discussions throughout my Ph.D., I would not be able to put together this vital publication.

Last but not least, I would like to thank my compassionate friends from various phases of life, who have always provided me with appropriate guidance, taught me lessons from their mistakes, encouraged me during tough times, and constantly influenced me to aim for better things.

Dedication

I dedicate this thesis to my dad, Malla Reddy Legala, for his constant motivation and emotional support, which always encourages me to strive for bigger things. I am always indebted to the unwavering support of my mom, sister, and family during these times, which significantly contributed to the successful completion of this work.

I love you all sincerely.

Table of Contents

Examining Committee Membership ii

Author's Declaration iii

Statement of Contribution iv

Abstract v

Acknowledgments vii

Dedication viii

List of Figures xiv

List of Tables xxi

Chapter 1 Introduction 1

1.1 Background 1

1.2 Principle of Proton Exchange Membrane Fuel Cell (PEMFC) 3

1.3 Principle of Lithium-Ion Battery (LIB) 7

1.4 Modeling of Electrochemical Energy Systems 10

1.4.1 Empirical Models 11

1.4.2 Physics-based Models 12

1.4.3 Data-based Models 13

1.5 Objectives and Scope 14

Chapter 2 Machine Learning Techniques for Data-Based Modeling 17

2.1 Artificial Neural Network (ANN) 17

2.1.1 Linearity and Non-linearity of the System 24

2.1.2 Activation Functions 24

2.1.3 Dropout Probability 25

2.1.4 Training and Calibration 26

2.2 Support Vector Machine Regressor (SVR) 27

Chapter 3 Literature Survey 29
3.1 Machine Learning Models for PEMFC System 29
3.2 Machine Learning Models for LIB System 32
3.3 Limitations in the Existing Literature and Data-Based Models 37
Chapter 4 Predicting PEMFC Performance and Membrane Dynamics 39
4.1 Data Acquisition 40
4.1.1 Data Conditioning / Preprocessing: 42
4.2 Neural Network Hyper Parameters 42
4.2.1 Nodes & Hidden Layers 42
4.2.2 Feature Vectors 43
4.2.3 Loss Function 43
4.3 ANN Architecture and Design Parameters 43
4.3.1 ANN for Dataset1 (Semi-Empirical) 44
4.3.2 ANN on Dataset2 (1D-CFD) 45
4.4 Results and Discussion 46
4.4.1 SVR for Dataset1 and Dataset2 46
4.4.2 ANN for Dataset1 (semi-emp) 47
4.5 ANN Results for Dataset 2 (1-D CFD) 50
4.6 Summary 56
Chapter 5 Modeling of Proton Exchange Membrane Fuel Cell Degradation Dynamics 58
5.1 Introduction 59
5.2 Experimental Procedure 62
5.3 Data-based Modeling 67
5.3.1 Feed-forward ANN 68
5.3.2 Data preprocessing 69

5.3.3 PEMFC model feature vectors and prediction attributes 70
5.3.4 ANN Design and Hyperparameters 70
5.4 Results and Discussion 78
5.4.1 Prediction of PEMFC Voltage Degradation 79
5.4.2 Prediction of PEMFC Temperature Dynamics 80
5.4.3 Prediction of PEMFC Pressure Dynamics 81
5.4.4 Prediction of PEMFC transient dynamics and model robustness 83
5.5 Summary 86
Chapter 6 Hybrid Databased Modeling to Predict Thermal Behavior of LIB 87
6.1 Introduction 88
6.2 2. Data Acquisition 90
6.3 System Modeling 91
6.3.1 State Estimation using EKF 92
6.3.2 Physics-based state equation 93
6.3.3 ECM-based state equation 94
6.3.4 Measurement function 95
6.3.5 ANN Modeling 97
6.4 Results and Discussion 100
6.4.1 EKF Prediction Case 1: Measurement noise > Process noise 101
6.4.2 EKF Prediction Case 2: Measurement noise < Process noise 102
6.4.3 EKF Prediction Case 3: Faulty initialization of the state 103
6.4.4 Heat Generation Rate Prediction 105
6.4.5 Simulated Thermal Management System Control 107
6.4.6 Sensor Diagnostics 108
6.5 Summary 111

Chapter 7 Predicting Spatial Temperature Gradients During Exothermic Reactions 113
7.1 Introduction 114
7.2 Experimental Procedure 117
7.3 Data-based Modeling 122
7.3.1 Feed-forward ANN 123
7.3.2 Data Preprocessing 124
7.3.3 DPF thermal model feature vectors and prediction attributes 124
7.3.4 Hyperparameter Calibration 126
7.4 Results and Discussion 128
7.4.1 Scenario 1: Soot Load = 3g/L, AR-DTI Temperature = 560°C 131
7.4.2 Scenario 2: Soot Load = 4g/L, AR-DTI Temperature = 550°C 132
7.4.3 Scenario 3: Soot Load = 5g/L, AR-DTI Temperature = 525°C and Scenario 4: Soot Load = 5g/L, AR-DTI Temperature = 560°C 133
7.4.4 Scenario 5: Soot Load = 6g/L, AR-DTI Temperature = 550°C and Scenario 6: Soot Load = 7g/L, AR-DTI Temperature = 525°C 134
7.4.5 Scenario 7: Soot Load = 4g/L, AR-DTI Temperature = 560°C (Field Data) 135
7.5 Summary 138
Chapter 8 Predicting Fuel Cell-Battery Hybrid Power System Dynamics 139
8.1 Introduction 140
8.2 Data Acquisition Procedure 142
8.3 Vehicle Data 145
8.4 Machine learning models/Data-based Modeling 150
8.4.1 Feature vector and prediction variable selection 150
8.4.2 Neural network architecture and hyperparameter tuning 151
8.5 Results and Discussion 153
8.5.1 HwFET Cycle (Highway Fuel Economy Test) 154

8.5.2 FTP Cycle (Federal Test Procedure) 157
8.5.3 Gradient Cycle 160
8.6 Summary 164
Chapter 9 Conclusions and Future Work 165
9.1 Conclusions 165
9.2 Future Work 167
References 168
Appendices 193
Appendix A 193
Appendix B 202

List of Figures

Figure 1.1 Working of proton exchange membrane fuel cells [23] 4
Figure 1.2 Polarization curve of fuel cell:(a) Polarization regions (b) Deviation from reversible cell voltage [14], [26] 5
Figure 1.3 Illustration of reaction mechanism inside of a LiFePO4 cell [30] 8
Figure 1.4 Polarization curve of the battery [29] 9
Figure 1.5 Equivalent Fuel Cell Model: Dicks- Larminie model [19] 11
Figure 2.1 Schematic of the nth neuron in the kth (hidden) layer and the pth neuron in the output layer of an artificial neural network, illustrating the network operation. 18
Figure 2.2 Fuel cell polarization curve nonlinearity for (a) different pressures and (b) different temperatures. 24
Figure 2.3 (a) Sigmoid function (red-colored curve) and its derivative (blue-colored curve); (b) Tanh function (red-colored curve) and its derivative (blue-colored curve); (c) Rectified linear unit function (red-colored curve) and its derivative (blue-colored curve) 25
Certain neuron connections within the network are randomly disconnected based on a specific probability value to prevent overfitting during the neural network's training process. This specific probability number is called dropout probability and needs to be calibrated depending on the data, predicted parameters, and accuracy needs. Figure 2.4 **Error! Reference source not found.**shows an example of a feed-forward neural network with and without dropout. The dropout probability uses a Bernoulli distribution (a probability distribution used with a parameter $1-p$) to model a binary random variable that takes on one of two possible outcomes: 1 (success) with probability $1-p$, and 0 (failure) with probability p. 25
Figure 2.5 Neuron connections: (a) without dropout; (b) with dropout. 26
Figure 2.6 (a) Classification of Support Vector Machine (SVM) [48] ; (b) SVM regression [49] 27
Figure 3.1 Schematic of artificial neural network architecture for fuel cell voltage prediction [50] 29
Figure 3.2 Results of the support vector regression algorithm for fuel cell voltage prediction [51] 30

Figure 3.3 Representation of a group method of data handling neural network for micro fuel cell [52] 30
Figure 3.4 Fuel cell hybrid model consisting of support vector machine and empirical equation [53] 31
Figure 3.5 Comparison of fuel cell attribute errors during validation [55] 31
Figure 3.6 Comparison of activation overpotential of fuel cell catalyst layer [57] 32
Figure 3.7 Autoregressive neural network result stack voltage (V) Vs. time (hours) [57] 32
Figure 3.8 Comparison of the measured internal temperature and the predicted internal temperature by CNN [58] 33
Figure 3.9 Comparison of experimentally measured heat generation and predicted values at 1C discharge rate [59] 34
Figure 3.10 Temperature difference of the battery pack under 18,639 different spacing combinations [60] 34
Figure 3.11 Schematic of the SOC estimation based on the neural network & unscented Kalman filter [61] 35
Figure 3.12 SOC estimation based on the neural network & extended Kalman filter – 1 [62] 36
Figure 3.13 SOC estimation based on the neural network & extended Kalman filter – 2 [63] 36
Figure 4.1 Schematic of physics-based semi-empirical voltage module [27] 40
Figure 4.2 Initial ANN design for Dataset1 44
Figure 4.3 Initial ANN design for Dataset2 45
Figure 4.4 SVR Results for Dataset1: (a) Training; (b) Validation. 46
Figure 4.5 Case 1 neural network result for Dataset1 considering MAE as loss function and no dropout: (a) Loss function / MAE Vs Training Epochs; (b) Voltage prediction 47
Figure 4.6 Case 2 neural network result for Dataset 1 considering MSE as loss function and no dropout: (a) Loss function / MSE Vs Training Epochs; (b) Voltage prediction. 48
Figure 4.7 Case 3 neural network result for Dataset1 considering MAE as Loss function with dropout: (a) Loss function / MAE Vs Training Epochs; (b) Voltage prediction. 49
Figure 4.8 Case 4 neural network result for Dataset1 considering MSE as Loss function with dropout: (a) Loss function / MSE Vs Training Epochs; (b) Voltage prediction. 50

Figure 4.9 Case 1 neural network result for Dataset 2 considering MAE as Loss function with no dropout: (a) Loss function / MAE Vs Training Epochs; (b) Voltage prediction; (c) Resistance prediction; (d) Lambda prediction 51
Figure 4.10 Case 2 neural network result for Dataset2 considering MSE as Loss function with no dropout: (a) Loss function / MAE Vs Training Epochs; (b) Voltage prediction; (c) Resistance prediction; (d) Lambda prediction 52
Figure 4.11 Case 3 neural network result for Dataset2 considering MAE as Loss function with dropout: (a) Loss function / MAE Vs Training Epochs; (b) Voltage prediction; (c) Resistance prediction; (d) Lambda prediction 54
Figure 4.12 Case 4 neural network result for Dataset 2 considering MSE as loss function with dropout: (a) Loss function / MSE Vs Training Epochs; (b) Voltage prediction; (c) Membrane resistance prediction; (d) Membrane hydration (Lambda) prediction 55
Figure 5.1 Cross plot of PEMFC operational parameters [experimental data] (a) Fuel cell inputs - 1; (b) Fuel cell inputs – 2; (c) Fuel cell inputs – 3; (d) Fuel cell outputs 67
Figure 5.2 Schematic of the neural network and backpropagation [45] 68
Figure 5.3 Schematic of the proposed fuel cell neural network-fuel cell degradation 72
Figure 5.4 Graphical representation of Rectified linear unit function (red-colored curve) and derivative (blue-colored curve) [45] 72
Figure 5.5 Results of the neural network hyperparameter iteration: A; B; C; D 76
Figure 5.6 (a) Cell current at various sample points; (b) AST cycles at various sample points ... 79
Figure 5.7 ANN predicted voltage degradation. (a) Voltage vs sample points; (b) Voltage vs cell current 80
Figure 5.8 Fuel cell reactant inlet temperature profile 81
Figure 5.9 ANN predicted fuel cell temperature dynamics [Red-Experimental Value; Blue–Predicted Value] (a) Anode reactant outlet temperature; (b) Cathode reactant outlet temperature 81
Figure 5.10 Fuel cell reactant inlet pressure profile 82
Figure 5.11 ANN predicted fuel cell pressure dynamics [Red-Experimental Value; Blue–Predicted Value] (a) Anode reactant outlet pressure; (b) Cathode reactant outlet pressure 83
Figure 5.12 ANN voltage prediction during transient conditions with measurement noise 84

Figure 5.13 ANN pressure dynamics prediction during transient conditions with measurement noise 84
Figure 5.14 ANN prediction error histogram (a) Cell voltage; (b) Anode outlet pressure; (c) Cathode outlet pressure; (d) Anode outlet temperature; (e) Cathode outlet temperature 85
Figure 6.1 Schematic of the proposed artificial neural network architecture with EKF 89
Figure 6.2 Schematic of the Lithium Ion Battery (LIB) experimental setup with the calorimeter90
Figure 6.3 The equivalent circular model (ECM) consists of one resistance and one capacitance (RC) for a lithium-ion battery (LIB). 94
Figure 6.4 Battery voltage during discharge expressed as a function of the depth of discharge (DOD) as the measurement function, based on the correlation of experimental results [34] in terms of an 8th order polynomial) 95
Figure 6.5 ANN design and calibration (a) Regression plots of all the hyperparameter iterations tabulated in Table 6-2; (b) The artificial neural network (ANN) layout for the lithium-ion battery (LIB) thermal model;(c) Graphical representation of Tansig function(red) and its derivative(blue) 100
Figure 6.6 Comparison of the DOD estimation by the extended Kalman Filter (EKF) and direct coulomb counting (CC) method with the experimentally measured data by the automated battery test station (ABTS) for the case of the measurement noise larger than the process noise; magnified view on the right 102
Figure 6.7 Comparison of the DOD estimation by the extended Kalman Filter (EKF) and direct coulomb counting (CC) method with the experimentally measured data by the automated battery test station (ABTS) for the case of the measurement noise **less than** the process noise; magnified view on the right 103
Figure 6.8 Comparison of the DOD estimation by the extended Kalman Filter (EKF) and direct coulomb counting (CC) method with the experimentally measured data by the automated battery test station (ABTS) when the initial values of DOD are estimated significantly incorrectly; magnified view on the right 104
Figure 6.9 Comparison of the DOD estimation by the extended Kalman Filter (EKF) and direct coulomb counting (CC) method with the experimentally measured data by the automated battery test station (ABTS) when the initial values of DOD are estimated significantly incorrectly, but the parameters in the EKF are properly tuned 104

Figure 6.10 A standalone ANN model performance for LIB thermal behavior (heat generation rate): (a)ANN accuracy for individual data points; and (b) ANN prediction vs true value..... 105
Figure 6.11 CC-ANN and EKF-ANN model performance for LIB heat generation rate: (a) instantaneous heat generation rate, (b) total heat output generated, (c) relative error of the total heat output generated between the ANN models and the experimental results..... 106
Figure 6.12 Thermal management system performance based on LIB thermal EKF-ANN model 108
Figure 6.13 The performance of the ANN model predictions with current sensor fault through comparison with the respective experimental results; (a) DOD; (b) Instantaneous heat generation rate; (c) Total Heat output generated, (d) Relative error of total heat output generated..... 109
Figure 6.14 Deviation of the ANN model with voltage sensor fault; (a) EKF DOD prediction, (b) Instantaneous heat generation rate for the CC-ANN and EKF-ANN output, (c) Total heat output generated, (d) Relative error of total heat output generated 110
Figure 7.1 Engine test cell schematic. 118
Figure 7.2 Experimental procedure: (a) Flow process, (b) AR-DTI Cycle. 119
Figure 7.3 DPF Instrumentation Pattern where the radial direction is represented by X direction, and the dominant axial flow direction by Y direction. 120
Figure 7.4 Cross plot for the operating parameters: (a) Exhaust flow parameters, (b) Exhaust temperature parameters. 122
Figure 7.5 ANN model performance on normalized data after training: Error vs. Epochs and predicted five random temperatures chosen out of 47 presented here (output dataset). 127
Figure 7.6 Illustration of DPF cross-section instrumentation with 18 thermocouples. 128
Figure 7.7 ANN model performance on the DPF periphery locations (pristine data/denormalized). 129
Figure 7.8 ANN performance in a time series prediction during multiple regeneration sequences measured vs predicted periphery temperatures at the location of (a) A & B; (b) C & E; (c) D & F. 130
Figure 7.9 Contour plot for DPF thermal gradient: ANN prediction vs experimental measurement at the soot loading of 3g/L and the DPF inlet gas temperature of 560°C. 132
Figure 7.10 Contour plot for DPF thermal gradient: ANN prediction vs experimental measurement at the soot loading of 4g/L and the DPF inlet gas temperature of 550°C. 133

Figure 7.11 Contour plot for DPF thermal gradient: ANN prediction vs experimental measurement at the soot loading of 4g/L and the DPF inlet gas temperature of 525°C. 134
Figure 7.12 Contour plot for DPF thermal gradient: ANN prediction vs experimental measurement at the soot loading of 5g/L and the DPF inlet gas temperature of 560°C. 134
Figure 7.13 Contour plot for DPF thermal gradient: ANN prediction vs experimental measurement at the soot loading of 6g/L and the DPF inlet gas temperature of 550°C (Scenario 5). 135
Figure 7.14 Contour plot for DPF thermal gradient: ANN prediction vs experimental measurement at the soot loading of 7g/L and the DPF inlet gas temperature of 525°C (Scenario 6). 135
Figure 7.15 Contour plot for DPF thermal gradient: ANN prediction vs experimental measurement at the soot loading of 4g/L and the DPF inlet gas temperature of 560°C (Scenario 7 where the experimental data has not been used for the model training and validation, or the so-called unexposed or new data, and the experimental measurement is the field data where the soot distribution may not be as uniform as for the previous scenarios of laboratory tests.) 136
Figure 8.1 2021 Toyota Mirai 2 fuel cell electric vehicle. (A) Schematic of, and (B) the actual layout (under the hood) of, the fuel cell-lithium-ion battery hybrid powertrain system. 145
Figure 8.2 The electrical attributes of the 2021 Toyota Mirai 2 fuel cell electric vehicle under various loading conditions, as represented by the data acquired in this study: (A) Fuel cell (FC) Stack; (B) Lithium-ion battery (LiB) Pack. 147
Figure 8.3 The thermal attributes of the 2021 Toyota Mirai 2 fuel cell electric vehicle under various loading conditions, as represented by the data acquired in this study: (A) Fuel cell (FC) Stack; (B) Lithium-ion battery (LiB) Pack. 148
Figure 8.4. The reactant attributes of the 2021 Toyota Mirai 2 fuel cell electric vehicle under various loading conditions, as represented by the data acquired in this study: (A) Anode; (B) Cathode. 149
Figure 8.5 Schematic of the input, output and architecture of the neural network adopted in the present study. 152
Figure 8.6 Prediction accuracy of the trained neural network for various hybrid system attributes 153
Figure 8.7 The performance of the present neural network model for the vehicle operating on HwFET (Highway Fuel Economy Test) Cycle. 155

Figure 8.8 The fuel cell-battery hybrid power system dynamics and the prediction accuracy of the developed neural network model during a vehicle deceleration and acceleration event for the vehicle operating on the HwFET (Highway Fuel Economy Test) Cycle. 156
Figure 8.9 The performance of the present neural network model for the vehicle operating on the FTP (Federal Test Procedure) Cycle..... 158
Figure 8.10 The hybrid power system dynamics and the prediction accuracy of the developed neural network model during high-frequency deceleration and acceleration events for the vehicle operating on the FTP (Federal Test Procedure) Cycle..... 159
Figure 8.11 The performance of the present neural network model for the vehicle operating on the Gradient Cycle. 161
Figure 8.12 The hybrid power system dynamics and the prediction accuracy of the present neural network model during extreme driving conditions at the rated power for the vehicle operating on the Gradient Cycle. 162

List of Tables

Table 4-1 Inputs and output parameters of Dataset1 41
Table 4-2 Inputs and output parameters of Dataset2 41
Table 4-3 Initial ANN parameters for Dataset1 44
Table 4-4 Initial ANN parameters for Dataset2 45
Table 4-5 Initial SVR parameters for Dataset1 46
Table 4-6 Voltage prediction accuracy of SVR and ANN on physics-based semi-empirical data (Dataset1) 57
Table 4-7 ANN prediction accuracy (using dropout) on 1-D CFD data (Dataset2) for all output vectors 57
Table 5-1 Feature vectors and prediction attributes for the present fuel cell ANN model 71
Table 5-2 Neural network hyperparameter iteration details 77
Table 5-3 Finalized neural network hyperparameters. 77
Table 5-4 Sample points and fuel cell degradation levels 78
Table 6-1 Correlation of SOC and DOD 92
Table 6-2 ANN Hyperparameter Iteration Results 98
Table 6-3 Design parameters of the artificial neural network (ANN) for lithium-ion battery (LIB) thermal model 100
Table 6-4 The extended Kalman filter (EKF) iterations and tuning parameters 101
Table 6-5 Relative error for the final heat output prediction value of all the models 111
Table 7-1 Diesel particulate filter (DPF) test matrix 120
Table 7-2 Feature vectors for the present DPF thermal ANN model 125
Table 7-3 Final DPF ANN model hyperparameter values 126
Table 7-4 DPF contour plot data presentation 131
Table 7-5 A summary of the percentage error in the ANN predicted bed temperature 137
Table 8-1 Specification for the 2021 Mirai 2nd generation fuel cell electric vehicle (FCEV) tested in the present study. 142
Table 8-2 Feature vectors and prediction variables adopted in the present study 151
Table 8-3 Neural network hyperparameters optimized for the present study 152

Table 8-4 Error attributes for the model predicted fuel cell-battery electric-electric hybrid power system attributes over the different drive cycles investigated. 163

Chapter 1 Introduction

1.1 Background

Climate change due to greenhouse gas emissions is regarded as the most immediate threat to the planet, affecting every single entity and habitat in some or another manner, and one of the significant sources of greenhouse gas emissions is the transport sector (automotive, locomotive, shipping, and aircraft industries) [1], [2]. Especially the automotive vehicles (passenger and commercial vehicles), which are essentially the workhorses of the global economy, currently consume vast quantities of fossil fuels and emit large amounts of carbon, nitrogen oxide, and particle matter, thereby not only impacting climate change but also deteriorating the air quality in major cities [2]. The world has realized the impact of industrial and vehicular emission activity during the COVID-19 pandemic, where most countries have pledged in some manner to reduce the total carbon emissions and committed to an early phaseout of fossil fuel-based energy, propulsion technology that has been an inalienable part of the modern developed economies for over hundred years by moving towards renewable and hydrogen-based economies [3], [4].

Many developing and developed countries worldwide are proposing energy policies focusing on developing, adopting, and commercializing electrochemical energy systems such as batteries and fuel cells as the centerpiece in their transition to green energy [3], [5], [6]. Both batteries and fuel cells are slated to gradually replace most fossil fuel-based combustion technologies due to their higher efficiency and almost nonexistent tailpipe emission in the transport sector, especially in passenger and commercial road transport vehicles [7], [8]. These electrochemical devices achieve this efficiency by electrochemical oxidation of reactants instead of typical combustion, leading to lower losses during the conversion of chemical energy. If the reactant has no hydrocarbon compounds, the resultant emissions are free of carbon and particulate matter [9]. Considering the uncertainty in oil prices and stricter emissions regulations, the high energy and power density of batteries and fuel cells make them ideal for electrified vehicles, as a promising alternative, and are in full-scale commercialization [10]. However, these electrochemical energy systems have their fair share of complex challenges when compared to an internal combustion engine, such as efficiency, range of operation, durability, and chemical,

thermal, and physical degradation affecting their long-term performance, especially considering the modern vehicle's operational environment [10], [11]. These challenges can be overcome by understanding, monitoring, operating, and controlling different internal states and the output attributes of these electrochemical energy systems in a defined operational zone. Pairing various electrochemical energy devices to meet the functional requirements can only be possible by developing an accurate model of these electrochemical energy systems that can predict dynamic behavior and estimate the state of internal parameters where measurement by a sensor is neither feasible nor economical [12], [13].

A fuel cell is an electrochemical energy conversion device that directly converts the chemical energy of reactants (fuels and oxidants) into electrical energy through electrochemical oxidation and reduction reactions. [14]. Fuel cell is an open system where reactants must be constantly fed into the system from the external environment (pressurized tanks and ambient surroundings) to produce electrical energy continuously. The reactants for fuel cells, typically hydrogen (fuel) and oxygen (oxidant), are fed into two electrodes, the anode and the cathode, respectively, separated by an electrolyte [14]. Fuel cells can be broadly categorized based on the fuel type, electrolyte, and operating temperature; however, this thesis focuses on low-temperature hydrogen Proton exchange Membrane Fuel cells (PEMFC). PEMFC consists of a solid polymer membrane that transports protons from anode to cathode during electrochemical reactions and is one of the most widely used in automotive and portable power generation applications due to its efficiency and range of operating temperature, as well as technical maturity [10].

A battery is an electrochemical energy storage device that stores electrical energy in the form of chemical energy during charging and converts it back to electrical during the discharge process [15], [16]. A typical battery pack comprises multiple cells, and each cell consists of 2 electrodes (anode, cathode), an electrolyte, and a separator. Batteries are regarded as a closed system where reactants are stored internally, and the ions resulting from electrochemical reactions travel between the electrodes through the electrolyte during charge and discharge reactions. Batteries are typically classified based on their chemistry, and this proposal focuses on the Lithium-Ion Battery (LIB) system, which is the most widely adopted in electric vehicles and portable electronics due to its superior power density, energy density, and stability [7], [8], [10].

During the charging and discharging process of a Li-ion battery, lithium ions are inserted or extracted from the interstitial space between the atomic layers of the electrodes [15], [16].

In most practical applications, a PEMFC is designed as an energy conversion unit and is operated in conjunction with a battery module as a hybrid system to meet the energy demand and efficiency requirements. To effectively manage such a fuel cell hybrid system, especially in a vehicle environment, a robust fuel cell and battery model (plant model) is necessary to evaluate and calibrate the hybrid system behavior, performance, and efficiency over various operating conditions and to develop fault diagnostics. Accurate characterization and modeling of PEMFC and LIB systems are essential in designing the corresponding stack size, balance of plant, and control strategy to improve durability and interoperability [12], [17], [18], [19].

1.2 Principle of Proton Exchange Membrane Fuel Cell (PEMFC)

The fuel cell principle was discovered in 1839 by William R. Grove, a British physicist [20]. PEMFC working on hydrogen is similar to other fuel cells, generating electricity (DC) through electrochemical oxidation of hydrogen and reduction of oxygen. PEMFC also incorporates the use of platinum as a catalyst (catalysis) to enhance the rate of reaction [14]. A polymer electrolyte membrane is sandwiched between anode and cathode, which only allows protons to pass through it, and electrons are then forced to travel through the external circuit, providing electric power to the load. Hydrogen (H_2) is introduced at the anode, which is a porous electrode consisting of a catalyst layer where hydrogen is oxidized to form protons (H+) and electrons (e-); this reaction is referred to as hydrogen oxidation reaction (HOR). Similarly, Oxygen (O_2) is introduced at the cathode, another porous electrode also consisting of a catalyst layer thicker than the anode catalyst layer where the protons, electrons, and oxygen combine to form water and heat; this reaction is referred to as oxygen reduction reaction (ORR). The electrochemical reactions involved are listed as follows, and a schematic of PEMFC working is shown in Figure 1.1 [14], [21], [22].

At the anode: $$H_2 \Rightarrow 2H^+ + 2e^- \quad (1.1)$$

At the cathode: $$\tfrac{1}{2} O_2 + 2H^+ + 2e^- \Rightarrow H_2O \quad (1.2)$$

Overall: $$H_2 + \tfrac{1}{2} O_2 \Rightarrow H_2O + Heat + Electricity \quad (1.3)$$

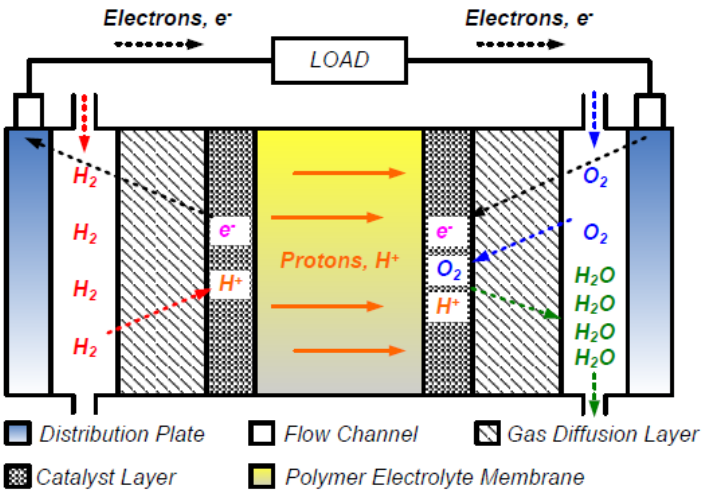


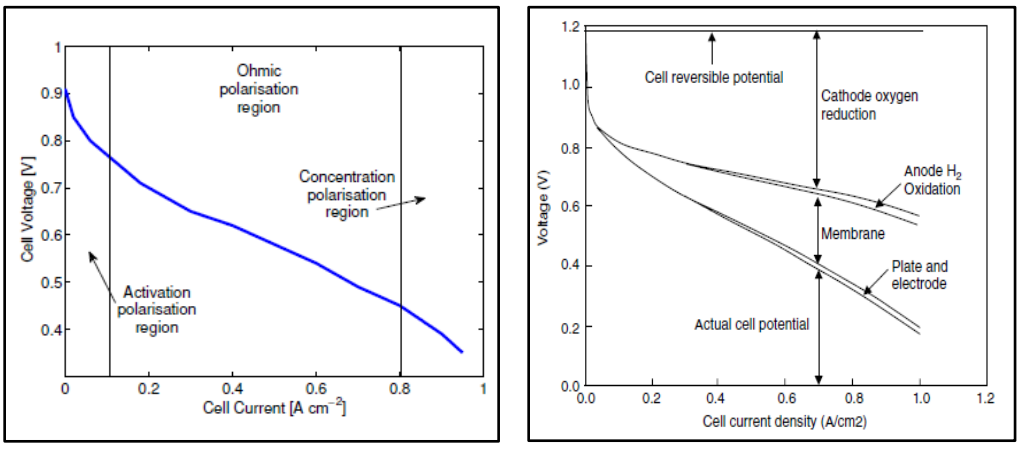
Figure 1.1 Working of proton exchange membrane fuel cells [23]

Typically, reactants are fed through the bipolar plate for uniform distribution; the porous gas diffusion layers comprise carbon fibers that facilitate reactants and product transport. The catalyst layers are made from platinum carbon particles (PTC), pore space, and ionomer material that help with the transport of ions, electrons, reactants, and products resulting from the catalysis [11], [14], [23]. The membrane in a PEMFC is one of the most critical components made from perfluoro sulfonic acid (PFSA), which has a similar PTFE-like polymer backbone and a sulphonic acid group. From an operational point, the PFSA membrane needs to be at 70-90 °C and optimally hydrated for the PEMFC to work efficiently [24], [25]. The membrane resistance increases as the membrane water content decreases, resulting in lower efficiency. Excess hydration will result in the flooding of fuel cells, leading to a catastrophic failure due to the collapse of reactant and product transport. The hydration of the membrane is typically controlled by adjusting the humidity and temperature of reactant gas flowing in along with the overall fuel cell temperature [26]. Due to the electrochemical oxidation, the product water is formed at the boundary of the catalyst layer and membrane, where the reactant gas interacts with the catalyst and electrolyte. The water formed should be removed efficiently as water accumulation decreases the number of sites for the gas exchange and chemical reaction [14], [26]. In short, the reactant flow rate, operational temperature, and gas composition (reactant + water vapor) affect the reactant partial pressure and humidity at the catalyst site, which needs to be controlled precisely. The reversible cell voltage E^0 of a PEMFC operating on hydrogen and oxygen at the standard pressure and temperature of 1 atm and 25˚C is around 1.23V, derived from the Gibbs free energy change (Δg), the maximum available

energy for external work [14]. The Nernst equation incorporating the change in Δg with respect to the reactant pressure and temperature, represents the reversible cell voltage E_{Cell} under any operating condition, and is shown below:

$$\Delta g = nFE^0; \quad E_{Cell} = E^0 + \frac{RT}{2F} \ln \left(\frac{P_H_2 . P_O_2^{\frac{1}{2}}}{P_H_2O}\right) \qquad (1.4)$$

where n is the number of moles of electrons transferred during operation, F is Faraday's constant, E^0 is the open-circuit voltage at the standard pressure and temperature, R is the universal gas constant (8.314 $JK^{-1}\ mol^{-1}$), T is the absolute temperature and P_H_2, P_O_2, P_H_2O are the partial pressures of the hydrogen, oxygen, and water vapor, respectively [27]. PEMFC voltage and current outputs under operation vary depending on the reactant concentration, membrane hydration, and operating temperature. As the operating temperature is increased, the catalytic activity increases, resulting in lower activation overpotential. However, the degradation rate and ohmic resistance can sometimes be impacted, resulting in performance issues. PEMFC output characteristics are represented as a polarization curve, as shown in Figure 1.2.



(a) *(b)*

Figure 1.2 Polarization curve of fuel cell:(a) Polarization regions (b) Deviation from reversible cell voltage *[14], [26]*

The polarization curve plots fuel cell output voltage versus fuel cell current density. The difference between reversible voltage (maximum theoretical) and actual voltage is referred to as overpotential. This overpotential can be classified into three categories, as listed.

a) Activation Overpotential – is caused by the resistance of electrochemical reactions (break and form bonds), which is highly influenced by the cathode reaction conditions and dominant in the region of low current densities

b) Ohmic Overpotential – It is caused by the resistance of materials to the flow of electrons and protons. Membrane resistance to the proton conduction is the most dominant factor and it increases with the current density and is highly influenced by the operating temperature, the thickness of the membrane, and membrane water content

c) Concentration Overpotential—This is due to the loss of reactant concentration at the catalyst site. At high current densities, the reactant consumption rate is higher than the replenishment rate, leading to an exponential decay of voltage due to the starvation of reactants. This is the predominant loss at high current densities (closer to the limiting current density).

The final fuel cell voltage and overpotential can be mathematically represented as shown below.

$$v_{fc} = E_{Cell} - v_{\text{act}} - v_{\text{ohm}} - v_{\text{conc}} \qquad (1.5)$$

where v_{fc} is the final fuel cell output voltage, E_{Cell} is the reversible fuel cell voltage; v_{act}, v_{ohm}, v_{conc} refer to the fuel cell activation overpotential, ohmic overpotential, and concentration overpotential, respectively. In practice, the final voltage output of a single PEMFC depends on the operating condition and is between 0 and 1V; typically, during a regular operation, it is around 0.7V. Like other electrochemical energy devices, multiple cells are stacked to generate the required voltage, which is called stack voltage. Unlike other electrochemical energy systems such as batteries, there is no concept of charge or discharge, and it produces power if there is an adequate supply of reactants. The electrochemical reactions occur at the triple-phase boundary where (1) gases interact with the active catalyst (pore space), (2) the presence of a pathway to conduct electrons away from the catalyst site (Pt/C phase), (3) the availability of an ionic conductor to move the protons into the membrane (ionomer phase) [14], [23].

To summarize, a PEMFC's output voltage is determined by the operating conditions such as fuel cell temperature, reactants supply pressures, the status of membrane hydration (lambda), current density, the composition of the anode, cathode (catalyst, ionomer, pore space), evacuation of water, flow distribution in bipolar plates. Further, the durability of the fuel cell is determined by individual components such as bipolar plates, gas diffusion layers, catalyst layers, and

membrane health, all of which are impacted by operating conditions; therefore, an accurate model is necessary not only to monitor, control and operate efficiently but also to estimate the long-term performance, the total useful life of a fuel cell and diagnostics of the associated system.

1.3 Principle of Lithium-Ion Battery (LIB)

The battery is the most prevalent electrochemical energy storage device that converts chemical energy to electrical energy and vice versa during discharge and charge [15], [16]. Lithium-ion-based chemistries are the most commercialized battery technologies in the automotive and portable electronics industry primarily due to their higher power density, energy density, stability, and minimal memory effect [28]. The charge and discharge process of the Lithium-Ion Battery (LIB) involves the insertion (lithiation) and extraction (delithiation) of lithium ions within the electrodes undergoing electrochemical oxidation and reduction. A typical LIB consists of multiple cells, and each cell is made up of two electrodes (anode, cathode), an electrolyte, and a separator [29]. An anode is regarded as the negative electrode during the discharge of the battery, where it generates the electrons (that pass through the external circuit) and lithium ions (pass through the electrolyte). It is oxidized during the electrochemical reaction, whereas the cathode is regarded as the positive electrode during discharge that accepts the electrons from the external circuit and lithium-ion from the electrolyte, completing the circuit and is reduced during the electrochemical reaction. The electrolyte facilitates the ion conduction medium while maintaining a low reactivity with other components and high thermal stability. The separator is a microporous layer that electrically isolates the electrodes during operation, and these pores in the separator collapse at high temperatures, ceasing the movement of lithium-ion across electrodes and reducing the probability of thermal runaway [29]. This thesis research considers the use of a prismatic $LiFePO_4$ 20 Ah battery from A123 Systems for experimentation, and the electrochemical reactions involved during the charge and discharge process are as follows [15]

At the anode: $Li_xC_6 \Rightarrow C_6 + xLi^+ + xe^-$ (1.6)

At the cathode: $Li_{1-x}FePO_4 + xLi^+ + xe^- \Rightarrow LiFePO_4$ (1.7)

Overall: $Li_{1-x}FePO_4 + Li_xC_6 \Rightarrow LiFePO_4 + C_6$ (1.8)

Under external load during the discharge, the reaction proceeds from left to right and in the reverse direction during the charging process. An illustration of the reaction mechanism during charging and discharging is shown in Figure 1.3.

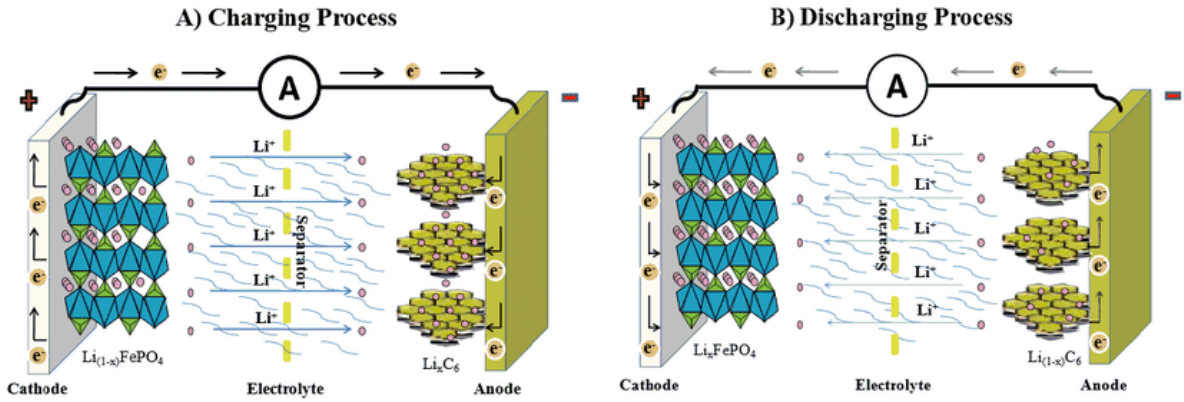


Figure 1.3 Illustration of reaction mechanism inside of a LiFePO4 cell [30]

Similar to other electrochemical energy systems, Gibbs free energy (Δg) expresses the maximum available electric energy and can be coupled with the Nernst equation as follows to estimate the final voltage output of the battery [31].

$$\Delta g = nFE^0; \;\; E_{Cell} = E^0 + \frac{RT}{nF} \ln \left(\frac{a_C^c a_D^d}{a_A^a a_B^b}\right) \qquad (1.9)$$

where n is the number of moles of electrons transferred during operation, F is Faraday's constant, E^0 is the standard potential, R is the universal gas constant, T is absolute temperature, $a_A{}^a$ and $a_B{}^b$ are the chemical activities of the reactants at the anode and cathode, respectively, and $a_C{}^c$ and $a_D{}^d$ are the chemical activities of the products of oxidation and reduction at the anode and cathode, respectively, where chemical activities of the species depend on the battery chemistry 'a' is a logarithmic function.

Similar to fuel cell working, a polarization curve is used to depict the losses associated with battery voltage during operation, such as activation polarization, concentration polarization, and ohmic polarization, all of which increase with the current flow deviating from theoretical cell voltage as shown in Figure 1.4 [29]. Here, activation polarization is caused by the electrochemical reaction of the reactants at the anode and cathode. In contrast, concentration polarization occurs due to the mass transport resistance forming a gradient at the electrolyte and electrode interface. The ohmic

polarization is due to the battery's internal resistance to the current flow, and all of these polarizations cause electrical energy to be converted to heat, contributing to the reduction in final cell voltage. It can be expressed as follows:

$$v_{\text{battery}} = E_{Cell} - [v_{\text{act}} + v_{\text{conc}}]_{\text{anode}} - [v_{\text{act}} + v_{\text{conc}}]_{\text{cathode}} - IR \quad (1.10)$$

where v_{battery} is the final output voltage, E_{Cell} is the open-circuit voltage, I is the current of the cell, and R is the internal resistance of the cell, v_{act}, v_{conc} refer to the activation overpotential and concentration overpotential, respectively. A battery polarization curve depends on the battery type, chemistry, and operating conditions. It can be obtained by measuring the steady-state voltage response of the battery by systematically varying the current density. Stabilization time after each step change in current is essential for the system to reach a steady state with respect to voltage during data acquisition for an accurate polarization curve.

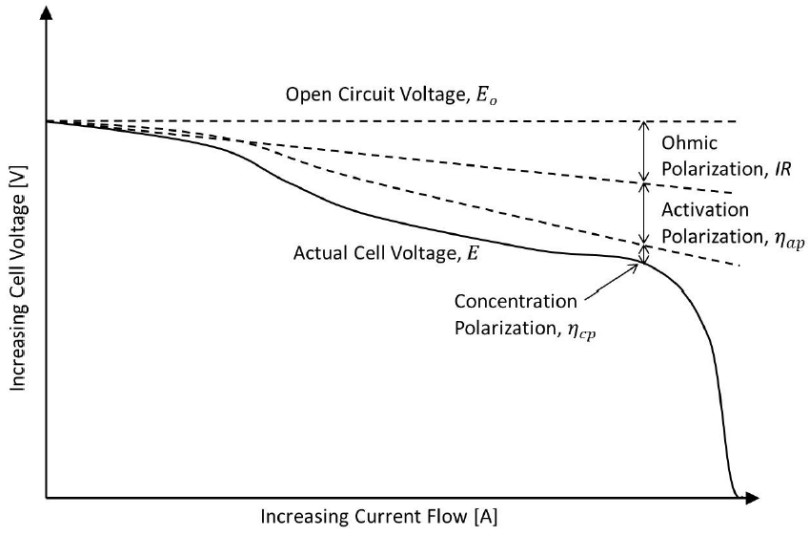


Figure 1.4 Polarization curve of the battery [29]

Battery performance and thermal behavior (heat generation profile) depend on the characteristics of the polarization curve. To understand a battery's performance, other attributes such as capacity, current charge or discharge rate, and State of Charge (SOC) [15] should also be considered. Capacity is a measure of the total charge or electrical energy that can be stored in the battery, often expressed as ampere-hours (Ah) or in watts-hours (Wh). Current charge or discharge rate is the input or output current of the battery during operation, measured as ampere. However, it can also be expressed as C-rate (h^{-1}) (dividing the specified current by the battery capacity). SOC

is defined as the current capacity of a battery divided by the total battery capacity (maximum) measured as a percentage or expressed between zero (0) and one (1), zero being fully discharged and one being fully charged. Depth Of Discharge (DOD) is the opposite viewpoint of the SOC and can be expressed as follows:

$$SOC + DOD = 1; \Rightarrow DOD\ of\ 0.2 = SOC\ of\ 0.8 \quad (1.11)$$

LIB voltage output, heat output is similar to fuel cells and other electrochemical devices, which are governed by operating conditions such as temperature, reactant, and product concentrations (SOC/DOD, Capacity), operating current, and associated cell polarization factors (overpotentials). Therefore, an accurate battery model is necessary to monitor these operating conditions and estimate the internal states to effectively predict the battery performance and heat generation output. This will aid in the effective control and operation of efficient hybrid systems, the prediction of aging, and the diagnostics of the battery and associated systems.

1.4 Modeling of Electrochemical Energy Systems

A model refers to a virtual entity representing the actual system and emulating its behavior, which is also called a plant model. A well-built model will reflect all the system's characteristics in terms of output relations and sensitivities, depending on the requirements. In general, physical systems modeling can be broadly categorized into empirical models, consisting of equivalent circuit models, and mathematical models, which can further be divided into physics-based models and data-based models [32], [33]. Empirical models establish the relationship between the inputs and outputs of the plant through various coefficients based on experimental data and curve fitting. These empirical models neither represent nor consider the physical laws and operating principles involved [34], [35], [36]. Mathematical models are predominantly based on the governing principles of the system rather than curve fitting, where the physical laws or data relations are represented in their mathematical form to establish a relation between the inputs and outputs of the system [37], [38], [39]. Unlike empirical models, these physics-based and data-based models use sound architecture and fundamental theories to reflect the system's behavior and characteristics.

A typical electrochemical device plant model needs to incorporate effects related to various temperatures, reactant concentrations, operating current, environmental factors overpotentials, mechanics of porous media, polymer membrane (fuel cell), microscopic gas diffusion channels, reactant/product flooding, ion transportation & chemical kinetics across various operating conditions resulting in complex interactions affecting the accuracy of the plant model [11], [40].

1.4.1 Empirical Models

Empirical models/equivalent models do not accommodate actual system components and require intensive calibration, and are not suitable for performance prediction, especially when incorporating fluid, thermal management, gas dynamics, and material degradation aspects of the electrochemical system. Equivalent models are a perfect example of the empirical modeling technique of various equivalent fuel cell, and battery models in use, where they represent the behavior of the plant through a series of resistors, inductors, capacitors, and voltage sources, as shown in Figure 1.5 [19], [35].

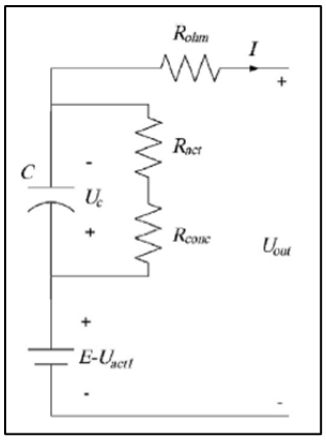


Figure 1.5 Equivalent Fuel Cell Model: Dicks- Larminie model [19]

A change in current immediately changes the voltage drop across this resistor. The capacitor, C, acts as the charge double layer, which delays the dissipation of electronic charges near the electrolyte/electrode interface. A voltage source models the Nernst voltage. UC is the capacitor voltage [V], E and T are the Nernst instantaneous voltage [V], and absolute temperature [K]. In other words, the overpotentials are represented by various resistors, the voltage source represents the reversible voltage, and the capacitor simulates the charge storage (the electrochemical double layer effect at the interface between electrode and membrane electrolyte). Solving this circuit with appropriate values will calibrate the system to mimic the V-I

characteristics of the fuel cell system using the following equations [19]. These models are highly advantageous for analyzing the electrical aspect of the fuel cell and, therefore, are extremely useful for supervisory control purposes where the system's energy storage and distribution are the objective. These simple equivalent models can easily be integrated into an existing conventional or hybrid system to analyze the system energy balance and efficiency improvement aspects. A major disadvantage of such a model is that it has no physical interpretation, cannot be scaled, and requires intensive calibration effort for field application or minor modification [34], [35], [36].

1.4.2 Physics-based Models

Physics-based models require a thorough understanding of the working mechanisms and component interactions considering time and spatial elements. These physics-based models can further be categorized based on dimensionality (1D,2D, and 3D), lumped, distributed, and time-domain (continuous, discrete). However, modeling the physics behind complicated system interactions such as electrochemical reactions and electrode-electrolyte-membrane mechanics is extremely complex, experimentally tedious, requires a lot of sensors to validate, and is computationally intensive. However, this model does not require huge sets of data to build the model but requires a detailed understanding of the physics involved, fundamental information regarding material characteristics, reactant interaction mechanisms, representative math, and computationally intensive fluid dynamics calculations, all of which are limitations when it comes to real-time applications [37], [38], [39].

Zero-dimensional (0-D) models are a perfect example of physics-based models where the system is represented through a series of ordinary differential equations to establish the rate of change of parameters with time, disregarding the spatial distribution [1]. If the spatial aspects are considered, such as length, area, and volume, in addition to time, then such a system is represented with the partial differential equations resulting in 1-D, 2-D, and 3-D models, respectively. These physics-based models, when applied to mechatronic systems, provide us with a thorough analysis of systems performance and influencing mechanisms; thereby, further improvements and control mechanisms can be proposed [18], [26]. However, modeling the physics behind complicated system interactions such as electrochemical reactions and combustions is extremely complex,

experimentally tedious, and computationally intensive, presenting a bottleneck in terms of its usage for in-vehicle applications.

1.4.3 Data-based Models

Data-based models are quite in contrast with the physics-based models, where the entire input-output relations of the plant model are established primarily based on the experimental data using statistics, probability, and network architecture. Here, vast amounts of experimental data are required to train the mathematical algorithms to identify and validate the system dynamics. This modeling is already used in various industries for control and diagnosis purposes. Database modeling can be at the component or system level based on the data availability and the capability to measure certain states. Neural networks and fuzzy logic architecture were perfect examples of such data-based models. The number of neural layers and variables depends on target accuracy, computational power, and application. This kind of modeling is also called a black box model due to the lack of understanding of governing principles and interaction mechanisms behind the physical system.

These models help us predict the outcomes of complicated system interactions, which can be useful for control and diagnosis but may not be that helpful in validating, improving, and simulating new mechanisms virtually. Data-based models help us avoid the complexities of physics-based models and intensive calibration and provide better accuracy in most cases, especially where the complex mechanisms cannot be modeled using governing equations [41], [42], [43], [44]. These models help us to have a quicker turnaround in the development phase, and multiple iterations are feasible relatively without adding to the development time and by avoiding complex physics, which can help in real-time system identification, controls, and diagnostics. Considering the electrochemical system commercialization timeline, it is essential to develop Data-Based Models to reap the maximum benefits in today's age. Artificial Neural Networks (ANN) and Support Vector Machine (SVM) based classifiers and regressors are a few data-based modeling techniques prominent in energy systems and real-time automotive applications.

1.5 Objectives and Scope

Researchers across the globe are on the quest to develop and commercialize electrochemical energy systems (PEMFC, LIB) for automotive applications and green energy transition. However, the complex nature of these systems, especially the electrolyte membrane mechanics of PEMFC, thermal behavior of LIB, fault detection mechanisms, and electrochemical system aging, still needs to be fully understood. There is a pressing need for accurate modeling of electrochemical energy systems to unlock their full potential and improve their reliability and safety. The scope of this thesis covers the development of data-based models using virtual, experimental, and real-world data to predict electrochemical and thermal attributes of energy systems, which have the potential to monitor, control, and diagnose systems. This study directly addresses this need by focusing on developing accurate data-based models and correlations between operational attributes. The models developed have the potential to be applied in real-time to hybrid fuel cell systems, i.e., both PEMFC and LIB systems, making our research immediately relevant to the field. The objectives of this thesis study are as follows:

1. Develop machine learning models (digital twins) to predict system performance, voltage degradation, system outputs, and internal states (component-level).
    i. Develop plant models based on the data derived from computationally intensive high-fidelity physics-based (CFD) or empirical models.
    ii. Formulate the voltage degradation behavior as a regression problem, a proposed alternative to time series models, by introducing the accelerated stress test (AST) cycles/electrode catalyst surface area (ECSA).
2. Develop data-based models that accurately predict thermal behavior and spatial temperature gradients that can be used for real-time monitoring, controls, and diagnostics based on experimental data.
    i. Develop hybrid data-based models that accurately predict the instantaneous heat release rate, total heat output, and detect sensor faults.
    ii. Develop a comprehensive data-based model to predict spatial temperature distribution and temperature dynamics during exothermic reactions.

3. Develop an accurate and computationally fast data-based model for fuel cell-battery powertrain systems to monitor and predict hybrid system dynamics in real-time based on vehicle data.

The chapters of this thesis are organized as follows:

Chapter 2 discusses the background and numerical representation of data-based modeling techniques. It provides a detailed working description of the neural network and support vector regressor algorithm, along with the associated terminology and hyperparameter calibration process. Data nonlinearity, various activation functions, and the implementation of dropout techniques are also discussed in detail. Chapter 3 briefly discusses a few of the latest data-based models published in the literature, their associated applications for PEMFC and LIB systems, and their limitations.

Chapter 4 meticulously evaluated the viability of the data-based models by using the data gathered from cell-level physics-based and semi-empirical models and simulated various fuel cell operating conditions in a virtual environment. This data was then rigorously analyzed, conditioned, and organized to develop data-based models that are essentially digital twins of the simulated physics-based models. The models developed in this study demonstrated exceptional accuracy and computational speed in predicting the fuel cell voltage and membrane internal states, faithfully replicating the nonlinear behavior of the computational fluid dynamics-based fuel cell model.

Chapter 5 delves into the usage of cell-level experimental data from the G20 to train and develop the data-based model. Here, a comprehensive multi-input-multi-output neural network model is conceptualized to simultaneously predict the fuel cell voltage degradation over time and the change in temperature and reactant attributes. Regression problem formulation, data preprocessing, and iterative model calibration process are discussed in detail. The trained neural network model evaluation results are also discussed when predicting the cell output voltage, reactants' outlet pressure, and temperature.

Chapter 6 introduces a hybrid data-based model, which is a combination of physics-based governing equations and machine-learning techniques. Here, a novel approach of using a neural network in combination with an extended Kalman filter was developed to accurately predict the heat generation rate of the LIB during discharge, where the experimental data generated from the

battery test station was used to train the neural network. The trained hybrid model predicted the heat generation rate of the LIB with great accuracy when compared to the experimental results, and the model was able to identify sensor faults by comparing the cumulative heat output value.

Chapter 7 discusses a data-based modeling approach to predict thermal behavior and spatial temperature distribution during an exothermic reaction. As the availability of exothermic thermal runway data from the LIB system is limited, a diesel particulate filter was regenerated at various soot loads to generate exothermic data of an open system, similar to the state of charge of a LIB system, the soot level inside the filter served as the system's internal state, and additional parallels between cell temperature and filter bed and exhaust temperatures can be drawn for comparison purposes. Performance attributes of the trained neural network to predict spatial temperature distribution and peak bed temperatures during an exothermic reaction are elaborated.

Chapter 8 discusses the development of a data-based model based on supervised machine learning to predict fuel cell hybrid power system dynamics in a Toyota Mirai vehicle—data acquisition process from the vehicle under various driving conditions, data analytics, conditioning, preprocessing, and formulation are discussed in detail. The performance and insights into the trained neural network’s prediction of the dynamics of hybrid power systems, such as minimum cell voltages, system temperatures, and hybrid system behavior, are discussed at length.

In summary, the novel contributions of the thesis can be summarized as follows:

1. Developed a surrogate data-based model (digital twin) to predict PEMFC performance and membrane dynamics based on data derived from the physics-based models.
2. Developed a comprehensive multi-input, multi-output data-based model to predict the voltage degradation, temperature, and pressure dynamics of the PEMFC across various operating conditions based on experimental cell-level data.
3. Developed a hybrid data-based model (a combination of Kalman Filter and Neural Network) to predict the thermal behavior of the LIB and demonstrated the applicability of controls and diagnostics.
4. Developed a data-based model to predict the thermal gradient and peak temperatures during an exothermic reaction as an alternative to complex computational fluid dynamics models
5. Conceptualized and developed a data-based model to predict the powertrain dynamics of a fuel cell battery hybrid vehicle across different drive cycles.

Chapter 2 Machine Learning Techniques for Data-Based Modeling

***This chapter is adapted from Legala, Adithya, et al. "*Machine learning modeling for proton exchange membrane fuel cell performance*." Energy and AI, vol. 10, Nov. 2022, p. 100183, doi: 10.1016/j.egyai.2022.100183.

Modeling physical systems involves solving multi-input multi-output (MIMO) problems that require advanced data-modeling techniques to capture the intricate relationships between system input and output variables. Although there are numerous supervised machine-learning techniques, artificial neural network and support vector machine regressor are the most prominently used in the space of electrochemical and thermal system modeling. This chapter summarizes the working of neural network and support vector machine regressor and their associated attributes. Following background information is adapted from lecture notes and literature [45] [46].

2.1 Artificial Neural Network (ANN)

An Artificial Neural Network (ANN) is a combination of neurons, which are the basic processing units that regulate computational activity based on the designated activation function and associated inputs. In terms of functionality, this architecture is a clone of the biological neuron, and with the help of a backpropagation algorithm, it can solve and model regressions accurately.

With no loss of generality, let's consider a neural network consisting of an input layer $(k-1)$, a hidden layer k and an output layer $(k+1)$ as shown in Figure 2.1. Here the input layer $(k-1)$ contains input data to the neural network, hence the output of the neurons in the input layer is simply the input data itself (without any processing). The neurons in the hidden layer (k) process the data from the neurons in the input layer using their respective weights $W_{nm}^{(k)}(m=1,2,\dots,r)$, biases $b_n^{(k)}$ $(m=1,2,\dots,r)$ and applies an activation function, to produce an output which is then fed into the neurons in the output layer. It might be pointed out that the weights and biases are normally different for each neuron, and the activation function can be also different for each neuron (the so-called heterogeneous networks), which is not standard neural network architecture, or

simply identical for all the neurons (the homogeneous networks). In this instance, a common activation function is considered for all the neurons. The output layer $(k+1)$ then takes the processed outputs from the hidden layer, applies the weights, biases, and activation function to produce the final predicted value of the network $\hat{\mathbf{y}}$. A schematic of the neural network is shown in Figure 2.1 where for the clarity of description on how such a network works only one neuron in the hidden layer is shown being connected to the neurons in the input layer, and likewise only one neuron in the output layer is shown being connected to the neurons in the hidden layer. In reality all the neurons in the hidden layer are connected to all the neurons in the input layer, respectively; and all the neurons in the output layer are connected to all the neurons in the hidden layer, respectively.

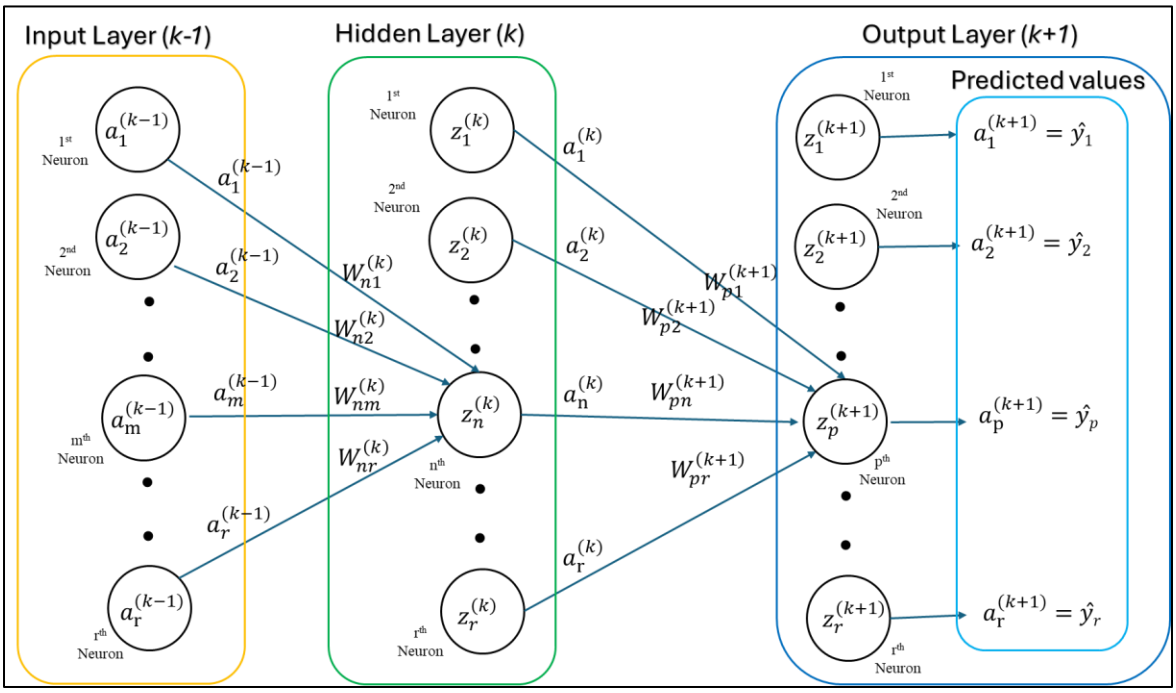


Figure 2.1 Schematic of the nth neuron in the kth (hidden) layer and the pth neuron in the output layer of an artificial neural network, illustrating the network operation.

Neural network processing can be divided into two distinctive phases: forward propagation, error calculation and backpropagation. First, neural network is initialized with weights $W_{nm}^{(k)}$ and biases $b_n^{(k)}$ that are small random values (e.g., drawn from a uniform or Gaussian distribution), here $W_{nm}^{(k)}$ represents the weight connecting neuron m in layer $k-1$ to neuron n in layer k, and $b_n^{(k)}$ represents bias of the neuron. In this case, let's assume that the input layer $(k-1)$ has r neurons that represent input features as

$$\mathbf{a}^{(k-1)} = \left[a_1^{(k-1)}, a_2^{(k-1)}, \ldots, a_r^{(k-1)}\right] \quad (2.1)$$

These inputs are fed into the network's hidden layer (k) where the input features are processed by using weights, biases, and an activation function resulting in outputs from the hidden layer (k) represented as

$$\mathbf{a}^{(k)} = \left[a_1^{(k)}, a_2^{(k)}, \ldots, a_r^{(k)}\right] \quad (2.2)$$

These outputs of the hidden layer are further processed by the output layer $(k+1)$ to calculate the final predicted value represented as

$$\hat{\mathbf{y}} = \mathbf{a}^{(k+1)} = \left[a_1^{(k+1)}, a_2^{(k+1)}, \ldots, a_r^{(k+1)}\right] \quad (2.3)$$

Forward Propagation:

During the forward propagation phase, the outputs of each neuron in the hidden layer are computed first from the data from the input layer before applying the activation function.

The pre-activation value for neuron n in layer k is:

$$z_n^{(k)} = \sum_{m=1}^{r} W_{nm}^{(k)} a_m^{(k-1)} + b_n^{(k)} \quad (2.4)$$

Here $W_{nm}^{(k)}$ is the weight connecting neuron m in layer $(k-1)$ to neuron n in layer (k),

$b_n^{(k)}$ is the bias associated with neuron n in layer (k),

$a_m^{(k-1)}$ is the activation (output) of neuron m in the previous layer.

The summation over m indicates that the contributions from all neurons in layer $k-1$ are aggregated for neuron n in layer k and the activation function is applied over the resultant summation with the bias considered.

The post-activation value is obtained by applying the activation function σ to $z_n^{(k)}$:

$$a_n^{(k)} = \sigma\left(z_n^{(k)}\right) \quad (2.5)$$

This is the output of neuron n in hidden layer (k), i.e., $a_n^{(k)}$

Similarly, the output layer $(k+1)$, process the outputs of all the hidden layer neurons and calculates the final predicted value $\hat{\mathbf{y}} = \mathbf{a}^{(k+1)}$.

$$z_n^{(k+1)} = \sum_{m=1}^{r} W_{pn}^{(k+1)} a_m^{(k)} + b_n^{(k+1)} \tag{2.6}$$

$$a_n^{(k+1)} = \sigma\left(z_n^{(k+1)}\right) = \hat{y}_n \tag{2.7}$$

After the forward propagation the network calculates a predicted value $\hat{\mathbf{y}}$ which is then compared to the desired value or true value to calculate if the prediction is within the accepted tolerance (error) if not the error backpropagation is implemented to update all the weights and bias.

Error Backpropagation:

The primary goal is to minimize the loss function which measures the discrepancy between the predicted output of the network and the true target. This is achieved by adjusting the network's parameters (weights and biases) using gradient descent. Once the predicted values $\hat{\mathbf{y}}$ are computed, they are compared with their corresponding actual (true) values to determine the error that might exist. If the error is less than a pre-specified tolerance, the predicted values are accepted, and the network is considered established. Normally the error would be larger than the tolerance, hence is required to be reduced to or less than the tolerance. Therefore, this error information is used to adjust (or revise) the weights and biases in the output and hidden layers in order to reduce the error to the acceptable level. This process is called error backpropagation, as described below. The error (or loss) for a single output neuron n is defined as:

$$E_n = \frac{1}{2}(y_n - \hat{y}_n)^2 \text{ (squared error loss for online training)} \tag{2.8}$$

where y_n is the true value. Similarly, the total error for all the outputs from all the neurons in the entire output layer can be written as:

$$E = \sum_{n=1}^{r} \frac{1}{2}(y_n - \hat{y}_n)^2 \text{ for online training, or} \tag{2.9}$$

$$E = \sum_{n=1}^{r} \frac{1}{r}(y_n - \hat{y}_n)^2 \text{ for batch training} \tag{2.10}$$

Both versions of the above error expressions can be used, depending on whether it is online training or batch training. In the case of online training, weights are updated immediately after each individual data point is processed i.e., after each error calculation and the factor 1/2 simplifies the derivative during backpropagation, in this case as it will become clear later when the backpropagation process is described. On the contrary during batch training weights are updated once per full dataset thereby the factor 1/r. In the batch propagation the cumulative error over all is calculated and the weights are updated by using the cumulative error.

Error signal (δ) is a quantity that captures how much a neuron's activation (or pre-activation) contributes to the overall loss of the network. It is the gradient of the loss E respect to the neuron's pre-activation i.e., is the derivative of the error with respect to the pre activation, it calculates the impact of neuron's output on the total error. Error function is used to update the weights during backpropagation, guiding the network to reduce the error in subsequent iterations, which is a vector quantity i.e., one value for each neuron in every layer.

Error signal for neuron n in layer $(k+1)$ is calculated as follows:

The partial derivative of the loss with respect to the pre-activation $z_n^{(k+1)}$:

$$\delta_n^{(k+1)} = \frac{\partial E}{\partial z_n^{(k+1)}} = \frac{\partial E}{\partial \hat{y}_n} \cdot \frac{\partial \hat{y}_n}{\partial z_n^{(k+1)}} \tag{2.11}$$

$\frac{\partial E}{\partial \hat{y}_n}$ is the sensitivity of the loss function to the output and $\frac{\partial \hat{y}_n}{\partial z_n^{(k+1)}}$ is derivative of the activation function analyzing the impact of pre activation function on the output of neuron.

$$\frac{\partial E}{\partial \hat{y}_n} = -(\tfrac{1}{2})(2)\,(y_n - \hat{y}_n) = -(y_n - \hat{y}_n) \tag{2.12}$$

$$\frac{\partial \hat{y}_n}{\partial z_n^{(k+1)}} = \sigma'\left(z_n^{(k+1)}\right) \tag{2.13}$$

For the squared error loss and activation σ, the above equation becomes:

$$\delta_n^{(k+1)} = -(y_n - \hat{y}_n) \cdot \sigma'\left(z_n^{(k+1)}\right) \tag{2.14}$$

The chain rule allows us to break down this dependency step by step, layer by layer. Thereby the error signal for neuron n in layer (k) using the chain rule, the error propagates backward:

$$\delta_{\mathrm{n}}^{(k)} = \frac{\partial E}{\partial z_n^{(k)}} \tag{2.16}$$

$$\delta_{\mathrm{n}}^{(k)} = \sum_{p=1}^{r} \frac{\partial E}{\partial z_p^{(k+1)}} \cdot \frac{\partial z_p^{(k+1)}}{\partial z_{\mathrm{n}}^{(k)}} \tag{2.17}$$

Where $z_p^{(k+1)}$ is the pre-activation value of neuron p in the next layer $(k+1)$ and $z_n^{(k)}$ is the pre-activation value of neuron n in the current layer k. The summation aggregates the contributions from all neurons in the next layer because the error signal of a hidden neuron depends on its influence on all neurons in the subsequent layer. The relationship between $z_p^{(k+1)}$ and $z_n^{(k)}$ is determined by the weights $W_{pn}^{(k+1)}$ connecting the two layers:

$$z_p^{(k+1)} = \sum_{n=1}^{r} W_{pn}^{(k+1)} \cdot a_n^{(k)} \tag{2.18}$$

Taking the derivative:

$$\frac{\partial z_p^{(k+1)}}{\partial z_n^{(k)}} = W_{pn}^{(k+1)} \tag{2.19}$$

The output of neuron n in the hidden layer is:

$$a_n^{(k)} = \sigma\left(z_n^{(k)}\right) \tag{2.20}$$

The derivative is:

$$\frac{\partial a_n^{(k)}}{\partial z_n^{(k)}} = \sigma'\left(z_n^{(k)}\right) \tag{2.21}$$

$$\delta_n^{(k)} = \frac{\partial E}{\partial z_n^{(k)}} = \sum_{p=1}^{r} \delta_p^{(k+1)} W_{pn}^{(k+1)} \cdot \sigma'\left(z_n^{(k)}\right) \tag{2.22}$$

where $W_{pn}^{(k+1)}$ are the weights connecting neuron n in layer k to neuron p in layer $k+1$.

Gradients are then computed to update the weights and biases during the training to update the weights and bias values that are used to reduce the error. Gradient for weight $W_{nm}^{(k)}$ connecting neuron m in layer $k-1$ to neuron n in layer k is calculated as follows:

$$\frac{\partial E}{\partial W_{nm}^{(k)}} = \delta_n^{(k)} \cdot a_m^{(k-1)} \tag{2.23}$$

For bias $b_n^{(k)}$ in layer k :

$$\frac{\partial E}{\partial b_n^{(k)}} = \delta_n^{(k)} \tag{2.24}$$

Once the gradients are computed the new weights are calculated by using the gradient descent

$$W_{nm(new)}^{(k)} = W_{nm(old)}^{(k)} - \eta \frac{\partial E}{\partial W_{nm}^{(k)}} \tag{2.25}$$

$$b_{n(new)}^{(k)} = b_{n(old)}^{(k)} - \eta \frac{\partial E}{\partial b_n^{(k)}} \tag{2.25}$$

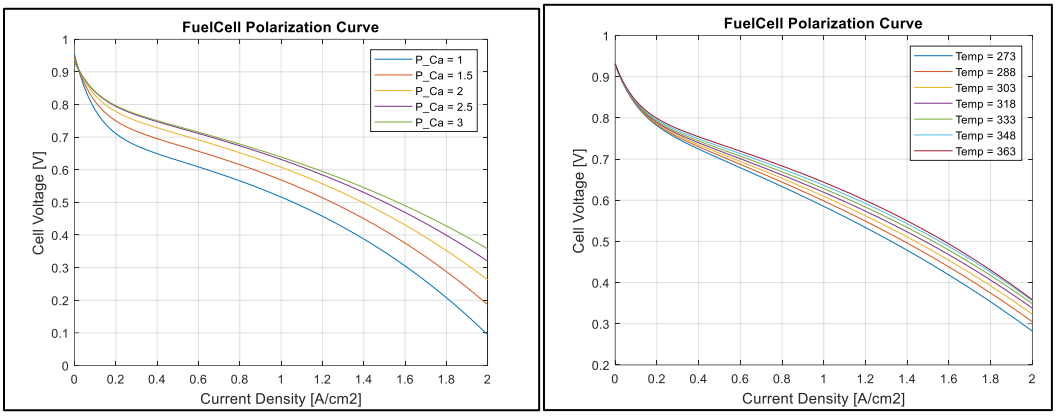
$W_{nm(new)}^{(k)}$ and $b_{n(new)}^{(k)}$ are the new weight and bias, respectively, η is the learning rate,

$W_{nm(old)}^{(k)}$ and $b_{n(old)}^{(k)}$ are the old weight and bias, respectively

Additional information, sample numerical and associated optimizers are available in the appendix A adapted from lecture notes [46].

2.1.1 *Linearity and Non-linearity of the System*

In the case of a PEMFC or LIB, the model must represent the device's linear and non-linear behavior, depending on the operational zone. The system characteristics are typically nonlinear (exponential) at low and high current density conditions, as shown in Figure 2.2.



(a) *(b)*

Figure 2.2 Fuel cell polarization curve nonlinearity for (a) different pressures and (b) different temperatures.

2.1.2 *Activation Functions*

The activation functions dictate the non-linearity of the neural networks depending on the sensitivity of the input feature vectors. Various nonlinear functions are considered to model this neural network, and a quick mention of a few activation functions that are considered in this study.

i. Sigmoid (Logistic function): The Sigmoid function was introduced to Artificial Neural Networks (ANN) in the 1990s to replace the step function, and the output is centered around 0.5, a graphical representation of the sigmoid function and its derivative is shown in Figure 2.3. The sigmoid function has a well-defined nonzero derivative, helping stochastic gradient descent to improve at every epoch. Significant issues are vanishing gradient and computationally expensive [47].

ii. Hyperbolic Tangent (Tanh): Tanh has characteristics like Sigmoid and can work with Gradient Descent. Tanh function output is centered around 0; a graphical representation of the Tanh function and its derivative is shown in Figure 2.3. Like sigmoid, it is also subjected to vanishing gradient and is computationally expensive [47].

iii. Rectified Linear Unit (ReLU): It is primarily implemented in deep learning, and the ReLU function is composed of two linear pieces to account for non-linearities; a graphical representation of the ReLU function and its derivative is shown in Figure 2.3. Unlike Sigmoid and Tanh, the output of ReLU does not have a maximum value, helping it address the vanishing gradient issue. ReLU is computationally easy as there is no exponential operation [47].

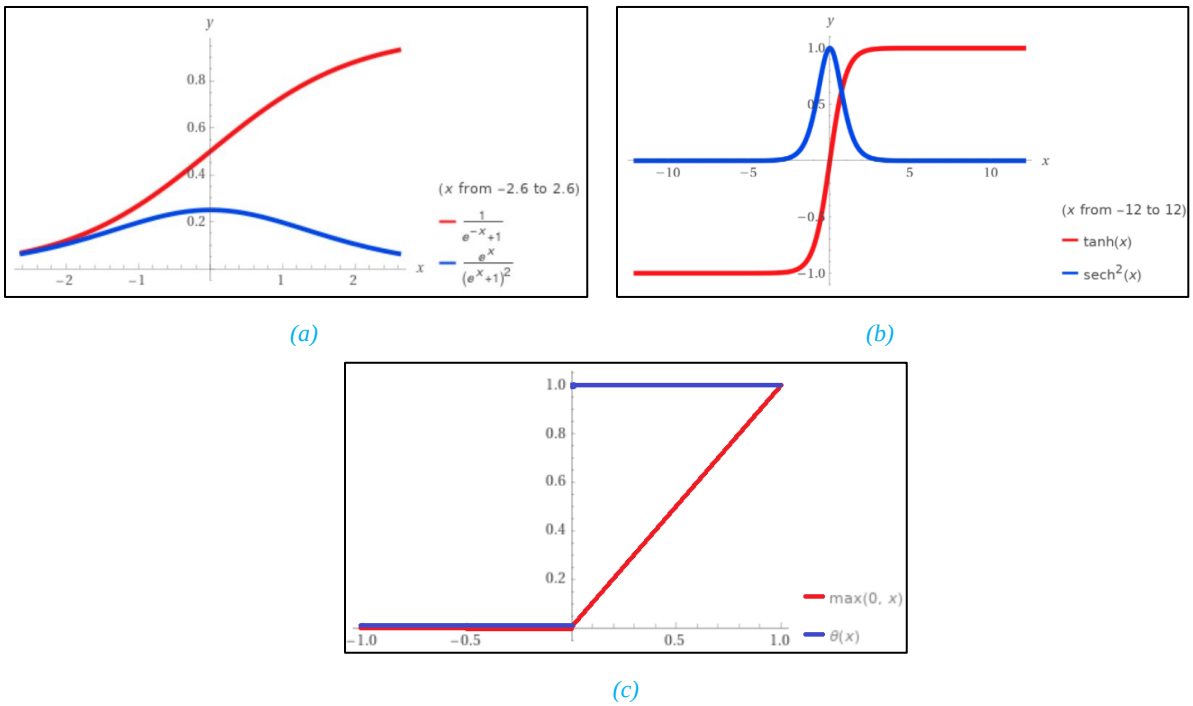


Figure 2.3 (a) Sigmoid function (red-colored curve) and its derivative (blue-colored curve); (b) Tanh function (red-colored curve) and its derivative (blue-colored curve); (c) Rectified linear unit function (red-colored curve) and its derivative (blue-colored curve)

2.1.3 Dropout Probability

Certain neuron connections within the network are randomly disconnected based on a specific probability value to prevent overfitting during the neural network's training process. This specific probability number is called dropout probability and needs to be calibrated depending on the data, predicted parameters, and accuracy needs. Figure 2.4 **Error! Reference source not found.**shows an example of a feed-forward neural network with and without dropout. The dropout probability uses a Bernoulli distribution (a probability distribution used with a parameter $1-p$) to model a binary random variable that takes on one of two possible outcomes: 1 (success) with probability $1-p$, and 0 (failure) with probability p.

A Bernoulli random variable m is defined by the following probability mass function (PMF):

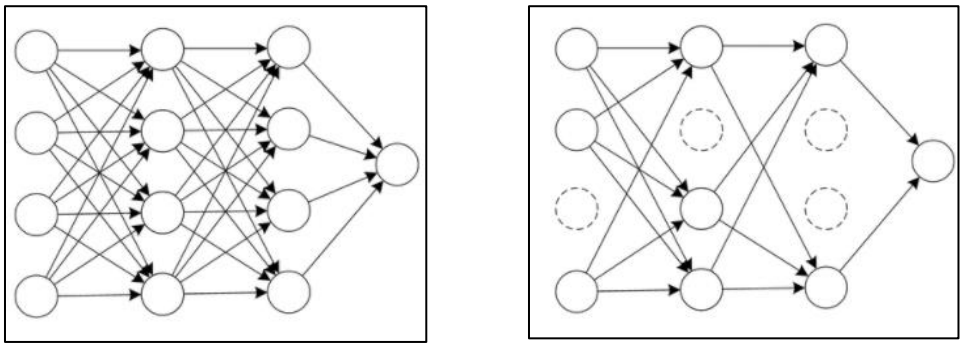
$$P(m=1) = 1-p \qquad (2.26)$$

$$P(m = 0) = p \qquad (2.27)$$

$m = 1$: The event occurs (neuron is retained in the dropout case).

$m = 0$: The event does not occur (neuron is dropped in the dropout case).

p : The probability of dropping a unit (dropout rate – calibrated).



(a) *(b)*

Figure 2.5 Neuron connections: (a) without dropout; (b) with dropout.

2.1.4 Training and Calibration

Parameters like learning rates, loss function, number of epochs, and correction factors are calibrated to prevent any overtraining or undertraining of the models by validating with the available testing data. All the iterations are ranked by quantifying the final error with the help of coefficient of determination (r-squared/R^2) and root mean square error (RMSE), as defined below, in addition to mean absolute error (MAE) and mean squared error (MSE),

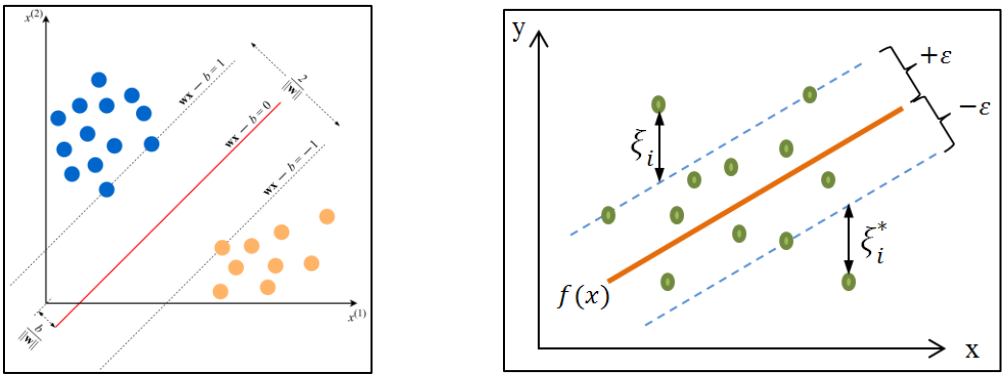
$$R^2 = 1 - \frac{\text{sum squared regression (SSR)}}{\text{the total sum of squares (SST)}} \qquad (2.28)$$

$$RMSE = \sqrt{\frac{\sum_{i=1}^{n} \|y(i) - \hat{y}(i)\|^2}{n}} \qquad (2.29)$$

where n is the number of data points, $y(i)$ is the i-th measurement value, and $\hat{y}(i)$ is the corresponding value of prediction.

2.2 Support Vector Machine Regressor (SVR)

Support Vector Machine (SVM) is one of the most used techniques to resolve classification problems. The SVM helps us to find a line/hyperplane (in multidimensional space) that separates two classes. A decision boundary serves as a demarcation line to split the classes from each other. Support Vector Machine Regressor (SVR) uses a similar concept to approximate mapping from multiple input feature vectors to output based on a training sample. Here, the objective is to consider the points within the decision boundary line and tune the SVR to incorporate the maximum number of points, parallelly minimizing the ||w|| = (|+ε|) + (|-ε|), where ||w|| is the weight vector norm and epsilon 'ε' is a margin around the regression line where there is no penalty. ||w|| measures the complexity of the regression function and is minimized in the optimization, 'ε' sets the margin of tolerance for error and indirectly influences ||w||. The major tunable parameters are epsilon 'ε' and penalty factor 'C', here 'C' is the regularization parameter that controls the trade-off between model complexity and tolerance for errors. 'ε' in the SVR model refers to the epsilon tube within which no penalty is imposed in the loss function for data points predicted within a distance ξ from the actual value. Figure 2.5 shows a sample data set along with the corresponding SVM and SVR implementation.



(a) *(b)*

Figure 2.6 (a) Classification of Support Vector Machine (SVM) [48] *; (b) SVM regression* [49]

Only data points lying outside the epsilon tube contribute to the error. The objective of the SVR is to minimize the following functions.

$$\text{Minimize } \frac{1}{2} \| \mathbf{w} \|^2 + C \sum_{i=1}^{m} (\xi_i + \xi_i^*) \qquad (2.30)$$

Complying with the following constraints

$$\boldsymbol{y_i} - (\mathbf{w} \cdot \mathbf{x}_i) - b \leq \varepsilon + \xi_i \quad (2.31)$$

$$(\mathbf{w} \cdot \mathbf{x}_i) + b - \boldsymbol{y_i} \leq \varepsilon + \xi_i^* \quad (2.32)$$

$$\xi_i, \xi_i^* \geq 0, i = 1, \ldots, m \quad (2.33)$$

where $\mathbf{x}_i$ is the input feature vector, $\boldsymbol{y_i}$ is the target variable (observed or actual output associated with $\mathbf{x}_i$), m is the total number of data points, and $\mathbf{w}$, b, and $\boldsymbol{\xi}$ are the pseudo hyperparameters, where w is the weight vector, b is the bias, and ξ is the distance from the boundary determined by the SVR based on the data and epsilon (ε) , regularization parameter C, are the tunable parameters acting as design variables.

Chapter 3 Literature Survey

This chapter summarizes the available literature and recent data-based models that use the latest machine-learning techniques to address the problems of the PEMFC and LIB systems.

3.1 Machine Learning Models for PEMFC System

A fuel cell is an open electrochemical energy system with a wide variety of feature vectors, almost like an internal combustion engine, with charge induction (reactant + fuel) and exhaust attributes that provide a wide range of data acquisition options. Machine learning applications to develop data-based models are relatively in an early stage for the fuel cell area. Wang [50] has summarized the recent application of neural networks and other machine algorithms to predict the performance, material selection, and durability estimation of fuel cells and their components. Figure 3.1 shows a feed-forward artificial neural network schematic, where current, temperature, pressure, flow rate, and humidity are used as feature vectors (inputs) to predict the fuel cell's voltage output.

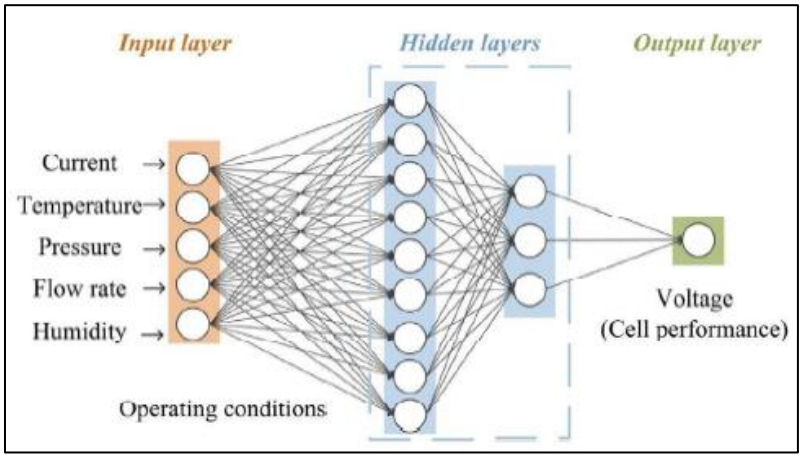


Figure 3.1 Schematic of artificial neural network architecture for fuel cell voltage prediction [50]

Similarly, Kheirandish [51] used Support Vector Machine Regression (SVR) to model a PEMFC and successfully predicted the system's voltage, power, and efficiency aspects. The results and boundaries of the SVR algorithm are shown in Figure 3.2 which illustrates the correlation between ANN and SVR on the same dataset where both the algorithm's prediction values are in agreement with each other.

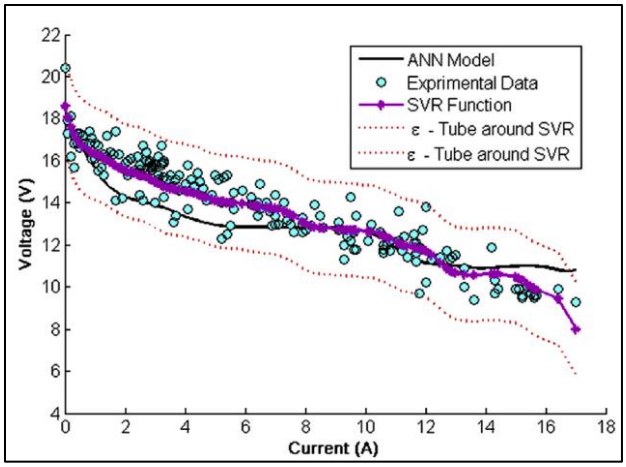


Figure 3.2 Results of the support vector regression algorithm for fuel cell voltage prediction [51]

Mehrpooya [52] had developed a hybrid neural network method to model a micro PEMFC which consists of a Group Method of Data Handling (GMDH) neural network and empirical equations incorporated with the help of a genetic algorithm where humidity (x1), temperature (x2), oxygen flow rate (x3), hydrogen flow rate (x4), current density (x5) are considered as input feature vectors [52]. Figure 3.3 shows the GMDH neural network and the input features (x1, x2,…x5).

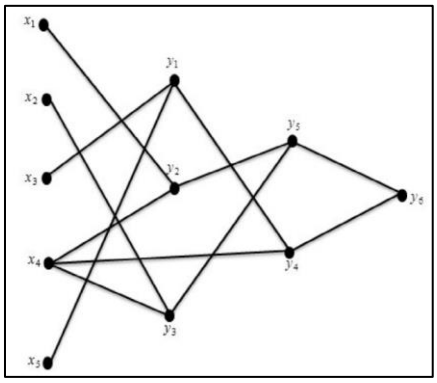


Figure 3.3 Representation of a group method of data handling neural network for micro fuel cell [52]

Han has used a similar hybrid approach with the implementation of SVR to account for various operating conditions in combination with a voltage empirical equation to predict the PEMFC polarization curve [53] Figure 3.4 shows a schematic representation of the hybrid architecture, which combines SVM and an empirical equation for the fuel cell.

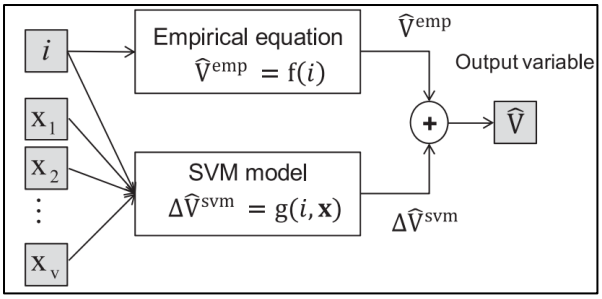


Figure 3.4 Fuel cell hybrid model consisting of support vector machine and empirical equation [53]

Han also has conducted a comparative study of ANN and SVR to predict the performance of PEMFC operation and estimated the effects of varying reactant pressure and cell temperature across the range of operating conditions [54]. Deng has used a state-space system in combination with a recurrent neural network (RNN) to derive a new control-oriented data-driven model for PEMFCs and predicted the stack temperature, voltage, power, and other parameters with reasonable accuracy [55]. Figure 3.5 shows the final error values of various predicted fuel cell output attributes.

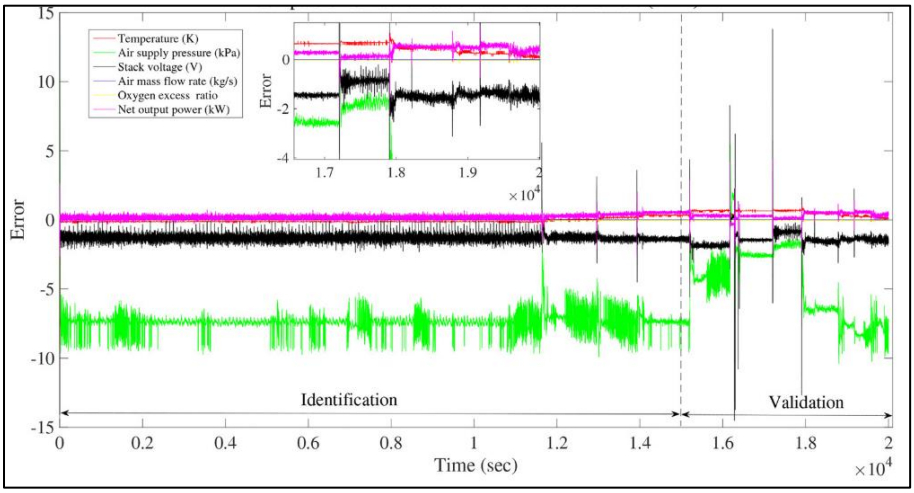


Figure 3.5 Comparison of fuel cell attribute errors during validation [55]

Khajeh developed a hybrid model by combining the physics-based catalyst layer model with neural networks where ionomer film covering the agglomerate, agglomerate radius, platinum, and carbon loading, membrane content, gas diffusion layer (GDL) penetration content, and catalyst layer (CL) thickness are used as input feature vectors to predict the activation overpotential[56]. A comparison between actual activation overpotential and model-predicted activation overpotential is shown in Figure 3.6.

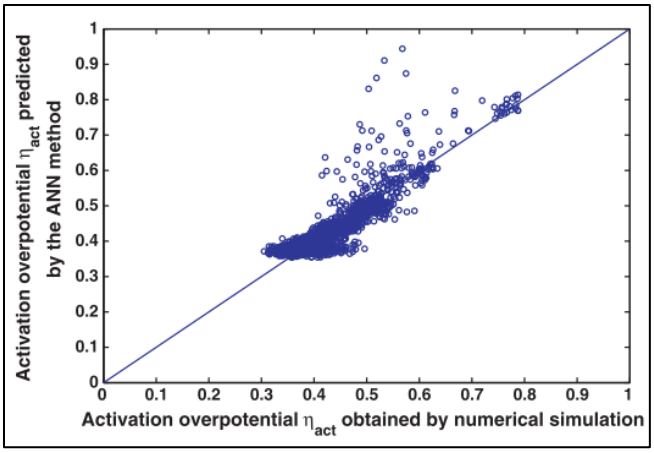
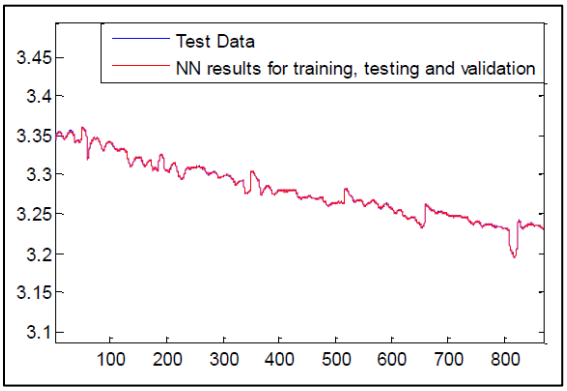


Figure 3.6 Comparison of activation overpotential of fuel cell catalyst layer [57]

Similarly, the durability aspects of PEMFC such as state of health and voltage over time can be predicted by an autoregressive neural network as shown by Mao and Jackson using 1200 hours of PEMFC operational data [57]. Figure 3.7 shows the accuracy of the voltage predicted compared with the test data over the fuel cell's life.



X-Axis – Time (Hours); Y-Axis -Stack Voltage

Figure 3.7 Autoregressive neural network result stack voltage (V) Vs. time (hours) [57]

3.2 Machine Learning Models for LIB System

Similar to PEMFC, the LIB system is an electrochemical system that consists of complex chemical kinetics and ion transportation phenomena; however, since it is a closed system, there are no external reactant input or product exhaust parameters, relatively reducing the number of

available feature vectors to the model. There are four major measurement parameters in a LIB system, which are operating current, temperature, voltage, and total resistance/impedance typically, numerous machine learning models in this area are used to predict the internal states of the LIB, which cannot be measured by a sensor but needs to be estimated such as State of Charge (SOC) or State of Health (SOH). LIB system operation generates heat due to the various overpotentials associated with charging and discharging; this heat, in turn, raises the temperature of the battery environment, affecting the system's overall performance unless dissipated appropriately using a thermal management system. Here is a quick summary of available data-based models that study the aspect of the LIB thermal behavior modeling and its impact on performance

Wang [58] has used a Convolution Neural Network (CNN) and linear regression to predict the internal temperature of the LIB pack, as shown in Figure 3.8. Here, the external temperature measurement was used as input feature vectors to predict the internal temperatures within the LIB pack in real-time with a mean square error of 0.047.

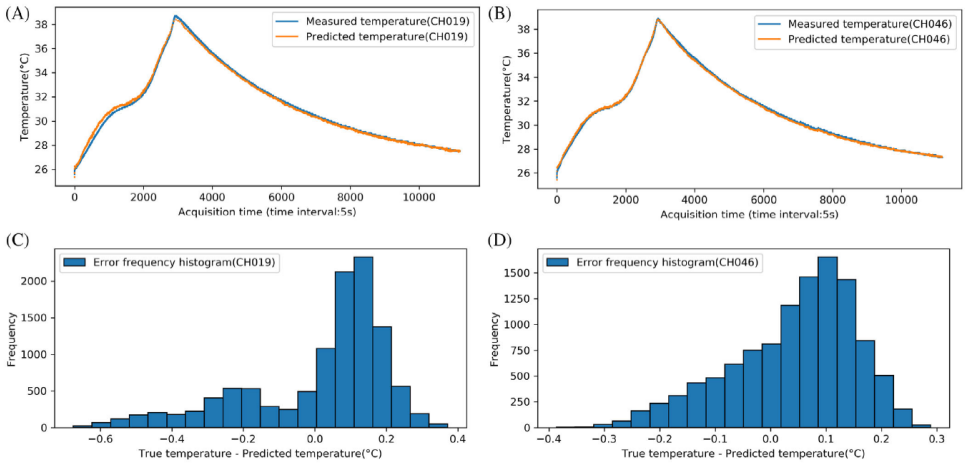


Figure 3.8 Comparison of the measured internal temperature and the predicted internal temperature by CNN [58]

Shashank has implemented a neural network-based model to predict the heat generated by a LIB under various ambient temperatures and nominal capacities as shown in Figure 3.9. This study considered the use of DOD, nominal capacity, ambient temperature, and discharge rate as the feature vectors for a feed-forward neural network with one hidden layer consisting of six

neurons and the Levenberg–Marquardt algorithm of MATLAB to predict the heat generated in $LiFePO_4$ pouch cell with good accuracy [59].

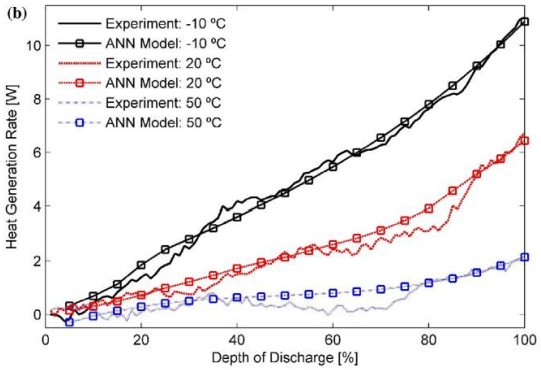


Figure 3.9 Comparison of experimentally measured heat generation and predicted values at 1C discharge rate [59]

Qian [60] has optimized the heat dissipation aspect of the LIB system using a combination of neural networks and the computational fluid dynamics (CFD) method, where CFD is used to simulate the flow field and temperature field of the LIB at different battery spacings. These spacing parameters and resultant temperatures are used to train the neural network to predict the optimal battery spacing and temperature difference, demonstrating a correlation between battery spacing and temperature gradient across different cells; predicted temperature differences at various spacing combinations can be seen in Figure 3.10.

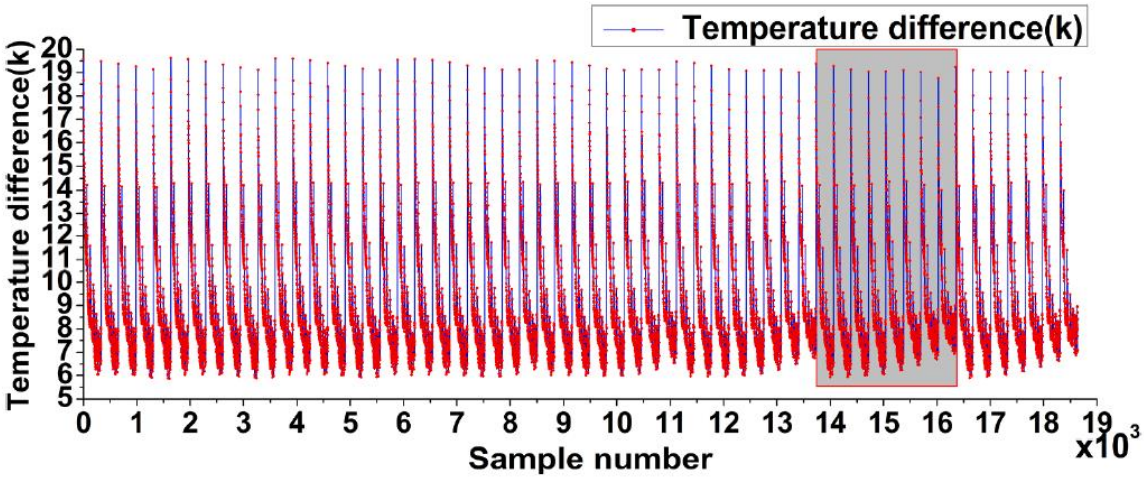


Figure 3.10 Temperature difference of the battery pack under 18,639 different spacing combinations [60]

There are a few cases where both ANN and various versions of Kalman Filter (KF) have been used in conjunction to model LIB specifically to improve the estimation of SOC. Multiple versions of KF have already been adopted in the automotive industry and consumer electronics for LIB energy management. Wei and Nicholas [61] have used an ANN model to predict the SOC of LiFePO4 by using the current, voltage, and temperature of the battery, which is coupled with an unscented Kalman filter (UKF) to reduce the associated errors of ANN during operation a schematic of the integrated system is represented in Figure 3.11.

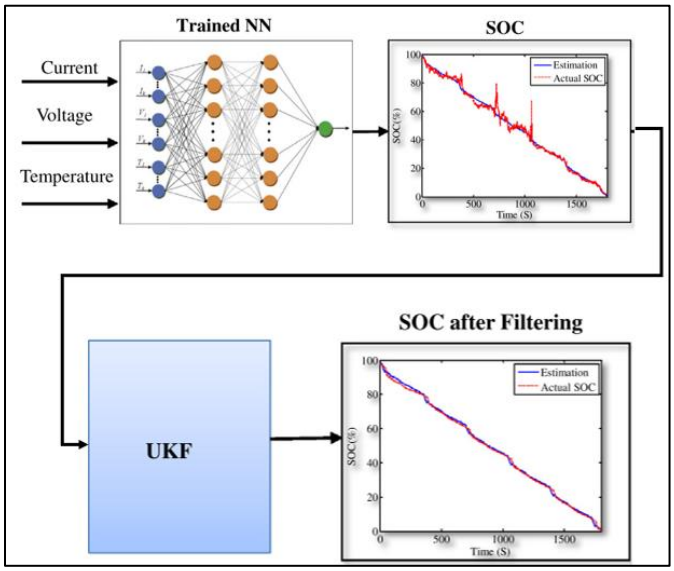


Figure 3.11 Schematic of the SOC estimation based on the neural network & unscented Kalman filter *[61]*

Amin [5] has demonstrated using KF, EKF, and augmented Kalman filter along with ANN to accurately predict the LIB's SOC and state of health (SOH), where Kalman filter estimates the internal parameters of the equivalent circuit models. Similarly, both Chen [62] and Dao [63] have integrated the EKF (which estimates the SOC of the previous time step) with an ANN to predict the current SOC of the LIB. Schematics for both systems can be seen in the Figure 3.12 and Figure 3.13 respectively.

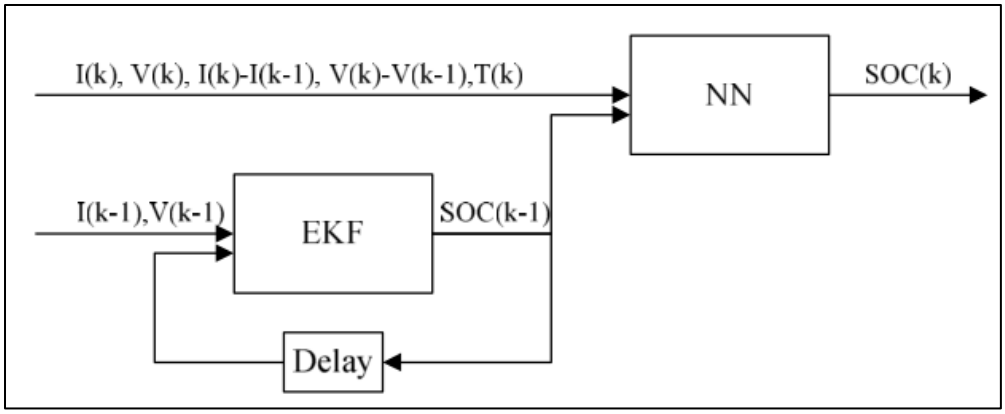


Figure 3.12 SOC estimation based on the neural network & extended Kalman filter – 1 [62]

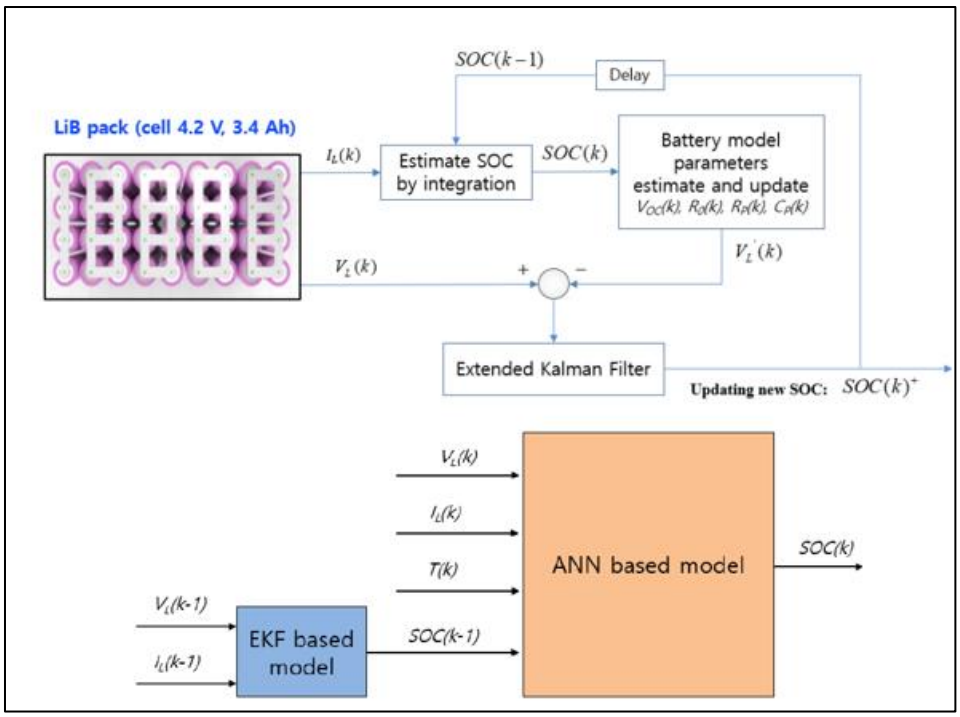


Figure 3.13 SOC estimation based on the neural network & extended Kalman filter – 2 [63]

This type of modeling with ANN and EKF can be regarded as a hybrid model as it incorporates both the characteristics of data-based modeling and elements of equivalent circuit, physics-based modeling. From the above examples, it is evident that SOC estimation through ANN and KF is an established technique that can be further modified to predict the thermal behavior of the LIB. Currently, most of the existing physics-based and data-based models in the literature focus on the accuracy of the SOC/DOD prediction or the thermal behavior of the LIB system. However, it is evident from the literature that both DOD and thermal behavior are interdependent. Therefore,

it is essential to develop a LIB model that simultaneously estimates the DOD and heat generation rate in real-time, and the hybrid data-based models are uniquely poised for this purpose.

3.3 Limitations in the Existing Literature and Data-Based Models

From the above literature, it can be concluded that a stand-alone neural network model and other machine learning algorithms can be used to develop detailed data-based models for various applications. However, almost all the models rely on vast sets of initial experimental data, which can be time-consuming and expensive to explore when implementing new algorithms. However, this problem can be solved if large sets of data can be generated by physics-based models validated by a relatively small number of experiments covering a range of operating conditions. This approach bypasses the tedious experimentation or at least during the initial algorithm development phase, serving as test data for performance demonstration.

Many algorithms are already in commercial use (battery management systems) to estimate the internal state of electrochemical energy systems (e.g., SOC) to optimize and manage the system's energy requirements. After considering the catastrophic nature of thermal runaway, the critical need for a model to predict the thermal behavior of the electrochemical system, especially batteries, was identified. However, the research related to algorithms correlating the internal states with the heat generation rate (thermal behavior) and performance of electrochemical energy systems, especially in real-time application, is not yet prevalent and the current focus of this study is to address this by a hybrid approach of combining an artificial neural network (ANN) algorithm predicting the heat generation rate supplemented with an extended Kalman filter (EKF) estimating the instantaneous internal state of the system (e.g., SOC/DOD of the LIB)

Predicting the PEMFC thermal behavior and membrane mechanics is critical in optimizing thermal and water management in PEMFC to prevent uneven distribution of current, heat, aging, and membrane hydration. Dry membranes create excessive membrane resistance, and flooding creates reactant transport issues impacting cell performance and degradation. However, no data-based models predict the spatial temperature distribution, membrane hydration state, or the associated resistance. This study proposes to develop a data-based model that can be applied in real-time to predict thermal gradients, cell aging, and membrane dynamics, improving the performance and durability of the PEMFC system and other energy systems. Considering the

projected scale and commercial usage, electrochemical energy systems require such models to prevent catastrophic failures and improve reliability.

Although there has been a significant amount of research in developing databased and detailed physics-based models both in empirical and fluid dynamics domains to predict voltages, there have been very few studies that venture into the aspect of developing surrogate databased models based on the existing physics-based models that can accurately replicate their behavior. These surrogate models, also referred to as the digital twins of physics-based models, have the potential to be implemented in a real-time environment, making the best of both worlds in terms of accuracy and computational speed and removing their limitations. Based on the literature review, most studies focus on the cell degradation problem as a time-series event and require vast amounts of degradation data spanning over months. A few studies predict cell voltage degradation as a function of accelerated aging or based on electrochemical properties as a regression model and can be extremely useful as it reduces the tedious hours spent on aging studies by accelerating the aging process.

Studies investigating the aspect of developing data-based models and hybrid data-based models to predict the thermal behavior and thermal gradients associated with electrochemical systems are minimal, especially when the explicit material properties of such systems are unavailable and by considering the need for such models both from a system controls and diagnostics perspective. Finally, almost no studies published in the literature to the best of our knowledge investigate the development of such data-based models based on actual vehicle data and the model's applicability in a transient environment when predicting the electrochemical or thermal attributes in a vehicle. Based on the identified research gaps, models, limitations, and unexplored research areas serve as the motivation for the current thesis.

Chapter 4 Predicting PEMFC Performance and Membrane Dynamics

***This chapter is adapted from Legala, Adithya, et al. "*Machine learning modeling for proton exchange membrane fuel cell performance*." Energy and AI, vol. 10, Nov. 2022, p. 100183, doi:10.1016/j.egyai.2022.100183.

This chapter discusses machine learning methods for developing data-based models to predict PEMFC performance attributes and internal states. Techniques such as Artificial Neural Network (ANN) and Support Vector Machine Regressor (SVR) are implemented to predict the cell voltage, membrane resistance, and membrane hydration level for various operating conditions. Varying input features such as cell current, temperature, reactant pressures, and humidity are introduced to evaluate the model's accuracy, especially under extreme conditions. This study considers two data sets acquired from a physics-based semiempirical model and a 1-D reduced-dimension Computational Fluid Dynamics model. Data preprocessing and hyperparameter tuning procedures are investigated and extensively used to calibrate the artificial neural network layers and support vector regressors to predict fuel cell attributes. ANN clearly shows an advantage over SVR, especially on a multivariable output regression. However, the SVR is advantageous for modeling simple regressions as it greatly reduces the level of computation without sacrificing accuracy. Data-based models for PEMFC are successfully developed on both the data sets by adopting advanced modeling techniques and calibration procedures such as ANN incorporating the dropout technique, resulting in an $R^2 \geq 0.99$ for all the predicted variables, demonstrating the ability to build accurate data-based models solely on data from validated physics-based models, reducing the dependency on extensive experimentation.

4.1 Data Acquisition

The necessary data for data-based modeling is gathered from actual PEMFC testing or through the simulation of computer models that have been validated under a wide range of operating conditions and represent real-world behaviors. Here, in this case, the data is acquired from physics-based models validated using experimental data available in the literature. Dataset1 is generated by simulating a semi-empirical physics-based model across different operating conditions in MATLAB [27]. Figure 4.1 shows a schematic of the inputs and output variables of the voltage module, where varying current, temperature, membrane hydration (lambda), and reactant pressures are used to predict the fuel cell's voltage output.

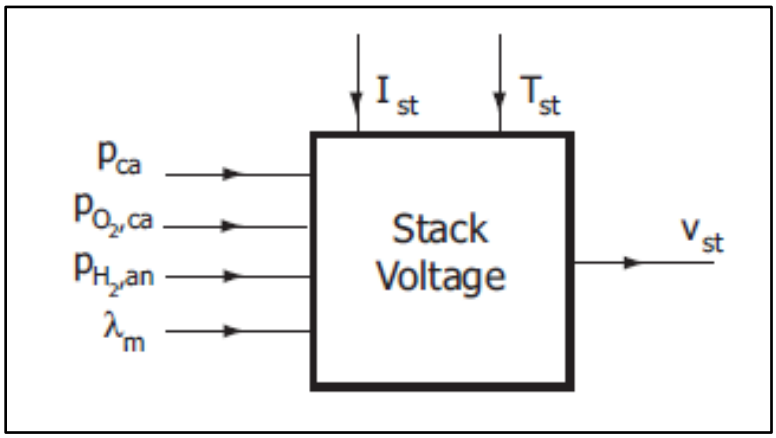


Figure 4.1 Schematic of physics-based semi-empirical voltage module [27]

As the model has been derived from the physics-based formulas, the input feature vectors for the data-based model remain the same. A 1-D physics-based CFD model generates another data set (from here on referred to as Dataset2) [23] which had been experimentally validated. Here, varying currents, temperatures, and humidity are used to predict the voltage output, membrane resistance, and membrane hydration level at constant reactant concentration and operating pressures. Dataset 1 and Dataset 2, along with their ranges, data distribution, and cross plots, are illustrated in Appendix A. Semi-empirical equations used to reconstruct the model used for Dataset 1 are also listed in Appendix B.

Dataset1 and Dataset2's feature vectors (input) and predicted variables (output) are listed in Table 4-1 and Table 4-2, respectively.

Table 4-1 Inputs and output parameters of Dataset1

Inputs (Feature Vectors)	Output
Current	Fuel Cell Voltage
Temperature	
Cathode Pressure	
O2 Partial Pressure	
H2 Partial Pressure	
Membrane Hydration (Lambda)	

Table 4-2 Inputs and output parameters of Dataset2

Inputs (Feature Vectors)	Output
Current	Fuel Cell Voltage
Temperature	Membrane Resistance
Relative Humidity	Membrane Hydration (Lambda)

The input and output attributes of the data-based models are chosen based on the governing physics of the system [64], [65], [66]. Since the objective of the present study is to develop a sufficiently accurate data-driven model for control, diagnostic, and prognostic purposes, that is, to predict fuel cell performance and internal states for a given design and construction of fuel cells, the six model inputs selected for Dataset1 to predict the voltage are the fuel cell operating conditions, which are also used as the input conditions for the physics-based models. The three model inputs selected for Dataset 2 to predict voltage, membrane resistance, and membrane hydration are cell output current, the temperature of the stack, and relative humidity at the cell inlet (assuming there is no change in reactant pressures to limit the iterable parameters in the simulation considering the tedious computational process), all of which have a direct correlation based on governing equations of CFD model and are necessary parameters to build a control or diagnostics model. Both datasets are independent, and membrane hydration (Lambda) is considered an input vector in Dataset 1 and as a predicted attribute in Dataset 2 as one is based on

semi-empirical equations and the other being a CFD predicted parameter; this shows the potential of the models to be cascaded if necessary. Each dataset consists of a total of 1100 data points, which are split into a ratio of 70:30 for training and validation. The data sets, and the range of operational parameters are given in the appendix. No data points are excluded as the validated physics-based model simulations generate the datasets without any measurement or process noise.

4.1.1 Data Conditioning / Preprocessing:

As all the input feature vectors and output vectors differ in scale, nonlinearity, and sensitivity to the model, normalization is necessary for both the input feature vectors and target output vectors before introducing them to the neural network and SVR algorithms. As all the feature vectors and output parameters are non-negative physical entities, it has been decided that normalization between 0 and 1 is appropriate. The normalization process is as shown below:

$$x_{normalized} = (x - x_{minimum}) / (x_{maximum} - x_{minimum}) \quad (4.1)$$

Dataset1 and Dataset2 are normalized between 0 and 1, and results after normalization of Dataset1 and Dataset2 are also shown in appendix B.

4.2 Neural Network Hyper Parameters

Hyperparameters are calibration entities of the neural network that depend on the system and input data; these attributes must be selected and tuned to successfully predict the output variable with sufficient accuracy while optimizing the computational time and power. This calibration will help to model the behavior of the output variable and calibrate the model sensitivity based on the operating condition; a few of these attributes are discussed as follows.

4.2.1 Nodes & Hidden Layers

Based on the initial literature review and considering similar physical systems, it is concluded that a neural network with two hidden layers is a good starting point. Initially, 50 neurons per hidden layer were considered for the model, but after repeated simulations with various neuron combinations, it was reduced to 10 neurons per hidden layer.

4.2.2 Feature Vectors

As this data is generated from physics-based models, the inputs of these physics-based models can be used as input feature vectors for machine learning algorithms. So, for Dataset1, the feature vectors are PEMFC current, stack temperature, total cathode pressure, O_2 and H2 partial pressures, and membrane hydration (lambda). For Dataset2, the feature vectors are PEMFC current, temperature and relative humidity normalized between 0 and 1.

4.2.3 Loss Function

Generally, Mean Square Error (MSE), Mean Absolute Error (MAE), and Huber are used to solve the regression in a neural network. In this case, both MAE and MSE are considered. The mathematical representation of MAE and MSE is given below:

$$\text{MAE} = \frac{1}{n}\sum_{j=1}^{n}\left|y_j - \hat{y}_j\right| \qquad (4.2)$$

$$\text{MSE} = \frac{1}{n}\sum_{i=1}^{n}(y_i - \hat{y}_i)^2 \qquad (4.3)$$

where n = number of elements, y_j is the actual (true value) $\hat{y}_j$ is the predicted (output) value.

4.3 ANN Architecture and Design Parameters

Typically, a neural network can have any number of hidden layers or neurons, and a network with more than 2 or 3 hidden layers is considered a deep neural network, whereas a network with only 1 or 2 hidden layers is regarded as a shallow neural network. A deep neural network requires larger computational capability and training time, which is typically used for image or complex time series regressions and object classification [66], whereas a shallow neural network relatively consumes less computational power and training time and is primarily used for modeling regressions and pattern recognition. Considering that the current fuel cell output parameter prediction can be regarded as a mathematical regression, a shallow feed-forward neural network is chosen. A preliminary investigation of the neural network performance with multiple hidden layers ranging from one to four, each containing 50 neurons, is evaluated, and the network with two hidden layers provided the best value when considering the computational power required, network training time, and resulting accuracy after multiple iterations. Hence, it was decided to model the neural network with two hidden layers.

4.3.1 ANN for Dataset1 (Semi-Empirical)

The following are the initial structural parameters of the ANN algorithm that is applied to the semi-empirical data (Dataset1), which consists of the following input features: PEMFC current, temperature, total cathode pressure, O2, and H2 partial pressures, and membrane hydration (lambda). These are listed in Table 4-3, and the initial ANN design for Dataset1 is shown in Figure 4.2 Initial ANN design for Dataset1.

Table 4-3 Initial ANN parameters for Dataset1

Inputs feature vectors	6
Output parameters	1
Hidden layers	2
Nodes/ Neurons	10
Activation function	ReLU-1,2 layer Linear - Final
Loss function	'MAE' / 'MSE'
Learning Rate (Lr)	0.055
Iterations/Epochs	100
Momentum/correction	0.9
Dropout probability	0

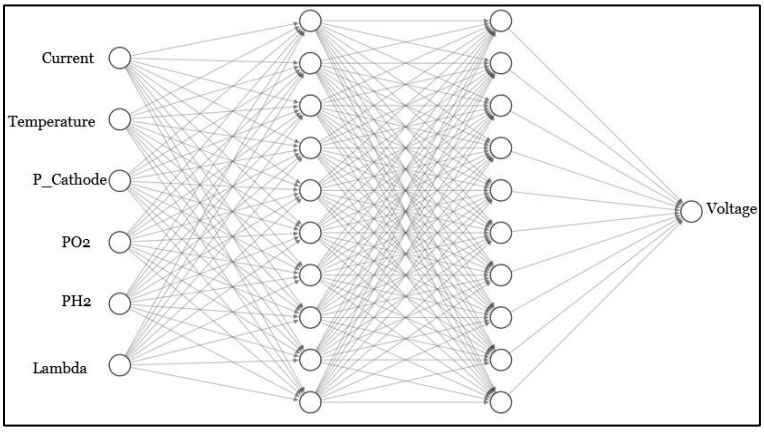


Figure 4.2 Initial ANN design for Dataset1

4.3.2 ANN on Dataset2 (1D-CFD)

The initial structural parameters of the ANN that are applied to the 1-D CFD data (Dataset2) consist of the following input feature vectors: PEMFC current, temperature, and relative humidity. The output parameters are the predicted corresponding voltage, membrane resistance, and membrane hydration (lambda). These are listed in Table 4-4, and the initial ANN design for Dataset2 is shown in Figure 4.3.

Table 4-4 Initial ANN parameters for Dataset2

Inputs feature vectors	3
Output parameters	3
Hidden layers	2
Nodes	10
Activation function	ReLU-1,2 layer Linear - Final
Loss function	'MAE' / 'MSE'
Learning Rate (Lr)	0.025
Iterations/Epochs	100
Momentum/correction	0.9
Dropout probability	0

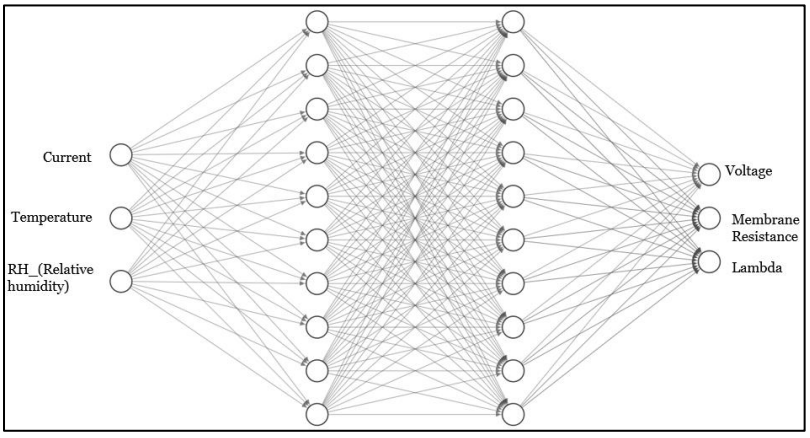


Figure 4.3 Initial ANN design for Dataset2

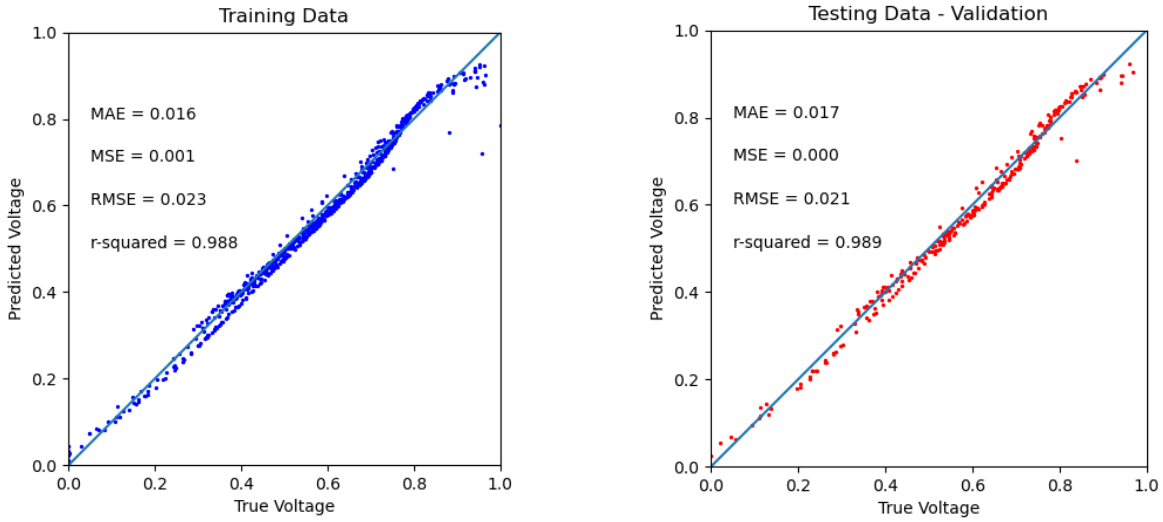
4.4 Results and Discussion

4.4.1 SVR for Dataset1 and Dataset2

SVR technique is applied to Dataset1 with similar feature vectors to ANN, is used to predict PEMFC voltage, and comprises the following design attributes and hyperparameters as listed in Table 4-5, the final results of the SVR for Dataset1 during the training and validation are shown in Figure 4.4.

Table 4-5 Initial SVR parameters for Dataset1

Inputs feature vectors	6
Output parameters	1
Epsilon	0.025
C	1.0
Training data points	770
Validation data points	330



(a) (b)

Figure 4.4 SVR Results for Dataset1: (a) Training; (b) Validation.

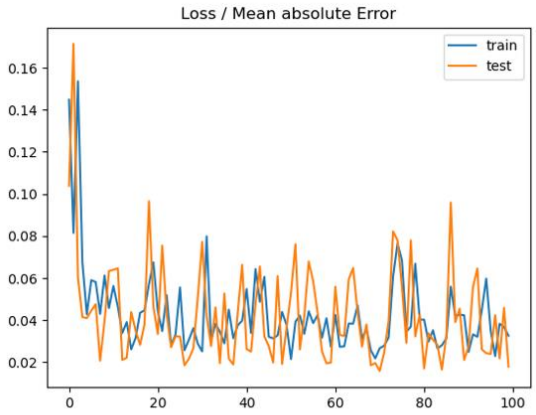
The above plots show that R^2 values are very close to 0.99 for both training and testing data. Thus, we can conclude that the SVR technique is executed flawlessly and can accurately predict the fuel cell voltage bearing a few extreme boundary conditions. Considering the relatively limited tunable parameters in SVR, the results are considered reasonably accurate and in agreement with the available literature [51], [54]. For Dataset2, which is a multi-output regression problem, the SVR could not accurately converge and is not complex enough to model the associated nonlinearity. However, independent SVR models can be developed and tuned to model each output vector of Dataset2.

4.4.2 ANN for Dataset1 (semi-emp)

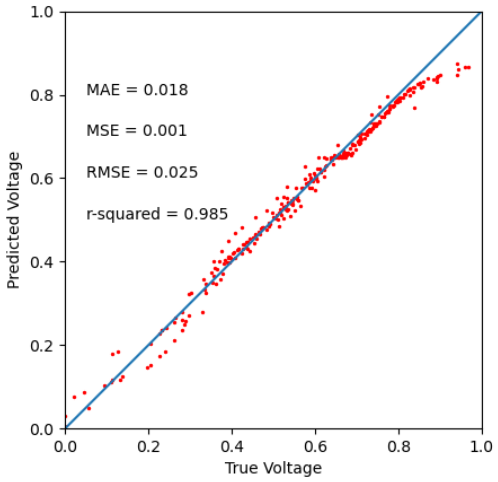
The initial results of the ANN for Dataset 1, comprising six inputs, one output, two hidden layers, and hyperparameters, as listed in Table 4-3, with specific loss functions, are presented below.

Case 1: Mean Absolute Error (MAE) With No Dropout

After investigation, the optimal ANN model hyperparameters are determined to be as follows: Loss function = MAE; Lr = 0.055; no dropout; and number of neurons per layer = 10. The initial results of the ANN fuel cell model developed using Dataset 1 with MAE as a loss function and the hyperparameters mentioned above are shown in Figure 4.5.



(a)



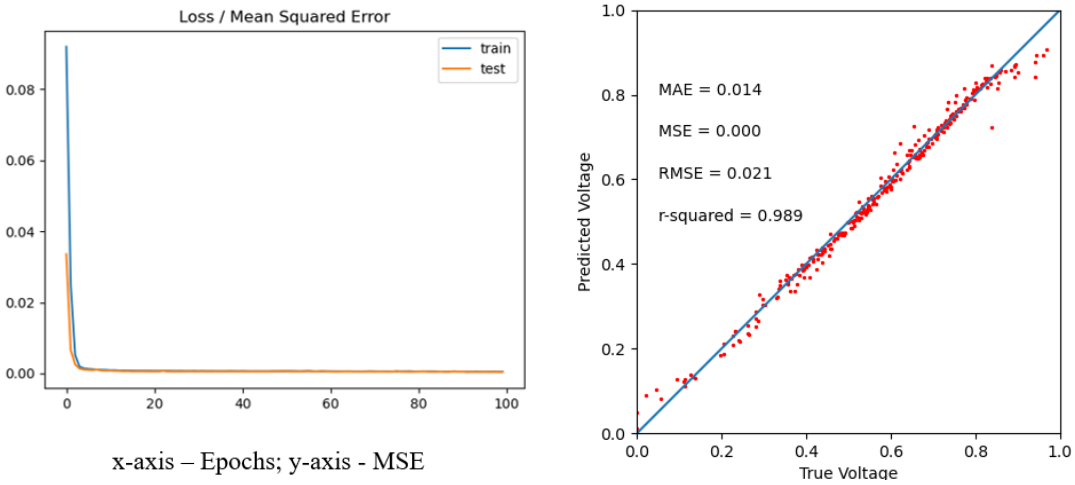
(b)

Figure 4.5 Case 1 neural network result for Dataset1 considering MAE as loss function and no dropout: (a) Loss function / MAE Vs Training Epochs; (b) Voltage prediction

As Figure 4.5 shows that the ANN is accurate and its structure (layers) is suitable for this regression. However, even after 100 epochs, the loss function is still unstable, with fluctuating MAE values. As such, there is a need to investigate other loss functions, such as MSE.

Case 2: Mean Squared Error (MSE) With No Dropout

After investigation, the optimal ANN model hyperparameters are found to be: Loss function = MSE, Lr = 0.055; no dropout; number of neurons per layer = 10. The results of the ANN with MSE as the loss function and with the hyperparameters mentioned above are shown in Figure 4.6.



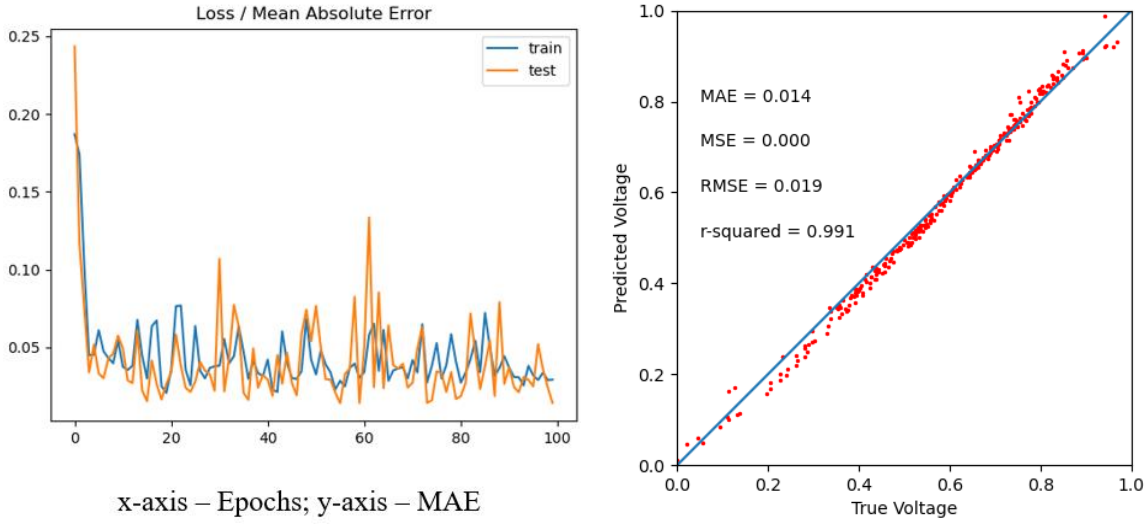
(a) (b)

Figure 4.6 Case 2 neural network result for Dataset 1 considering MSE as loss function and no dropout: (a) Loss function / MSE Vs Training Epochs; (b) Voltage prediction.

The MSE loss function reduces quickly with the iteration epochs and without observable fluctuations; hence, it is considered stabilized and offers a good accuracy for the neural network with the R^2 value of 0.989. However, it is slightly behind in terms of accuracy at extreme boundary conditions, i.e., Voltage values below 0.15 and above 0.85 – these extreme cell voltage values are normally outside the range of practical operation of PEMFCs. However, to improve the accuracy for these extreme voltage values, the number of neurons in each layer is increased, and the dropout technique is incorporated for both loss functions, which are presented next.

Case 3: Mean Absolute Error (MAE) With Dropout Consideration

The optimal ANN model hyperparameters are determined through extensive analysis: Loss function = MAE, Lr = 0.055; number of neurons per layer = 20 in both hidden layers; dropout probability is 0.5 for both hidden layers. The corresponding results of the ANN with MAE as the loss function incorporating dropout in both hidden layers and with the hyperparameters as mentioned earlier are shown in Figure 4.7.



(a) (b)

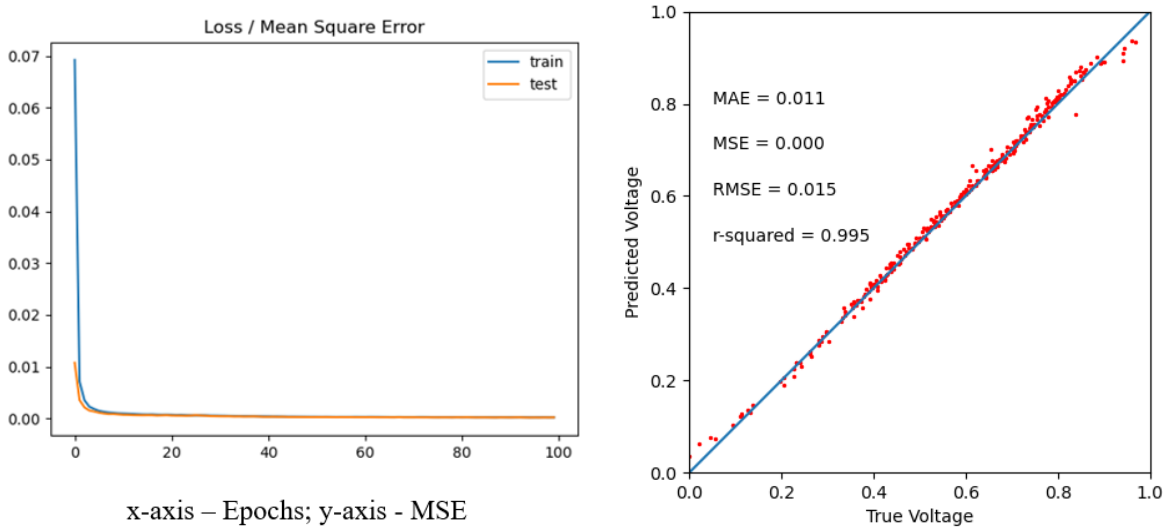
Figure 4.7 Case 3 neural network result for Dataset1 considering MAE as Loss function with dropout: (a) Loss function / MAE Vs Training Epochs; (b) Voltage prediction.

Again, the MAE loss function is still unstable, as shown in Figure 4.7, but considering the encouraging results shown in Figure 4.6 with the improved accuracy (R^2 value is increased to 0.991), the loss function is replaced by MSE, and a similar dropout technique is introduced to the model by increasing the number of neurons and altering the drop probability, as shown next.

Case 4: Mean Squared Error (MSE) With Dropout Consideration

After considerable analysis, the optimal ANN model hyperparameters are determined as: Loss function = MSE, Lr = 0.055; number of neurons per layer = 30 in both hidden layers; dropout probability = 0.5 for the 1st hidden layer and 0.25 for the 2nd hidden layer. The results of the ANN

with MSE as the loss function incorporating varying dropout probability in both hidden layers and the hyperparameters as mentioned above are shown in Figure 4.8.



(a) (b)

Figure 4.8 Case 4 neural network result for Dataset1 considering MSE as Loss function with dropout: (a) Loss function / MSE Vs Training Epochs; (b) Voltage prediction.

From Figure 4.8, it is noted that introducing the dropout technique has resulted in a considerable improvement in the accuracy of the predicted voltage, with the R^2 value of 0.995, especially considering the nonlinearity in the extreme boundary conditions (voltage less than 0.15 V and great than 0.85 V). Clearly, the use of MSE as the loss function and adoption of the dropout technique improves the accuracy of the results with fewer epoch levels (or iterations) needed to reach converged calculations.

4.5 ANN Results for Dataset 2 (1-D CFD)

The results of the ANN for Dataset2, comprising three inputs, three outputs, two hidden layers, and hyperparameters, as listed in Table 4-4, along with specific loss functions, are presented below.

Case 1: Mean Absolute Error (MAE) With No Dropout

The optimal ANN model hyperparameters are determined as following extensive investigation: Loss function = MAE, Lr = 0.025, no dropout, and number of neurons per layer = 10. The initial

results of the ANN fuel cell model developed using Dataset 2 with MAE as the loss function and the hyperparameters mentioned above are shown in Figure 4.9.

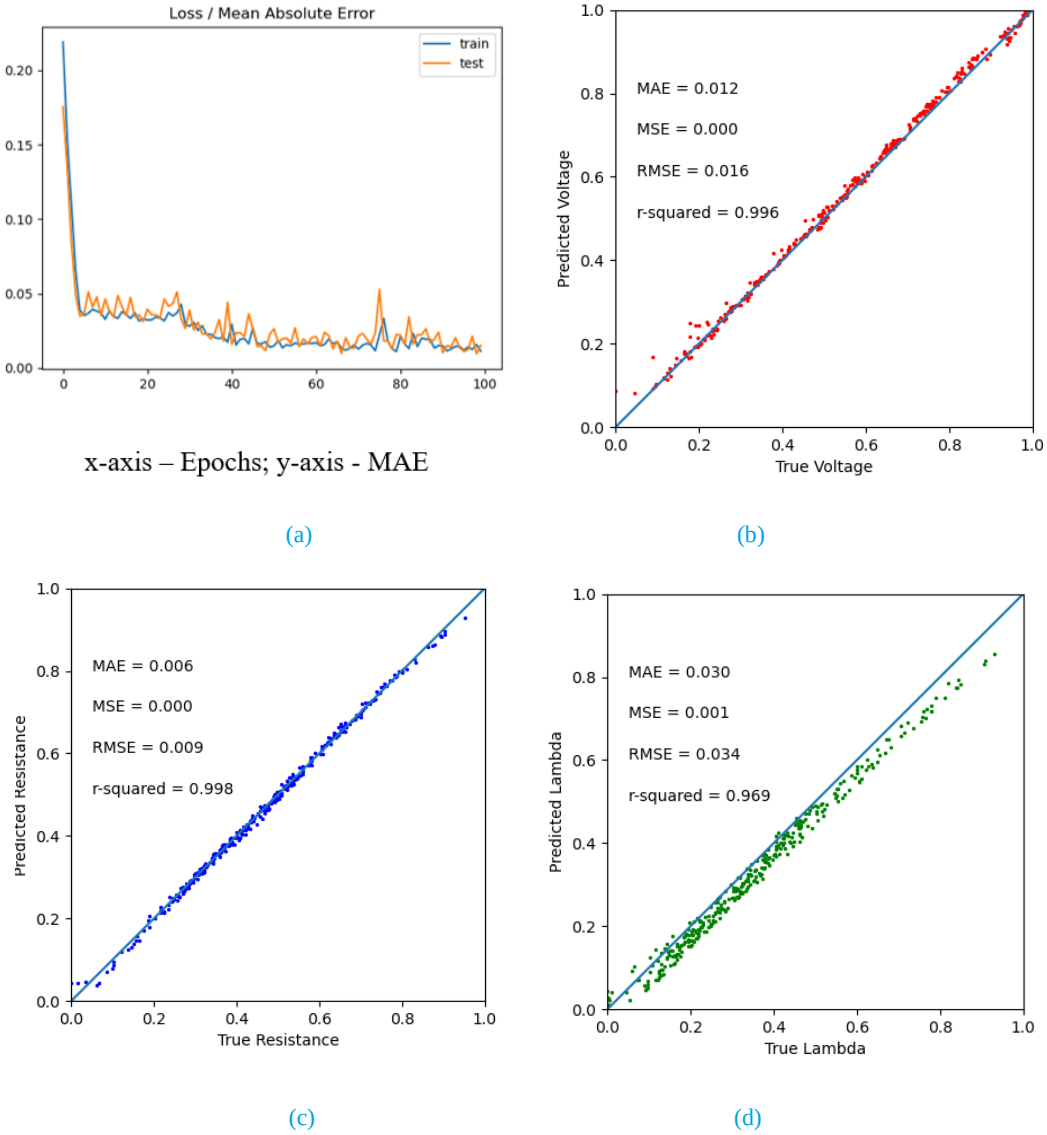


Figure 4.9 Case 1 neural network result for Dataset 2 considering MAE as Loss function with no dropout: (a) Loss function / MAE Vs Training Epochs; (b) Voltage prediction; (c) Resistance prediction; (d) Lambda prediction

Despite this being a multi-output regression problem, this neural network architecture has quite good accuracy for all three parameters, suggesting that the chosen design and hyperparameters are close to being ideal. The loss function (MAE) output is also relatively stabilized, though fluctuations over the level of epochs are clearly present after 100 epochs. The accuracy in the predicted lambda (R^2 value of 0.969, as compared with R^2 value of 0.996 and 0.998 for the predicted cell voltage and resistance) can be improved further since most of the data points

are persistently located beneath the correlation curve. To achieve this the loss function is replaced with MSE for further analysis, similar to the cases for Dataset 1.

Case 2: Mean Squared Error (MSE) With No Dropout

After considerable investigation, the optimal ANN model hyperparameters are determined to be: Loss function = MSE; Lr = 0.025; no dropout; and number of neurons per layer = 10. The results of the ANN with MSE as the loss function and the hyperparameters mentioned above are shown in Figure 4.10. The hyperparameter values considered are precisely the same as in the previous case, except for the change in the loss function.

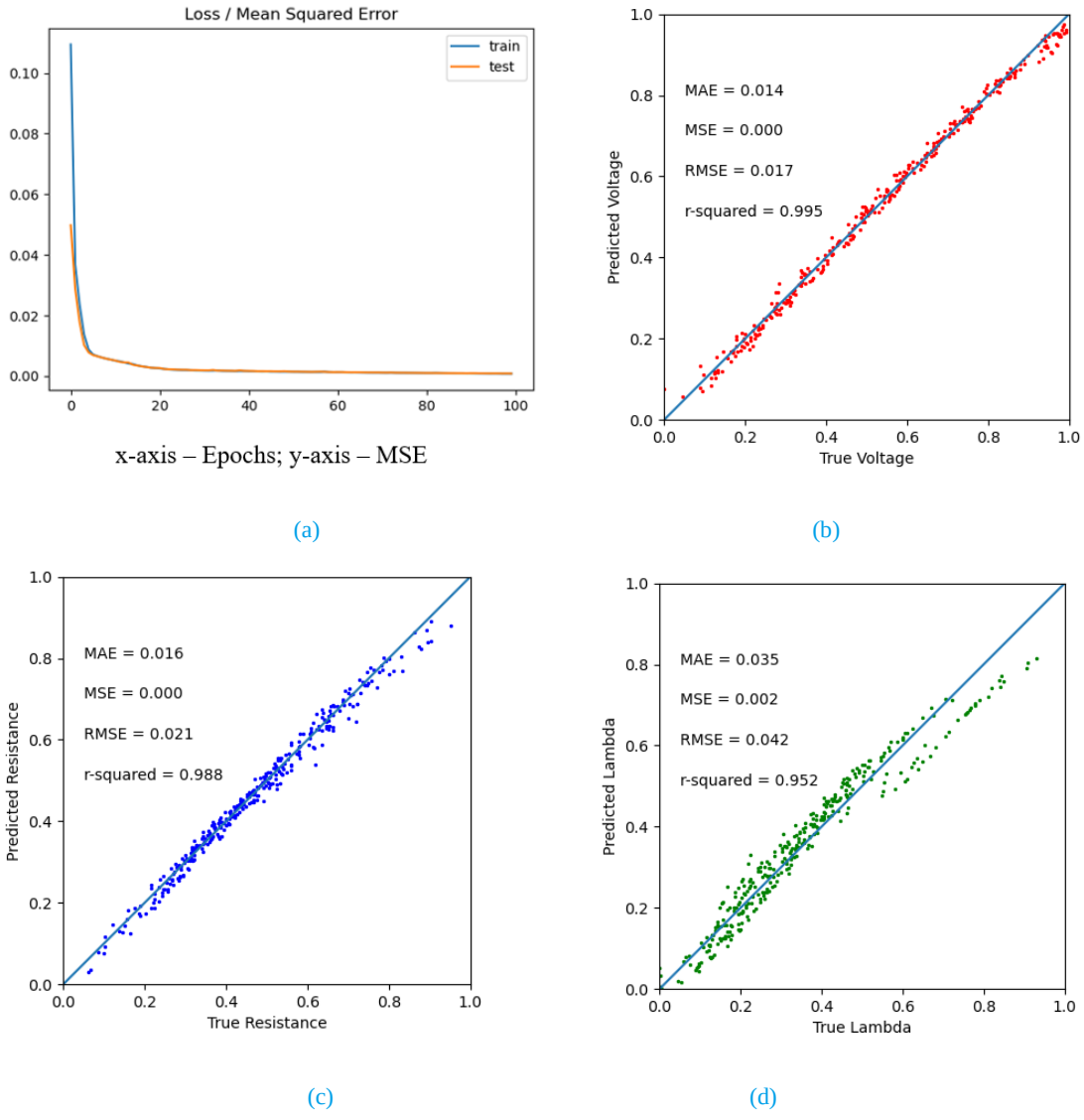
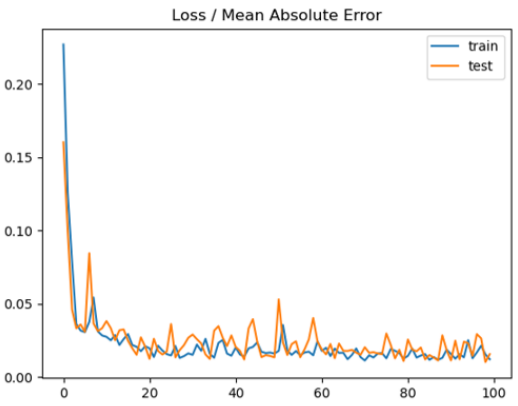


Figure 4.10 Case 2 neural network result for Dataset2 considering MSE as Loss function with no dropout: (a) Loss function / MAE Vs Training Epochs; (b) Voltage prediction; (c) Resistance prediction; (d) Lambda prediction

As it is observed from Figure 4.10 The change in the loss function was counterproductive and did not fully achieve the desired results even after stabilizing the error value. The R^2 values for the predicted three parameters, 0.995, 0.988, and 0.952 for cell voltage, resistance, and membrane hydration, respectively, are slightly smaller than in the previous case. After several iterations of hyperparameters resulting in no significant change, the dropout technique was again introduced by increasing the number of neurons for further investigation.

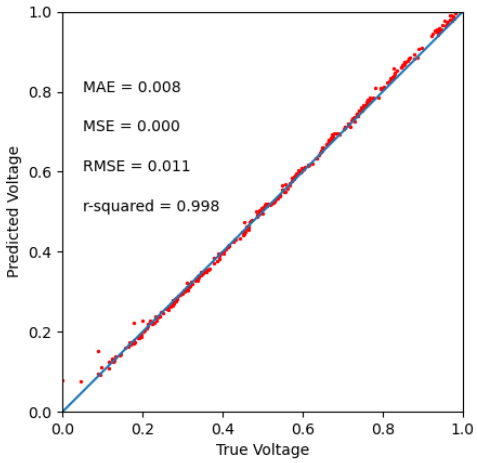
Case 3: Mean Absolute Error (MAE) With Dropout Consideration

After extensive investigation, the optimal ANN model hyperparameters are determined as follows: Loss function = MAE; Lr = 0.025; number of neurons per layer = 20 in both hidden layers; and dropout probability = 0. 25 for both hidden layers. The results of the ANN with MAE as the loss function incorporating dropout probability in both hidden layers and the hyperparameters, as mentioned earlier, are shown in Figure 4.11.

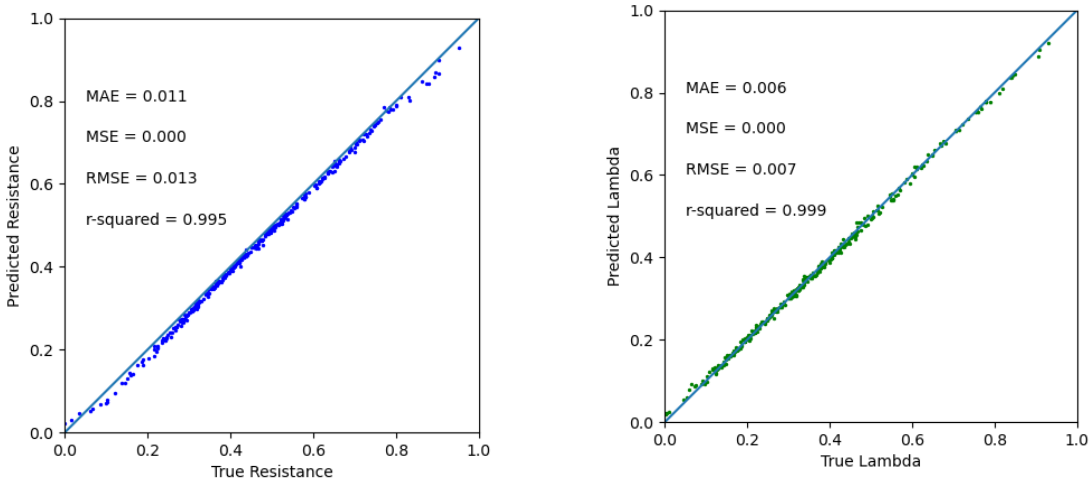


x-axis – Epochs; y-axis – MAE

(a)



(b)



(c) (d)

Figure 4.11 Case 3 neural network result for Dataset2 considering MAE as Loss function with dropout: (a) Loss function / MAE Vs Training Epochs; (b) Voltage prediction; (c) Resistance prediction; (d) Lambda prediction

From the above plots, it can be observed that introducing the dropout technique on this ANN (Dataset2) has also significantly improved the accuracy of all the predicted parameters. Considering the minor fluctuations in the MAE error function, even after 100 epochs, the loss function is replaced with MSE for further analysis.

Case 4: Mean Squared Error (MSE) With Dropout Consideration

After extensive tuning, the epochs are increased to 1000, whereas the number of neurons per layer is reduced to 10 compared with the previous cases. This indicates that more time is needed for the training, but once it is trained, it is much easier to compute the various predictions from the trained model. The trained ANN model has the following optimal model hyperparameters: Loss function = MSE; Lr = 0.025; the number of neurons per layer = 10 in both hidden layers; and dropout probability = 0. 25 for both hidden layers. The results of the ANN model with MAE as the loss function incorporating dropout probability in both hidden layers and the hyperparameters mentioned above are shown in Figure 4.12.

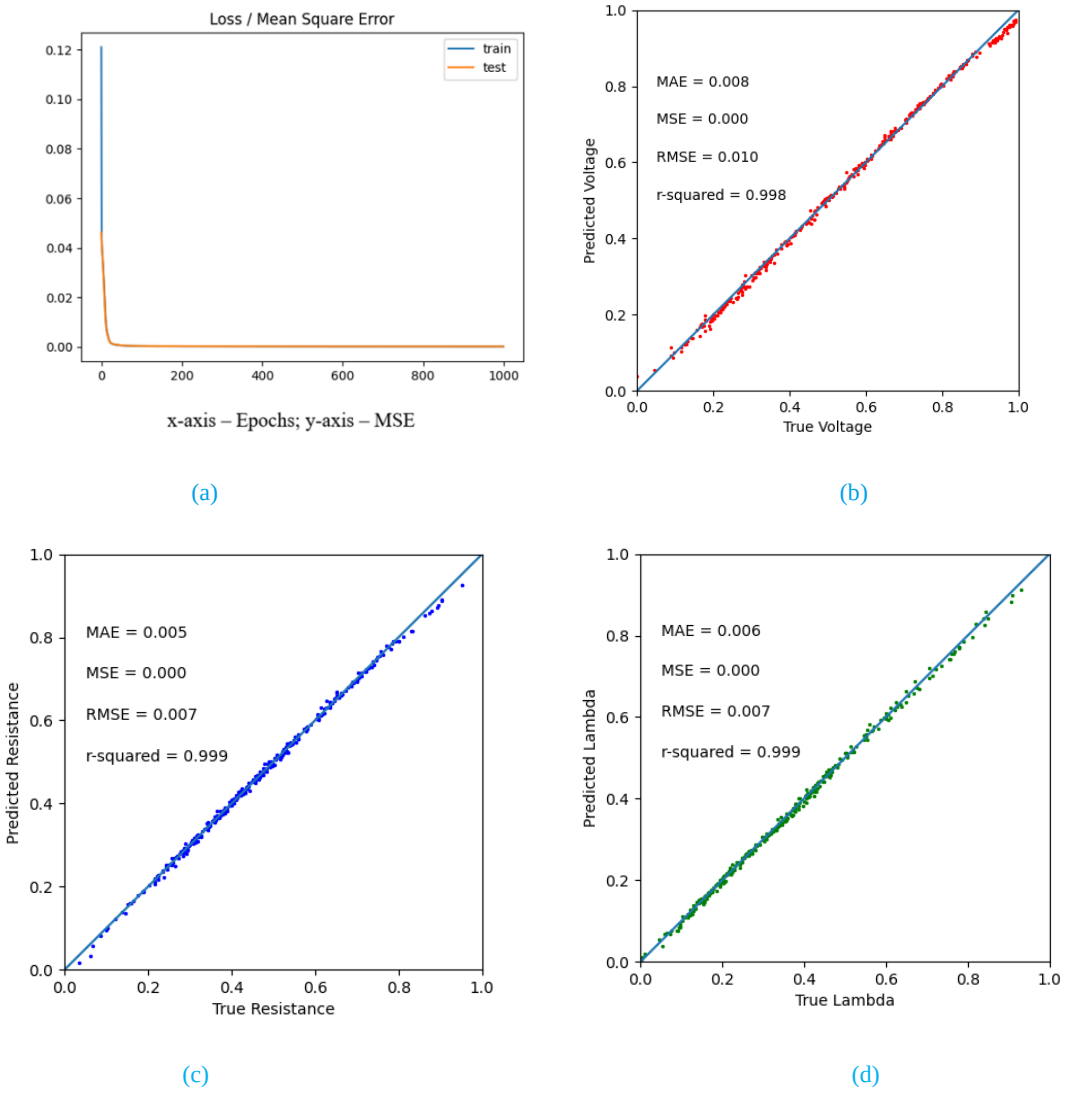


Figure 4.12 Case 4 neural network result for Dataset 2 considering MSE as loss function with dropout: (a) Loss function / MSE Vs Training Epochs; (b) Voltage prediction; (c) Membrane resistance prediction; (d) Membrane hydration (Lambda) prediction

From the above results, it can be concluded that changing the loss function to MSE, increasing the number of epochs to 1000, and implementing the dropout technique improved the multi-output regression performance and can accurately predict all the output parameters. It is clear that MSE is reduced quickly without fluctuations over the training epochs (iterations), and the predicted cell voltage, membrane resistance, and membrane hydration have the best accuracy of all the models investigated so far, with the R^2 value of 0.998, 0.999 and 0.999, respectively, and the MAE less than 0.01.

4.6 Summary

In this study, artificial neural network (ANN) and support vector machine regressor (SVR) have been used as the machine learning methods to develop data-based models for the performance attributes and internal states of proton exchange membrane fuel cell (PEMFC). PEMFC operating conditions such as cell current, temperature, reactant pressures, and humidity are used as input feature parameters, while the output parameters include the predicted cell voltage, membrane resistance, and membrane hydration level for various operating conditions. The accuracy of the data-based models is evaluated, especially under extreme conditions. The data used for the present modeling study are acquired, respectively, from i) a physics-based semi-empirical model (referred to as Dataset1), and ii) a dimensionally reduced 1-D Computational Fluid Dynamics (CFD) model that has been validated with experimental results (referred to as Dataset2). A total of 1100 data points for each dataset have been generated that cover the entire range of PEMFC operations. 70% of the data points are used for training, while the remaining 30% of data points are used for testing/validation.

It is demonstrated that ANN clearly shows an advantage in comparison with SVR, especially on a multivariable output regression. However, the SVR is advantageous for modeling simple regressions as it dramatically reduces the level of computation without sacrificing accuracy. It is further shown that the machine learning techniques incorporating the dropout technique can provide very accurate predictions with $R^2 \geq 0.99$ for all the predicted variables. This demonstrates the ability to build accurate data-based models solely on data from validated physics-based models, reducing the dependency on extensive experimentation. The final prediction accuracy in terms of R^2, root mean square error (RMSE), and mean absolute error (MAE) for ANN and SVR algorithms after tuning for both the datasets to predict voltage, membrane resistance, and lambda is tabulated in Table 4-6 and Table 4-7 for comparison.

Table 4-6 Voltage prediction accuracy of SVR and ANN on physics-based semi-empirical data (Dataset1)

Algorithm	Dropout	R^2 Value	RMSE	MAE
SVR	N/A	0.989	0.021	0.017
ANN-MAE	No	0.985	0.025	0.018
	Yes	0.991	0.019	0.014
ANN-MSE	No	0.989	0.021	0.014
	Yes	0.995	0.015	0.011

Table 4-7 ANN prediction accuracy (using dropout) on 1-D CFD data (Dataset2) for all output vectors

Algorithm	Dropout	Predicted Parameter	R^2 Value	RMSE	MAE
ANN-MAE	No	Cell Voltage	0.996	0.016	0.012
	Yes		0.998	0.011	0.008
	No	Membrane Resistance	0.998	0.009	0.006
	Yes		0.995	0.013	0.011
	No	Membrane Hydration (Lambda)	0.969	0.034	0.030
	Yes		0.999	0.007	0.006
ANN-MSE	No	Cell Voltage	0.995	0.017	0.014
	Yes		0.998	0.01	0.008
	No	Membrane Resistance	0.988	0.021	0.016
	Yes		0.999	0.007	0.005
	No	Membrane Hydration (Lambda)	0.952	0.042	0.035
	Yes		0.999	0.007	0.006

The present study indicates that additional feature vectors such as electrochemical impedance, interfacial resistances between layers, poisoning effect, ageing, and catalyst leaching may be considered for better diagnostics and prognostics of PEMFC operation, including water flooding, reactant starvation, membrane mechanics, state of health, and remaining state of useful life.

Chapter 5 Modeling of Proton Exchange Membrane Fuel Cell Degradation Dynamics

*This chapter is adapted from Legala, Adithya, et al. "*Data-based modeling of proton exchange membrane fuel cell performance and degradation dynamics*." Energy Conversion and Management, vol. 296, Sept. 2023, p. 117668, doi:10.1016/j.enconman.2023.117668.

This chapter delves into the use of the data-based modeling technique, artificial neural network (ANN), which was adopted to comprehend performance degradation and thermal and pressure dynamics. Experimental data consisting of polarization and cyclic voltammetry data are acquired after every 6,000 accelerated stress test (AST) degradation cycles as stipulated by the US Department of Energy guidelines. Over 40,000 test cases were considered for training and evaluating the neural network comprising data from 30,000 full-cell AST cycles. Fuel cell operating temperatures, pressures, flow rates, and relative humidities are varied to capture the entire spectrum of PEMFC performance characteristics. Parameters such as the number of AST cycles endured, or instantaneous catalyst electrode surface area, operating current density, reactant flow rate, relative humidity, system temperature, and pressure are considered as feature vectors (inputs) to predict cell output voltage, reactant outlet pressure, and temperature for both anode and cathode streams. Data preprocessing and batch learning are implemented in Python to improve prediction accuracy and computational time; considering the substantial nonlinear data sets, various Keras library optimizers and corresponding hyperparameters are investigated for better convergence. The trained neural network model is evaluated on 15,000 test cases resulting in an $R2 \geq 0.995$ for all the predicted variables, demonstrating the capability of data-based models to accurately predict the nonlinear behavior of such electrochemical systems with minimal processing time, advocating for their application in real-time system monitoring, controls and diagnostics.

5.1 Introduction

The impact of industrial and vehicular emissions on air quality and ecology has been recognized for a long time, especially during the Covid-19 pandemic [67], [68]. It is imperative to decarbonize our economies for climate change mitigation and energy security [69], [70]. The transport and energy sectors are at the forefront of undergoing this historical clean energy transition, and proton exchange membrane fuel cell (PEMFC) is one of the most commercially anticipated technologies projected to lead this transition [6], [10]. PEMFC is a complex electrochemical device that converts the chemical energy of reactants directly into electrical energy through a series of oxidation and reduction reactions [14]. PEMFC's high efficiency, specific energy, and power density with zero emissions at the point of use make it an ideal choice for heavy-duty transportation and remote power applications [71]. PEMFC, being a thermodynamically open system, unlike a battery, can continuously generate electrical energy if reactants are fed into the system, eliminating the device downtime for charging and avoiding the need for mammoth cell stacks [14], [71].

Like any other electrochemical system, the performance and efficiency of the PEMFC depend on its operation and design, such as fuel cell temperature, reactants supply pressures, the status of membrane hydration (lambda), current density, the composition and structure of the electrode (catalyst, ionomer, pore space), removal of water, flow distribution in cell structure and flow channels built on the bipolar plates [11], [24], [25], [72]. Further, its durability or degradation behavior is determined by the mechanical and chemical stability of individual cell components such as membrane, bipolar plates, and, most importantly, catalyst layers, which consist of precious metals, support, and ionomer, all of which are affected by operating conditions [11], [24], [72], [73]. The durability of these individual components affects the long-term performance, a fuel cell's total useful life, and associated system diagnostics. A PEMFC operating in a natural world environment is exposed to impurities such as sulfur, oxides of carbon, nitrogen, and metals either through fuel or air, which can cause catalyst poisoning or deactivation, leading to chemical degradation [11], [24], [72]. Similarly, thermal and humidity cycling under compression in the fuel cell causes hydrothermal aging where the membrane is subjected to excessive swelling and shrinking, which can lead to catalyst leaching, sintering, deactivation, and loss of structural membrane rigidity further leading to the formation of pinholes [73]. Loss of pore space due to disruption of the gas diffusion layer (GDL) structure can lead to mass transport resistance, causing

starvation and flooding inside the PEMFC electrodes. Constant voltage cycling throughout the life of PEMFC can cause electrochemical-related aging, leading to the degradation of metallic bipolar plates, catalyst layers, and membranes due to forming radicals. Depending on the operational environment, application, and calibration, these aging mechanisms can simultaneously occur in a fuel cell, leading to various degradation behaviors and characteristics [11]. Degradation in the PEMFC affects not only the output voltage (or efficiency) of the cell but also its pressure and temperature-related dynamics due to the deactivation of the catalyst, change in pore space, and membrane structural deterioration [74], which in turn impact the performance degradation and reliability of the cells.

Additionally, unlike combustion engines, there are no significant visual or audible indicators during operation for an electrochemical system like PEMFC that can be used as an identifier to detect degradation or abnormalities before a catastrophic failure. Only the data from internal stack electrical, thermal, and pressure residual signatures can be used to identify degradation and malfunctions in the PEMFC; this is a significant safety challenge during the commercial operations of such systems [18], [75], [76]. Considering these PEMFC operational challenges, there is a definitive need for a PEMFC model that can accurately monitor the system response, predict the system performance, and estimate the degradation rate. The model must be able to predict output attributes not only from a voltage perspective but also from a thermal and pressure dynamics perspective at various levels of cell degradation for real-time diagnostics and prognostics.

Traditionally, PEMFC uses the equivalent circuit models (ECM) to replicate the behavior of the fuel cell, predominantly for system controls [35], [36], [77], [78]; however, these models cannot comprehend the complete degradation or thermal or pressure dynamics. Computational fluid dynamics (CFD) models for PEMFC are robust enough to predict the fluctuations in the thermal and pressure domain; however, due to the fundamental assumptions in the model, considering all the degradation behaviors simultaneously over a long period of operations is challenging, especially without explicit material properties. Physics-based electrochemical models can predict the state of health degradation with an acceptable error but are limited to the aging mechanisms and assumptions considered [79], [80]. Modern-day hardware and computational limitations allow the deployment of ECM models, which are computationally simple on the embedded controller. However, due to their complex physics-based differential equations, the

three-dimensional CFD models cannot be used on any real-time embedded systems. Modeling these individual degradation behaviors through a physics-based or electro-chemistry-based model requires the availability of detailed material properties, design attributes, and a comprehensive understanding of every physical phenomenon encountered and their compounded effect of mutual interactions, which may not be possible at every instance leading to assumptions and default limitations of the model capabilities. This complexity and lack of transparency in fuel cell material properties make a case for adopting non-traditional techniques, such as artificial neural networks (ANN), to resolve such complex issues [57], [80], [81], [82].

Robust data-based models for PEMFC are in the early stage of development due to the inherent non-traditional modeling approach and limited availability of experimental or validated simulation data in the public domain; physics-based models dominate. However, the rise of computational power, data acquisition technology, and the complexity and interconnectivity of modern energy/propulsion systems are pushing for a data-based approach. Chang et al [83] proposed a non-linear recurrent dynamic neural network to predict the remaining useful life of PEMFC by estimating the PEMFC voltage at various time intervals by utilizing the PEMFC operational data of 150 to 650 hours; however, this approach involved the accumulation of large sets of experimental data (operating the PEMFC for up to 1000 hours) and also application of locally weighted regression to preprocess the data. Zuo [84] has used a long short-term memory network approach to predict the PEMFC degradation by estimating the cell voltage and this approach also consists of pre-conditioning the data by using a Savitzky-Golay filter to remove measurement noise. Ma et al [85] applied a grid long short-term neural network to predict long-term voltage loss in the PEMFC where operating current, voltage, and temperature are considered as feature vectors; however, utilizing this deep learning approach is computationally expensive to predict the cell voltage in an on-board diagnostic setup. Silva [86] has applied the adaptive neuro-fuzzy logic approach to solving the problem of PEMFC prognostics, focusing on real-time application to predict PEMFC voltage with great accuracy. However, this approach does not consider thermal and pressure dynamics. Simon [87] has used the unique echo state network concept by replacing the hidden layers with neuron reservoirs and estimating the Hurst exponent in the ANN framework to predict cell voltage, but the algorithm needed to be more robust to comprehend the transitive behavior. Vichard [88] has also used the echo state network-based neural network architecture by considering the total electric charge applied to the system as a relevant input to accurately predict

the cell voltage over 5000 hours of PEMFC experimental data, but results show that no less than 60% (3000 hours) training data is necessary for good accuracy. Pahon [89] demonstrated the application of signal processing techniques for fuel cell diagnostics and degradation by considering the relative entropy and output voltage; however, the thermal and pressure dynamics of the system are not considered limiting the possibility of detecting fuel cell flooding and hot spot formation. Chen [90] has combined the grey neural network model method with the particle swarm optimization technique to predict the degradation in the PEMFC by using a minimal amount of initial operational data but, only 50 hours of data is considered for the validation, and only the cell voltage is predicted with nominal accuracy.

Most of the existing literature formulates the degradation behavior of the PEMFC as a complex time series problem and needs hundreds of hours of fuel cell operational data to capture the degradation behavior. To the best of our knowledge, no existing data-based model can track accurately the degradation behavior along with temperature and pressure dynamics of the PEMFC system that can be simultaneously used for diagnostics and prognostics. Therefore, the objective of this study is to tackle the above-mentioned gap in the literature by contributing the following:

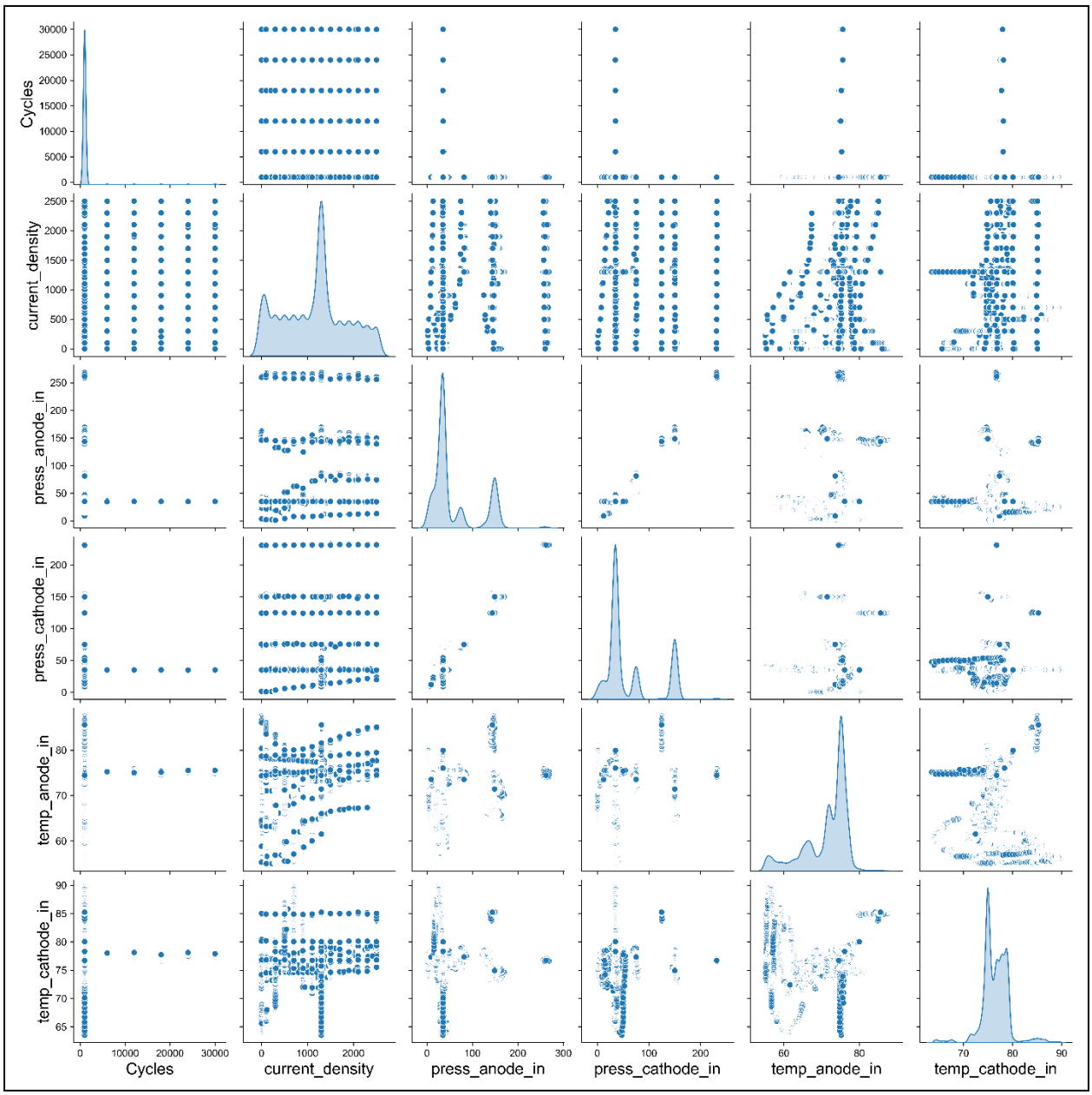
1. Development of a comprehensive multi-input multi-output data-based model that can predict the voltage degradation, temperature, and pressure dynamics of the PEMFC across various operating conditions.
2. Formulating the PEMFC voltage degradation behavior as a regression problem, a proposed alternative to time series models by introducing the concept of endured accelerated stress test (AST) cycles and electrode catalyst surface area (ECSA).
3. The proposed method and training technique avoid the need for any additional signal conditioning and data filtering techniques, demonstrating the model's robust capability to predict voltage and pressure fluctuations.
4. The proposed method is applicable for both steady conditions and during transition operations to predict temperature and voltage behaviors demonstrating the feasibility for on-board diagnostic application.

5.2 Experimental Procedure

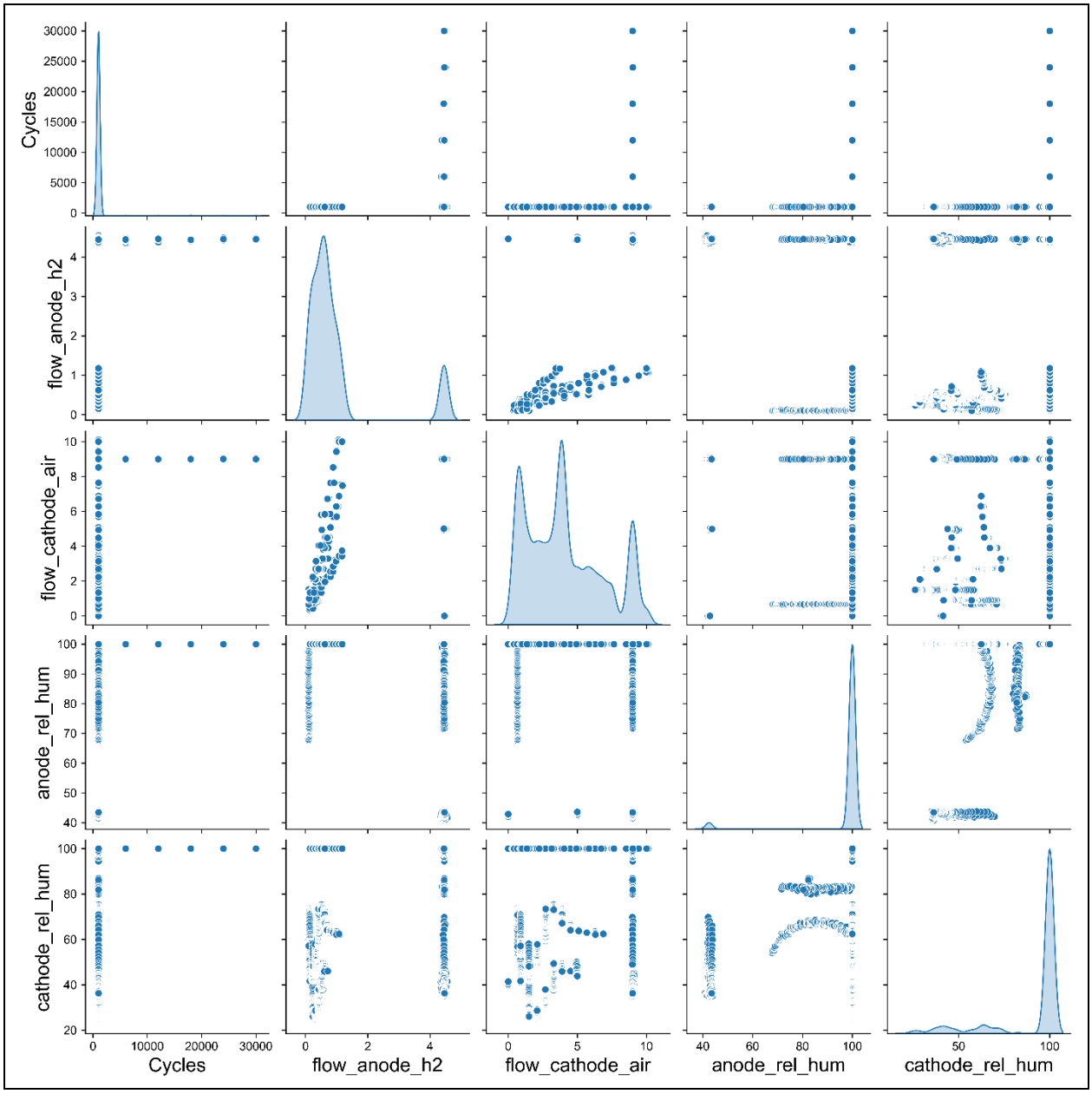
First, a customized membrane electrode assembly (MEA) for the fuel cell is manufactured in the lab using a commercially available 60% Pt/C catalyst. A homogenous catalyst ink is prepared

with ethanol, deionized water, Aquivion as an ionomer and a total Pt (catalyst) loading of 0.5 mg/cm^2. The membrane is uniformly coated with the catalyst ink and sandwiched between known porosity gas diffusion layers consisting of a microporous layer and a macroporous substrate, completing the seven layered MEA. The total active surface area of the MEA is around 45 cm^2 and is encapsulated between the bipolar plates and sealed under compression to prevent any leakage of reactants during operation, thus completing the PEMFC assembly. The entire experimental data is generated using the Automated Greenlight G20 fuel cell test station. The initial performance (baseline) of the prepared fuel cell is evaluated by capturing the data from the polarization curve of the fuel cell at various operating conditions, such as at various stoichiometric ratios obtained by changing the flow rate of both hydrogen (0.1 to 4.5 slpm) and air (0.65 to 9 slpm), operating under various anode (0.5 to 270 kPa) and cathode (0.5 to 230 kPa) pressures, at different fuel cell and reactant temperatures (55 to 90 °C), under various reactants relative humidity conditions (20 to 100 % Rh). These PEMFC working conditions during the baseline evaluation are chosen to capture the data from the entire fuel cell operational spectrum where the sensitivities associated with each input parameter to the fuel cell output can be modeled [91], [92], [93]. After establishing the initial baseline, PEMFC is subjected to 30,000 accelerated stress test (AST) cycles to induce degradation of catalyst layers by cycling the voltage through the fuel cell as per the U.S Department of Energy guidelines[94]. The data from polarization curves and cyclic voltammetry are collected every 6000 cycles to analyze the system performance degradation and electrode catalyst surface area (ECSA). The crossplot of all the PEMFC's operating conditions (system inputs) and polarization curve data (outputs) during the baseline evaluation and after degradation evaluation collected during the experiment are shown in Figure 5.1. The data acquired during this experimental procedure consists of an acceptable signal noise level and is not subjected to any filtering or smoothening techniques to evaluate the algorithms' robustness. Figure 5.1 emphasizes the correlations between the various PEMFC experimental attributes using pair plots, which is a combination of multiple scatter plots (here, the nonlinearity of the data can be visualized and analyzed) and kernel density estimate (KDE) plot (diagonal plots illustrate the smoothed underlying data distribution). Scatter plots in Figure 5.1 help identify if two corresponding variables have linear or nonlinear correlations (e.g., exponential, logarithmic, etc.) or if it is random (no correlation). Gap data analysis (gaps in operating ranges) from KDE plots of various parameters illustrated in Figure 5.1 indicate that only reactant humidity and endplate temperature

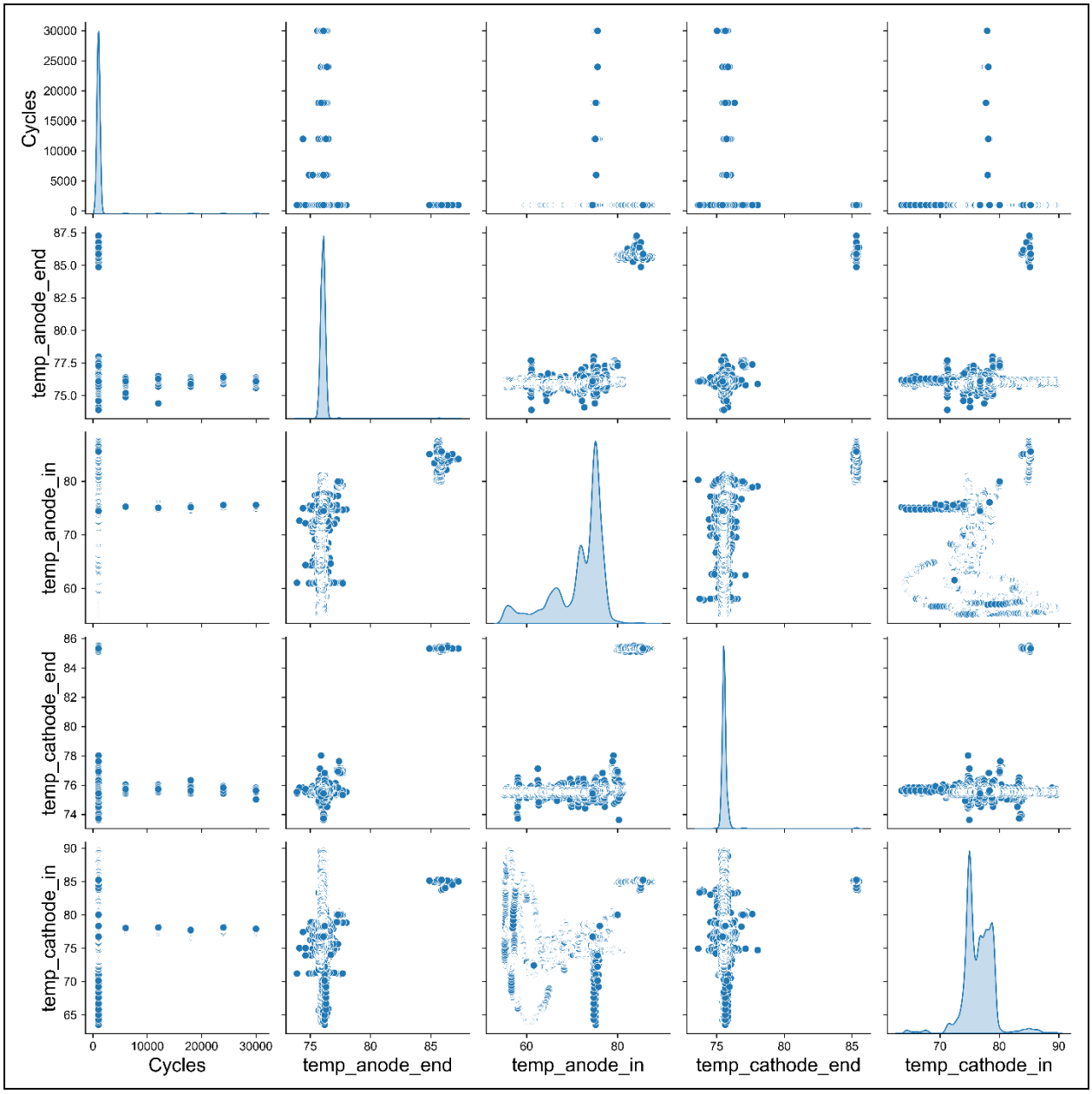
attributes have a clustered distribution, whereas the rest are dispersed across the operational regime. Further, Figure 5.1 illustrates the variability of PEMFC outputs at different operating conditions and their respective nonlinearity and distribution with the operating current.



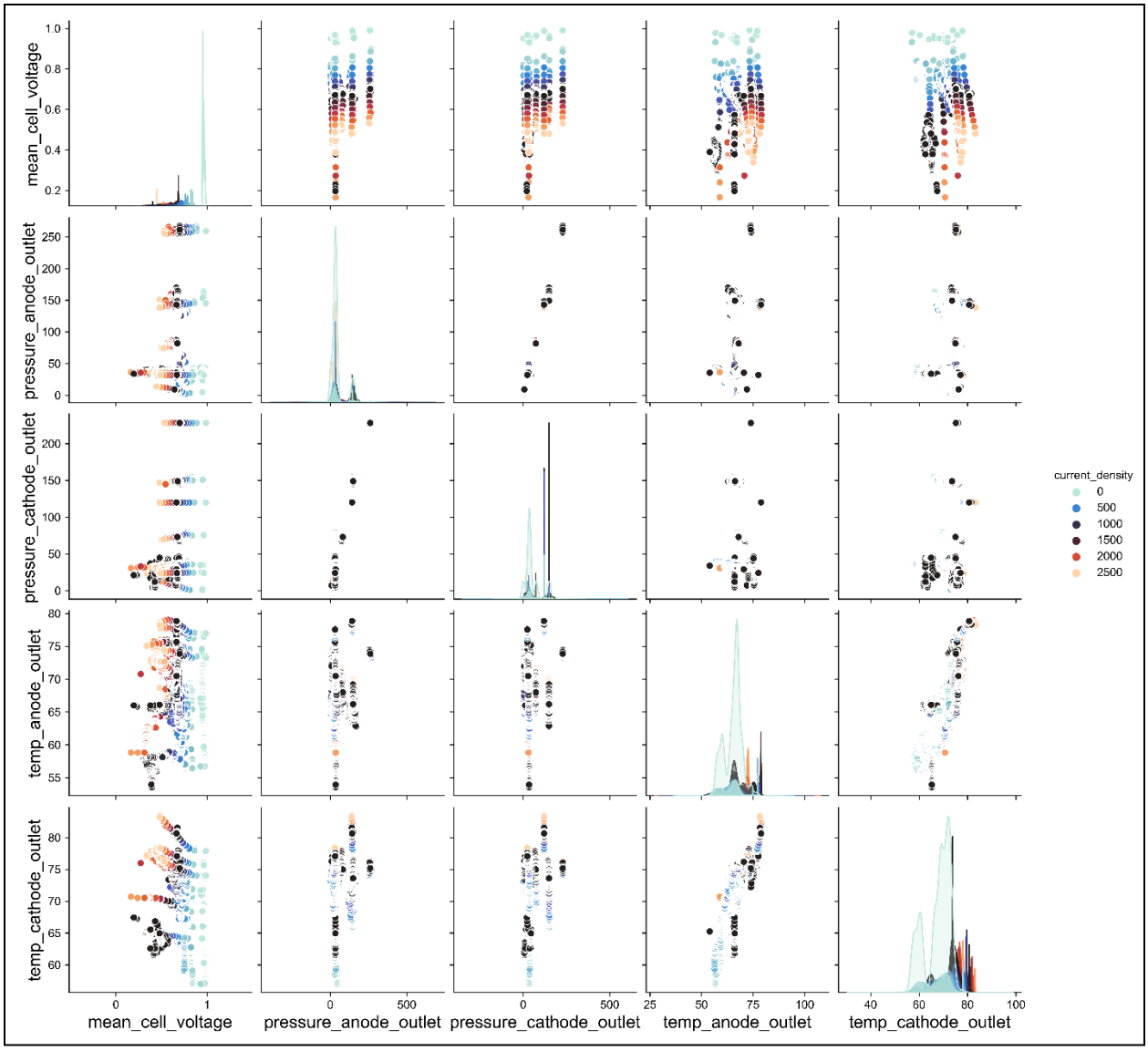
(a)


Cycles
flow_anode_h2
flow_cathode_air
anode_rel_hum
cathode_rel_hum
0
10000
20000
30000
0
2
4
0
5
10
40
60
80
100
50
100

(b)


Cycles
temp_anode_end
temp_anode_in
temp_cathode_end
temp_cathode_in
0
10000
20000
30000
75
80
85
60
80
75
80
85
70
80
90

(c)



(d)

Figure 5.1 Cross plot of PEMFC operational parameters [experimental data] (a) Fuel cell inputs -1; (b) Fuel cell inputs – 2; (c) Fuel cell inputs – 3; (d) Fuel cell outputs

5.3 Data-based Modeling

After considering nonlinearity in the data set and the initial literature survey, the modelling aspect is formulated as a multi-input multi-output regression problem and feed-forward artificial neural network (ANN) architecture is chosen. The degradation aspect of the PEMFC is introduced into the model by either considering the number of AST cycles endured or the instantaneous ECSA

calculated by the cyclic voltammetry data as the input factor. Using the parameter of endured AST cycles/ECSA as an input indirectly introduces the concept of fuel cell run time into the model; here, a correlation between real-world fuel cell operational time and degradation associated with the number of AST cycles/ECSA is necessary, which varies on the type of application and system calibration that can be determined experimentally. This approach eliminates the need for complex time series-based recurrent neural networks or long short-term networks, reducing computational complexity and processing time to predict the degradation level and associated corrections.

5.3.1 Feed-forward ANN

Feed-forward ANN architecture is one of the most widely used data-based modeling techniques for supervised learning, which is inspired by the human biological neural network consisting of layers of interconnected neurons [95], [96], [97]. A neuron in an ANN is the fundamental processing unit, where it receives the information from other neurons, complies with an output depending on embedded mathematical functions (also referred to as activation functions), and transmits output to the next neuron. In a feed-forward ANN, the flow of information transmission is only in one direction, i.e., from the input layers (input attributes are introduced here) to subsequent hidden layers (which host interconnected neurons from multiple layers). Each node in the output layer is connected to the nodes in the preceding hidden layer, which provides a final output. A schematic of the neural network is shown in Figure 5.2. The error backpropagation process calibrates the weights and biases associated with each neuron based on the difference between the desired and targeted output. This error is then continuously propagated backward through each layer of the neurons to adjust their corresponding weights and biases until reaching the desired output that meets the specified accuracy.

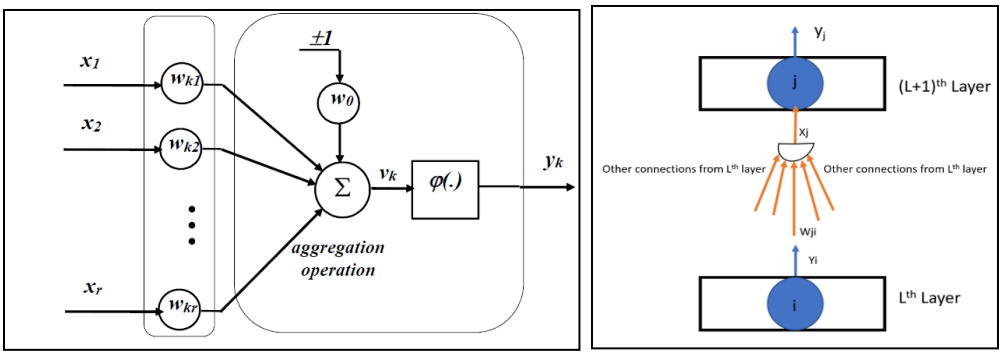


Figure 5.2 Schematic of the neural network and backpropagation [45]

The activation function embedded in the neurons introduces the nonlinear behavior to the model; the accuracy, training, and computational time requirements determine the number of hidden layers and associated neurons in each layer. Considering the nonlinearity of the data, training parameters such as learning rate, optimizers, and neuron interconnection probabilities should be calibrated. All these factors, from the structure of the neural network to the training attributes, are considered hyperparameters tuned to achieve the required level of accuracy. Detailed information on ANN architecture, activation functions, mathematical formulation, and calibration is discussed in Chapter 2 and Chapter 4. [45].

5.3.2 Data preprocessing

Data preprocessing is necessary to transform the data in an organized way at specific scales without altering the fundamental nature of the data. aspects. This preprocessing can help improve the neural network's performance by making Normalization one of the most common preprocessing steps implemented on the input data before it is fed into a neural network, as all the inputs and outputs correlate differently in nonlinearity and sensitivity learning the weights of the synapses (connections) between neurons easier. The Min-Max Normalization method is one of the most common ways to implement normalization on the data [98], [99], [100], [101], where the data scales to a fixed range, usually between 0 and 1. It is calculated by subtracting the minimum value from each data point and dividing the result by the range (maximum value minus minimum value) as shown below:

$$X_{Normalized} = \frac{(\mathrm{X} - X_{Minimum})}{(X_{Maximum} - X_{Minimum})}$$

In some cases, the decimal scaling method [98], [99], [100], [101] can be implemented where the data scales by multiplying each value by a power of 10 and rounding to the nearest integer. This method can be helpful for data with a wide range of values but a relatively small variance. In this case, the Min-Max normalization method is implemented as all the PEMFC operational input parameters and output attributes are non-negative physical entities with a smaller range.

5.3.3 PEMFC model feature vectors and prediction attributes

In a neural network, the input dataset is typically organized into multiple individual input arrays, also referred to as feature vector arrays. These arrays of inputs represent the input variable characteristics at a particular sample or instance. For PEMFCs, feature vectors (input) are initially selected by considering the governing physics and chemical kinetics involved and further screened based on the ability to measure or estimate accurately and reliably. After deliberations, the following parameters are chosen as the feature vectors (inputs) for the PEMFC ANN model: the number of AST cycles endured or current electrode catalyst surface area, operating current density, anode fuel flow rate, cathode oxidant flow rate, anode reactant humidity, cathode oxidant humidity, anode operating pressure, cathode operating pressure, the temperature at anode bipolar plate, the temperature at cathode bipolar plate, the anode inlet temperature, and cathode inlet temperature. The target variables in an ANN, also called prediction variables, are the final outputs of the neural network, which can either be a classification decision or a regression value. For the PEMFC model, the prediction variables are chosen to capture the residual from electrical, thermal, and pressure signatures. The cell output voltage, outlet pressure, and temperature for both anode and cathode streams are chosen as prediction variables that can help diagnose abnormal behavior or estimate degradation performance. The feature vectors (inputs) and prediction variables (outputs) for the present PEMFC model are listed in Table 5-1, and the schematic of the neural network is shown in Figure 5.3.

5.3.4 ANN Design and Hyperparameters

The feed-forward ANN has multiple structural attributes and hyperparameters that must be optimized and calibrated to accurately model the PEMFC's response in linear and nonlinear regions. The following hyperparameters and factors are considered during the initial ANN design and training phases.

5.3.4.1 Activation Function

Considering that the PEMFC polarization curve has both linear and nonlinear regions, the chosen activation function in the ANN should be able to comprehend both linear and nonlinear responses depending on the feature vectors. The activation function introduces nonlinearity into the network and allows it to learn more complex relationships in the data. Several different activation functions can be used in an ANN, each with unique properties and challenges such as

Sigmoid, Tanh, and Swish [102], [103], [104], [105]. However, most activation functions incorporate exponential operations, resulting in higher computational power and processing time. Considering the computational efficiency, a non-exponential activation function Rectified linear unit (ReLU) [102], [103], [104], [105] is chosen for the present PEMFC modeling after multiple iterations, as it is computationally simple and yields better results in both linear and nonlinear regions by addressing the vanishing gradient problem. Graphical representation and behavior of the ReLU function and its derivative are shown in Figure 5.4.

Table 5-1 Feature vectors and prediction attributes for the present fuel cell ANN model

Feature Vectors (Inputs)	**Prediction attributes (Outputs)**
ECSA / AST Cycles Current Density Anode Fuel Flow Cathode Oxidant Flow Anode Humidity Cathode Humidity Anode Operating Pressure Cathode Operating Pressure Temperature at Anode Bipolar Plate Temperature at Cathode Bipolar Plate Temperature Anode In Temperature Cathode In	Cell Output Voltage Anode Pressure Out Cathode Pressure Out Temp Anode Out Temp Cathode Out

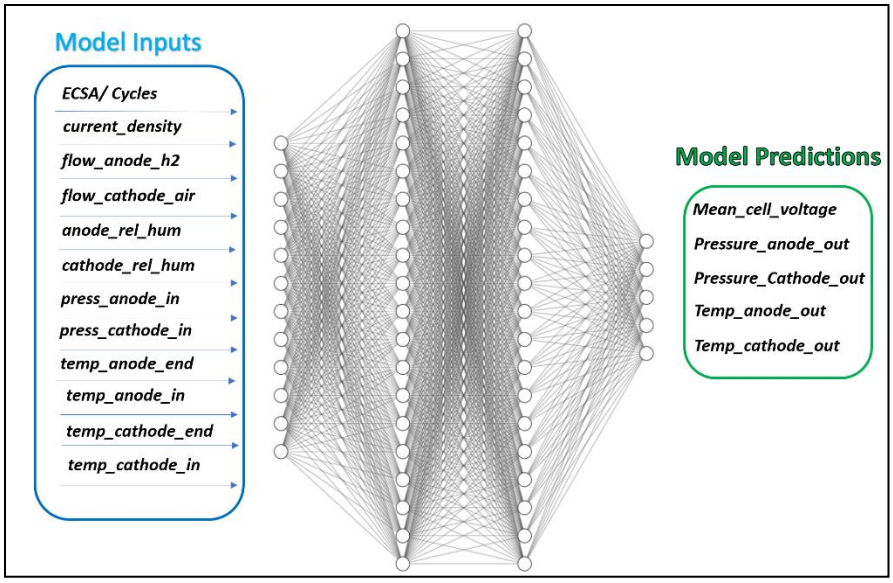


Figure 5.3 Schematic of the proposed fuel cell neural network-fuel cell degradation

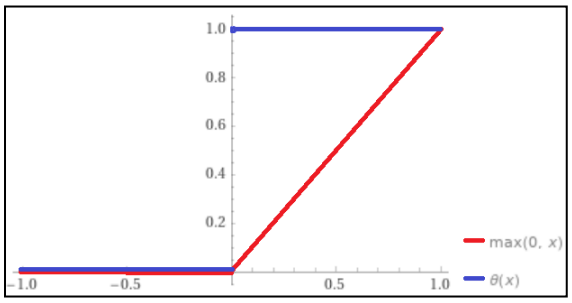


Figure 5.4 Graphical representation of Rectified linear unit function (red-colored curve) and derivative (blue-colored curve) [45]

5.3.4.2 Hidden layers and nodes

In the ANN, a hidden layer is defined as a layer of neurons that are not directly connected to the feature vectors or prediction variables of the network, whereas nodes are defined as the number of neurons in each hidden layer. ANN with less than two hidden layers is considered a shallow neural network, and a deep neural network has more than two hidden layers. The number of hidden layers and nodes significantly impacts the model's ability to learn and generalize to new data and requires experimentation to find the best configuration based on the required accuracy, available computational power, model robustness, model training time, and data set characteristics. Excessive hidden layers and neurons can lead to overfitting of the model, which regularization

techniques, such as dropout and weight decay can prevent. In this case, multiple iterations of hidden layers, neurons per hidden layer, are simulated with a common activation function to evaluate the accuracy, training time, and processing time. A few results of these iterations are discussed in the follow-up sections and illustrated in Figure 5.5.

5.3.4.3 Optimizer, learning rate and epochs

An optimizer is a mathematical algorithm that calibrates the weights and biases of the connections between neurons in an artificial neural network (ANN) to minimize the error between the predicted and true values. The learning rate is the main hyperparameter of the optimizer algorithm that needs to be calibrated, and this learning rate determines the step size at which the optimizer modifies the weights. Too big of a learning rate may lead to skipping the global minima, resulting in oscillation or divergence, and too small of a learning rate may lead to longer training times and processing power. Epoch represents a single iteration of the training dataset, during which the weights and biases of the connections between neurons are updated based on the error. The combination of learning rate and epochs should be balanced, as any deficiency might result in either underfitting or overfitting the model.

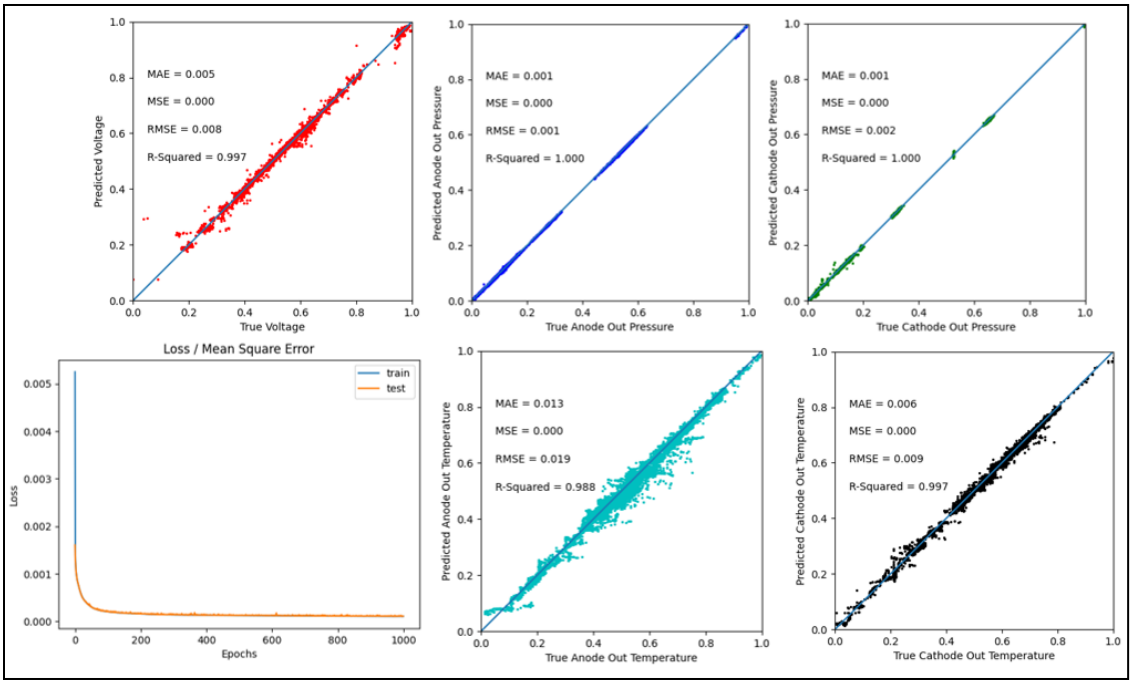
Several different optimizers, such as Stochastic gradient descent (SGD), Adaptive Moment Estimation (Adam), and Resilient Propagation (RProp), are available in Python's Keras library for regression problems [106], [107], [108]. The performance of both SGD and Adam optimizers are evaluated in this study: SGD updates the weights based on the gradient of the loss function with respect to associated weights. SGD has the advantage of being easy to implement and fast to compute, but it is sensitive to the learning rate and may not always converge to a global minimum. On the other hand, the Adam optimizer combines the concept of SGD and momentum, where an exponentially decaying average of past gradients is used to scale the learning rate, which can help the model converge more robustly at a faster pace. For the Adam optimizer, both the learning rate and decay rate act as hyperparameters, providing further flexibility in calibration. The results of these iterations are discussed in the follow-up sections and illustrated in Figure 5.5.

5.3.4.4 Batch learning vs Single-shot approach

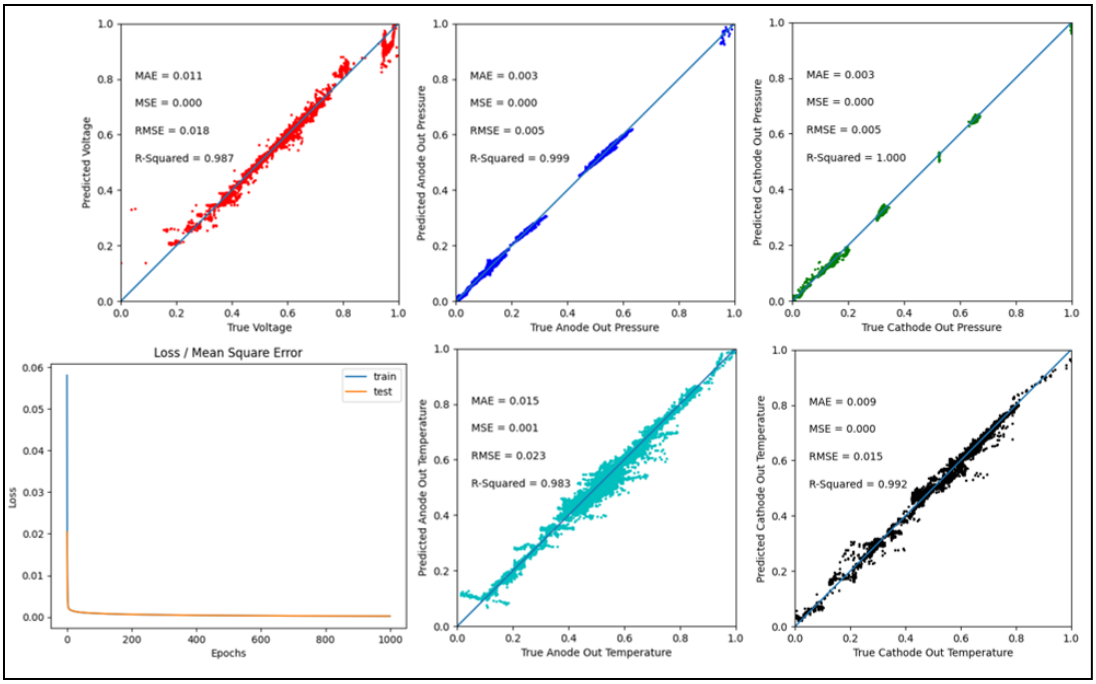
Batch and single-shot learning are two approaches to exposing the data set to the ANN during training [109], [110], [111]. The difference between both approaches is that in batch learning, the

model is trained using a fixed dataset, and the weights or biases of the connections between neurons are modified after processing the entire dataset. In single-shot learning, the model is trained using a single instance of the data and the weights and biases are updated immediately after each instance. Batch learning is used when the dataset is large enough to be processed in a reasonable amount of time and can be more computationally efficient, leading to a better generalization performance, as it considers the entire dataset when updating the weights. Whereas single-shot learning is applied on small datasets, allowing the model to learn and adapt more quickly to new data, it can be less accurate and more prone to overfitting, as it only considers the specific single instance to update the weights and bias values. Considering that the current data set has more than 40,000 test cases, a multi-input multi-output (MIMO) regression batch learning approach is implemented, where the impact of different batch sizes is investigated to compare the processing times and accuracy of the model. A batch learning approach with a batch size of 500 to 5000 points resulted in a training time of under 10 minutes.

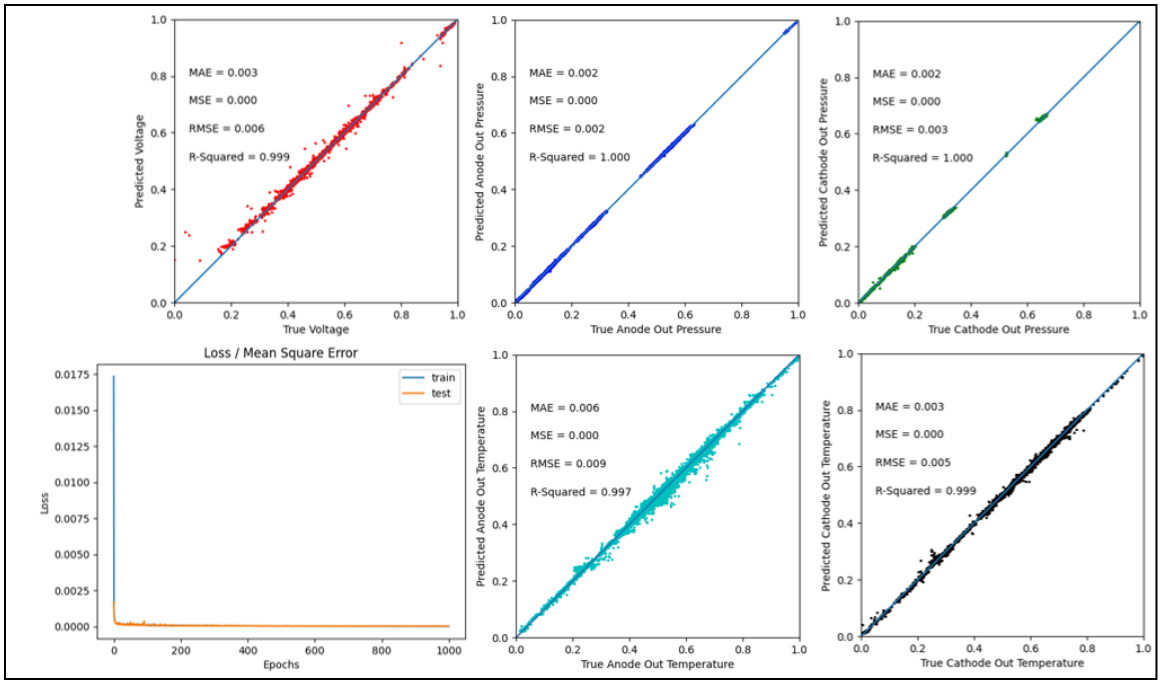
The prediction results of a few ANN model iterations and associated hyperparameters are shown in Figure 5.5 and tabulated in Table 5-2. The iteration process is initiated with Iteration A (shallow neural network consisting of only two hidden layers and 50 neurons) with 0.25 dropout probability, and associated hyperparameters such as learning rate are tuned in an iterative process to achieve minimum acceptable prediction error. The initial results from the iteration for pressure attributes are excellent; however, voltage and temperature prediction accuracy could be better considering the normalized data. Based on this observation, a second Iteration B is investigated (deep neural network consisting of only three hidden layers and 150 neurons) with 0.5 dropout probability and similarly tuned with various hyperparameters. The performance of the neural network at extreme conditions is not adequate and, in some cases, worse than Iteration A. Iteration C is built upon Iteration B by replacing the SGD optimizer with Adam and increasing the neurons per layer, which yielded a much better performance when compared to Iteration A and B. Iteration C despite demonstrating an excellent prediction accuracy is still a deep neural network with three hidden layers which takes a considerable amount of training and processing time, to resolve this Iteration D with similar Adam optimizer and increased dropout probability is configured on a shallow neural network consisting of only two hidden layers and associated hyperparameters are tuned. Iteration D performed relatively similarly to Iteration C, with minimal training and processing time for the neural network.



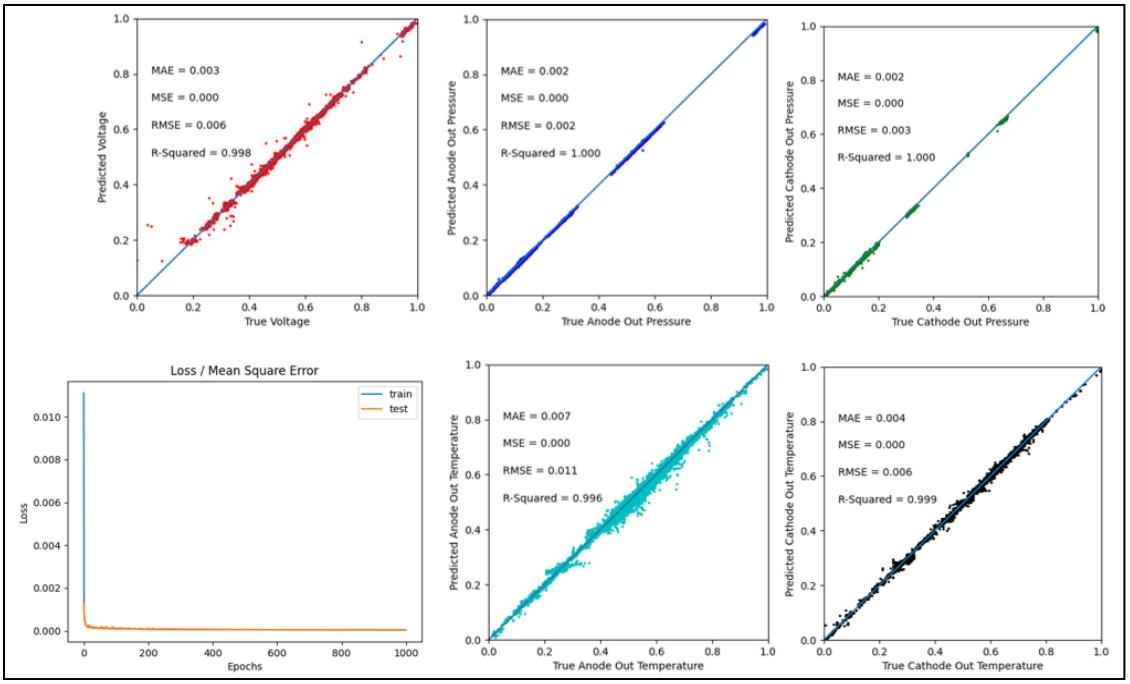
A. ReLU-2H-50N-0.25DP-0.025lr_0.9M_1000epch_SGD



B. ReLU_3H_150N_50P_0.025lr_0.9M_1000Epch_1000Batch_Size_SGD



C. ReLU_3H_500N_0.5P_0.0025lr_0.9Beta1_1000epch_1000batch_Adam



D. ReLU_2H_150N_0.75P_0.005lr_0.9Beta1_1000epch_500batch_Adam

Figure 5.5 Results of the neural network hyperparameter iteration: A; B; C; D

Table 5-2 Neural network hyperparameter iteration details

Iteration	Hidden layers	Neurons per layer	Dropout Probability	Optimizer	Learning Rate	Batch Size
A	2	50	0.25	SGD	0.025	32
B	3	150	0.5	SGD	0.0025	1000
C	3	500	0.5	Adam	0.0025	1000
D	***2***	***150***	***0.75***	***Adam***	***0.005***	***500***

After considering the iteration results and computational efficiency, iteration D had the best overall accuracy, with an R^2 value greater than 0.995, and was selected as the final architecture and hyperparameters of the ANN, as tabulated in Table 5-3.

Table 5-3 Finalized neural network hyperparameters.

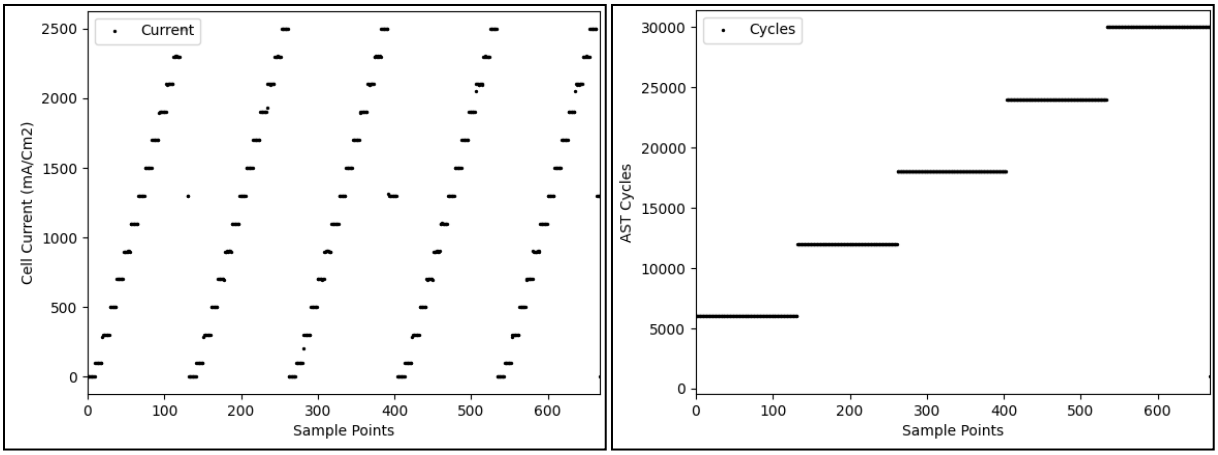
Hyperparameters	Values
Inputs feature vectors	12
Output parameters	5
Hidden layers	2
Nodes / Neurons	150
Activation function	ReLU-1st ,2nd layer; Linear – final layer
Loss function	'MSE'
Optimizer	Adam
Learning Rate (Lr)	0.005
Beta_1 (decay factor)	0.9
Iterations / Epochs	1000
Dropout probability	0.75
Batch Size	500
Training Time	5 Mins

5.4 Results and Discussion

This section evaluates the PEMFC model performance after training by comparing the final prediction attributes to their actual experimental values (true values). However, it must be noted that the recorded experimental values can induce measurement noise due to instrumentation procedures and interference from another physiological process. The performance of the PEMFC model to predict output voltage, temperature, and pressure after various AST degradation cycles is discussed in sections 5.4.1, 5.4.2, and 5.4.3, respectively. Sample points and associated degradation conditions (AST cycles) and cell current are tabulated in Table 5-4 and represented in Figure 5.6. During the polarization curve evaluation, the varying feature vector (input) data to the PEMFC model are the operating cell current and the AST cycles, the relative humidity of reactants (which is maintained at 100%), the cell temperature (stabilized at 75°C), reactant inlet pressures (maintained at 35kPag), and the flow rate of hydrogen (set at 4.5 SLPM) and the air (set at 9 SLPM). Section 5.4.4 discusses the PEMFC model's effectiveness over transient operating conditions at widely varied temperatures, pressures, flow rates, humidities, and current densities.

Table 5-4 Sample points and fuel cell degradation levels

Sample Points	Cell degradation level (Endured AST Cycles)
1-132	6000
133- 262	12000
263-404	18000
405-534	24000
535-668	30000

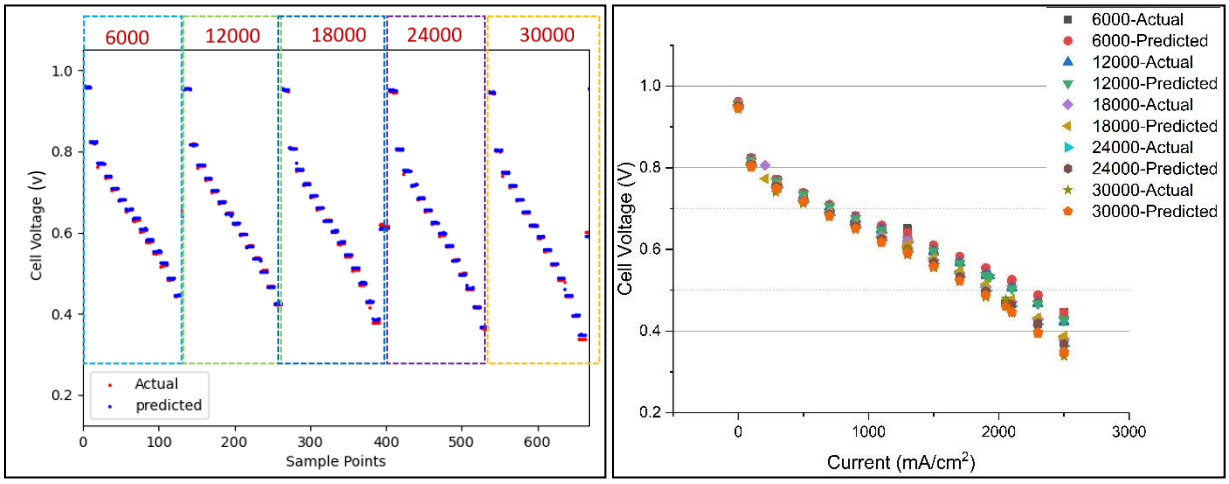


(a) (b)

Figure 5.6 (a) Cell current at various sample points; (b) AST cycles at various sample points

5.4.1 Prediction of PEMFC Voltage Degradation

For the first 6000 AST cycles, there was no observable (statistically significant) degradation in the cell performance; as a result, the 6000th cycle is considered the new baseline. The polarization curve is evaluated every 6000 cycles under the same conditions, and the model shows an excellent correlation between the actual (true/experimental) and model-predicted value. The sample data points of polarization curves with their actual and predicted voltage values at various current densities are shown in Figure 5.7. As observed, the initial OCV at various levels of degradation is relatively unchanged. However, the cell voltage at mid to higher current densities shows considerable degradation in performance, and the model accurately captures the voltage degradation trend.



(a) (b)

Figure 5.7 ANN predicted voltage degradation. (a) Voltage vs sample points; (b) Voltage vs cell current

5.4.2 Prediction of PEMFC Temperature Dynamics

Similarly, the temperature of the outlet gases at both the anode and cathode is measured during the polarization curve evaluation every 6000 cycles. The AST cycles had a minimal effect on the temperature dynamics, as expected, due to the electrochemical aging process, which does not impact the structural properties of the membrane. Figure 5.8 and Figure 5.9 show that anode and cathode outlet temperatures exhibit different trend patterns and variations. Both exhibit temperature rises with increasing current density, but there is an observable dip on the anode side, suspected to be due to the back diffusion of water from the cathode to the anode at higher operating currents, reducing the anode outlet temperature. The relative variability in temperature dip between 6000 cycles and rest can be attributed to the change in the water retention capacity of the membrane due to aging, impacting the water back diffusion process, thereby affecting the anode out reactant temperature at high current densities [112]. The temperature change is around 2°C to 4°C at normal operating conditions for a single cell; when multiple cells and stacks are considered, this temperature change will be more significant, especially if a hotspot is encountered due to PEMFC pinhole formation or due to any change in membrane ohmic resistance. Considering that the current model can predict similar minute temperature patterns at various operating conditions, this approach can be scaled up for diagnostic purposes to predict hot spot formation and membrane dehydration by recognizing the errors and patterns that deviate from normal behavior. It might be mentioned that the temperature anomalies observed in Figure 5.9 (b) around the sample point of 400 at the temperature of around 75.5°C are due to the transition in the operating current, that is, the operating current has been reduced after the peak current condition, as this is also observable in both Figure 5.6 and Figure 5.7.

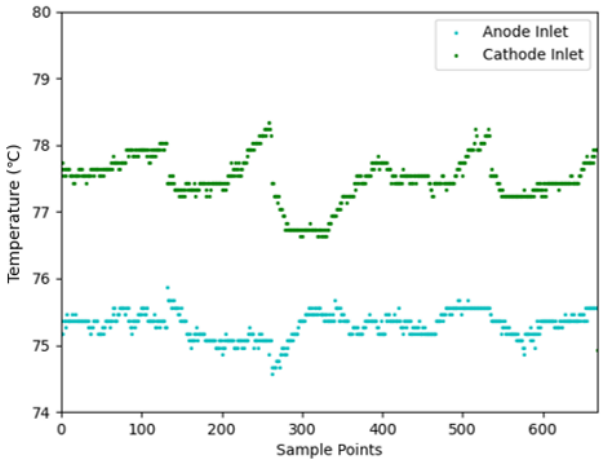
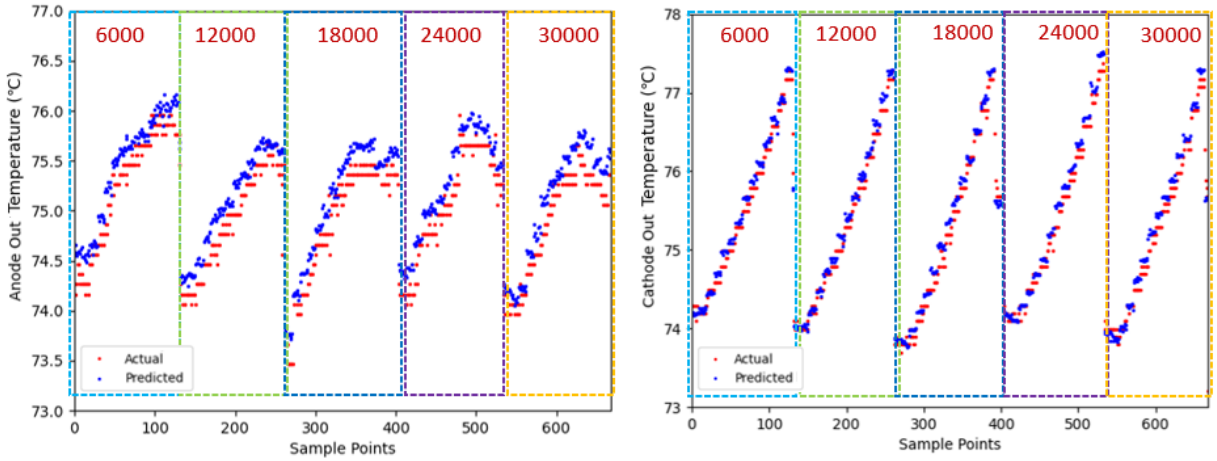


Figure 5.8 Fuel cell reactant inlet temperature profile



(a) (b)

Figure 5.9 ANN predicted fuel cell temperature dynamics [Red-Experimental Value; Blue–Predicted Value] (a) Anode reactant outlet temperature; (b) Cathode reactant outlet temperature

5.4.3 Prediction of PEMFC Pressure Dynamics

Similar to temperature dynamics, the PEMFC model can accurately predict pressure drop across the fuel cell, which changes with resistance to mass transport of reactants and products (all pressures are designated relative to gauge pressure). However, during a constant reactant flowrate, the fluctuations in reactant outlet pressures are minimal (only a few Pascals) unless there is a significant blockage due to water; Figure 5.10 and Figure 5.11 illustrate only a specific operating cycle with varying current and constant reactant flow rate (at various AST cycles), and the algorithm prediction performance echoes the AST cycling, as seen in early figures. This is because the current data-based model is predominantly tuned to predict pressure fluctuations at transient

conditions, for which it performs robustly with great accuracy, as shown in the following subsection (section 5.4.4). As such, the current model could be further tuned or optimized for this duty cycle of constant reactant flow rates, and the transient performance results at different operating pressure ranges are shown in section 5.4.4. As expected, the pressure drop across the cathode is higher, resulting in lower cathode outlet pressures due to the high reactant flow rate. The AST cycles had minimal effect on the pressure dynamics as the degradation mechanism does not impact the gas diffusion layers, gaskets, and bipolar plate structure, which can be observed in the figures. A minute outlet pressure drop at high current conditions can be noted on the cathode side, indicating minimal flooding. However, similar to the change in temperature, pressure drops across multiple cells and stacks will be a magnitude higher and increase during flooding at higher current densities. Considering the current PEMFC model's performance level to track pressure drop across a single cell, it can be scaled up to detect flooding in PMEFC during abnormal operations.

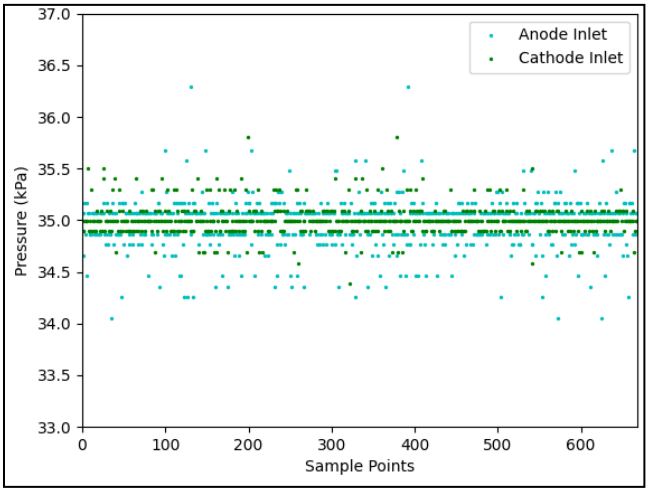
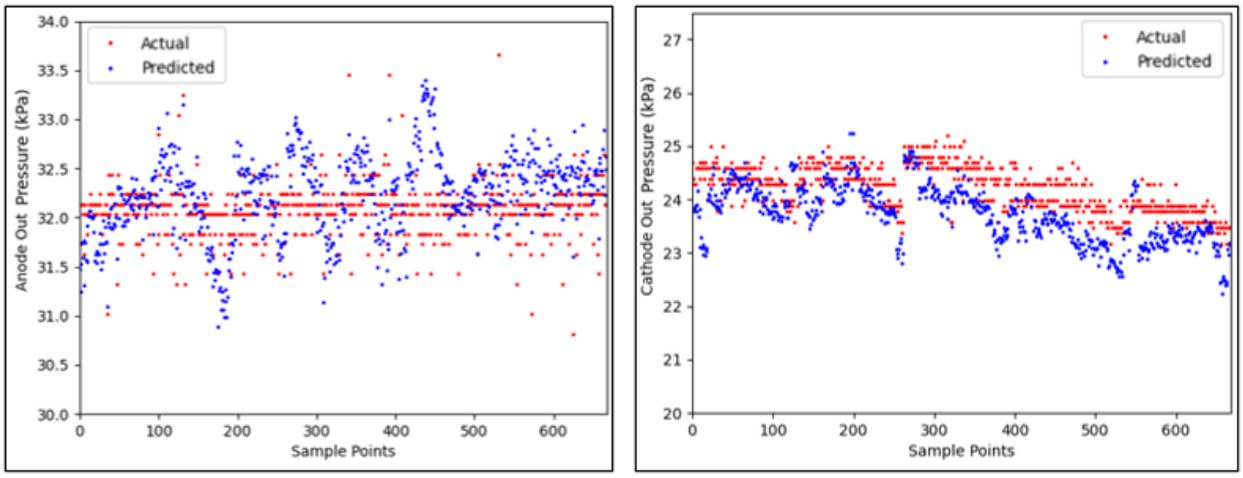


Figure 5.10 Fuel cell reactant inlet pressure profile



(a) (b)

Figure 5.11 ANN predicted fuel cell pressure dynamics [Red-Experimental Value; Blue–Predicted Value] (a) Anode reactant outlet pressure; (b) Cathode reactant outlet pressure

5.4.4 Prediction of PEMFC transient dynamics and model robustness

Although fuel cells are designed primarily to operate under steady-state conditions, the transient operating points are critical, and the PEMFC model must show good correlations during these transient conditions. The data acquisition system can also be subjected to measurement noise during these transition processes due to the inherent limitations of sensors and data sampling intervals. The experimental data has inherent measurement noise due to the limitation of current, voltage sensors' precision (electrical interference), and the influence of water condensation on thermocouples and pressure transducers. The data-based PEMFC model can not only predict the system outputs accurately at different operating zones (high and low pressure, temperatures, and currents) but also has excellent robustness when dealing with sensor noise and unstable conditions, as shown in Figure 5.12 and Figure 5.13, advocating its suitability and adoption for on-board diagnostics applications. The algorithm also accurately predicts the pressure fluctuation in transient operation relatively better than the steady state, as illustrated in Figure 5.13, across various pressure ranges. The overall performance of the data-based PEMFC model's prediction capability is evaluated across a wide range of operating conditions, including steady state, transient, low and high current densities, low and high reactant flow rates, pressures, and temperatures, and the associated error statistics across 41,255 data points are represented using histograms as shown in Figure 5.14. Most of the prediction attributes are within 5 % error,

emphasizing the algorithm's accuracy and robustness, especially considering that measurement data is not filtered.

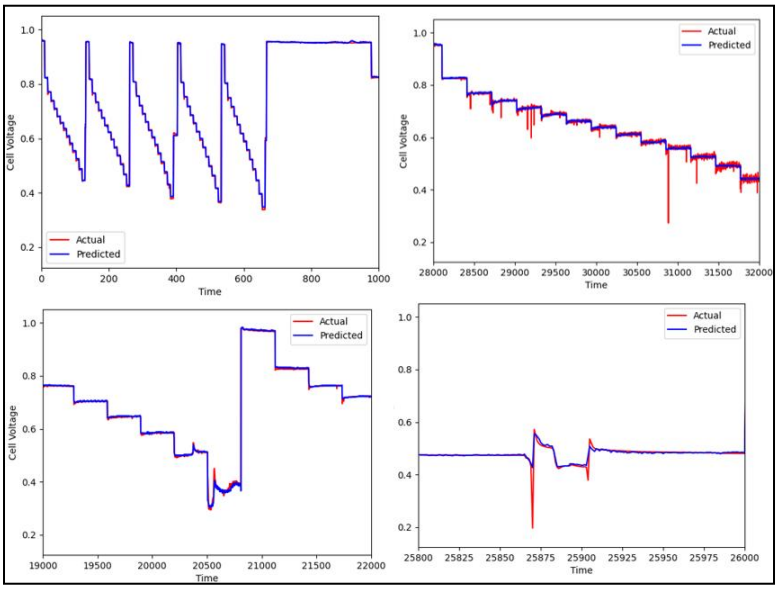


Figure 5.12 ANN voltage prediction during transient conditions with measurement noise

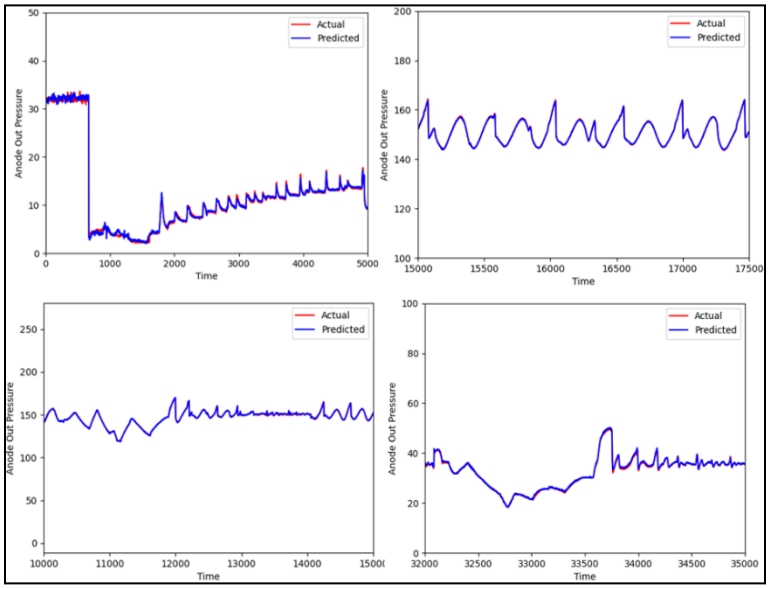
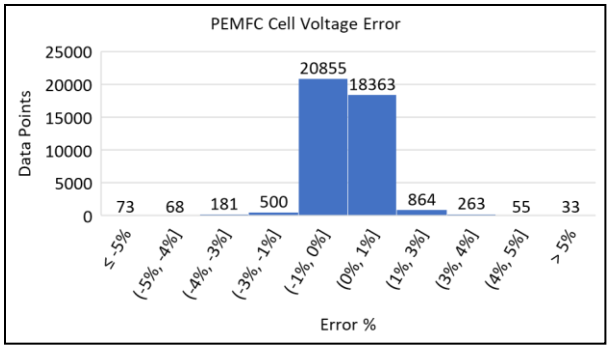
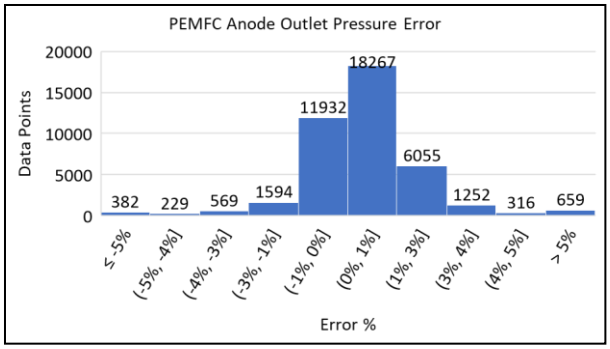


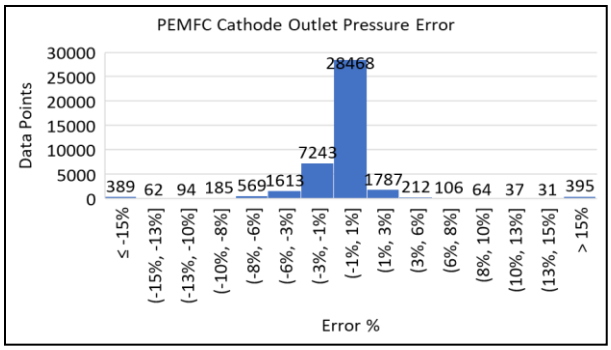
Figure 5.13 ANN pressure dynamics prediction during transient conditions with measurement noise



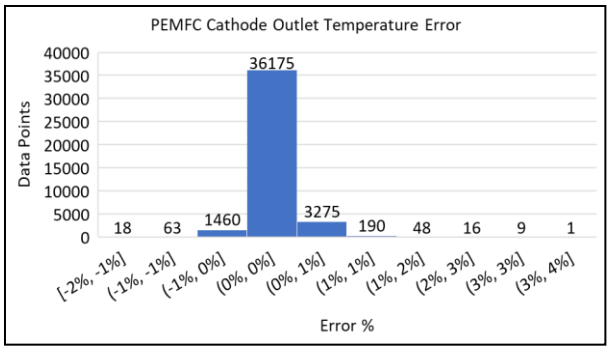
(a)



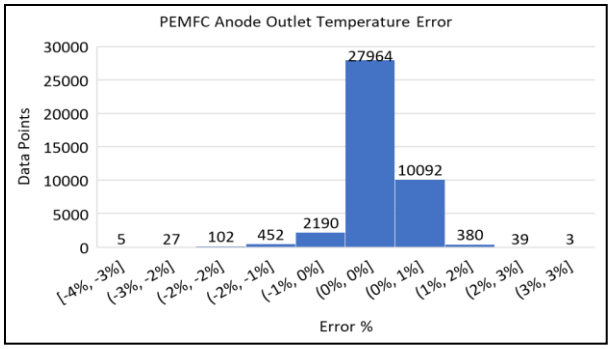
(b)



(c)



(d)



(e)

Figure 5.14 ANN prediction error histogram (a) Cell voltage; (b) Anode outlet pressure; (c) Cathode outlet pressure; (d) Anode outlet temperature; (e) Cathode outlet temperature

5.5 Summary

In this study, a multi-input and multi-output data-based model for proton exchange membrane fuel cell (PEMFC) trained on experimental data using feed-forward neural network architecture is successfully developed to predict the voltage degradation, temperature, and pressure dynamics of fuel cell over various operating conditions. Twelve fuel cell operating parameters are considered as feature vectors (inputs) to simultaneously predict five prediction attributes (fuel cell outputs) that can be used to diagnose fuel cell operation and degradation. An experimental dataset consisting of over 40,000 test cases, including data from various degradation levels, is used for training and validation of the neural network and is purposefully not subjected to any data filtering or smoothening. The voltage degradation behavior is formulated as a regression problem, using the endured accelerated stress test (AST) cycles to input the neural network's degradation factor. Multiple iterations of model hyperparameters, optimizers, and batch learning are implemented to improve the accuracy and robustness of the neural network. The model demonstrates excellent accuracy with $R^2 \geq 0.995$ for all the predicted variables upon normalized and pristine data during the validation phase and on new data across multiple operating conditions, enabling the model to track voltage, temperature, and pressure patterns, a majority within 5% error. The PEMFC neural network can track the voltage, temperature, and pressure fluctuation in the presence of degradation, measurement noise, and transition conditions, exhibiting excellent robustness and demonstrating the feasibility of such models for onboard diagnostic purposes.

Chapter 6 Hybrid Databased Modeling to Predict Thermal Behavior of LIB

This chapter aims to demonstrate the capability of hybrid-based models to predict the heat generation rate of electrochemical systems, control the thermal management system and detect sensor faults in a battery management system

*This chapter is adapted from Legala, Adithya, et al. "*Hybrid data-based modeling for the prediction and diagnostics of Li-ion battery thermal behaviors*." Energy and AI, vol. 10, Aug. 2022, p. 100194, doi:10.1016/j.egyai.2022.100194.

The world has seen a significant emphasis on transitioning to green energy sources to combat global warming, and Lithium-Ion Battery (LIB) technology is at the forefront of this process. Lithium-ion battery (LIB) has been deployed for the electrification of the transport sector as a key strategy for climate change mitigation and adaptation. However, it has significant technical challenges, such as thermal runaway, requiring a good understanding and accurate prediction of the LIB thermal behavior (heat generation rate). In this study, a novel hybrid approach using an Artificial Neural Network (ANN) is developed for predicting the heat generation rate with discharge current, output voltage, ambient temperature, cell surface temperature, and Depth of Discharge (DOD) as the feature vectors (inputs); where the DOD is estimated with an Extended Kalman Filter (EKF), and direct Coulomb Counting (CC) method. A shallow neural network utilizing the Marquette-Levenberg algorithm is designed and calibrated using over 8000 cases of testing data. It is shown that the predicted heat generation rate of LIB agrees well with the experimental results with an accuracy of $R > 0.995$. Further potential of this hybrid data-based model is evaluated by simulating a thermal management system control and by introducing voltage and current sensor faults for diagnostic purposes. It is shown that, when compared to the experimental value, the relative error of the total heat output generated is less than 2% when there is no sensor fault, and greater than 50% and 25%, respectively, with an induced failure of the current and voltage sensor, demonstrating the ability to build accurate models relying solely on LIB discharge data for sensor diagnostics. This study highlights the combination of using battery thermal behavior with machine learning for real-time battery system monitoring, controls, and field diagnostics.

6.1 Introduction

Current uncertainty in oil prices, rising greenhouse gases, and vehicle emission regulations are significantly changing the automobile industry's market outlook. [1], [3], [69], [115]. The proposed changes intend to replace internal combustion engine vehicles with electrified vehicles, predominantly with battery electric vehicles (BEV) [3], [5], [7], [8]. The battery is the most prevalent electrochemical energy storage device that converts chemical energy to electrical energy and vice versa during discharge and charge operations, involving the insertion (lithiation) and extraction (delithiation) of lithium ions [8]–[10]. Lithium-ion-based chemistries are the most commercialized battery technologies in the automotive and portable electronics industries primarily due to their high-power density, energy density, stability, and minimal memory effect [11]. However, Lithium-ion battery (LIB) operation generates heat due to various overpotentials and electrochemical reactions associated with charging and discharging [116]. This heat generation of the LIB mimics a nonlinear function and also raises the temperature of the battery, which in turn increases exothermic chemical reaction, resulting in a further increase in temperature, leading to the phenomena referred to as thermal runaway [117], [118], [119], [120]. The battery heat generation rate knowledgis essential to designing an efficient thermal management system to improve the battery performance and associated fail-safe safety systems [121], [122]. LIB heat generation rate during discharge depends primarily on discharge current, voltage, ambient temperature, cell surface temperature, and the State of Charge (SOC)/Depth of Discharge (DOD) of LIB (which represents the currently available battery capacity) [59], [116]. Therefore, prediction, diagnostics, and prognostics of LIB thermal behavior are significant for safe and efficient operation in practice.

Traditional battery thermal behavior models are dominated by physics-based models such as Computational Fluid Dynamics (CFD), lumped thermal models and heat transfer models which rely on material conduction properties, cooling system attributes and heat transfer mechanics to estimate the total heat output of the battery [123], [124], [125], [126]. These physics-based modeling techniques, though accurate, cannot be used in a real-time system for field monitoring or control due to the complex computation involved, thereby limiting their use only to the developmental phase. Data-based models (AI-based) are in contrast with the physics-based models where the entire input-output relations of the model are determined experimentally without prior knowledge of material conduction properties, and internal attributes and can also be implemented

in real-time on the field due to their fast computation [41], [42], [127]. Considering the advantages this study focuses on the hybrid approach of using data-based models supplemented with physics-based/empirical-equivalent model techniques to predict the heat generation aspect of the LIB. The LIB system is an electrochemical system that consists of complex chemical kinetics and ion transport phenomena; however, since it is a closed system, there are no external reactant input or product exhaust parameters, relatively reducing the number of available feature vectors for the development of the data-based models. There are only four major measurement parameters in a LIB system: operating current, temperature, voltage, and total resistance/impedance, which are typically used in numerous machine learning models in this area to predict the State of Charge (SOC) or State of Health (SOH) [128], [129].

This chapter discusses a novel approach to using an Artificial Neural Network (ANN) for predicting the heat generation rate coupled with an Extended Kalman Filter to estimate the corresponding SOC/DOD of the LIB, as shown in Figure 6.1. This type of modeling with ANN and EKF can be regarded as a hybrid model as it incorporates both the characteristics of data-based modeling and elements of equivalent circuit, physics-based modeling. From the literature, it is evident that SOC estimation through ANN and EKF is an established technique that can be further modified to predict the thermal behavior of the LIB.

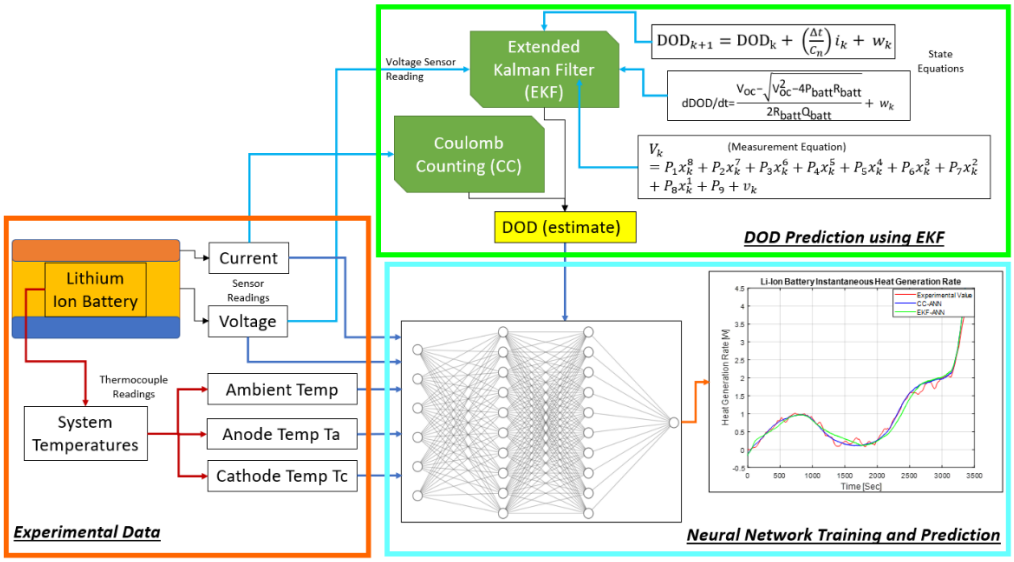


Figure 6.1 Schematic of the proposed artificial neural network architecture with EKF

6.2 2. Data Acquisition

The data for the development and calibration of the ANN and EKF model in MATLAB is obtained experimentally by discharging a commercially available prismatic Li-ion battery (LiFePO4) from A123 at various operating conditions [36], [37]. The heat generation rate of the 20 Ah LiFePO4 prismatic battery from A123 during discharge is measured with the help of a custom-built calorimeter using High-Density Polyethylene (HDPE) and a schematic of the experimental setup is shown in Figure 6.2 [36]. The charge and discharge cycles of the battery are controlled by Greenlight Innovations G12-200 multichannel battery test station also referred to as the Automated Battery Test Station (ABTS), with an accuracy of around 0.2 A and 0.05 V in source current and voltage control, respectively, and 0.03 A in current sink control, and 0.06 A in current measurement. The heat generation rate is calculated with the help of the convolution theorem, as described in the previous publication [36]. The battery discharge tests were conducted at various discharge rates (0.25C, 0.5C, 1C, 2C, and 3C) and various ambient operating temperatures (-10°C, 0°C, 20°C, 30°C, 40°C). Further description and explanation of the experimental setup are published in [36]. The following test conditions are chosen to replicate the expected battery's application environment and operating conditions.

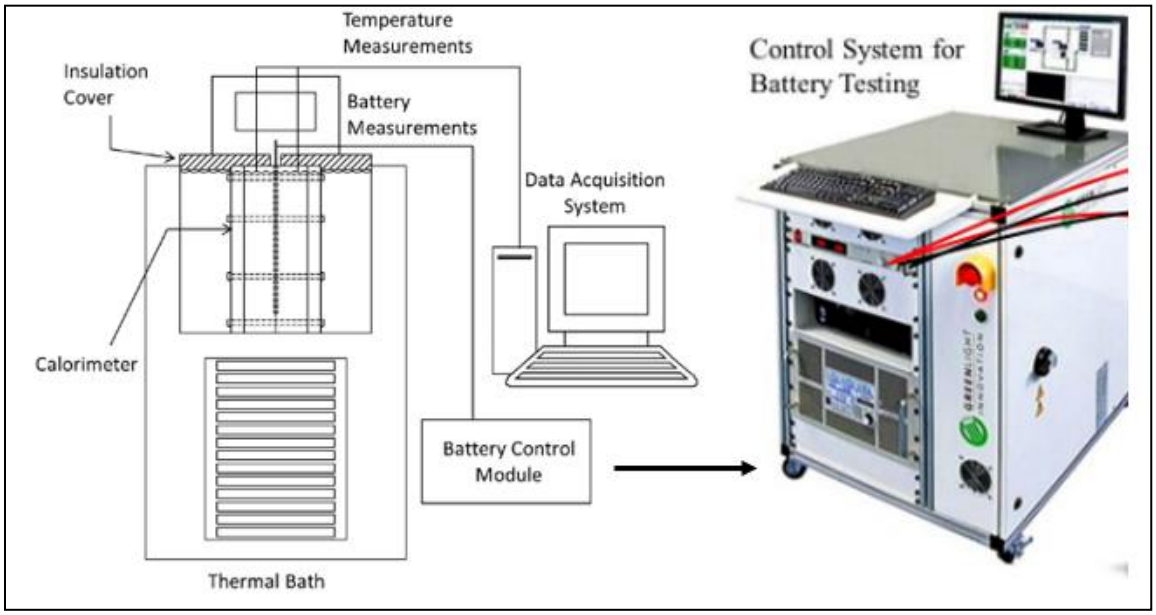


Figure 6.2 Schematic of the Lithium Ion Battery (LIB) experimental setup with the calorimeter

6.3 System Modeling

The Artificial Neural Network (ANN) modeling of LIB thermal behavior requires either State of Charge (SOC) / Depth of Discharge (DOD) along with other parameters as the inputs to the ANN models. While other parameters such as battery voltage, current drawn from the battery, ambient temperature and battery surface temperature can be measured for the training and validation of the ANN models developed, in practice SOC/DOD cannot be measured directly, though can be estimated based on other directly measurable quantities. SOC/DOD can be estimated by the Coulomb Counting (CC) method however this CC method requires accurate knowledge of the initial SOC/DOD, solely relies on the current sensor and is highly subjected to sensor noises (error accumulates over time). Another approach to estimating SOC/DOD is by using the Extended Kalman Filter (EKF) technique which relies upon a voltage sensor and doesn't require the knowledge of the initial SOC/DOD. This study presents a novel approach of using an Artificial Neural Network (ANN) for predicting the heat generation rate coupled with an Extended Kalman Filter (EKF) to estimate the corresponding State of Charge (SOC) / Depth of Discharge (DOD) of the LIB, parallelly an ANN coupled with a direct CC model is also developed in conjunction to aid in the controls and diagnostics process as shown in Figure 6.1.

Two different EKF estimation models are designed based on the state equations derived from (i) the equivalent circuit model and (ii) the coulomb counting equation, respectively, to predict the SOC/DOD. The inputs to the system are discharge current, battery output voltage, ambient temperature, and cell surface temperatures. The predicted outputs are DOD, heat generated, and control system (cooling) output, represented by the radiator fan's status. A current and voltage sensor fault are virtually simulated by altering the respective data signal with an offset (bias) to evaluate the diagnostics aspect of the data-based model. SOC can be correlated to the depth of discharge (DOD) as it is an observation from an opposite perspective change in the current direction (charge vs discharge); the sum of SOC and DOD is always equal to 1 so that the DOD can be predicted by the SOC algorithms [131]. To simplify from here, DOD is the only entity stated in the formulation (modifying the existing SOC algorithms) to maintain commonality with the literature; physically, we are estimating DOD. The relation between the SOC and DOD is illustrated as follows: the summation of SOC and DOD is always 1, i.e., $SOC + DOD = 1$; a DOD of 0.2 equals a SOC of 0.8. The representation of output current from the battery is represented as negative when referring to SOC and positive when referring to DOD. Under a constant discharge,

the SOC of the battery tends to zero, and the DOD of the battery approaches 1; for a fully charged battery, the initial SOC is 1, whereas the DOD is zero; SOC-DOD correlations are tabulated in Table 6-1.

Table 6-1 Correlation of SOC and DOD

Condition	***SOC***	***DOD***
40% battery charge	0.4	0.6
20% battery charge	0.2	0.8
Battery fully charged	1.0	0
Battery fully discharged	0	1.0

This hybrid development for the prediction of heat generation can be mainly divided into two parts, the first one is the development and tuning of the EKF to predict the DOD, and the second one is to develop and calibrate the artificial neural network by using the output of EKF and other parameters to predict the heat generation rate. That is, (i) State estimation using EKF for the DOD, and (ii) Predicting the output using ANN with the output being the LIB heat generation.

6.3.1 State Estimation using EKF

Kalman Filter (KF) is one of the most prevalent and mature techniques to estimate the dynamic state of the linear system by correlating the system's estimated output parameter with the sensor measurement value. The estimated state is more accurate than the sensor measurement value, which contains measurement uncertainties (or noise). The KF algorithm considers the input data and output data to estimate the system state ($\hat{x}_k$) such that it minimizes the mean squared error between the estimated system state and the true system state (x_k). KF assumes that the process (state equation) noise and measurement (sensor) noise are independent and acts as the optimum state estimator for the system. In the case of a non-linear system, linearization of the system at every time step (discretized) is necessary for better approximation, this aspect of linearization followed by KF implementation is commonly referred to as Extended Kalman Filter (EKF). The discretization time is calibrated according to the system's requirements. The LIB system is considered as a non-linear system, and a non-linear system is modeled as follows

$$x_{k+1} = f(x_k, u_k) + w_k \tag{6.1}$$

$$y_k = g(x_k, u_k) + v_k \tag{6.2}$$

where $x_k, u_k,$ and y_k represent the state of the system, input to the system, and system output, respectively, at an instance k. Equation (4.1) is referred to as the state equation, and Equation (4.2) is regarded as the measurement equation. w_k and v_k are the independent process noise and measurement noise whose covariance matrices are represented by Q and R. For the current LIB system, there is only one state that needs to be estimated, which is the DOD. Typically, DOD can be estimated by two methods: the first one is the coulomb counting (CC) method, which is a direct calculation of total charge relying solely on the current sensor reading:

$$\mathrm{DOD_T} = \mathrm{Initial_DOD} + \int_{t_0}^{T} \frac{I(\tau)}{C} d\tau \tag{6.3}$$

where t_0 is the initial time, T is the total time, I(τ) is the discharge current and C is the total capacity of the battery during operation. The second one is an estimation algorithm, in this case, the EKF algorithm serves this purpose where the state function which is in terms of DOD is expressed by either considering a physics-based coulomb counting (CC) derived state equation or an equivalent circuit model (ECM) based state equation coupled with a measurement equation derived from experimental data [132]. In this study, both approaches (state function) are modeled and explored.

6.3.2 <u>Physics-based state equation</u>

The CC method can be modified accordingly to represent a state equation by monitoring the amount of current drawn from the battery, thereby calculating the total charge output and adding it to the previous DOD value [133] as follows:

$$\mathrm{DOD}_{k+1} = \mathrm{DOD_k} + \left(\frac{\Delta t}{C_n}\right) i_k + w_k \tag{6.4}$$

where DOD_k is an inner state of the battery system, $i_k$is the measured input current, Δt is the time interval, and C_n presents the cell's nominal capacity w_k is the process noise associated with the equation, and its associated covariance initially needs to be estimated and tuned. The nominal capacity is a function of the operating temperature and age of the LIB system, which are determined by the experimental results.

6.3.3 ECM-based state equation

The equivalent circuit of the LIB is modeled as a voltage in series with a resistance and capacitor, as shown in Figure 6.3, relatively reducing the number of internal battery parameters, thereby reducing the associated computational complexity when compared to the first-order or second-order RC circuits [134], [135], [136]. Capacitance and resistance values of the battery are obtained by experimentally evaluating the battery at specific temperatures and discharge rates. Where V_{oc} is the open-circuit voltage, R_{batt} is the internal resistance, and Q_{batt} is the total capacity of the battery, all of which are determined by experimental data, and output battery power (P_{batt}) can be expressed as the difference between the reversible electrical power and power due to heat loss, mathematically expressed as follows [136]:

$$P_{batt}=V_{OC}I_{batt} - I_{batt}^2R_{batt} \tag{6.5}$$

The battery DOD using the coulomb counting can be determined as follows

$$\frac{d\text{DOD}}{dt} = \frac{I_{batt}}{Q_{batt}} \tag{6.6}$$

Considering the equations (5) and (6) the following DOD equation can be derived [136]:

$$\frac{d\text{DOD}}{dt} = \frac{V_{oc} - \sqrt{V_{oc}^2 - 4P_{batt}R_{batt}}}{2R_{batt}Q_{batt}} + w_k \tag{6.7}$$

where w_k is the process noise associated with the equation and associated covariance initially needs to be estimated and tuned appropriately. P_{batt} is also expressed as a function of DOD i.e., $P_{batt}=(m * \text{DOD} + C)$, where m and C are determined from the experimental results (m = -5.096 and C = 66.488) during the implementation of the EKF algorithm.

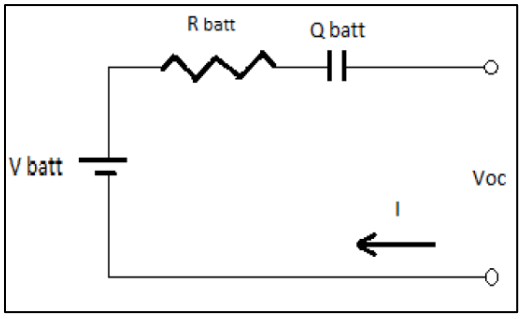


Figure 6.3 The equivalent circular model (ECM) consists of one resistance and one capacitance (RC) for a lithium-ion battery (LIB).

6.3.4 Measurement function

The measurement function, which is the voltage output of the battery, is derived from the experimental data (discharge curve of LIB for a specific discharge rate and temperature), and an accurate equation is framed using MATLAB curve fitting toolbox (8^{th} order polynomial) where the final voltage is expressed in terms of DOD as shown in Figure 6.4. This measurement equation can also be modeled by using the equivalent circuit equation; however, for the steady-state operation considered in this study, a direct measurement function is framed by using the experimental data as follows:

$$V_k = P_1 x_k^8 + P_2 x_k^7 + P_3 x_k^6 + P_4 x_k^5 + P_5 x_k^4 + P_6 x_k^3 + P_7 x_k^2 + P_8 x_k^1 + P_9 + v_k \qquad (6.8)$$

where x_k represents the DOD at the time instant *k*, and the values of the measurement function coefficients are given below:

P_1 = – 85.71; P_2 = 232.6; P_3 = – 203.6; P_4 = 22.2; P_5 = 65.77.
P_6 = – 40.28; P_7 = 9.509; P_8 = –1.094; P_9 = 3.311,

and v_k is the measurement (sensor) noise.

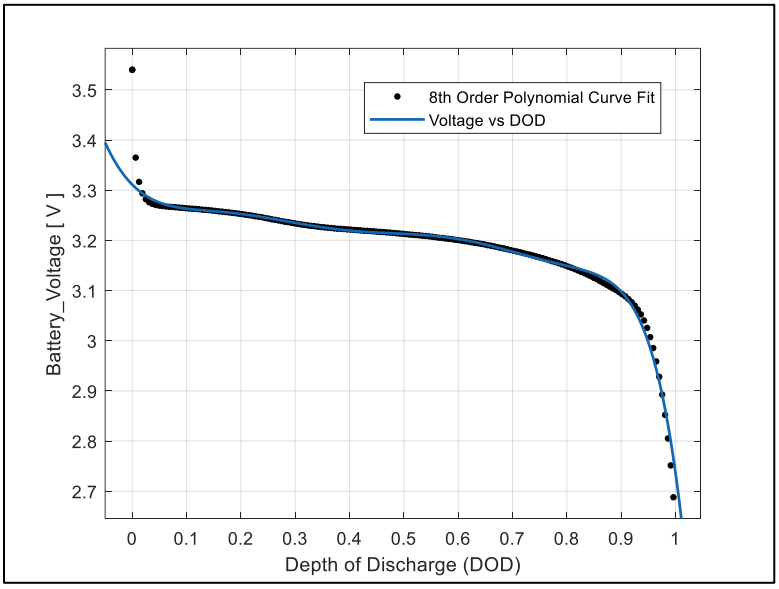


Figure 6.4 Battery voltage during discharge expressed as a function of the depth of discharge (DOD) as the measurement function, based on the correlation of experimental results [34] in terms of an 8th order polynomial)

Here are the steps involved in the implementation of the EKF algorithm for the physics-based state equation in the determination of DOD [62]:

Step 1: Predict a priori state $\mathbf{DOD}_k^-$:

$$\mathrm{DOD}_k^- = \mathrm{DOD}_{k-1}^+ + \left(\frac{\Delta t}{C_n}\right) i_{k-1} \qquad (6.9)$$

The a priori estimate of the DOD at time *k* is predicted based on the previous DOD value DOD_{k-1}^+ and the current i_{k-1}; Δt is the time step, and C_n is the nominal capacity of the battery.

Step 2: Predict a priori error covariance P_k^- at time k:

$$P_k^- = P_{k-1}^+ + \Sigma_w \qquad (6.10)$$

This step predicts the error covariance of the state estimate at time *k*, using the error covariance at time *k-1* and the noise covariance Σ_w.

Step 3: Compute the Kalman gain, Kg :

$$Kg_k = P_k^- * \frac{C_k}{[C_k * P_k^- * C_k + \Sigma_v]} \qquad \left(C_k = \frac{d[V(\mathrm{DOD}_k)]}{d[\mathrm{DOD}_k]}\right) \qquad (6.11)$$

The Kalman gain is calculated to update the estimate of DOD optimally. It uses the predicted error covariance P_k^- and the measurement mode.

C_k is the sensitivity of the measurement function V(DOD) to changes in DOD (a derivative of the voltage with respect to DOD). Σ_v is the covariance of the measurement noise.

Step 4: Update state estimation based on the observed voltage V_k' :

$$\mathrm{DOD}_{\mathrm{k}}^{+} = \mathrm{DOD}_{\mathrm{k}}^{-} + Kg_k * [V_k' - V_k] \quad (V_k \text{ from equation (6.8)}) \tag{6.12}$$

The state estimate $\mathrm{DOD}_{\mathrm{k}}^{+}$ is updated by incorporating the difference between the measured voltage V_k' and the predicted voltage V_k from the measurement function. The observed voltage V_k' comes from the sensor measurement, while the predicted voltage V_k is calculated using the measurement function.

Step 5. Error covariance P_k^-update to $P_k^+$for the next time step:

$$P_k^+ = (1 - Kg_k * C_k)P_k^- \tag{6.13}$$

$$\mathrm{DOD}_{\mathrm{k+1}} = \mathrm{DOD}_{\mathrm{k}}^{+} + \left(\frac{i\Delta t}{C_n}\right) i_k + w_k \tag{6.14}$$

The DOD at the next time step *k+1* is updated using the current DOD estimate and the current current i_k, w_k represents the process noise

DOD_k^-, P_k^-: Predicted DOD and error covariance at time *k*.

$\mathrm{DOD}_{\mathrm{k}}^{+}$, P_k^+: Updated DOD and error covariance at time *k*.

V_k, V_k' : Predicted and measured voltages. v_k: Sensor noise.

C_k: Sensitivity of voltage to DOD.

Σ_w, Σ_v : Process and measurement noise covariances

6.3.5 <u>ANN Modeling</u>

ANN is one of the widely used machine learning techniques based on the biological neuron, where a combination of neurons embedded with various activation functions process the computational activity to correlate the input and output attributes of the network. ANN model is designed for its architecture with respect to the number and type of hidden layers and nodes (neurons), the specific activation functions, training goals and numerical algorithms; and it is implemented by using the MATLAB NN toolbox, considering the ease of integration within

SIMULINK environment where over 8000 data points are being fed from LIB discharge curves (0.25C, 0.5C, 1C, 2C, and 3C) at various ambient temperatures (-10°C, 0°C, 20°C, 30°C, 40°C). It should be mentioned that for the 8000 data points used, 70% are used for training, 15% for validation and 15% for testing. After multiple iterations and optimization of the network structure, computational time, processing time, and hyperparameters, the ANN model is finalized with 2 hidden layers consisting of 10 neurons, each hidden layer; iteration results are plotted in Figure 6.5(a) and tabulated in Table 6-2. Levenberg-Marquet algorithm is applied for error propagation using the MATLAB neural network toolbox [59], [137], [138]. Levenberg-Marquardt Algorithm combines the gradient descent method (for global search) with the Gauss-Newton method (for faster convergence near the minimum). It uses a parameter, λ to adjust between gradient descent and Gauss-Newton. The neurons in the hidden layers use Tansig as the activation function, and the last output layer uses the linear activation function. Tansig in MATLAB is just an approximation of Tanh (hyperbolic tangent function), which is defined as follows.

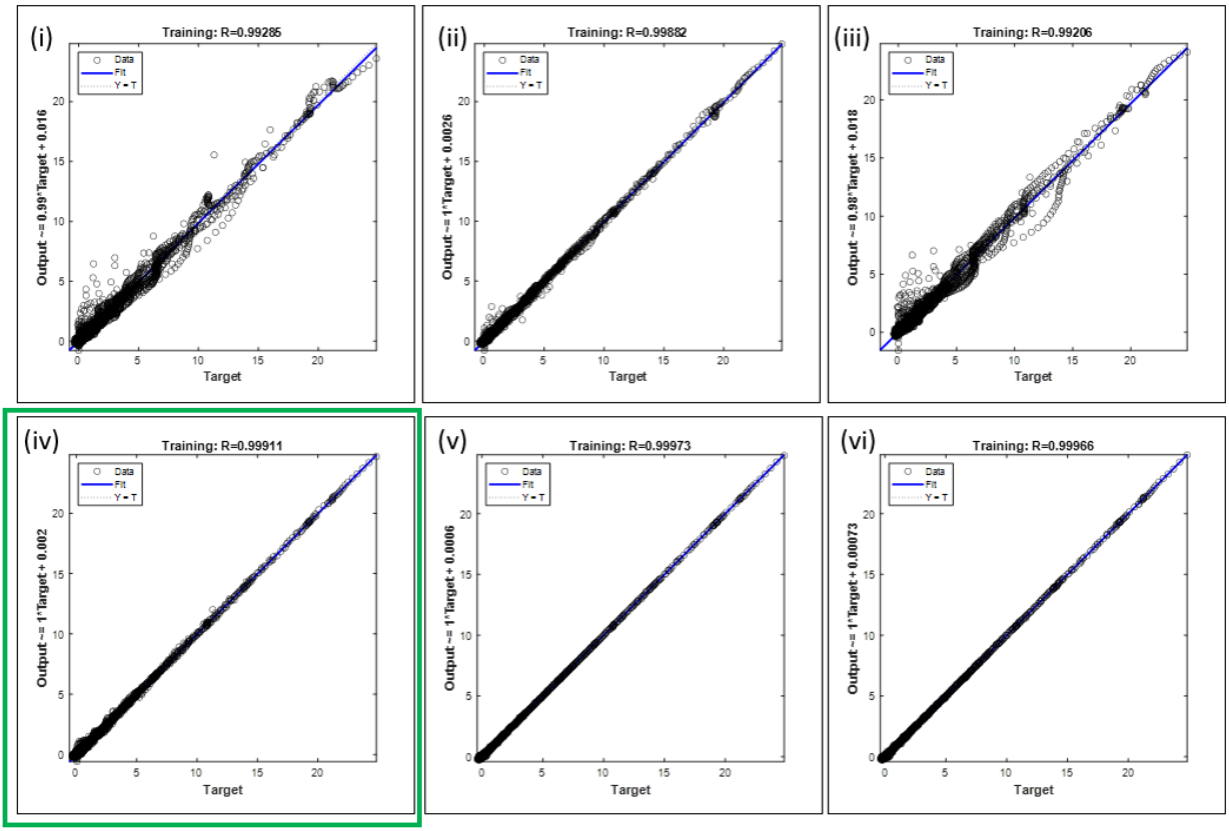
$$\text{Tansig}(x) = 2/(1 + \exp(-2 * x)) - 1 \qquad (4.16)$$

A schematic of the LIB ANN algorithm is represented in Figure 6.5(b), and a graphical representation of the tansig activation function and its derivative is shown in Figure 6.5(c); associated final ANN hyperparameters are tabulated in Table 6-3. The instantaneous current and voltage of the LIB system are measured by the Automated Battery Test Station (ABTS), DOD is estimated from the EKF model, ambient temperature and cell surface temperatures (Surface Temp Ta – anode, Surface Temp Tc – cathode) are measured by the thermocouples. Both the anode and cathode surface temperatures are considered for better accuracy, as the anode and cathode temperatures might differ under practical operating conditions. There was no necessity for any pre-processing or post-processing of data as the data acquisition system had minimal interference, low noise, and no outliers. Fundamentals of ANN architecture, activation functions, and workings of error back propagation algorithm are listed here [46]

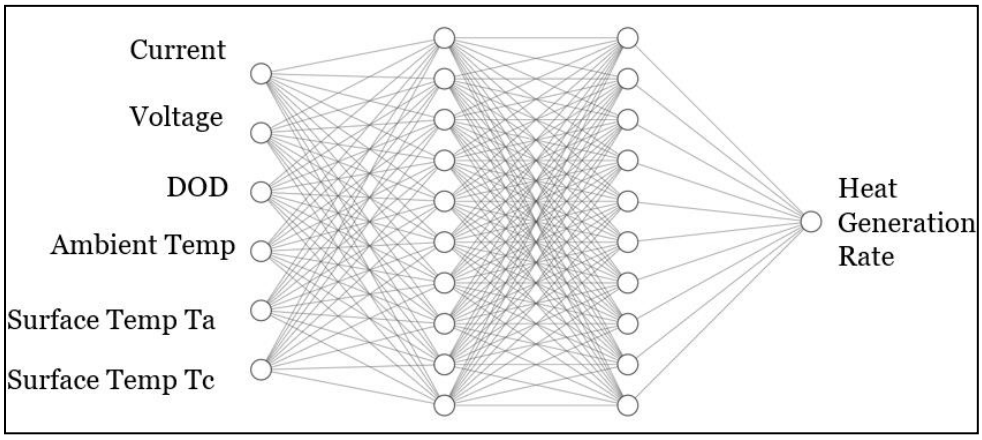
Table 6-2 ANN Hyperparameter Iteration Results

Iterations	Hidden Layers	Neurons	R-value
(i)	1	5	0.99285
(ii)	1	20	0.99882
(iii)	2	5	0.99206

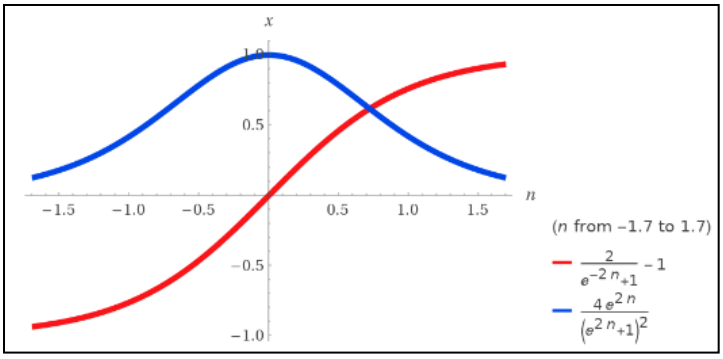
(iv)	***2***	***10***	***0.99911***
(v)	2	20	0.99973
(vi)	3	10	0.99966



(a)



(b)



(c)

Figure 6.5 ANN design and calibration (a) Regression plots of all the hyperparameter iterations tabulated in Table 6-2; (b) The artificial neural network (ANN) layout for the lithium-ion battery (LIB) thermal model;(c) Graphical representation of Tansig function(red) and its derivative(blue)

Table 6-3 Design parameters of the artificial neural network (ANN) for lithium-ion battery (LIB) thermal model

Inputs feature vectors	6
Output parameters	1
Hidden layers	2
Nodes / Neurons	10
Activation function	Tansig, Linear
Iterations / Epochs	1000
Training Goal	10^{-3}

6.4 Results and Discussion

The EKF algorithm is carried out by calibrating the covariance matrix of the measurement noise (R) and process noise (Q) and determining the discretization interval. The higher the noise value, the lesser the confidence of that aspect; hence, initial covariance values should be estimated and tuned depending on the system process noise and sensor measurement noise. The EKF tuning process follows the calibration guidelines in the literature [139]. The sensor covariance is initially estimated by considering the covariance of the voltage sensor data with the depth of discharge from the experimental data and calibrated further. The measurement noise (R) matrix represents the uncertainty in the sensor measurements and can be determined by computing the variance of

the measurement noise of the sensor and adjusting iteratively. The covariance for the process noise is estimated relative to the sensor noise and tuned during the process by observing the filter's performance to see if it's too sluggish or aggressive. As listed in Table 6-4, the following iterations (calibrations) of these EKF parameters are considered.

Table 6-4 The extended Kalman filter (EKF) iterations and tuning parameters

Iterations	Covariance of Measurement Noise (R)	Covariance of Process Noise (Q)	Condition
EKF Case 1	3.5E-2	1.25E-4	R > Q
EKF Case 2	2.4E-3	1.25E-2	Q > R
EKF Case 3	3.5E-2	1.25E-4	R > Q (faulty state initialization – unknown initial state)

Associated results of the EKF compared to direct coulomb counting (CC) and automated battery test station (ABTS) algorithm are presented in Figures 6.6, 6.7, 6.8, and 6.9 for the DOD changes as a function of discharge time. ABTS Corrected Value refers to the true DOD value measured by the test station, CC refers to the DOD value estimated solely from the coulomb counting method, EKF-ECM refers to the DOD value estimated by the EKF model using the ECM-based state function, and EKF-Phy refers to the DOD value estimated by the EKF model using the physics-based state coulomb counting derived state function.

6.4.1 EKF Prediction Case 1: Measurement noise > Process noise

In the first case, the covariance of the measurement (sensor) noise is considered to be larger than the covariance of the process noise (state function). Here, both the physics-based and ECM-based state functions are considered to have the same covariance of the process noise for comparison purposes. The initial state (DOD) is estimated as zero, which in this case is true as the cell is being discharged from full capacity. As shown in Figure 6.6, the DOD estimated by the EKF-Phy and EKF-ECM correlates well with the direct Coulomb Counting (CC) and ATBS measurement with a slight initial undershoot and overshoot. It should also be mentioned that more

confidence is placed in the state function for the present results. Both EKF algorithms, despite using different state equations, end up with almost the exact DOD estimation after the initial tuning when the input process noise is the same for both state equations. This indicates a good correlation between the ECM and the physics-based state equation's internal parameters.

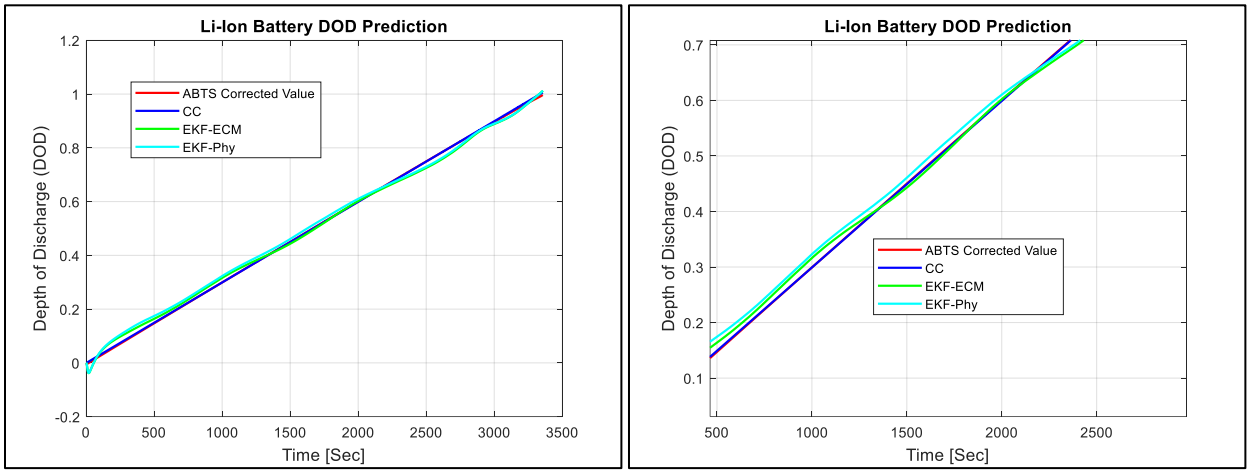


Figure 6.6 Comparison of the DOD estimation by the extended Kalman Filter (EKF) and direct coulomb counting (CC) method with the experimentally measured data by the automated battery test station (ABTS) for the case of the measurement noise larger than the process noise; magnified view on the right

6.4.2 EKF Prediction Case 2: Measurement noise < Process noise

In the second case, the covariance of the measurement (sensor) noise is considered to be **less than** the covariance of the process noise (state function), here both the physics-based, and ECM-based state function are still considered to have the same covariance of the process noise for comparison purposes. The initial state (DOD) is estimated as zero, which in this case is also true.

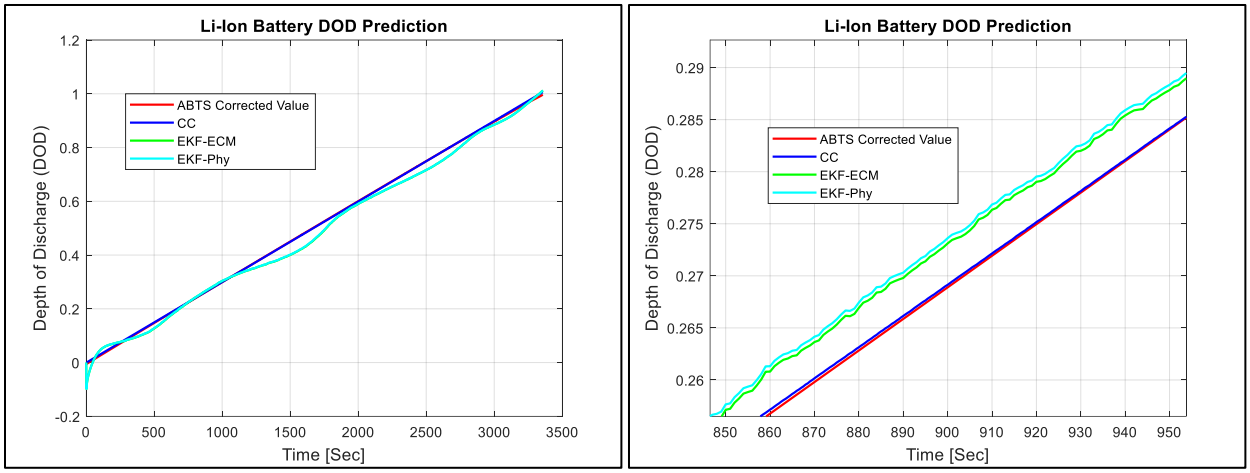


*Figure 6.7 Comparison of the DOD estimation by the extended Kalman Filter (EKF) and direct coulomb counting (CC) method with the experimentally measured data by the automated battery test station (ABTS) for the case of the measurement noise **less than** the process noise; magnified view on the right*

In Figure 6.7 the estimated DOD is still in good correlation with the coulomb counting method and ABTS measurement, with a slight undershoot, especially around the mid and lower end of the prediction. It is also to be mentioned that for the present results, more confidence is placed on the measurement function. From Figure 6.6 and Figure 6.7, the change in prediction can be observed by tuning the covariance value of the process noise and measurement noise.

6.4.3 EKF Prediction Case 3: Faulty initialization of the state

One of the biggest drawbacks of the direct coulomb counting method or other bookkeeping methods is that the initialization and sensor measurement errors will accumulate, resulting in increased state error over time. This can be resolved by using these EKF-based state estimation algorithms, as shown in Figure 6.8 significantly incorrect state initialization can still converge to true values over time. In this case, the initial state (DOD) of ECM-based EKF is initiated as 1 and physics-based EKF as 0.5, which is incorrect (faulty initialization) as the cell is discharged from full capacity. This illustrates the advantage of using the EKF estimation method rather than the direct coulomb counting method.

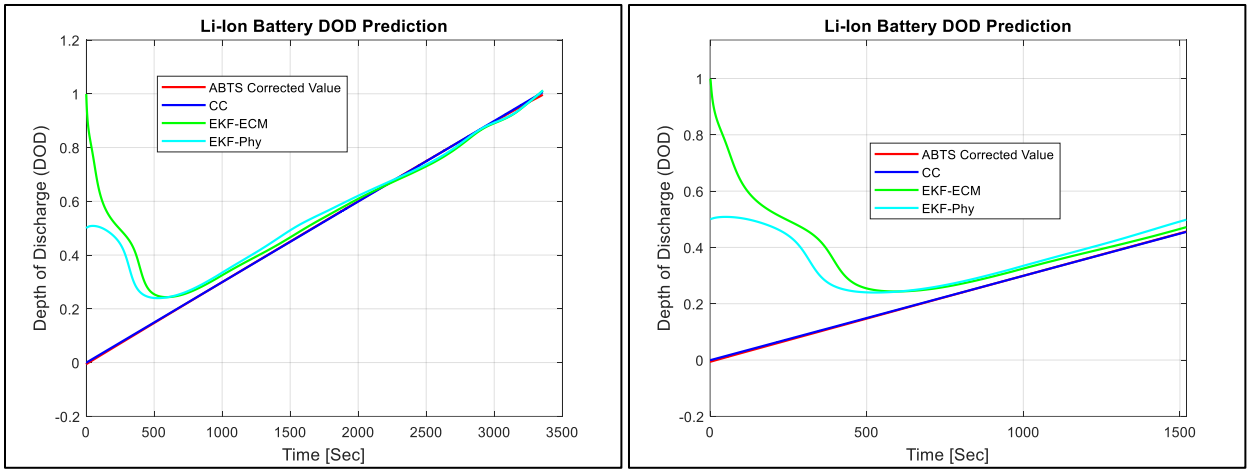


Figure 6.8 Comparison of the DOD estimation by the extended Kalman Filter (EKF) and direct coulomb counting (CC) method with the experimentally measured data by the automated battery test station (ABTS) when the initial values of DOD are estimated significantly incorrectly; magnified view on the right

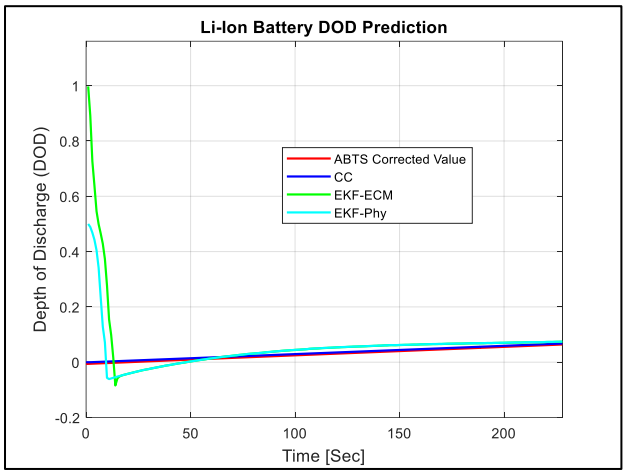


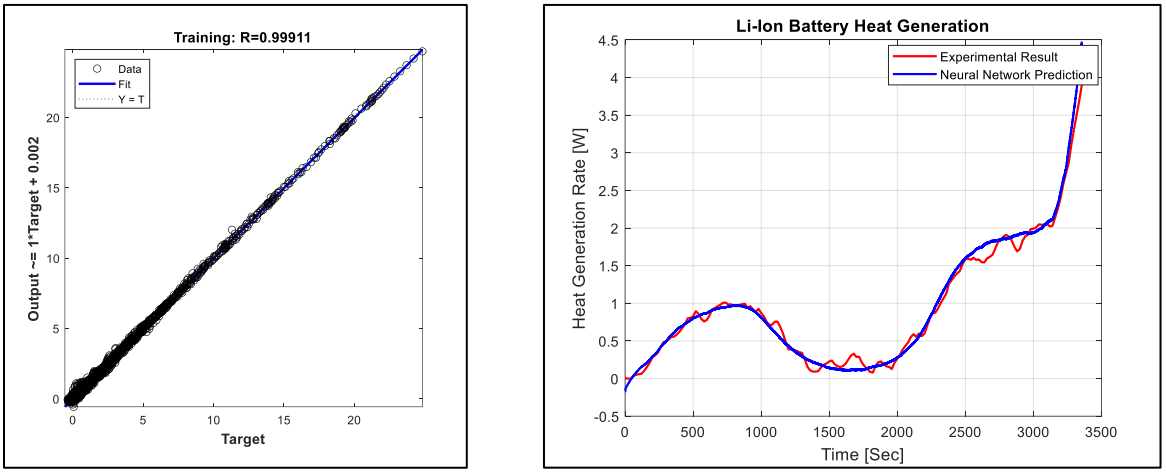
Figure 6.9 Comparison of the DOD estimation by the extended Kalman Filter (EKF) and direct coulomb counting (CC) method with the experimentally measured data by the automated battery test station (ABTS) when the initial values of DOD are estimated significantly incorrectly, but the parameters in the EKF are properly tuned

Figure 6.8 indicates that the initial convergence takes over 1000 seconds with the improperly tuned initial values of DOD used, and this is too long for automotive or consumer electronics applications. However, this situation can be resolved by further tuning of the parameters (modifying the covariance matrices, discretization time) in the EKF method, as shown in Figure 6.9, where the convergence to the true state is within 60 seconds, even though the initial DOD values are significantly off. If the EKF is too slow (lags behind changes), increase the Q to trust the model less and to react faster or decrease the R to trust measurements more. If the filter is too noisy (overreacts to measurements), decrease Q to smoothen the state estimate or increase

R to filter measurement noise. Considering the calibration procedure, and test cases it is concluded that the EKF is tuned appropriately and is accurately estimating the final DOD of the LIB despite faulty initialization and using different state functions.

6.4.4 Heat Generation Rate Prediction

From the above results and discussion, it might be concluded that the EKF performance is sufficiently accurate in estimating the DOD values of the LIB during discharge process. But before introducing the EKF estimation of the DOD, the ANN model performance is evaluated after training by comparing with individual data points (test data) and by also comparing the final heat generation rate predicted by ANN with the experimental value (true value) as shown in Figure 6.10. Here the input to the neural network is exclusively from the experimental data, i.e., instantaneous discharge current, voltage, DOD (estimated by ABTS), ambient temperature and cell surface temperatures (Surface Temp Ta – anode, Surface Temp Tc – cathode). The EKF state prediction (DOD) is not yet introduced to the ANN model to evaluate the independent accuracy of the standalone ANN model (assuming the estimated DOD is perfect).



(a) (b)

Figure 6.10 A standalone ANN model performance for LIB thermal behavior (heat generation rate): (a)ANN accuracy for individual data points; and (b) ANN prediction vs true value

It is seen from the results presented in Figure 6.10 that the standalone ANN model prediction shows excellent performance, when provided with accurate DOD data as input, agreeing

well with the measured heat generation rate. Thus it can be concluded that the ANN model is designed and calibrated with sufficient accuracy. Figure 6.11 shows the final heat generation rate prediction of the ANN with the DOD estimation by the EKF in comparison with the DOD estimated by the direct coulomb counting method as well as the true value (experimental results). Notice that the curve CC-ANN refers to the predicted heat generation rate with the DOD calculated directly from the coulomb counting method and ANN hybrid model, and EKF-ANN refers to the predicted heat generation rate with the DOD estimated from the EKF and ANN hybrid model.

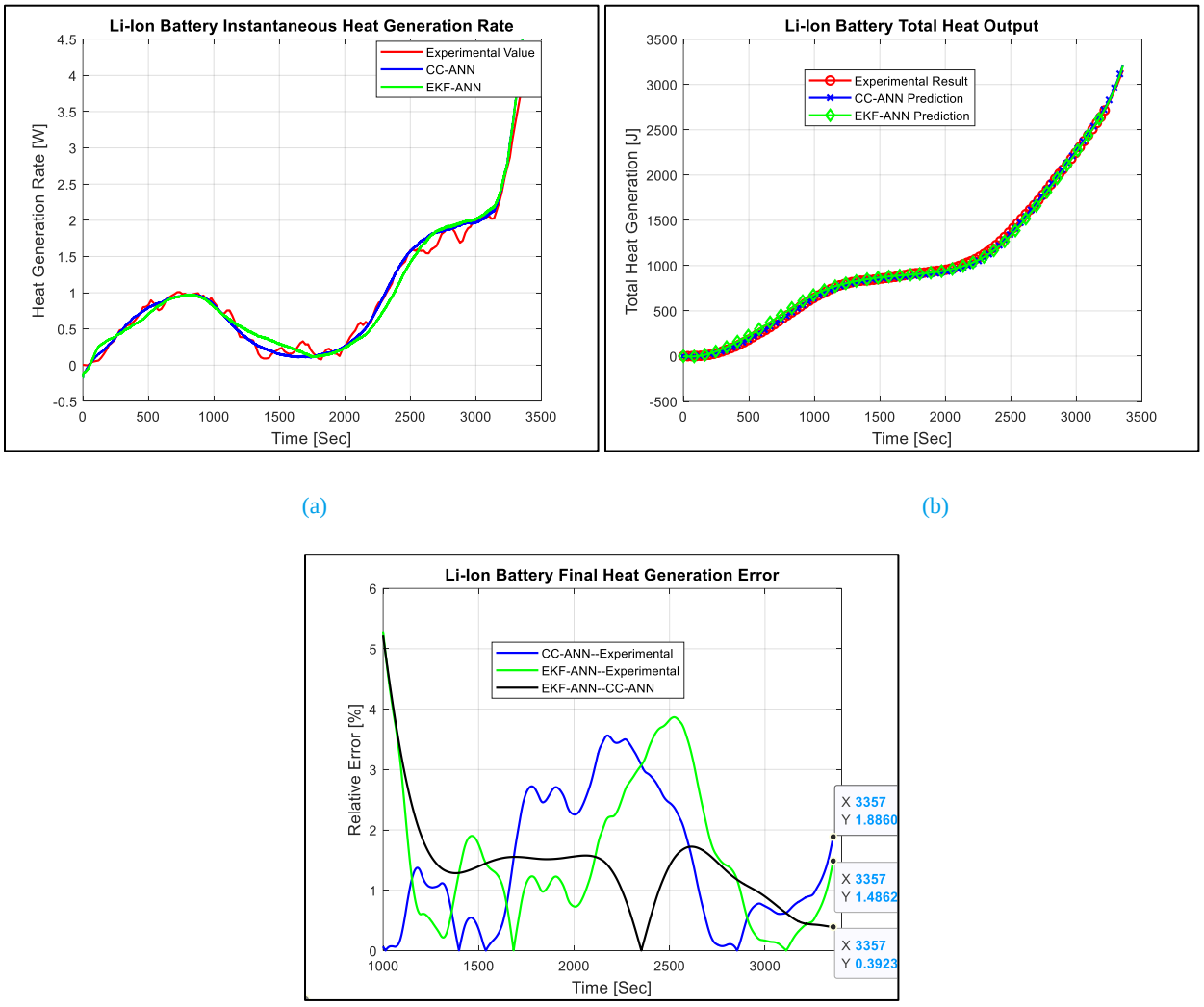


Figure 6.11 CC-ANN and EKF-ANN model performance for LIB heat generation rate: (a) instantaneous heat generation rate, (b) total heat output generated, (c) relative error of the total heat output generated between the ANN models and the experimental results

As observed from the results shown in Figure 6.11, the predicted instantaneous heat generation rate predicted by the EKF-ANN agrees with the predictions by the coulomb counting (CC) - ANN, and experimental results (true value). However, minor discrepancies can be observed as the experimental value is calculated at 20-second intervals, whereas the model output is calculated at every second. These discrepancies are nullified if the total heat generation value is considered over the entire period of battery discharge time; as Figure 6.11 indicates, a relative error of less than 2% is observed for both the CC-ANN and EKF-ANN model predictions when compared with the experimental value. The relative error between the two models CC-ANN and EKF-ANN predicted heat output value is around 0.39%. This demonstrates that both the EKF-ANN and CC-ANN model predictions are sufficiently accurate, and this hybrid approach of using state estimation with neural network yields accurate results when these two hybrid models are designed and calibrated appropriately with relevant data.

6.4.5 Simulated Thermal Management System Control

This level of accuracy from the hybrid data-based model can aid in replacing multiple temperature sensors, where such a model can periodically calculate the necessary data required for preliminary control. A hypothetical control situation is considered further to simulate a control system based on the hybrid data-based model predicting total heat generation over a period. Consider a thermal reservoir that can maintain a maximum of 1000 joules of heat emitted from the LIB and any further excess heat needs to be dissipated to the environment using a cooling system. A switching case (acting as a thermostat) governed by the output of the hybrid model, can be deployed to control and engage the actuator (radiator fan) facilitating heat dissipation. The total heat output of the LIB over time is obtained by integrating the heat generation rate, cooling system performance and fan status based on the EKF-ANN model are shown in Figure 6.12 for the above-mentioned control problem.

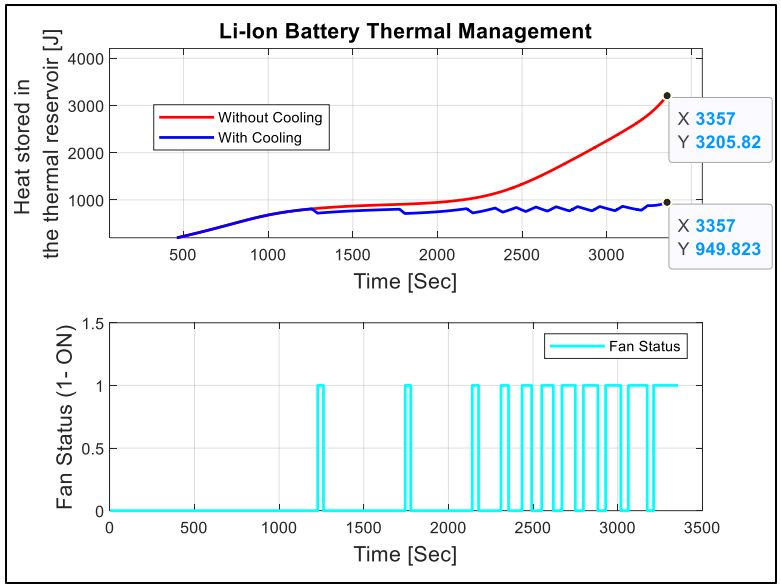


Figure 6.12 Thermal management system performance based on LIB thermal EKF-ANN model

From Figure 6.12 the total heat in the thermal reservoir with no cooling (no heat dissipation) can be noted to be above 3000 joules and with controlled cooling (heat dissipation by radiator fan) is below 1000 joules. The ON/OFF state of the radiator fan representing the actuation of the cooling system can be inferred from the fan status, where the duration of radiator fan engagement and frequency is governed by the total heat output value generated by integrating the output from the hybrid data-based model (EKF-ANN). Here the radiator fan is actuated/engaged (ON) when the reservoir is close to its limit of thermal energy storage, which is determined by the coolant temperature. This control method helps us to forgo the need to measure the temperature of the coolant, eliminating a temperature sensor requirement for control purposes.

6.4.6 Sensor Diagnostics

Such data-based models can also be used for real-time diagnostics as they are accurate and require relatively less computational power to analyze the deviation or anomaly in a specific situation. A simulated case of the current sensor fault is analyzed as follows: the simulation is carried out by modifying the current signal with an offset of 5A (creating a bias fault). The fault is affecting the coulomb counting methodology, thereby deviating the estimated DOD; however, the EKF prediction is not affected by the current sensor, resulting in no change of the estimated DOD value as shown in Figure 6.13.

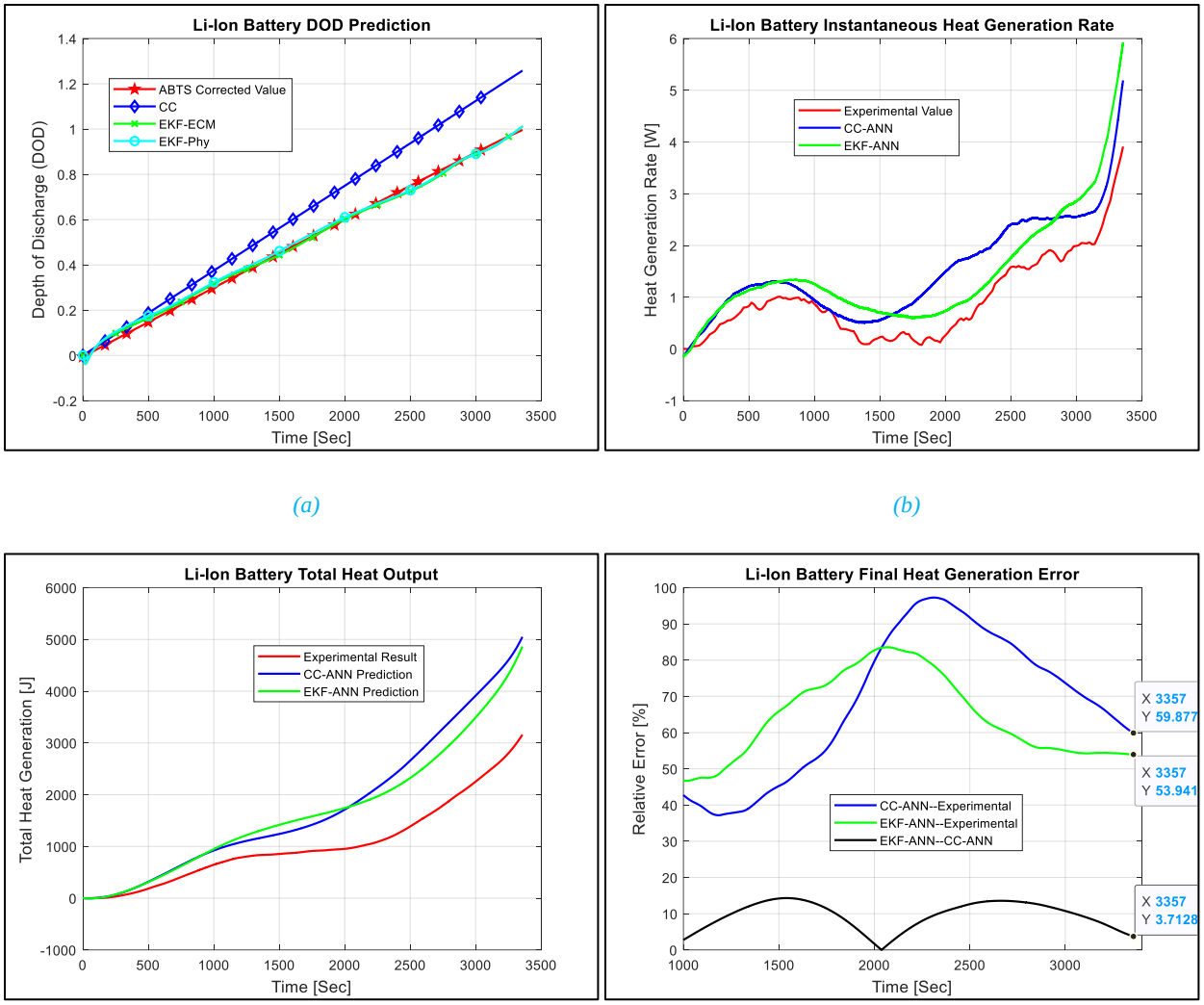


Figure 6.13 The performance of the ANN model predictions with current sensor fault through comparison with the respective experimental results; (a) DOD; (b) Instantaneous heat generation rate; (c) Total Heat output generated, (d) Relative error of total heat output generated

The heat generation rate predicted by both the CC-ANN and EKF-ANN models also deviates from the experimental value as the ANN is still affected by the current sensor reading. However, there is a significant change in the relative error and pattern of heat generation rate, and total heat output as shown in Figure 6.13, when compared to the experimental value both the CC-ANN and EKF- ANN models have resulted in relative error greater than 50% a significant increase from 2% (when there is no fault). The relative error between the CC-ANN and EKF-ANN predictions has also increased from 0.39% (when there is no fault) to 3.77%. Considering the deviation, the relative error among the models estimating the DOD, heat generation rate, and total

heat output a fault can be identified by establishing a threshold limit for the relative error by calibrating across various operating conditions. Similarly, when simulated with a voltage sensor fault (offset of 0.05V), the DOD estimation by the coulomb counting method is not affected, however, the EKF which depends on the voltage sensor measurement function loses the track and converges at the end. However, the deviation between the estimated DOD value of the CC-ANN model and the EKF-ANN model still is significant enough and can aid in fault recognition as shown in Figure 6.14.

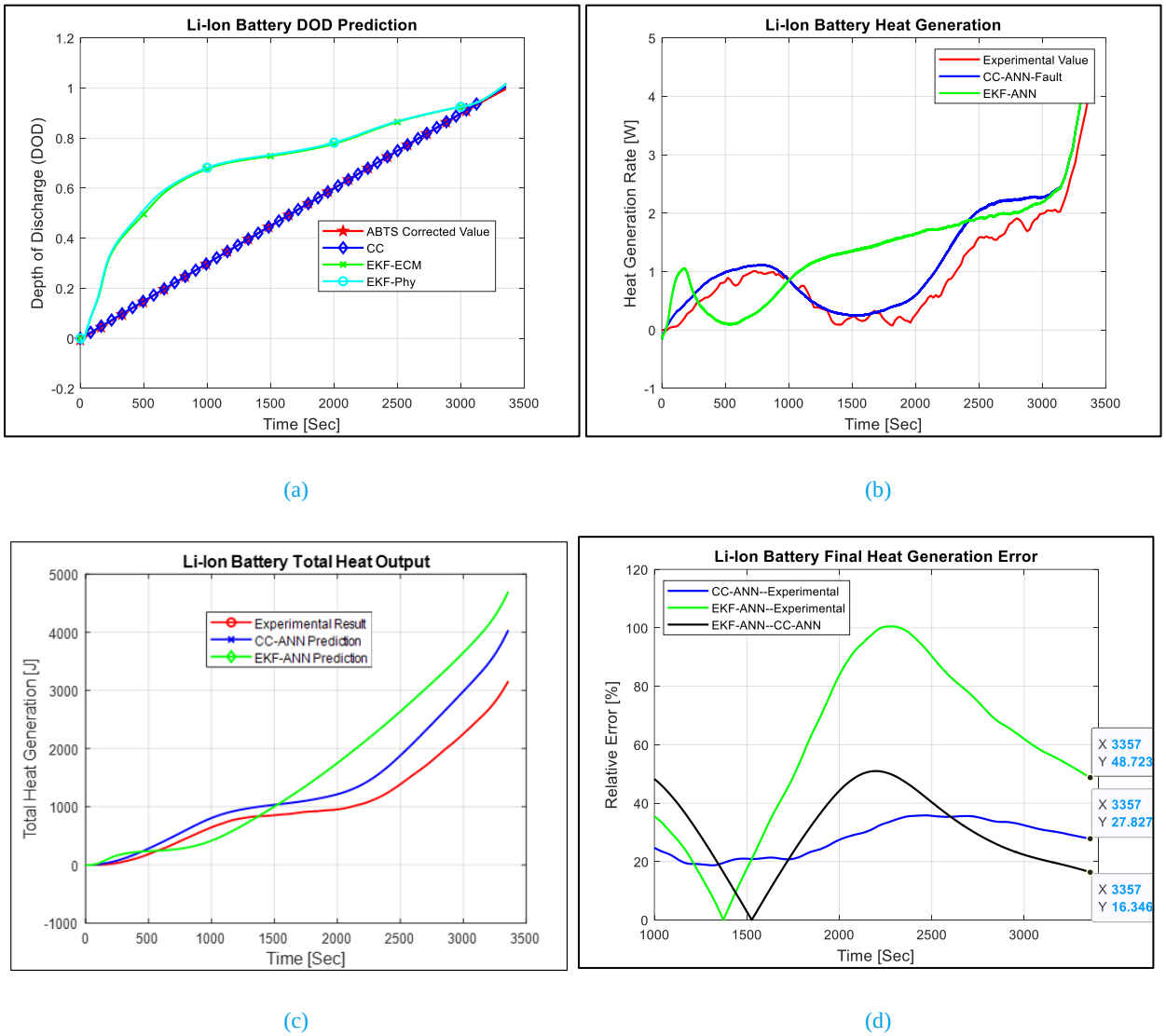


Figure 6.14 Deviation of the ANN model with voltage sensor fault; (a) EKF DOD prediction, (b) Instantaneous heat generation rate for the CC-ANN and EKF-ANN output, (c) Total heat output generated, (d) Relative error of total heat output generated

Similar to the current sensor fault, the predicted heat generation rate from both the CC-ANN and EKF-ANN models also deviates from the experimental value, as the voltage sensor reading will still affect the ANN. There is also a significant change in the relative error and pattern of heat generation rate and total heat output value, as shown in Figure 6.14; when compared to the experimental value, both the EKF-ANN and CC- ANN models have resulted in a relative error of 48.7% and 27.9%, respectively, a significant increase from 2% (when there is no fault). The relative error between the CC-ANN and EKF-ANN predictions has also increased from 0.39% (when there is no fault) to 16.3%. Considering the deviation and relative error among the models estimating the DOD, heat generation rate, and total heat output, a voltage fault can be identified by establishing a threshold limit for the relative error by calibrating across various operating conditions. The following results are tabulated in Table 6-5 demonstrate the potential of such data-based models, which can be implemented in real-time for onboard diagnostics by accurately calibrating the relative error between various data-based models. These models can also be further bolstered by utilizing pattern recognition algorithms for various sensors and operational faults.

Table 6-5 Relative error for the final heat output prediction value of all the models

Relative Error between the model	No-Fault	Current Sensor Fault	Voltage Sensor Fault
CC-ANN /Experimental Value	1.88%	59.9%	48.7%
EKF-ANN/Experimental Value	1.48%	53.9%	27.9%
CC-ANN/EKF-ANN	0.39%	3.71%	16.3%

6.5 Summary

In this study, a hybrid data-based model employing artificial neural network (ANN) architecture is developed to predict the heat generation rate and thermal behavior of lithium-ion battery (LIB) with battery discharge current, output voltage, ambient temperature, cell surface temperature, and depth of discharge (DOD) as the feature vectors (inputs), and the DOD is estimated with an extended Kalman filter (EKF), based on the state equations derived from the coulomb counting (CC) and equivalent circuit model (ECM), respectively, referred to as CC-ANN and ECM-ANN models. The EKFs are tuned accurately for faster convergence of state estimation to the true value irrespective of the state initialization. A shallow neural network utilizing the Marquette-Levenberg algorithm is designed and calibrated using over 8000 cases of the testing

data. It is shown that the predicted heat generation rate of LIB by both the CC-ANN and ECM-ANN models agrees well with the experimental results with an accuracy of $R^2 > 0.995$. When compared to the experimental value, the relative error for the total heat output generated is less than 2% for the case of normal sensor operation. Further potential of this hybrid data-based model is evaluated by simulating a thermal management system control and by introducing voltage and current sensor faults for diagnostic purposes. A switching logic emulating a thermostat operated by the output of the developed hybrid data-based model is integrated for the control of the thermal management system, effectively demonstrating the possibility of replacing additional temperature sensors. A simulated case of current sensor fault and voltage sensor fault is implemented and analyzed for the aspect of diagnostics by using CC-ANN and EKF-ANN model output. The relative error of the final heat output value predicted by CC-ANN and EKF-ANN models in comparison to the experimental value is greater than 50% with a current sensor fault and greater than 25% with a voltage sensor fault. This study has demonstrated the potential of such data-based models to monitor, control and diagnose electrochemical systems such as batteries on a real-time basis for field applications.

Chapter 7 Predicting Spatial Temperature Gradients During Exothermic Reactions

The chapter aims to demonstrate the capability of data-based models to predict spatial temperature gradients and temperature dynamics during exothermic reactions like thermal runaway and combustion. Considering the unavailability of good battery thermal runaway data, the model is developed using the data from the diesel particulate filter regeneration activity that mimics the exothermic reaction of a battery thermal runaway. In the filter case, soot load behaves as the system's internal state during an exothermic reaction, similar to the state of reactants inside a battery. Further parallels between cell temperature and filter bed and exhaust temperatures can be drawn for evaluation purposes.

***This chapter is adapted from Legala, Adithya, et al. "*Modeling of diesel particulate filter temperature dynamics during exotherm using neural networks*." Frontiers in Thermal Engineering, vol. 3, Oct. 2023, doi:10.3389/fther.2023.1265490.

Diesel Particulate Filter (DPF) in the diesel engine exhaust stream needs frequent regeneration (exotherm) to remove captured particulate matter (PM, or soot) without damaging to the porous DPF structure by controlling the peak temperatures and temperature gradients across the DPF. In this study, the temperature distribution in a DPF is measured at 42 strategic locations in the test DPF under various regeneration conditions of exhaust flow rates, regeneration temperatures, and soot loads. A data-based model with feed-forward neural network architecture is designed to model the thermal gradients and temperature dynamics of the DPF during the regeneration process. The neural network feature vector selection, network architecture, hyperparameter calibration process, measured data preprocessing, and experimental data acquisition procedure are evaluated. Over 7400 experimental data points at various regeneration temperatures, flow rates, and soot loads are used in training and validating the neural network model. It is found that the neural network model can accurately predict the 42 DPF bed temperatures simultaneously at different locations, and the time series analysis of both model-predicted and experimentally measured temperatures shows a good correlation. This indicates that the currently developed neural network model can provide the spatial distribution of temperature

in the DPF and comprehend the nonlinearity of the temperature dynamics due to DPF soot load at exothermic conditions. These results demonstrate that the data-based model can predict thermal gradients within a DPF, aiding in determining a safer DPF regeneration strategy, onboard diagnostics, and DPF development.

7.1 Introduction

Internal combustion diesel engines have had a considerable impact on the modern world; on the one hand, diesel engines have been the workhorses of the global economies for almost a century and are known for their reliability and fuel economy, resulting in their widespread adoption in commercial vehicles, shipping, and energy industries. On the other hand, diesel engine emissions are a significant source of air pollution and global warming, and contributes to various environmental and health problems [140], [141], [142]. The World Health Organization (WHO) has classified diesel engine exhaust as a Group 1 carcinogen, meaning it is a confirmed human carcinogen. Besides the harmful gaseous emissions, the diesel engine has a relatively high particulate emission or trade-off NO_x emission compared to gasoline engines [143], [144], [145]. The diesel particulate matter (PM) emission, also commonly referred to as soot, results from petrochemical combustion and consists of organic and inorganic particles [146], [147], [148]. PM has been linked to air quality issues, acid rain, and decreased visibility and can interact with other atmospheric pollutants to form secondary PM resulting in dense smog and a wide range of health problems[149], [150], [151]. In recent years, governments worldwide have imposed legislative regulations to reduce the emissions from diesel engines and compelled relevant industries to develop new technologies such as diesel particulate filters (DPF) and exhaust gas recirculation (EGR) [147], [152], [153], [154].

DPF is one of the leading emission control technologies that facilitate the modern diesel engine to meet the mandatory regulatory requirements by regulating the tailpipe out particulate emission [155], [156]. DPF is installed in the exhaust stream to trap the particulate emissions and is a critical part of the exhaust after-treatment system, usually located after the diesel oxidation catalyst. DPF consists of a porous ceramic filter (substrate) material, traditionally made of cordierite or silicon carbide, that captures the PM when exhaust gases flow through it [149], [157], [158], [159]. The filtration efficiency of the DPF increases with the trapped PM (soot) but also results in increased pressure drop across the DPF, which has negative consequences on the fuel economy and

eventually needs to be regenerated [160], [161]. DPF regeneration process removes the soot (PM) trapped by the filter where the PM accumulated is subjected to an oxidation process either passively (no fuel injection) or actively [161], [162], [163]. Passive regeneration occurs during regular engine operation, where the soot is removed with the help of NO_2 at typical exhaust temperatures between 300°C to 400°C. In contrast, active regeneration is a unique engine operation mode where fuel is dosed into the exhaust stream to create temperatures of more than 550°C to oxidize the soot with the help of O_2 in a controlled exothermic process [164], [165]. Like any other chemical reaction, reactants (exhaust gas and fuel) composition, flow rates, and temperatures play a critical role in the characteristics of exotherm and thermal gradients during the regeneration process. The primary objective of active DPF regeneration is to quickly oxidize the PM from the filter without damaging it by controlling the exotherms of the regeneration process. However, these exothermic reactions inside the DPF during regeneration create localized thermal stress on the DPF, which leads to a thermal gradient across the DPF and can result in cracking, melting, and other forms of structural damage to the [166], [167]. Excessive exothermic reactions can be caused by improper fuel injection (quantity and timing), insufficient airflow, and overloading of the DPF with soot [168], [169], [170], [171]. The extent of damage will depend on the peak bed temperatures, thermal gradient, geometric dimensions of the filter and the durability of the substrate material [167], [172]. Damaged DPF may not only compromise the filtration efficiency but also create excessive back pressure (where the channels collapse) due to the blockage of exhaust flow resulting in catastrophic failure of diesel engines. Improper regeneration and localized spikes in bed temperatures result in shortening the lifetime of the DPF, requiring costly replacement and a tedious process [173], [174], [175]. This problem can be solved by modelling DPF exotherms and understanding the peak bed temperatures, temperature gradients during active regeneration at various regeneration temperatures, soot loads, flow rates, and exhaust fuel injection quantities [175], [176], [177]. Few of the existing modelling techniques to predict the DPF exotherms and temperature dynamics are discussed as follows:

Bissett [178] developed a mathematical model for diesel particulate filter thermal regeneration using particle mass balance and energy balance equations where inlet gas temperature, mass velocity, oxygen mass fraction, and soot deposition thickness are considered model inputs to predict wall temperatures and temperature gradients. However, this mathematical model depends on many filter materials, exhaust gas properties and in-situ physical parameter correlation factors.

Hoon et al [179] modelled the uncontrolled soot regeneration inside the DPF in the presence of hydrocarbon slip by using a physics-based 0-D modeling technique to predict the transient thermal response, where the temperature, pressure and species concentration of the exhaust across the DPF is considered. In this case, the model assumes that the soot distribution and exhaust species concentration are uniform, which is impractical and relies on the DPF material, geometric parameters and exhaust gas properties. Boopathi [180] formulated a multi-zone model for electronic control units to predict substrate temperature by using the lumped model technique based on resistance node methodology; however, this model also assumes the soot distribution and soot inlet rate to be uniform and requires the concentrations and properties of exhaust gas species which is not ideal for the field application. Valeria [181] proposed a CFD-based soot regeneration model for catalyzed DPF; here, the model only deals with a single filter channel and is computationally intensive for field application. Aniseh [182] stimulated the active regeneration process inside the DPF to predict the temperature and differential pressure dynamics with the help of CFD techniques that rely on the filter's geometrical parameters; however, the system considered only constant exotherm temperature profiles. Zhao [183] developed a 3-D numerical simulation of soot regeneration on the Fluent platform by considering different regeneration rates, soot loads and oxygen concentrations to predict temperature contours and differential pressure across the DPF. However, this study lacks experimental validation and relies on all the physical properties and chemical reaction kinetics which are difficult to acquire accurately and reliably. Mitesh [184] successfully demonstrated the application of neural networks to predict the exotherm temperatures during the DPF regeneration and to control the hydrocarbon injection rate during the regeneration, however, there was no emphasis on thermal gradient prediction.

Most existing literature considers the DPF thermal behavior as a complex physics-based time series problem incorporating specific filter material, flow and soot depositions properties, and complex numerical and computational methods to capture the exothermic behavior. To the best of our knowledge, no existing data-based model can accurately track the complete thermal gradient along with the exotherm behavior of DPF during active regeneration. The focus of this study is to tackle the knowledge gap mentioned above in the literature by contributing the following:

1. Development of a comprehensive multi-input multi-output data-based model that can simultaneously predict multiple DPF bed temperatures during active regeneration at various soot loads and exhaust temperatures.
2. Formulation of the DPF thermal behaviour as a regression problem, introducing the engine operating conditions, exhaust stream constituents and DPF spatial temperature data.
3. The proposed model aids in developing a DPF regeneration strategy by accurately predicting the thermal gradient during regeneration across different soot loads, active regeneration temperatures, flow rates and fuel injection.

7.2 Experimental Procedure

The objective of the experimental setup was to generate a consistent PM (soot) from a diesel engine and capture the soot with the help of a DPF, followed by an active regeneration process at various conditions. A 15-litre commercially available heavy-duty diesel engine is the platform of choice, which is the most widely used in the transportation industry for class-8 trucks for long-haul heavy-duty cargo logistics. The engine platform has a high-pressure exhaust gas recirculation (EGR) system and a variable geometry turbocharger (VGT) calibrated to attain a consistent target soot loading rate. The airflow to the engine is measured with the help of a laminar flow element (LFE), fuel flow is measured with a calibrated Bronkhorst flow meter, and the exhaust flow rate (EFR) is calculated by adding the airflow rate and fuel flow rate. All the measurement equipment was calibrated with a maximum allowable point error of 2%. The after-treatment system consists of a diesel oxidation catalyst (DOC), DPF and selective catalytic reduction (SCR) catalyst-equipped with a diesel exhaust fluid (DEF) injector, all installed in the original configuration with instrumentation to acquire exhaust temperatures and gas composition data. The DPF is instrumented with multiple K-type thermocouples distributed spatially at critical locations to record bed temperatures. The exhaust gas of the diesel engine is partly then routed through a heat exchanger to further condition the soot to a specific temperature before being captured by the DPF. The soot loading rate (rate of soot captured by DPF) measured in grams per hour is closely controlled by attenuating the exhaust gas temperature, flow rate and oxygen percentage in the exhaust gas with the help of EGR and turbocharger. The following schematic, as shown in Figure 7.1, illustrates the engine platform and subsequent auxiliary systems in the test cell.

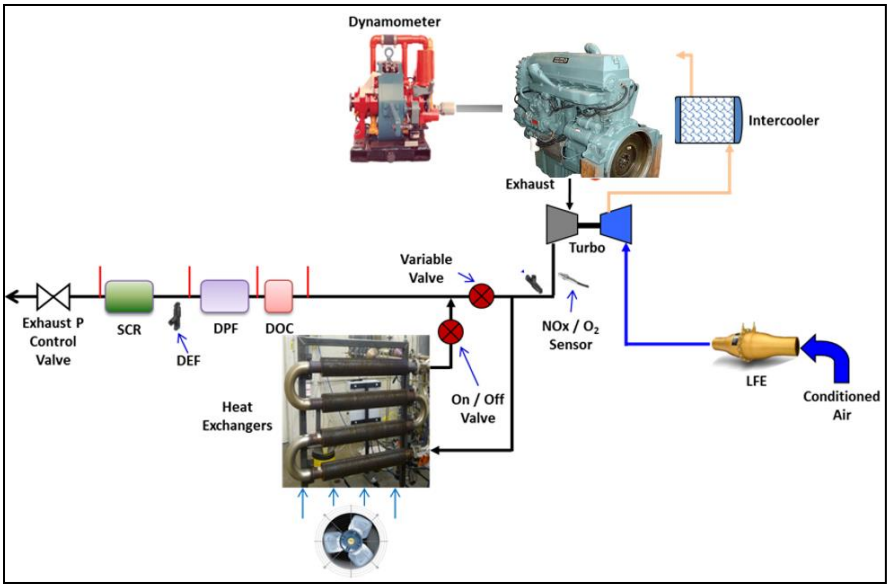
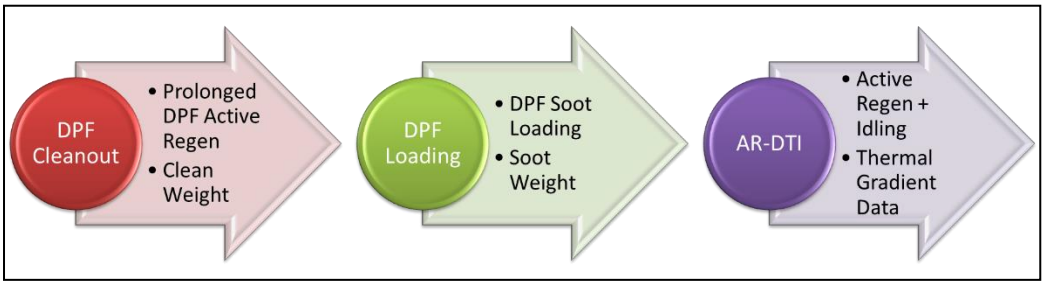


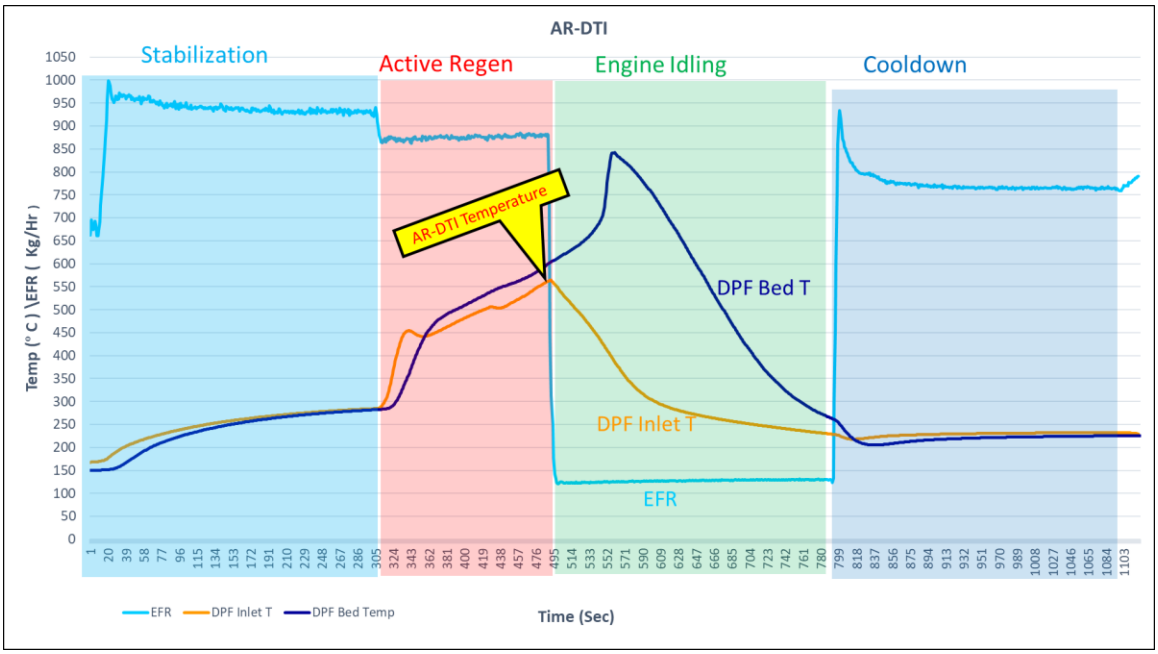
Figure 7.1 Engine test cell schematic.

The engine is mainly operated under stock calibration to generate power; however, specific actuators such as the EGR, VGT, and fuel injectors are controlled to reach a particular soot loading rate and regeneration rate. The experimental procedure is as follows: First, the DPF is entirely conditioned by subjecting the DPF to prolonged active regeneration at 625°C to remove any pre-existing soot; this process is referred to as 'DPF Cleanout'. The DPF is weighed at 200°C to record the initial hot weight, called 'Clean weight', and is then loaded with soot (PM) at a predetermined exhaust temperature and O_2. In this case, the exhaust temperature is maintained at 250°C with the help of a heat exchanger, and O_2 concentration in the exhaust is maintained at 9% to ensure that the characteristics of the soot are consistent; this process is called 'DPF Loading', and it is ensured that the DPF loading rate is repeatable. DPF is then weighed after the loading procedure to calculate soot weight, which is the net gain in DPF weight. The soot load on the DPF is quantified by grams of soot per liter volume of DPF, and the DPF loading procedure is repeated until it reaches the desired target. Once the DPF is loaded to the desired soot load, the DPF inlet gas is raised to a specific temperature by using the engine post-injection fuel, thereby initiating an active regeneration followed by an immediate engine idling process at various conditions called 'AR-DTI'. AR-DTI refers to active regeneration (AR) followed by a drop to idle (DTI); the peak DPF inlet temperature before dropping to idle is referred to as AR-DTI temperature and is explicitly illustrated in Figure 7.2. The DPF spatial thermal gradient data is acquired during the DTI, where peak DPF exothermic reaction occurs due to fuel and oxygen availability during active

regeneration and engine idling. The entire experimental procedure is illustrated in Figure 7.2 as a process flow diagram and with a sample AR-DTI cycle.



(a)



(b)

Figure 7.2 Experimental procedure: (a) Flow process, (b) AR-DTI Cycle.

Considering the DPF to be cylindrically symmetrical, a quarter of the DPF is instrumented with 47 thermocouples to provide simultaneous spatial bed temperature data at various cross-sections and radial locations; Figure 7.3 illustrates one of the instrumented cross-sections with 19 thermocouples.

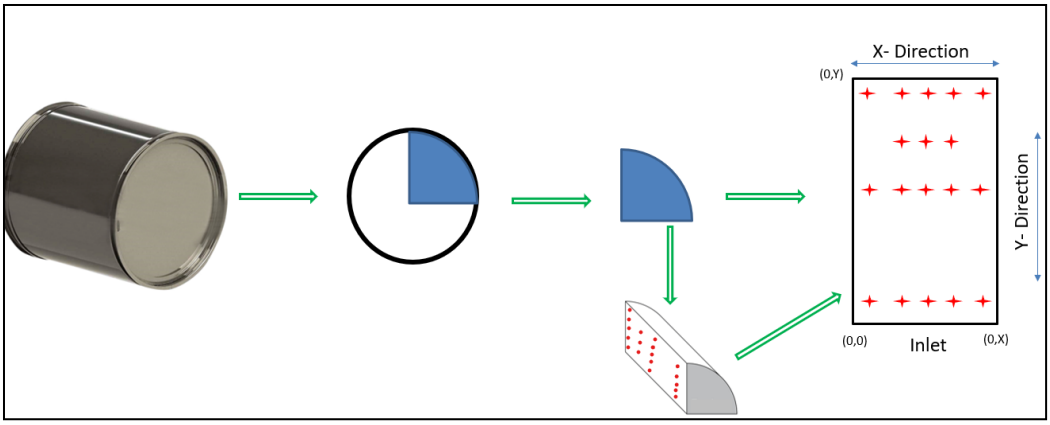


Figure 7.3 DPF Instrumentation Pattern where the radial direction is represented by X direction, and the dominant axial flow direction by Y direction.

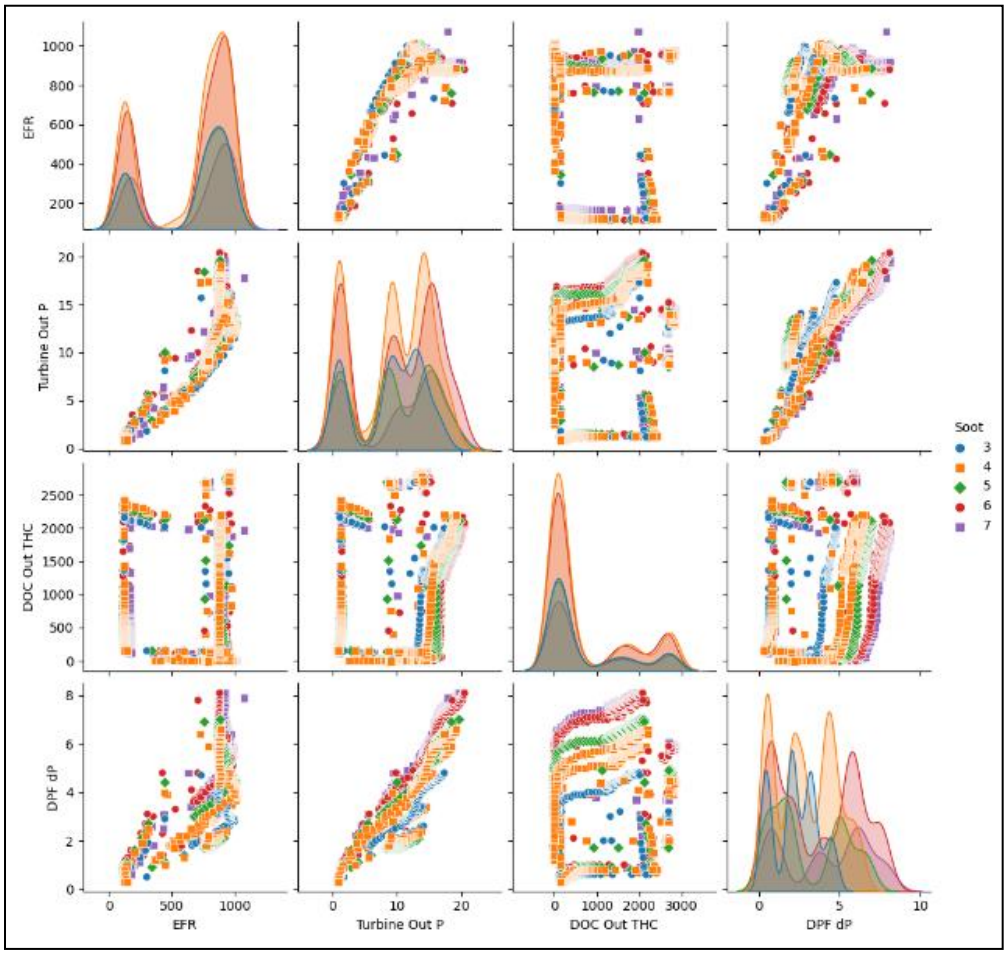
The test matrix for this experiment was developed to cover a broad spectrum of regeneration conditions without damaging the DPF by limiting the DPF bed temperatures to below 900°C during the exotherm. Table 7-1 summarizes the test matrix by tabulating various DPF soot loads and AR-DTI temperatures (Figure 7.2).

Table 7-1 Diesel particulate filter (DPF) test matrix

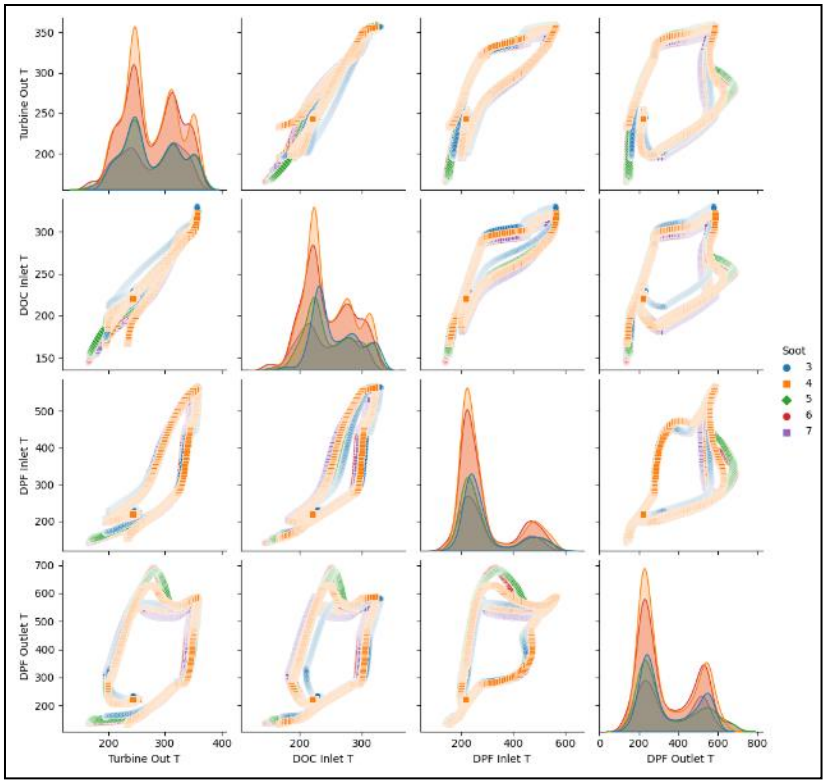
Test Case No	Soot Load (g/L)	AR-DTI Temperature (C)
1	3	560
2	4	550
3	5	525
4	5	560
5	6	550
6	7	525

The data acquired during the AR-DTI process is obtained at a 1 Hz sampling rate totaling around 7,400 data points at various exhaust flow rates, temperatures, and pressures. A complete correlation study among the engine operation and exhaust parameters is executed to understand the dominant factors. Data quality is further analyzed to verify the repeatability and parameter trends using pair plots, which allow us to represent both the impact (correlation) and distribution of one variable with other operating variables. Kernel density estimate (KDE) illustrates the

diagonal plots data using a continuous probability density curve. The data analytics and parameter correlation results are illustrated graphically using the pair plot shown in Figure 7.4.



(a)



(b)

Figure 7.4 Cross plot for the operating parameters: (a) Exhaust flow parameters, (b) Exhaust temperature parameters.

As shown in Figure 7.4, the DPF has been subjected to a wide variety of operating conditions, and the data collected during the exothermic active regeneration process shows a good correlation, demonstrating the data quality, i.e., free from measurement noise.

7.3 Data-based Modeling

Data-based modeling is a branch of machine learning that involves creating models based on large datasets and has been gaining popularity in thermal engineering for solving complex systems and heat transfer problems [185], [186], [187], [188]. The goal of data-based modeling is to identify patterns and relationships in the data that can be used to make predictions or gain insights into the underlying processes that generated the data [80], [189], [190]. Data-based modeling in engineering is a powerful tool for analyzing complex nonlinear systems where the established governing principles are too complex to model through equations and material properties. Considering the nonlinearity associated with the DPF exotherm data, a multi-input multi-output regression problem and feed-forward artificial neural network (ANN) architecture is chosen for the prediction of the DPF bed temperatures.

7.3.1 Feed-forward ANN

A neural network is a machine-learning algorithm inspired by the human biological brain, which consists of interconnected nodes, or "neurons," that work together to process and interpret data [191], [192], [193], [194], [195]. There are many neural network architectures and the most widely used one for regression problems is the feed-forward ANN architecture consisting of multiple layers: an input layer, some hidden layers, and an output layer. The input layer receives data in numerical values, then processed through the hidden layers, and the output layer produces a final regression result. Each neuron in a neural network is connected to other neurons through a series of weights, determining how strongly the neuron responds to input from other neurons. The training is achieved through a process known as backpropagation, where the network adjusts its weights based on the difference between its predicted output and the actual output [196], [197]. By iteratively adjusting its weights in response to feedback, the network can gradually improve its accuracy and better predict future outcomes; these iterations are called ‘epochs’. The critical challenge in designing a feed-forward neural network is determining the optimal architecture for the application, which involves choosing the appropriate number of layers, nodes, and activation functions and tuning the network's hyperparameters iteratively.

The combination of the activation function in the neuron, the number of hidden layers, and the optimization function are collectively known as hyperparameters, which determine the performance of a neural network. The activation function decides the neuron’s active status based on the input from the previous layer and how it processes the information to the subsequent layers. The most crucial role of activation functions in the hidden layers is introducing nonlinearity to the network; without it, the model cannot mimic complex nonlinear relationships between the input and output. Activation functions also assist in avoiding the problem of vanishing gradients where the gradients become too small during backpropagation, leading to slow or no learning. Increasing the number of hidden layers in a neural network can help the network learn more complex patterns in the data. However, adding too many hidden layers can lead to overfitting, and computational complexity, where the network becomes too complex to process and starts to accommodate the noise in the data. The choice of optimizer can significantly impact the speed at which the neural network converges during training. Optimizers with adaptive learning rates like Adam (Adaptive Moment Estimation) can help avoid local minima problems and feature regularization issues [198].

7.3.2 Data Preprocessing

Data preprocessing is essential to condition the data appropriately, involving filtering, normalization, standardization, feature selection and handling missing values by replacing them with the mean or median of the preceding data. The goal of preprocessing is to prepare the input data to be suitable for the neural network and improve its accuracy without altering the nature or pattern of the data. This study uses the normalization technique to scale the input data to a similar range to normalize parameter sensitivity, help the network converge faster during training, and improve model accuracy [199], [200]. The most common normalization technique is min-max scaling, calculated by subtracting the minimum value from each data point and dividing the result by the total range (the difference between the maximum value and minimum value). The data is not subjected to any further signal filtering (removing outliers) or data augmentation to improve the network robustness to field data.

7.3.3 DPF thermal model feature vectors and prediction attributes

The input feature vector is a set of input variables used to predict the output variable in a neural network regression problem. It should be chosen based on the domain knowledge of the problem and the data available from either experiments or validated simulations. The prediction attribute is the output variable the neural network tries to predict, also known as the target variable. It is essential to preprocess both the feature vectors and prediction attributes using techniques such as normalization to improve the neural network's performance after considering the data correlations and governing physics of the internal combustion engine and after-treatment system.

In this case, the temperature generated by exothermic reactions in the DPF is primarily governed by the process of igniting soot in the DPF; therefore, the soot load (amount of soot) present in the DPF directly impacts the temperature. The heat release rate will be governed by the amount (or the concentration) of fuel and oxygen in the exhaust flow that serves as reactants during this exothermic process and must be considered in the modelling. Change in fueling attributes can be incorporated from parameters such as total injected fuel quantity, including main injection and post-injection, the start of fuel injection (timing relative to crank angle), and total unburnt fuel exiting the DOC (raw fuel input to the DPF). During the exothermic process, the initial and subsequent temperatures of the exhaust gas feed in and out of the DPF also play a major role in dictating the heat generation rate and peak temperature inside the DPF. The differential pressure

across the DPF and turbine out pressure helps the model to incorporate some resemblance of soot distribution across the DPF because the same soot load can be distributed in various manners (channel plugs, wall deposits), affecting the temperature gradient. The physical attributes such as an instance of regen (time), exhaust flowrate and gas constituents are necessary for the model to incorporate all the changing thermofluid attributes and respective impacts. In addition, by considering the above phenomena, the wrapper method (to eliminate additional features iteratively based on performance) is used to finalize a total of 16 feature vectors (inputs) that are selected to predict bed temperatures accurately, consisting of engine operation and exhaust flow parameters, as listed in Table 7-2. It might be mentioned that engine out NOx strongly correlates with the engine out soot, and it might be included as an important feature vector as well. However, NOx emission in diesel engines is normally regulated with EGR based on engine out O_2 sensor feedback, as in the present experimental study; so the impact is indirectly accounted for. As a result, the concentration of NOx is not considered as a part of the feature vector in this study, but instead, engine-out exhaust O_2 concentration is included as one of the feature vectors, as shown in Table 7-2.

Table 7-2 Feature vectors for the present DPF thermal ANN model

Feature Vectors (Inputs)	
Engine Speed	Main Injection Fuel Quantity
Engine Torque	Start of Main Injection
Exhaust Flow Rate	Post Injection Fuel Quantity
Turbine Out Temperature	Engine Out Exhaust Oxygen Concentration (O_2 %)
Turbine Out Pressure	DOC Out Total Hydrocarbon (THC)
DOC Inlet Temperature	DPF Outlet Temperature
DPF Inlet Temperature	Time
DPF Differential Pressure (DPF dP)	Soot Load

7.3.4 Hyperparameter Calibration

The network's performance depends on the choice of hyperparameters, fixed design parameters set before training that cannot be learned during training, such as the number of hidden layers, neurons, activation function, learning rate, batch size, dropout probability and optimizers. A standard method for calibrating the hyperparameters is a grid or random search. In grid search, a range of values for each hyperparameter is specified, and the network is trained using all possible combinations of the hyperparameters. In random search, hyperparameters are randomly selected from the specified ranges, and the network is trained using these hyperparameters. The hyperparameters that yield the best performance on the validation set are chosen for the final model. After multiple trials and iterations, a combination of ReLU (Rectified Linear Unit), a non-exponential activation function, and a linear activation function is chosen for DPF thermal modeling. ReLU is mathematically defined as f(x) = max(0, x); The ReLU activation function is computationally efficient, making it a preferred choice for deep neural networks [201], [202]. ReLU activation produces sparse representations because it only activates a subset of the neurons in the network, helping to reduce overfitting and to improve generalization. After considering multiple combinations of hyperparameters, the final ANN design attributes are tabulated in Table 7-3. The final model prediction results are illustrated in Figure 7.5.

Table 7-3 Final DPF ANN model hyperparameter values

ANN Hyperparameters	***Final Value***
Feature Vectors (Inputs)	16
Target Variables (Outputs)	47 Bed Temperatures
Number of Hidden Layers	3
Number of Neurons for Hidden Layers	100 – 1st layer, 75 - 2nd layer, 50 – 3rd layer
Activation Function	‘ReLU’ – 1, 2, 3 Hidden layers
Optimizer	Adam (Learning Rate – 0.0105, beta_1 = 0.925)
Number of Data Points	Total: 7457, Training data: 4445, Validation data: 1905, Field Test Data: 1107

Batch Learning	100
Dropout Probability for Hidden Layers	0.55 – 1st layer, 0.35 - 2nd layer, 0.35 – 3rd layer

As observed in Figure 7.5, the trained ANN model accurately predicts the bed temperatures with the hyperparameters given above. Here five-bed temperatures from the set of 47-bed temperatures are selected randomly as a quick method to verify the model's performance. In the normalized data, the highest temperature is represented as 1, and the lowest is defined as zero. This analysis helps us identify the model performance at extreme (nonlinear) and mid-temperature (relatively linear) sections. If the predicted and experimental values match, all the points plotted will be precisely on the marked trace line; anything below the line is under prediction and above is overprediction by the model, corresponding to an error.

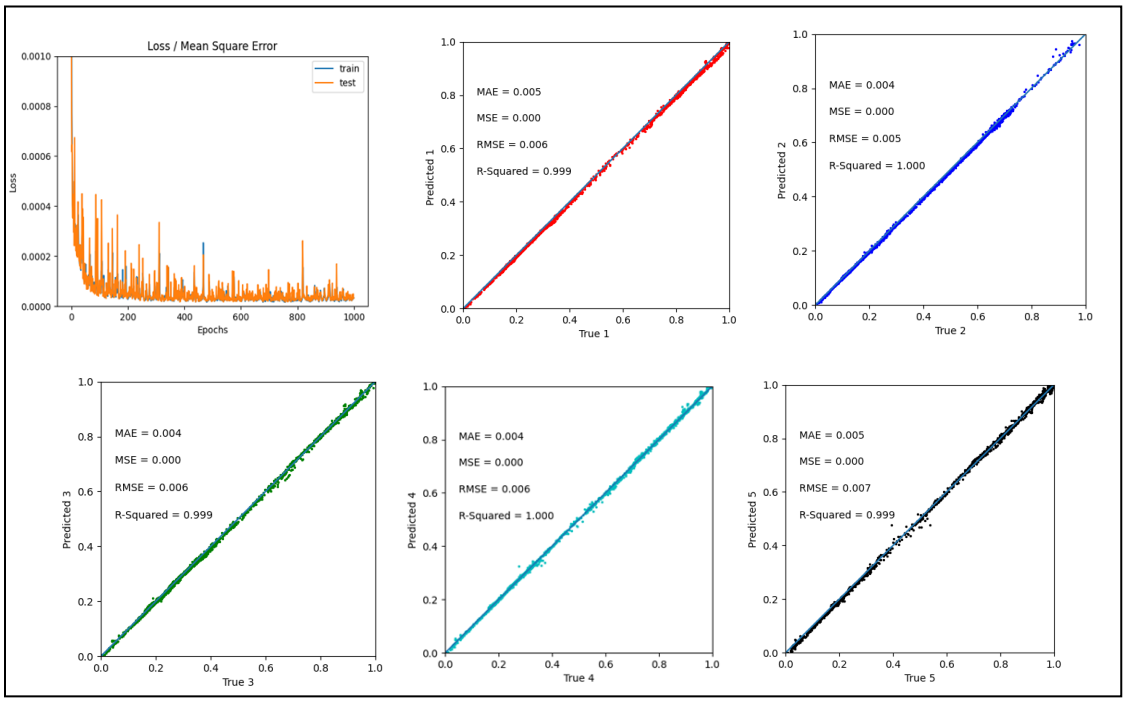


Figure 7.5 ANN model performance on normalized data after training: Error vs. Epochs and predicted five random temperatures chosen out of 47 presented here (output dataset).

7.4 Results and Discussion

This section evaluates the DTI thermal model performance after training by comparing the model-predicted bed temperatures to their experimental temperatures (true values) during the exothermic reactions. Considering that the representation of all 47 temperatures in graphs is too complicated, a single rectangular cross-section of the quarter DPF with six temperatures at the periphery is used to evaluate the model performance across the various regeneration conditions, as illustrated in Figure 7.6. The six periphery thermocouples are also designated with alphabets (A-F) for reference in subsequent analysis, as shown in Figure 7.6. This is because these six temperature values at the periphery of the DPF, including the inlet and exit, centerline and outer cylindrical surface, tend to have the largest errors for the model prediction, arising from the largest impact by the fluid flow, heat transfer with the material properties and pore structures of the DPF, soot distribution, soot oxidation kinetics and heat release rate, and the ambient conditions.

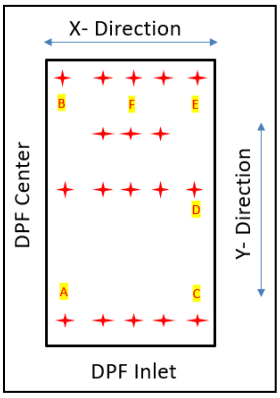


Figure 7.6 Illustration of DPF cross-section instrumentation with 18 thermocouples.

Figure 7.7 illustrates the model performance on the contemporary data (denormalized data) from the periphery thermocouples, where the model-predicted bed temperatures are compared to the experimental values at these locations. The periphery location on the DPF exhibits the most significant gradient covering the highest and lowest bed temperatures during the regeneration process (exothermic reaction). Considering the $R^2 > 0.999$, it can be concluded from Figure 7.7 that the model prediction across the spectrum is accurate in modeling the thermal gradients.

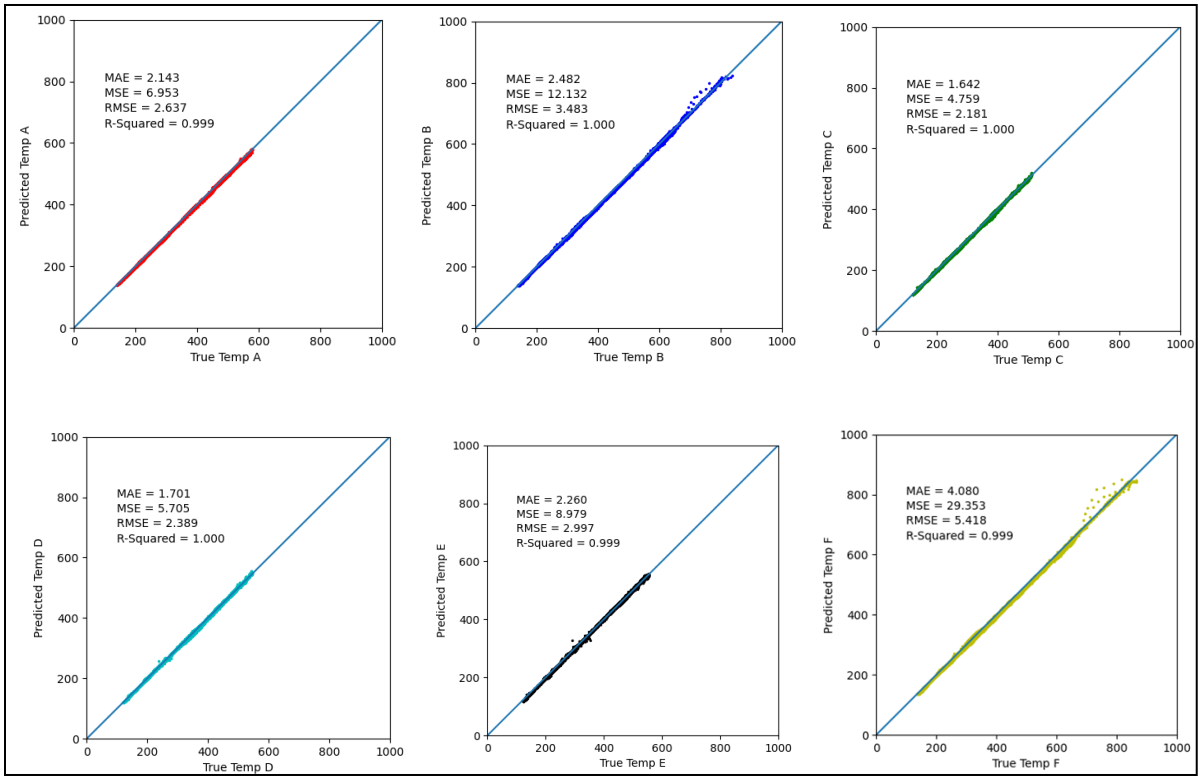
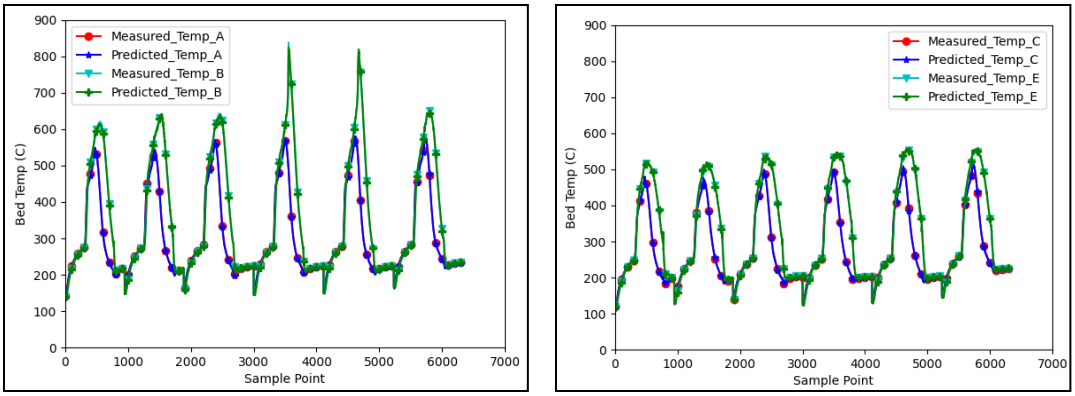
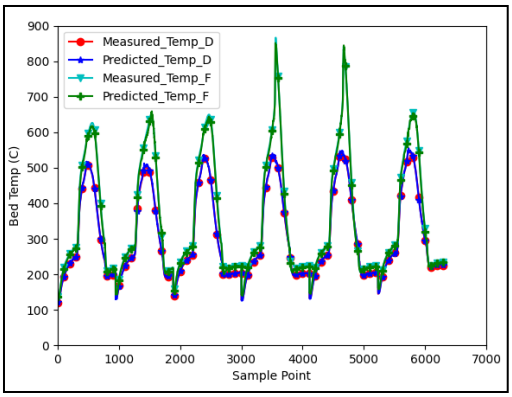


Figure 7.7 ANN model performance on the DPF periphery locations (pristine data/denormalized).

Figure 7.8 illustrates the model performance over the time series stitched together by combining various regeneration sequences; here, the model-predicted periphery bed temperatures are plotted against the respective experimental values. Each peak corresponds to an individual regeneration sequence at a specific temperature and soot load. Figure 7.8 shows bed temperatures at B and F, i.e., the DPF outlet periphery shows the highest exotherms. In contrast, A, C, and D, representing the DPF inlet periphery bed temperatures, show a relatively lower exothermic reaction. As the soot deposition pattern governs the exothermic response, these results agree with the literature, as the soot is predominantly deposited more towards the outlet side of the filter. Figure 7.8 also illustrates that the model accurately predicts the lower end of the temperature spectrum; however, there is a very slight underprediction at the peak exothermic case, which will contribute to some errors in the DPF thermal gradient calculation.



(a) *(b)*



(c)

Figure 7.8 ANN performance in a time series prediction during multiple regeneration sequences measured vs predicted periphery temperatures at the location of (a) A & B; (b) C & E; (c) D & F.

Plotting all the 18 thermocouple prediction data and comparing them with experimental data using a line plot at various conditions to illustrate model performance is graphically too intensive. This is resolved by creating a contour plot representing the DPF rectangular cross-sectional phase. X represents the radius of the cylindrical DPF, where 0 illustrates the center of the DPF. Y represents the length of the DPF (from the DPF inlet towards the outlet), and 0 defines the inlet cross-section; the contour plot's thermocouple/bed temperature locations are defined as 2-D cartesian coordinates, as tabulated in Table 7-4.

Table 7-4 DPF contour plot data presentation

DPF bed temperature location	X Coordinate	Y Coordinate	DPF bed temperature location	X Coordinate	Y Coordinate
1	0	1	10	3.76	5
2	0	4	11	3.76	6
3	0	6	12	5.64	1
4	1.88	1	13	5.64	4
5	1.88	4	14	5.64	5
6	1.88	5	15	5.64	6
7	1.88	6	16	6.4	1
8	3.76	1	17	6.4	4
9	3.76	4	18	6.4	6

The first six (6) DPF regeneration scenarios show the model performance when partial experimental data from these regeneration time series is used to train the model. Scenarios 1 to 6 consist of data used for training and validating where the regeneration conditions vary from light to heavy soot loads (3-7g/L) at various DPF inlet temperatures (525°C -560°C). 7th scenario can be considered as the model performance on field data where none of the data is ever used for training or validating the model (the neural network model is entirely unexposed to this data). In these scenarios, the DPF is loaded with a predetermined soot level and subjected to an active regeneration process. The DPF inlet exhaust temperature is raised to a specific temperature, referred to as AR-DTI temperature, by injecting fuel into the exhaust stream and immediately dropped to an engine idling condition providing excess oxygen to initiate exothermic soot regeneration. The contour plots presented in Figure 7.9 to Figure 7.15 illustrate a specific instant in the regeneration time series where the peak bed temperatures and maximum thermal gradients occur.

7.4.1 Scenario 1: Soot Load = 3g/L, AR-DTI Temperature = 560°C

In scenario 1, a DPF regeneration is considered with a light soot load (3g/L) and a high DPF inlet gas temperature of 560°C before dropping to idle, as the soot load is relatively low, the

thermal gradients are not expected to be high. As observed from Figure 7.9, the ANN model explicitly predicts the DPF bed temperatures, illustrating an accurate depiction of the DPF thermal gradients at the low soot load of 3g/L; the maximum error between the predicted and experimental values is around 1%. This evaluation shows that the model can easily predicate the lower end of the thermal gradient spectrum with great accuracy as the relative nonlinearity of the exotherm across the DPF is low.

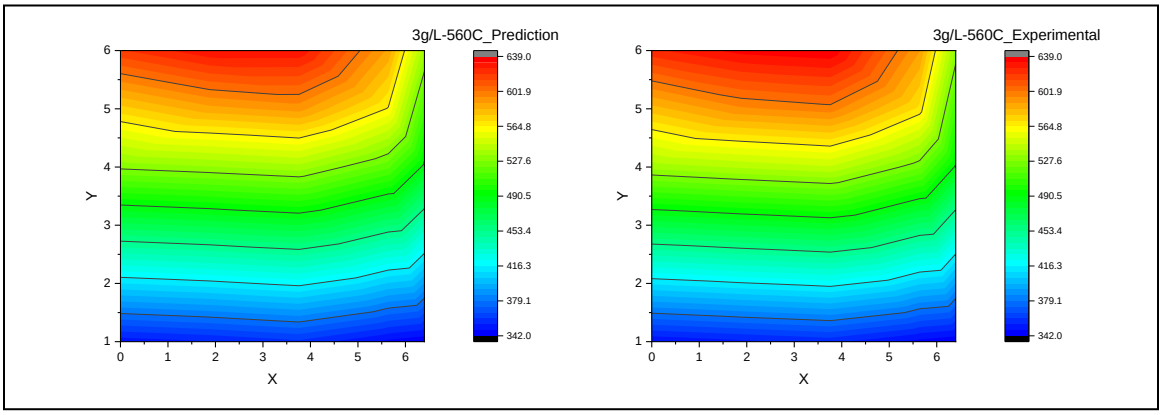


Figure 7.9 Contour plot for DPF thermal gradient: ANN prediction vs experimental measurement at the soot loading of 3g/L and the DPF inlet gas temperature of 560°C.

7.4.2 Scenario 2: Soot Load = 4g/L, AR-DTI Temperature = 550°C

Scenario 2 illustrates a DPF regeneration with a light to medium soot load (4g/L) and a high DPF inlet gas temperature of 560°C before dropping to the idle condition; as the soot load is relatively higher, the thermal gradients are also expected to be relatively higher when compared to the previous case, Scenario 1. Figure 7.10 presents the predicted and experimental DPF thermal gradient during the regeneration process, which is greater than Scenario 1; the model prediction performance in the regions where bed temperatures below 600°C is quite accurate (error < 1%), whereas the higher-end temperature prediction error, i.e., > 600°C, has increased to around 2% and also shows a slight gradient difference when comparing predicted against experimental thermal gradients closer to the DPF outlet. This difference in prediction and experimental data contours can be primarily attributed to the increased nonlinearity of the exothermic reaction at a higher soot load and higher DPF inlet temperature, for which the model seems not able to capture completely.

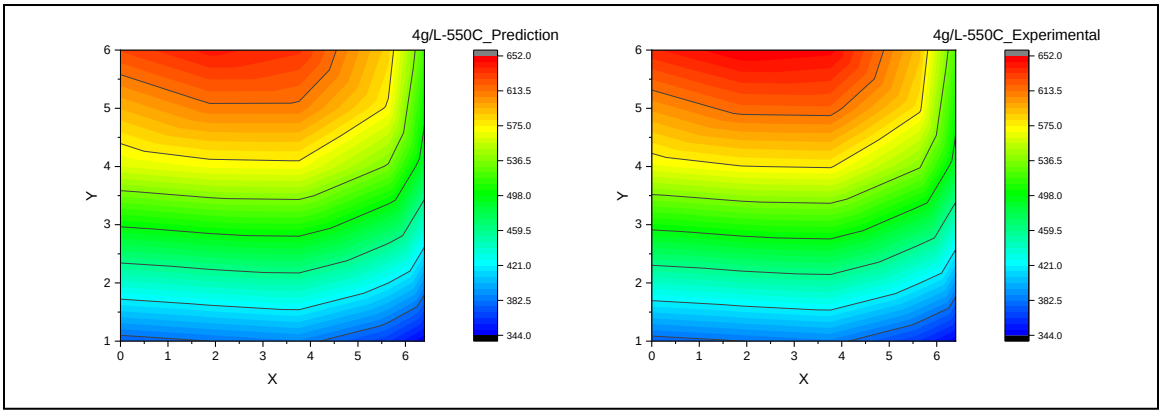


Figure 7.10 Contour plot for DPF thermal gradient: ANN prediction vs experimental measurement at the soot loading of 4g/L and the DPF inlet gas temperature of 550°C.

7.4.3 Scenario 3: Soot Load = 5g/L, AR-DTI Temperature = 525°C and Scenario 4: Soot Load = 5g/L, AR-DTI Temperature = 560°C

Scenario 3 and Scenario 4 are primarily considered to show the impact of DPF inlet temperatures on the thermal gradients during the regeneration. The soot load is kept at a constant 5 g/L (medium soot load) in both scenarios, but the DPF inlet gas temperature in Scenario 3 is maintained lower at 525°C; in contrast, Scenario 4 has its DPF inlet at a higher temperature of 560°C. This change in DPF inlet temperature of 25°C resulted in a peak bed variation of greater than 125°C, demonstrating the nonlinearity in the DPF temperature response to the inlet gas temperature during the exothermic reaction (regeneration). This is understandable since the rate of soot oxidation reaction; hence the heat release rate, is Arrhenius type having strongly nonlinear (exponential) temperature dependence. Similar to Scenario 2, the model prediction at the higher bed temperatures is prone to a minor error in Scenario 3, as observed in the thermal gradient contour plot shown in Figure 7.11. The maximum error between the prediction and experimental bed temperature values is still around 2%, even at the higher soot loads of 5g/L, demonstrating excellent model performance at the medium soot loads and lower DPF inlet temperature. Similarly, in Scenario 4, the model prediction error still holds perfect accuracy towards the DPF inlet region (at lower bed temperatures). However, the maximum error at the DPF outlet has increased to around 3% with a relative increase in contour plot distortion when comparing the predicted and experimental values, as shown in Figure 7.12, which can be again attributed to the model's limitation in capturing the nonlinearity completely.

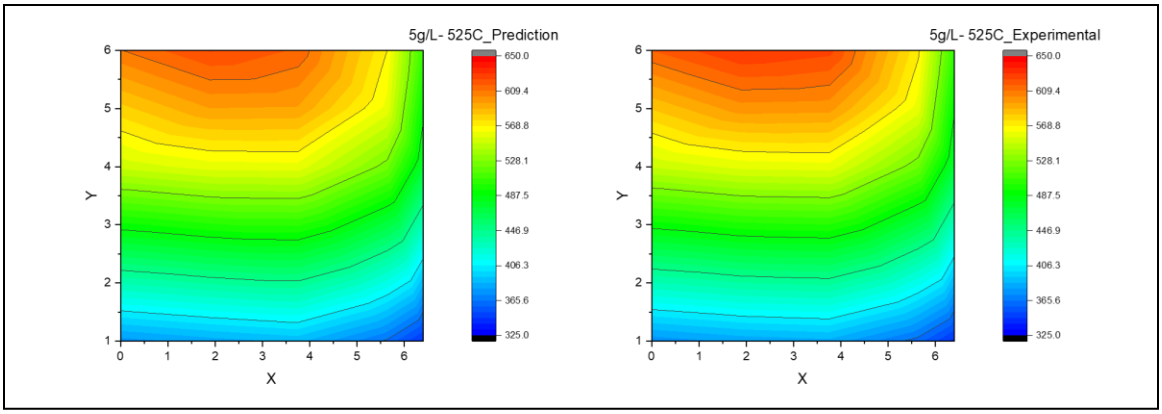


Figure 7.11 Contour plot for DPF thermal gradient: ANN prediction vs experimental measurement at the soot loading of 4g/L and the DPF inlet gas temperature of 525°C.

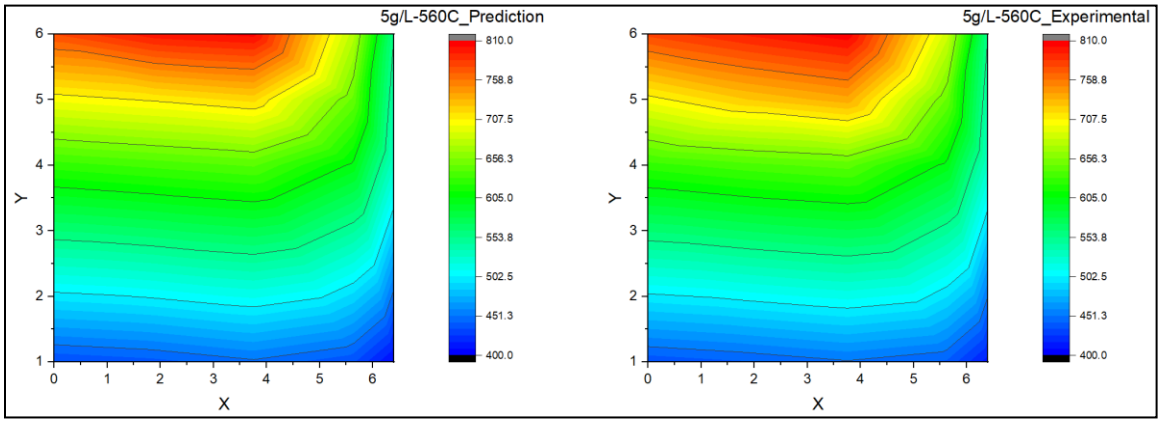


Figure 7.12 Contour plot for DPF thermal gradient: ANN prediction vs experimental measurement at the soot loading of 5g/L and the DPF inlet gas temperature of 560°C.

7.4.4 Scenario 5: Soot Load = 6g/L, AR-DTI Temperature = 550°C and Scenario 6: Soot Load = 7g/L, AR-DTI Temperature = 525°C

Both Scenarios 5 and 6 represent the high soot load conditions (6g/L and 7g/L) at both relatively high (550°C) and low (525°C) regeneration temperatures. In both cases, the maximum error between the prediction and experimental value is around 1~2% even when the peak bed temperatures are more than 800°C. It is seen that the ANN model is effectively validated when compared with the experimental results shown, as the model accurately predicts the DPF thermal gradients, as shown in Figure 7.13 and Figure 7.14. However, it can be observed that in regeneration conditions at higher DPF inlet temperature (> 550°C), the model predictions (contour plots) tend to deviate from the experimental value slightly but still within the acceptable accuracy.

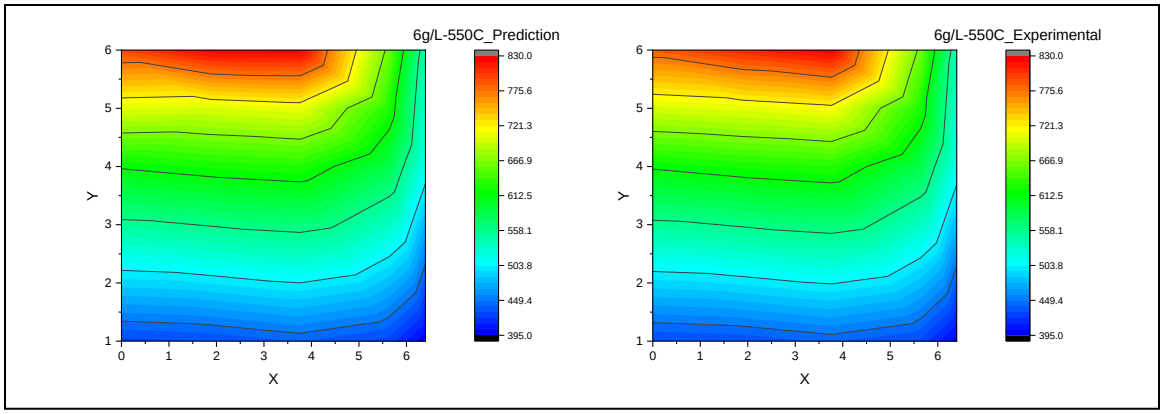


Figure 7.13 Contour plot for DPF thermal gradient: ANN prediction vs experimental measurement at the soot loading of 6g/L and the DPF inlet gas temperature of 550°C (Scenario 5).

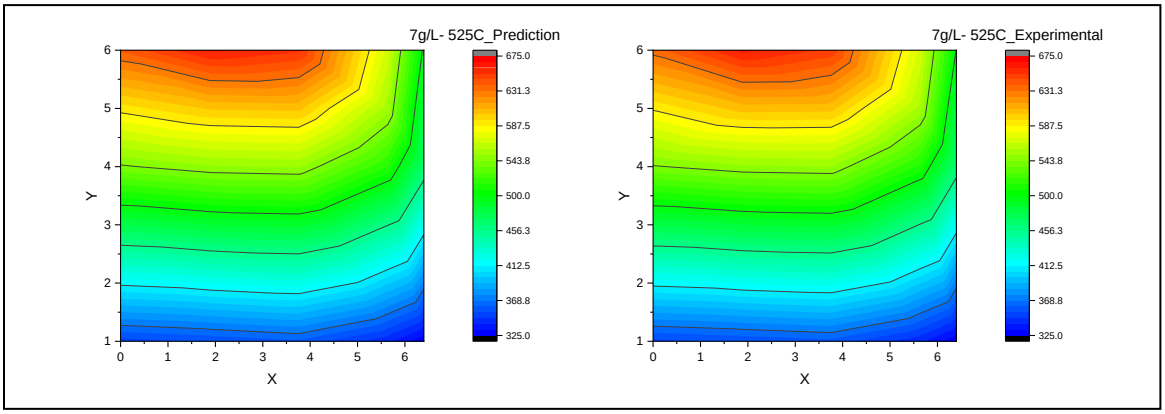


Figure 7.14 Contour plot for DPF thermal gradient: ANN prediction vs experimental measurement at the soot loading of 7g/L and the DPF inlet gas temperature of 525°C (Scenario 6).

7.4.5 Scenario 7: Soot Load = 4g/L, AR-DTI Temperature = 560°C (Field Data)

Scenario 7 represents the field data (test data) where the model is entirely exposed to new data from the regeneration on the same DPF and engine platform but at a different DPF soot load and active regeneration temperature combination, i.e., 4g/L and 560°C. It must also be noted that the soot deposition pattern inside the DPF is slightly variable during each regeneration sequence. Figure 7.15 illustrates the predicted DPF thermal gradient with the experimental values resulting in an error of 8% at the higher temperatures (> 600°C) and around 3% at the lower temperatures, even when the model is not trained on any data from this particular case. Considering the exothermic nature of the DPF regeneration, the model accuracy is outstanding on the field data, here the error can be attributed to the model's limitation in capturing the nonlinearity of the

temperature generated due to the exotherm at high DPF inlet temperatures and variability in soot distribution across the DPF.

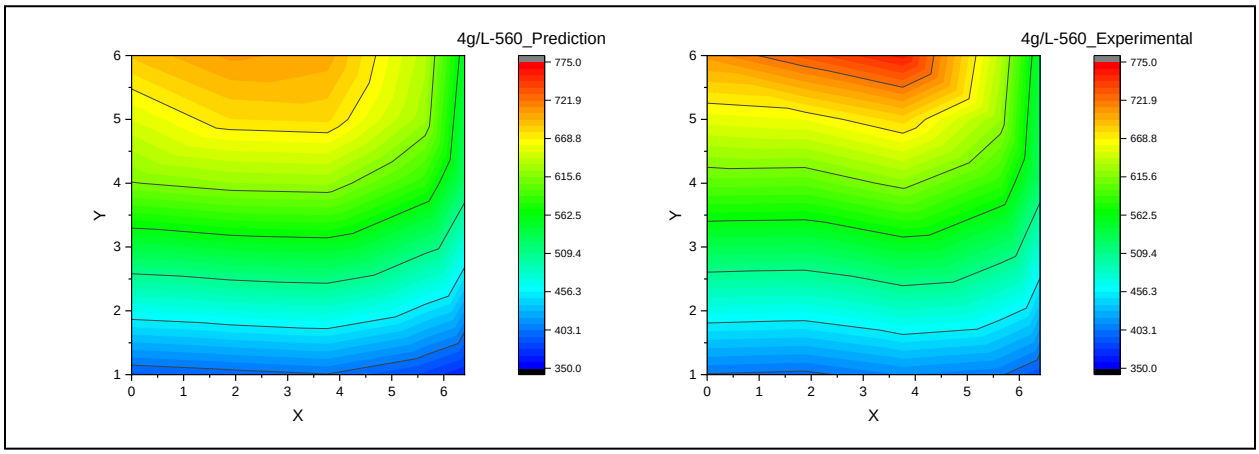


Figure 7.15 Contour plot for DPF thermal gradient: ANN prediction vs experimental measurement at the soot loading of 4g/L and the DPF inlet gas temperature of 560°C (Scenario 7 where the experimental data has not been used for the model training and validation, or the so-called unexposed or new data, and the experimental measurement is the field data where the soot distribution may not be as uniform as for the previous scenarios of laboratory tests.)

The percentage error (%) at the various locations and scenarios is tabulated in Table 7-5, summarizing the DPF thermal ANN model performance as developed. In most cases, the highest error occurs at the peak bed temperature location, i.e., the midpoint of the radius at the outlet side of the DPF. This error is due to the extreme nonlinearity of the exotherm, where the change in bed temperature is quite substantial, even for the slightest change in any input parameter. However, at the lower soot loads and regeneration temperatures, the nonlinearity of the exotherm is lower, resulting in relatively lower peak bed temperatures, which the model can predict more accurately. Despite this limitation, an error under 10% is acceptable for non-critical onboard diagnostics or developing DPF regeneration strategies.

Table 7-5 A summary of the percentage error in the ANN predicted bed temperature

X	Y	**Scenario 1**	**Scenario 2**	**Scenario 3**	**Scenario 4**	**Scenario 5**	**Scenario 6**	**Scenario 7**
0	1	0%	0%	0%	0%	0%	0%	-3%
0	4	-1%	-1%	0%	0%	0%	0%	2%
0	6	-1%	-2%	-1%	0%	1%	1%	-3%
1.88	1	0%	0%	0%	-1%	0%	0%	-1%
1.88	4	-1%	-1%	0%	0%	0%	0%	4%
1.88	5	-1%	-1%	-1%	-2%	-1%	0%	3%
1.88	6	-1%	-1%	-1%	0%	2%	0%	-4%
3.76	1	1%	0%	1%	0%	0%	0%	-2%
3.76	4	-1%	-1%	0%	0%	0%	0%	1%
3.76	5	-1%	-1%	-1%	-3%	-1%	0%	0%
3.76	*6*	*-1%*	*-2%*	*-2%*	*0%*	*0%*	*1%*	*-8%*
5.64	1	0%	0%	1%	-1%	-1%	0%	-5%
5.64	4	-1%	-1%	0%	0%	0%	0%	0%
5.64	5	-1%	-1%	0%	0%	0%	0%	0%
5.64	6	0%	-1%	0%	-1%	0%	0%	0%
6.4	1	0%	0%	0%	-2%	0%	0%	-5%
6.4	4	0%	-1%	0%	0%	0%	0%	0%
6.4	6	1%	0%	0%	0%	0%	0%	1%

7.5 Summary

In this study, a comprehensive data-based diesel particulate filter (DPF) thermal model based on a multi-input multi-output neural network is successfully developed to predict the thermal gradients across the DPF during an active regeneration (exothermic) event. An experimental methodology is formulated to instrument the DPF and generate consistent DPF exotherm temperatures during the active regeneration events. Over 7400 data points across various exhaust flow rates, regeneration temperatures and soot loads are generated through experimentation and utilized in training, validating and testing the data-based DPF thermal model. The hyperparameters of the neural network model are calibrated to predict the 47 DPF peak bed temperatures simultaneously measured at various spatial locations with an accuracy greater than $R^2 > 0.999$ in most cases. During the neural network performance evaluation, the time series analysis of both model-predicted and experimental bed temperatures shows a good correlation with slight under-prediction at bed temperatures higher than 800°C, which can be attributed to the strong nonlinearity of the exotherm temperature. The thermal contour plots generated by the model-predicted data across the first six scenarios result in an error of < 3 % when compared with the experimental data; however, the contour plot generated by the seventh scenario (field data), the model error rate approaches 10% at DPF outlet locations (bed temperatures > 700°C) and 2-3% at DPF inlet locations (bed temperatures < 600°C). These results demonstrate that the data-based model for DPF shows an acceptable level of accuracy in predicting thermal gradients across the spectrum, aiding in determining a safer DPF regeneration strategy, onboard diagnostics and DPF development.

Chapter 8 Predicting Fuel Cell-Battery Hybrid Power System Dynamics

This chapter demonstrates the data-based model's capability to predict a vehicle's hybrid dynamics during various driving conditions.

***This chapter is adapted from Legala, Adithya, et al. "*Machine Learning Modelling for Fuel Cell-Battery Hybrid Power System Dynamics in a Toyota Mirai 2 Vehicle Under Various Drive Cycles*." Energy and AI, Aug. 2024, p. 100415, doi:10.1016/j.egyai.2024.100415.

Electrification is considered essential for decarbonizing the mobility sector, and understanding and modeling the complex behavior of modern fuel cell-battery electric-electric hybrid power systems is challenging, especially for product development and diagnostics requiring quick turnaround and fast computation. This study develops a novel modeling approach, utilizing supervised machine learning algorithms, to replicate the dynamic characteristics of the fuel cell-battery hybrid power system in a 2021 Toyota Mirai 2nd generation (Mirai 2) vehicle under various drive cycles. The entire data for this study is collected by instrumenting the Mirai vehicle with in-house data acquisition devices and tapping into the Mirai controller area network bus during chassis dynamometer tests. A multi-input - multi-output, feed-forward artificial neural network architecture is designed to predict not only the fuel cell attributes, such as average minimum cell voltage, coolant, and cathode air outlet temperatures but also the battery hybrid system attributes, including lithium-ion battery pack voltage and temperature with the help of 15 system operating parameters. Over 21,0000 data points on various drive cycles having combinations of transient and near steady-state driving conditions are collected, out of which around 15,000 points are used for training the network and 6,000 for the evaluation of the model performance. Various data filtration techniques and neural network calibration processes are explored to condition the data and understand the impact on model performance. The calibrated neural network accurately predicts the hybrid power system dynamics with an R-squared value greater than 0.98, demonstrating the potential of machine learning algorithms for system development and diagnostics.

8.1 Introduction

Transport sector, including land transportation, surface ships, and aviation, contributes to about one-third of the world's anthropogenic greenhouse gas emissions [203], [204] and is recognized to be the most difficult to decarbonize due to its mobile, transient, and distributed nature and variable drive/load conditions as well as extensive infrastructure spread over large areas [205], [206]. Hence, electrification is essential for the decarbonization of the mobility sector, mainly through the development and deployment of battery electric, fuel cell electric, and fuel cell-battery electric-electric hybrid power systems – hybridization resolves range anxiety, offers fast refueling and fast load response, and alleviates the excessive degradation arising from variable load operations [207], [208], [209]. As a result, almost all fuel cell electric vehicles (FCEVs) are actually powered by fuel cell-battery hybrid systems, and the development and deployment of FCEVs will revolutionize sustainable transportation and address critical environmental challenges [210], [211].

The 2021 Toyota Mirai 2nd generation (hence often referred to as Mirai 2) marks a significant milestone in the development and commercialization of FCEVs, and its complex operational strategy, hybrid energy management, is regarded as a benchmark in the automotive industry [212], [213]. It is challenging to develop models of such complex fuel cell systems that can run in real-time for diagnostics and system development using traditional empirical or physics-based models, especially if the system attributes and material properties are not available [72], [80], [214], [215]. The dynamic nature of power demands and the interactions between the fuel cell and battery during various driving conditions require sophisticated modeling techniques to capture transient behaviors accurately across the drive cycle [216], [217], [218], [219]. Components such as the fuel cell stack exhibit non-linear behaviors due to electrochemical reactions, temperature variations, and humidity levels, and these nonlinearities require advanced mathematical modeling and computational approaches [27], [37], [220]. The fuel cell's core involves electrochemical reactions influenced by numerous factors, including catalyst properties, membrane conductivity, gas diffusion layers, liquid flow within the fuel cell, and the associated manifolds, which are critical for performance prediction [11], [23], [92] Considering the onboard diagnostics/prognostics and product development applications for an FCEV hybrid power system, a computationally fast and accurate model is essential to predict system outputs such as fuel cell voltage, fuel cell coolant out

temperature, fuel cell air outlet temperature, battery pack voltage, and battery temperature over various driving conditions.

Most of the existing literature on fuel cell-battery hybrid modeling and FCEV energy dynamics focuses on a cell level, small stacks, or a virtual environment; it is very limited for the development of models from a vehicle point of view and experimentally validating them on a drive cycle with the vehicle's data acquisition system and controller area network (CAN) bus signals. Mauro [221] developed an empirical powertrain model to understand and optimize the energy management in the Toyota Mirai based on the CAN data acquired from the vehicle while operating at Argonne National Laboratory. In this study, Mauro utilized multiple curve fitting models to somewhat replicate the behavior of fuel cell battery voltage dynamics but could not comprehend the thermal behavior. Such empirical models can help simulate the energy management strategy. Still, they cannot be used for diagnostics or system development as they lack a correlation with reactant pressures and flow rates. Venkata [222] has developed a fuel cell hybrid model to downsize the fuel cell stack and analyzed the behavior on various drive cycles in a MATLAB – SIMULINK-based virtual environment; however, this lacks any experimental validation and consideration of thermal constraints. Markus [223] has experimentally investigated the aspect of reverse engineering the Toyota Mirai vehicle by collecting the data and investigating the behavior of the hybrid system over different driving profiles, providing valuable insights; however, the study lacked the model development aspect that can replicate the behavior in a virtual environment. Tsuyoshi [224] published their research on developing a physics-based fuel cell control system for Mirai vehicles to address vehicle operation at sub-zero temperature conditions. This study considers the thermal aspects, water balance of the fuel cell hybrid system, and operational strategy but misses the role of battery dynamics, and most of the physical parameters needed for the model are not disclosed. Hasegawa [217] has comprehensively modeled the dynamics of the Mirai fuel cell system using the physics-based approach and considered all the reactant flow parameters and associated thermal attributes. However, such models cannot parallelly accommodate battery dynamics and will need another similar model to simulate hybrid dynamics.

The objective of the present study is therefore to develop an accurate and computationally fast predictive model for fuel cell-battery electric-electric hybrid power systems for vehicles, that can be used for the development and diagnostics of such hybrid systems in real time. The dynamic

behavior of the hybrid power system is measured when the FCEV, Toyota Mirai 2, is on chassis dynamometer tests under various drive cycles covering a broad spectrum of vehicle operating conditions. Then machine learning algorithms, such as neural networks, are developed based on these vehicle test data to achieve a rapid computational model with accurate prediction of the critical outputs of the fuel cell and battery dynamics over a drive cycle. Correlations between the hybrid system operating parameters are identified, and the appropriate feature vectors and prediction attributes are developed. The machine learning model is trained on data obtained from various drive cycles having combinations of near-steady-state and transient driving conditions, and their prediction accuracy is evaluated. The developed machine learning model is accurate and computationally fast to be useful for real-time diagnostics or system development.

8.2 Data Acquisition Procedure

The 2021 Toyota Mirai XLE, with the specifications listed in Table 8-1, was procured and instrumented with sensors to measure voltages, current, power, pressure, flow, temperature, and the OEM CAN signals. All signals were captured on state-of-the-art in-house data acquisition systems, and high-speed CAN signals from the non-OBD (on-board diagnostics) proprietary bus were reverse-engineered using SwRI intellectual property. A Yokogawa power analyzer was used to measure AC, DC, and power factor signals in the fuel cell, inverter, and motor. Wire routing had to be optimized to minimize electromagnetic interference between high-power motor power signals and data acquisition signals. The test matrix and vehicle instrumentation were focused on acquiring the vehicle data on relevant drive cycles using a chassis dynamometer. The driving tests extracted data on the hybrid operation of the fuel cell and battery during transient and near-steady-state maneuvers as specified by the driving cycles. Test data was used to evaluate and understand the behavior of fuel cell stack, high-voltage systems, lithium batteries, and drive motors.

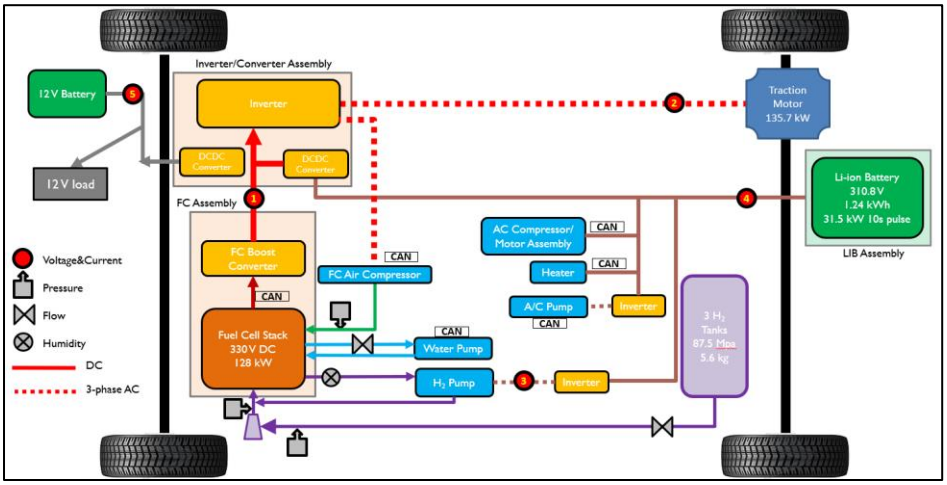
Table 8-1 Specification for the 2021 Mirai 2nd generation fuel cell electric vehicle (FCEV) tested in the present study.

Attribute	***Value***	
Range	402 mi (647 km)	Vehicle Specification
Fuel Economy - City/Highway/Combined	76/71/74 MPGe	
0 – 60 mph	9.0 s	
Maximum Speed	108 mph (175 km/h)	

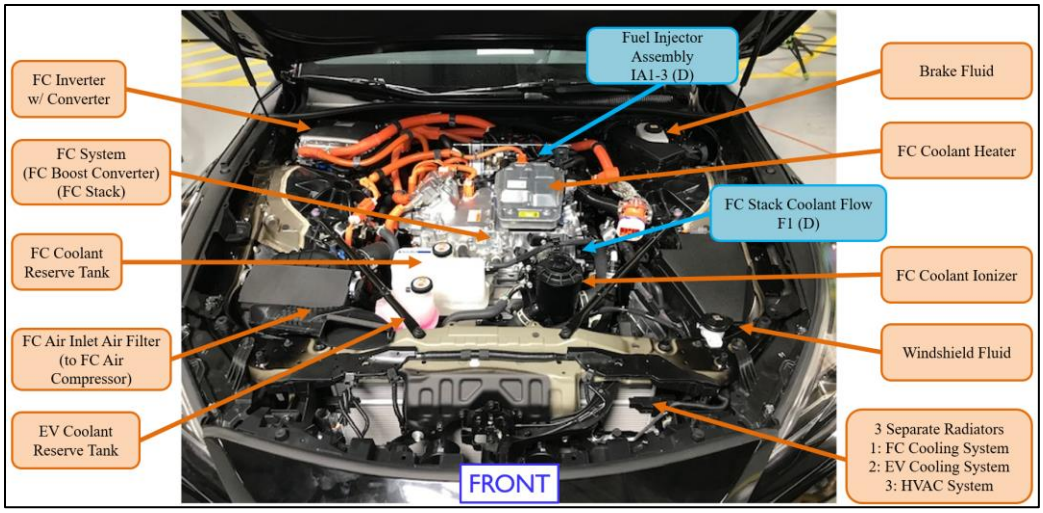
Fuel	Hydrogen (H_2)	
Purity of H_2	99.97%	
Storage	3 x Type Four hydrogen tanks	
Tank Capacity	5.6 kg (12.3 lbs)	
Power Plant	Fuel-Cell Electric	Fuel Cell (FC) Stack Specification
Number of Fuel Cells	330	
Specific Power Density	5.4 kW/l	
Power	128 kW (172 bhp)	
Aspiration	Inlet Air Compressor	
Motor Location	Rear wheel drive	Transmission Specification
Power	136 kW (182 hp)	
Torque	300 N-m (221 lb-ft)	
Battery Cells	84	Lithium Battery (LIB) Pack Specification
Nominal Voltage	310.8 V	
Energy Capacity	1.24 kWh / 4.0 Ah	
Peak Output	31.5 kW x 10 seconds	
Battery Pack Mass	44.6 kg	
Energy Density	27.6 Wh/kg	

Figure 8.1 illustrates the 2021 Mirai 2 FCEV powertrain architecture and the systems in the fuel cell (FC) compartment under the front hood. The air and hydrogen react in the FC stack to generate electrical potential, and the FC boost converter then steps up the FC stack voltage. The FC inverter with converter assembly receives power from the FC boost converter or the lithium-ion battery (LIB), depending on the direction of the demand. When the traction drive motor demands power, the inverter inverts the power from DC to 3-phase AC and sends power to the drive motor. When the regenerative braking is active, the converter converts the power from 3-phase AC to DC and sends power to the LIB to increase its state of charge (SOC). The LIB pack receives a charge from the FC boost converter when the SOC is low enough to accept a charge and when there is no drive motor demand on the LIB.

The chassis dynamometer tests were performed on a Horiba 48-inch single-roll chassis dynamometer. Chassis dynamometer coefficients and equivalent test weights were taken from the Environmental Protection Agency's (EPA) test car list. Dyno set coefficients were determined using test procedure SAE J2264 [225]. The vehicle was operated in dyno mode during all testing phases; following J2572 [226], the car was driven over the EPA Urban Dynamometer Driving Schedule (UDDS) [227] and the Highway Fuel Economy Test (HwFET) [227]. Vehicle data was acquired on UDDS, Federal Test Procedure (FTP) [227], Highway Fuel Economy Test (HwFET), Neutral Cycle (In neutral/idle), and Gradient Cycle (Grade Testing Cycle). The gradient cycle is a non-standard in-house cycle designed to record operational data by pushing the vehicle to maximum operating conditions. The Mirai vehicle was repeatedly operated at full pedal on the dyno at different loads and speeds during the gradient cycle until the vehicle changed operational strategies and finally hit a thermal derate.



(a)



(b)

Figure 8.1 2021 Toyota Mirai 2 fuel cell electric vehicle. (A) Schematic of, and (B) the actual layout (under the hood) of, the fuel cell-lithium-ion battery hybrid powertrain system.

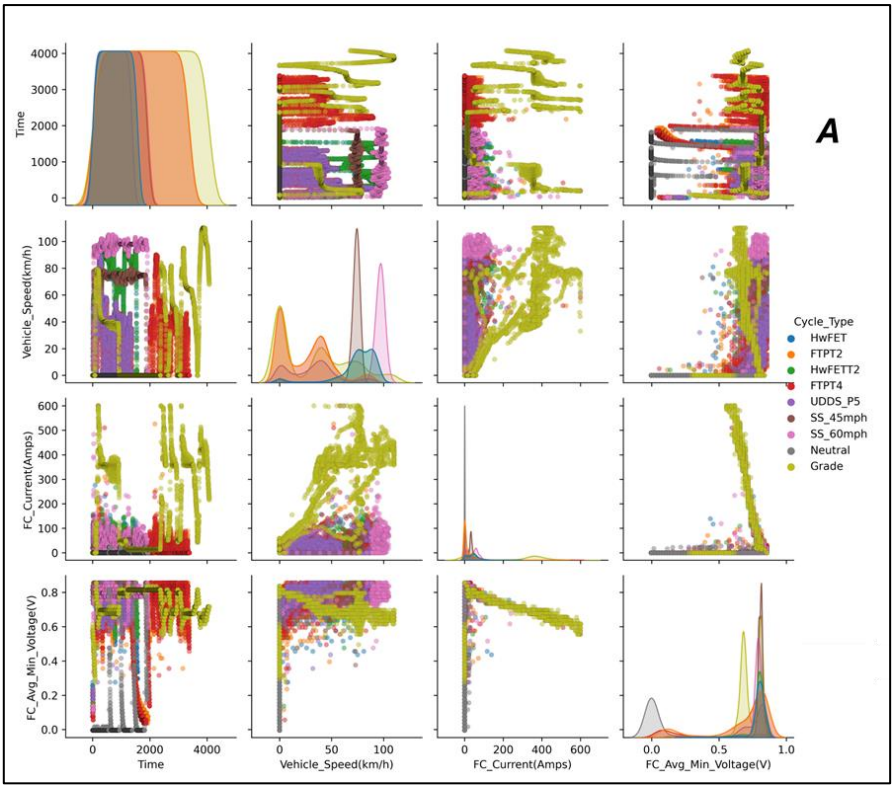
8.3 Vehicle Data

The operating parameters for the vehicle's fuel cell and battery system, such as stack current, voltage, reactant flow rates, reactant pressures, coolant temperatures, air temperatures, and vehicle speed, are acquired during the experimentation and illustrated using pair plots as shown in Figures 8.2, 8.3, and 8.4. A total of over 21,000 data points are collected for the vehicle running on various drive cycles, including transient and near-steady-state driving conditions. The Mirai vehicle, similar to other light-duty vehicles, predominantly operates by utilizing less than 50 kW of power and maintains the fuel cell stack coolant temperature around 55ºC to 65ºC during normal driving conditions, be standard or near steady-state drive cycles. The battery pack is maintained around 25ºC to 30ºC and at a state of charge (SOC) between 50% to 60 % when operated on standard drive cycles. However, during peak load conditions, i.e., during the gradient cycle, the fuel cell can produce close to 110-120 kW. The fuel cell coolant temperature rose close to 95ºC during the peak load, and exceeding this temperature resulted in a thermal derate condition to protect the fuel cell system; during these high loads, the battery pack's SOC also dropped to 20%, and the battery temperature rose to 35ºC. Figure 8.2 illustrates the correlation between the vehicle speed, fuel cell, and lithium battery operating parameters during various drive cycles; here, besides standard drive cycles, 'SS_45' and 'SS_60' refer to near-steady-state driving around 45 and 60 miles per hour, 'Neutral' refers to the vehicle in neutral/idle condition after running for a while. It can be noted from Figure 8.2 that a wide range of vehicle speeds from idle to 100 km/h are covered under the

test matrix. The gradient cycle pushes the fuel cell into an unusually high load condition, facilitating data acquisition in extreme conditions to cover the entire spectrum of the powertrain operation.

Figure 8.3 illustrates the thermal management system behavior of the fuel cell and battery; the data is very transient as the coolant and reactant flow attributes directly correlate to the vehicle's power demand, i.e., load on the fuel cell and battery. Neutral and gradient cycles are the two outlying conditions among all the drive cycles, as the load on the fuel cell is extremely low or high; this is reflected in the reactant and coolant flow rates being excessively high during the gradient cycle and the coolant temperature being very low during the idle (neutral) condition.

Figure 8.4 illustrates the fuel cell stack's reactant flow attributes over different drive cycles. Similar to the electrical and thermal parameters, the gradient cycle stands out with respect to the reactant flow rates and pressures. The anode (H_2) and cathode (air) reactant input follow stoichiometric correlation and exhibit transient behavior over the standard drive cycles.



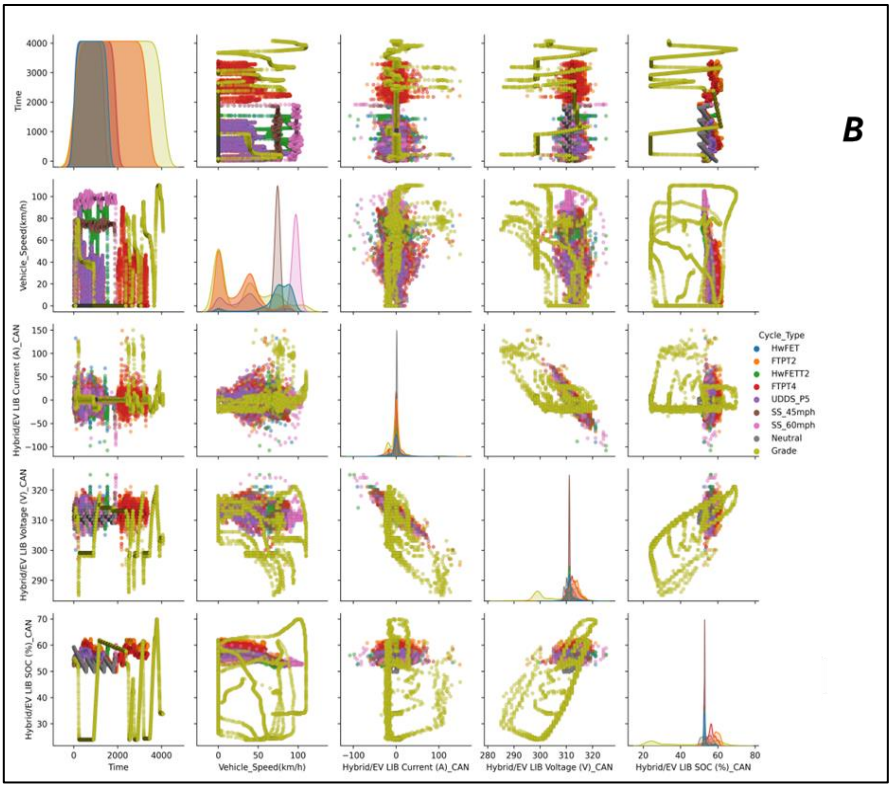
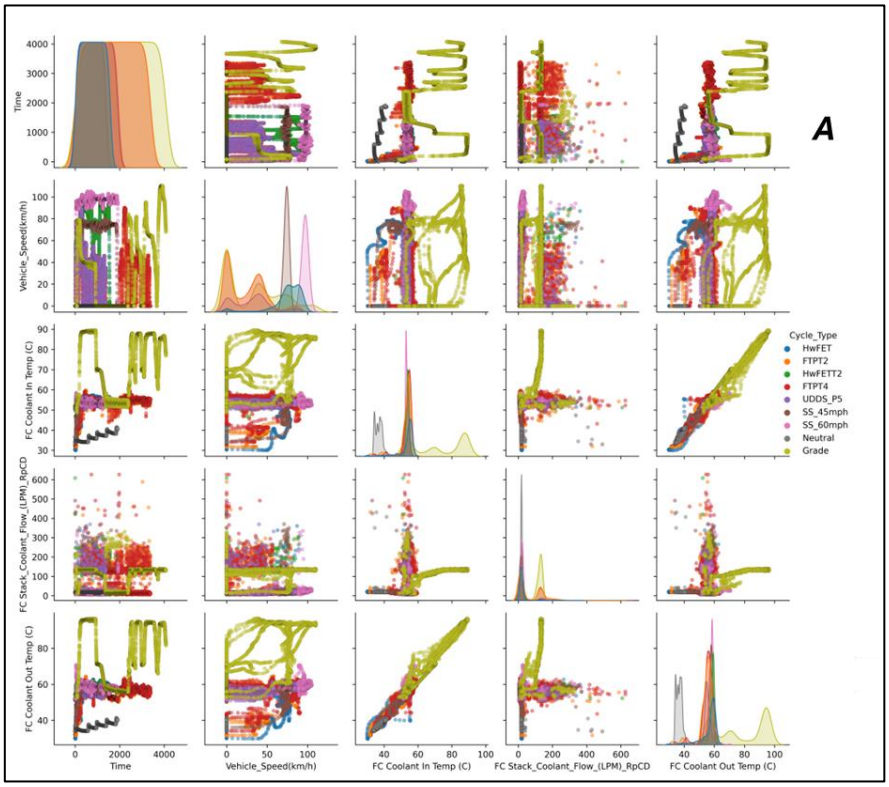


Figure 8.2 The electrical attributes of the 2021 Toyota Mirai 2 fuel cell electric vehicle under various loading conditions, as represented by the data acquired in this study: (A) Fuel cell (FC) Stack; (B) Lithium-ion battery (LiB) Pack.



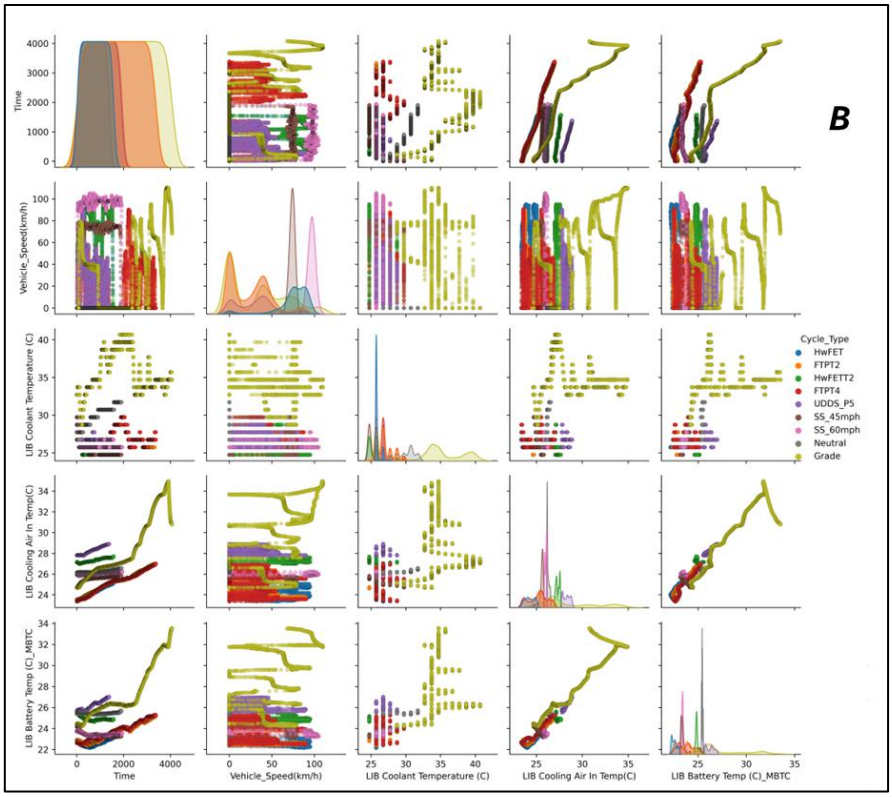
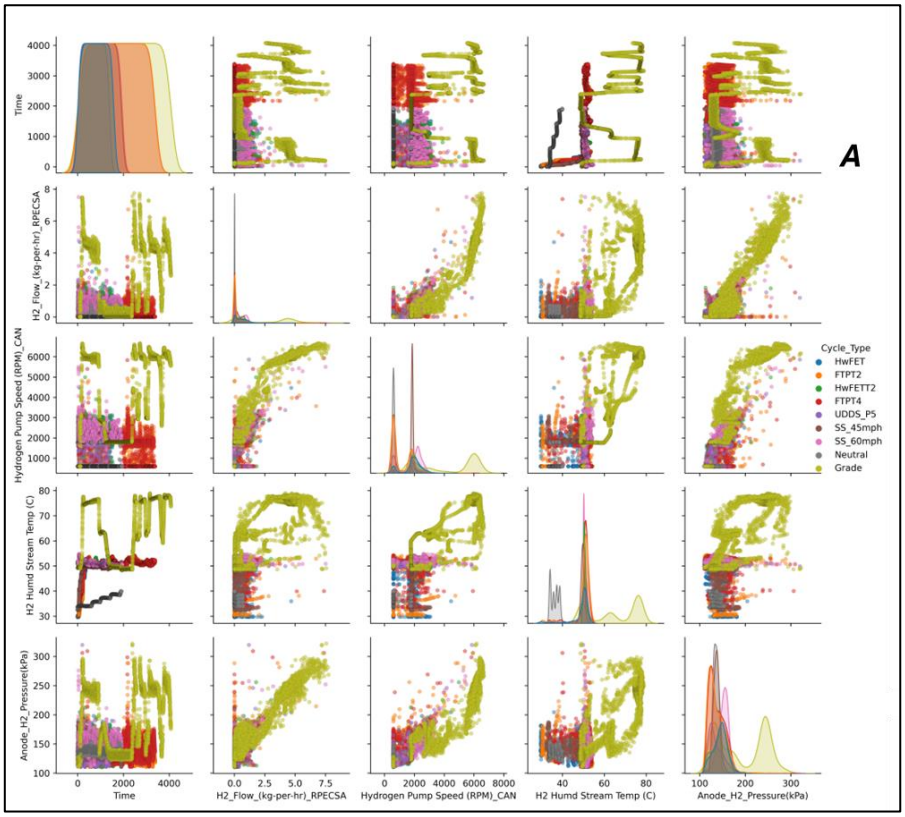


Figure 8.3 The thermal attributes of the 2021 Toyota Mirai 2 fuel cell electric vehicle under various loading conditions, as represented by the data acquired in this study: (A) Fuel cell (FC) Stack; (B) Lithium-ion battery (LiB) Pack.



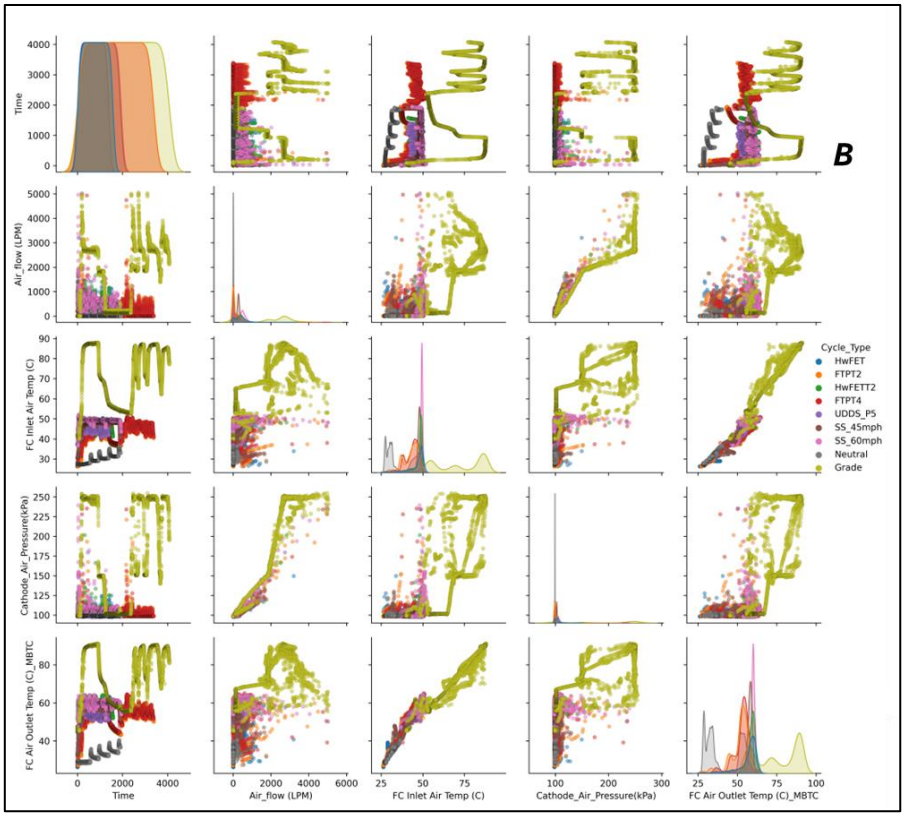


Figure 8.4. The reactant attributes of the 2021 Toyota Mirai 2 fuel cell electric vehicle under various loading conditions, as represented by the data acquired in this study: (A) Anode; (B) Cathode.

The bulk of the fuel cell stack's reactant and vehicle data is acquired through CAN, and one of the most taxing problems is signal noise, as the CAN bus operates in an electrically noisy environment, often leading to some signal interference. Despite the precautions to minimize electrical interference, some measurement noise is still present in acquiring the vehicle data in real-time during a chassis dynamometer test. It is thus challenging to use vehicle-level data to build advanced machine-learning algorithms to predict system dynamics by implementing data augmentation and signal-conditioning techniques. However, data such as system temperatures, reactant flow rates, and electrical attributes acquired through stand-alone data acquisition systems are relatively robust. As observed from the plots, the hybrid powertrain predominantly operates at the lower end of the spectrum when evaluated on standard drive cycles, and the gradient cycle helps us to capture the reactant flow data on the higher extremes. The pair plots illustrate that the data clusters and parameter correlations aid in understanding the system's nonlinearity; it can be concluded that the data acquired through vehicle testing covers most of the operating conditions for the fuel cell-lithium-ion battery hybrid power system (includes the vehicle operation data from idle to rated power and thermal derate conditions).

8.4 Machine learning models/Data-based Modeling

Machine learning techniques are a subset of artificial intelligence that helps develop algorithms that learn and make predictions based on data by recognizing patterns and correlations embedded in the data. These algorithms are adopted in many industries, particularly in sectors or applications that do not have well-defined governing equations or where the process is too complex for mathematical representation and solution. Supervised machine learning involves training a model on a defined dataset acquired from the system, where the input data is paired with the output data during the training process, allowing the model to learn the relationship between inputs and outputs of the system once the training is complete, the developed algorithm mimics the behavior of the system that is trained on.

Supervised machine learning, such as an artificial neural network, is particularly effective for regression prediction problems and is especially suited for multi-input - multi-output (MIMO) systems. Although there are different types of neural network architectures that can be considered for adoption, after analyzing the measurement noise and nonlinearity of the FCEV hybrid system parameters, a simple feed-forward neural network is considered for this study due to its robustness to noise compared to some time series networks. The structural schematic and working of a feed-forward neural network is available in literature [45], [220], [228], [229].

8.4.1 Feature vector and prediction variable selection

Accurately predicting the fuel cell voltage during various driving conditions purely with a physics-based model is a challenge from a vehicle point of view, and it is critical to understand the difference between the degradation profile and system fault. Similarly, predicting the thermal attributes, such as the fuel cell stack's coolant and air-out temperatures, is necessary to identify the formation of hot spots and system health before a catastrophic failure. Precise prediction of battery pack voltage and temperature not only helps from an energy management standpoint but also aids in identifying sensor faults and enhances the system's overall safety.

Because of the reasons mentioned above, fuel cell voltage, coolant out temperature, air outlet temperature, battery pack voltage, and battery temperature are selected as the five prediction variables (model outputs). Considering the fundamental physics and operational principles of electrochemical systems and the basics of thermal management systems, the following feature vectors (model inputs) specified in Table 8-2 are selected.

Table 8-2 Feature vectors and prediction variables adopted in the present study

Feature Vectors (Model Inputs)		***Prediction Variables (outputs)***
Vehicle-Speed	FC H_2 Flow	FC Avg Min Voltage
FC Stack Current	H_2 Pump Speed	FC Stack Coolant Out T
FC Stack Coolant In T	H_2 Humidity Stream Temp	FC Air Outlet T
FC Stack Coolant Flow	H_2 Post Injector Pressure	LIB Voltage
FC Stack Air In T	LIB Current	LIB Battery Temp
FC Stack Air In P	LIB SOC	
FC Air Flow	LIB Intake Air T	
LIB Coolant In Temp		

8.4.2 Neural network architecture and hyperparameter tuning

Determining the architecture and hyperparameter for a neural network to mimic the system is the most critical step in model development. Understanding the parameter correlation and nonlinearity of the system is necessary to select the activation function, hidden layers, and number of neurons. Considering the computational resources, shallow neural network architecture (two hidden layers) is preferred for automotive applications as deep neural networks require greater storage and higher computational power. An iterative approach chooses the hyperparameters and optimizers and correlates the performance and resultant processing time. A non-exponential activation function, the Rectified Linear Unit (ReLU), is selected due to its computational efficiency, nonlinearity, sparsity, and relatively quick convergence during training. Optimizing neural network architecture and hyperparameters involves combining domain knowledge and systematic experimentation. Considering the noise in the CAN data and the system's nonlinearity, a feed-forward neural network is chosen, as described earlier. In contrast, advanced time series-dependent neural network architectures may not yield any significant improvements and sometimes even lead to higher errors in prediction attributes when the data is noisy. The Savitzky-Golay filter [230] is tried with various observation windows and polynomials to smoothen the data without distorting the fundamental behavior of the attribute. Early stopping feature is implemented

to limit the epochs, prevent overfitting, and reduce training time. Any extreme outlier data points and noisy data attributes during the data acquisition process are omitted from the data set to prevent any bias or misleading patterns. The feed-forward neural network architecture developed is illustrated in Figure 8.5 and the tuned hyperparameters for the network are tabulated in Table 8-3.

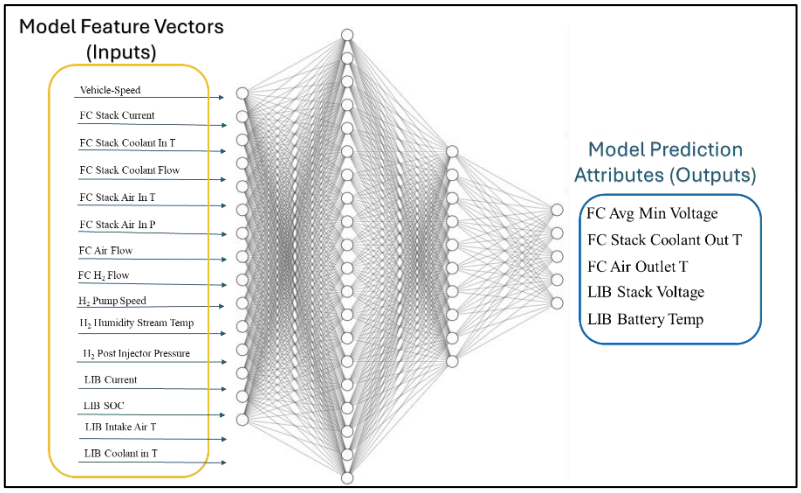


Figure 8.5 Schematic of the input, output and architecture of the neural network adopted in the present study.

Table 8-3 Neural network hyperparameters optimized for the present study

ANN Hyperparameters	***Final Value***
Feature Vectors (Inputs)	15
Target Variables (Outputs)	5
Number of Hidden Layers	2
Number of Neurons for Hidden Layers	250 – 1st layer, 150 - 2nd layer
Activation Function	'ReLU' – 1, 2 Hidden layers
Loss Function	Mean Square Error - 'MSE'
Optimizer	Adam (Learning Rate – 0.005, beta_1 = 0.975)
Number of Data Points	21,146 (Split: 70-Training/30 Validation)
Batch Learning	50
Dropout Probability for Hidden Layers	0.5 – 1st layer, 0.5 - 2nd layer
Loss function	MSE – Mean Squared Error

After tuning the neural network with the hyperparameters as given above, the prediction results after normalization are illustrated in Figure 8.6; here, the model can predict the output attributes with an accuracy of R-squared value greater than 0.98. In Figure 8.6 the points line up on the diagonal when the prediction and experimental values match, and the presence of the scattered points away from the diagonal suggests that some predictions are less accurate, which can be attributed to both noise in the dataset and the limitations of the model. There is a more significant spread of points at higher values, which might suggest that the data's noise or variability increases with the values' magnitude; however, it should be noted that the model should not be predicting the system noise as it indicates the overfitting of the model. In this case, the initial observation of the loss plot shows that training and testing losses are low and stable, suggesting that the model has effectively learned the patterns in the data without overfitting, making the model reliable for these regression tasks.

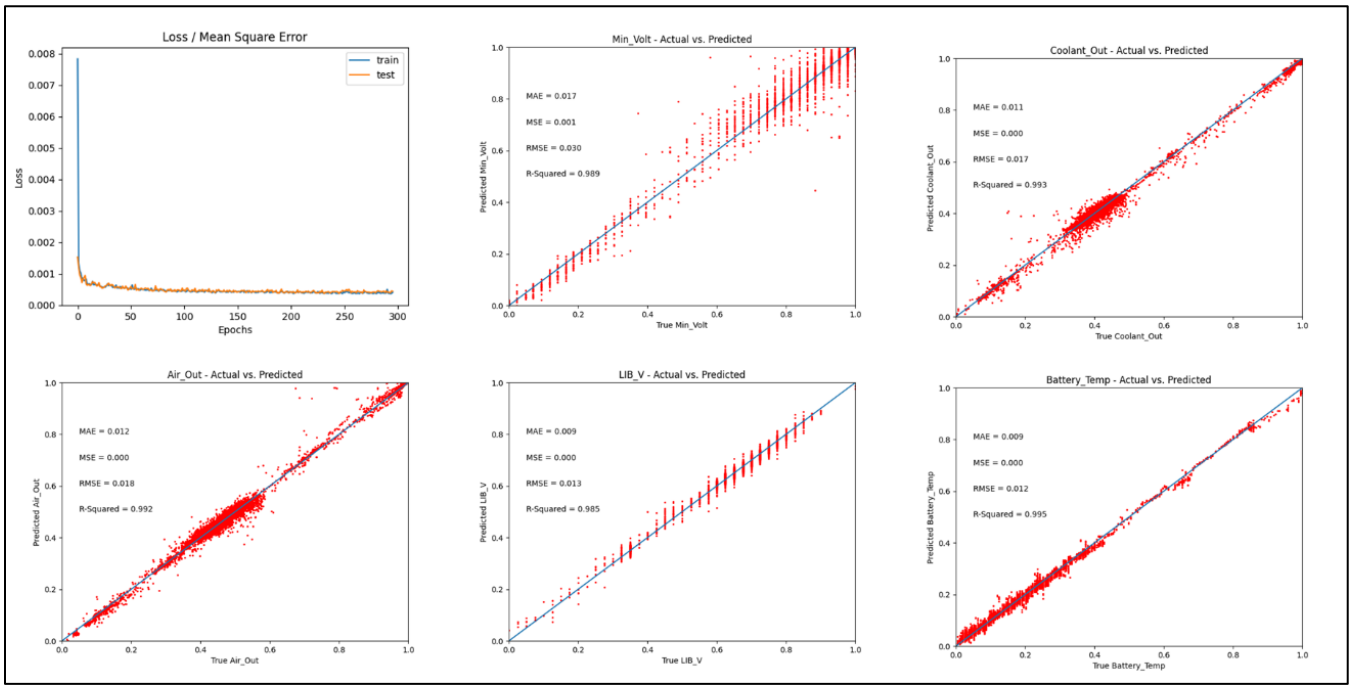


Figure 8.6 Prediction accuracy of the trained neural network for various hybrid system attributes

8.5 Results and Discussion

This section evaluates the performance of the trained model in the prediction of the dynamic characteristics of the Mirai's fuel cell-battery hybrid power system operating under various drive

cycles. Once the iteration results during the training are satisfactory, the input data from HwFET, FTP, and Gradient drive cycles are fed into the model as a time series (sequential) to assess the accuracy and the capability of the model developed.

8.5.1 HwFET Cycle (Highway Fuel Economy Test)

The HwFET cycle simulates the usual highway driving conditions, which is relatively stable compared to the FTP or Gradient cycle. The average speed is around 77.7 km/h, and the maximum speed reached during the test is approximately 97 km/h (60 mph), including the acceleration and deceleration phases to mimic real-world driving. The vehicle's operating parameters during the HwFET cycle are the model's input to predict the hybrid power system dynamics. The predicted values from the trained model compared to measurement are illustrated in Figure 8.7, from which it can be concluded that the model performance during the near steady-state or limited transient conditions is excellent. The model could predict minor changes in the system outputs but does not follow the system noise, demonstrating its robustness.

As it is seen from the vehicle speed subplot shown in Figure 8.8, the Mirai vehicle during HwFET is subjected to a hard deceleration and subsequent acceleration event that occurred around 800 seconds. During this deceleration, the vehicle speed was dropped to zero and accelerated to 60 km/hr; in this instance, a rapid change is observed in the fuel cell-battery hybrid dynamics where the average minimal fuel cell voltage falls below 0.6 V when the vehicle approached idle as both the hydrogen flow and fuel cell stack current drops to zero. On the other hand, LiB stack voltage spikes during deceleration because of the battery regeneration, which can be inferred from the negative LiB stack current. In both cases at the same deceleration instance, the model accurately predicts the drop in fuel cell voltage and increase in battery voltage during the deceleration by correlating the change in vehicle speed, hydrogen fuel flow, fuel cell, and battery current. Similarly, as the vehicle is accelerated, the fuel cell recovers or reverts back to the standard operating voltage of 0.8 V as the hydrogen flow is turned back on proportionally to the vehicle speed, and the LiB stack voltage falls back as the battery stack current is utilized for the vehicle acceleration. The temperature dynamics are relatively unchanged in the HwFET cycle, and the model could accommodate these minor changes by tracking these subtle changes. These results demonstrate the capability of the model to accurately predict the hybrid system dynamics by

correlating the vehicle's operational parameters in a near-steady state condition and during challenging decelerate-accelerate events.

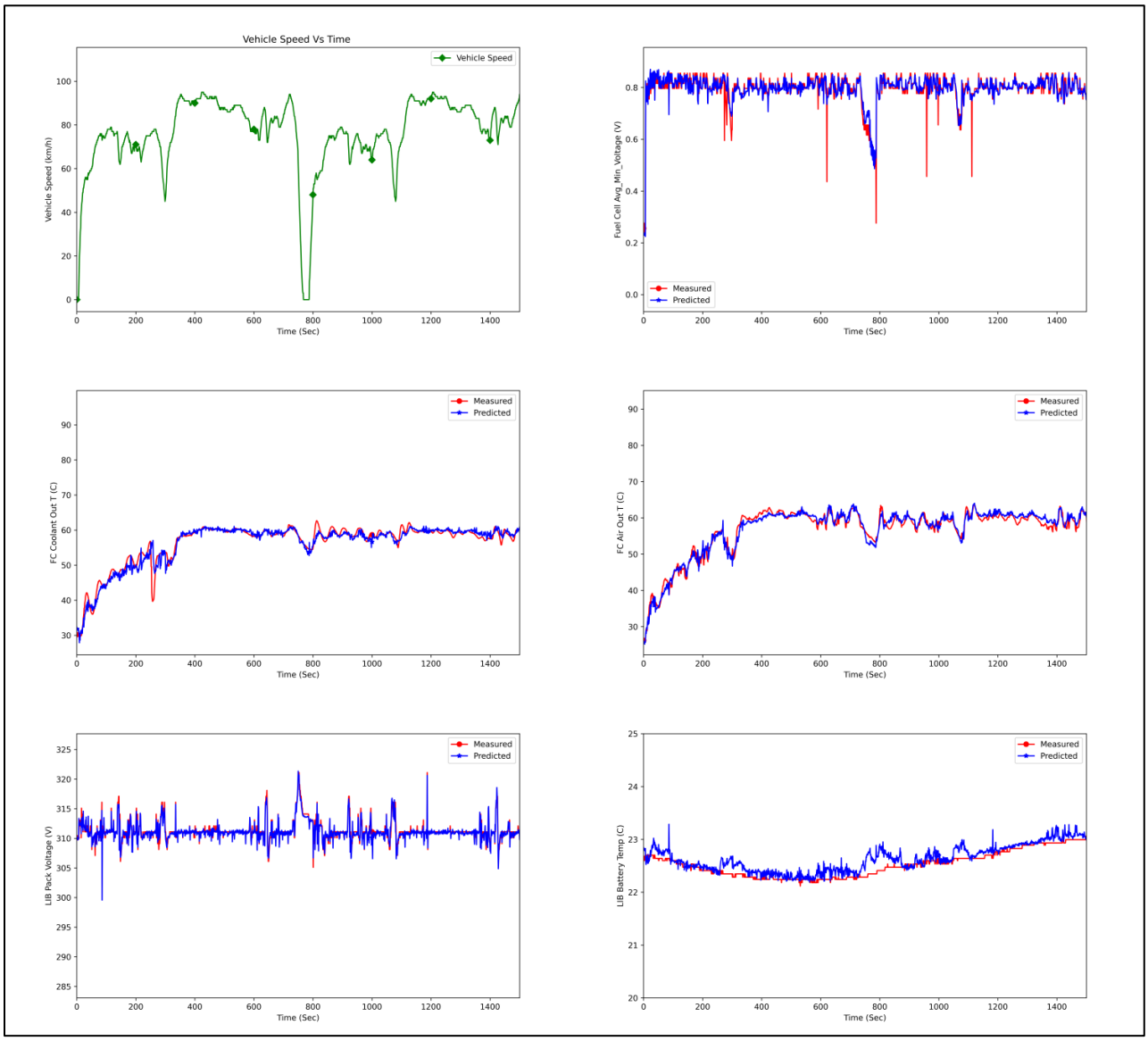


Figure 8.7 The performance of the present neural network model for the vehicle operating on HwFET (Highway Fuel Economy Test) Cycle.

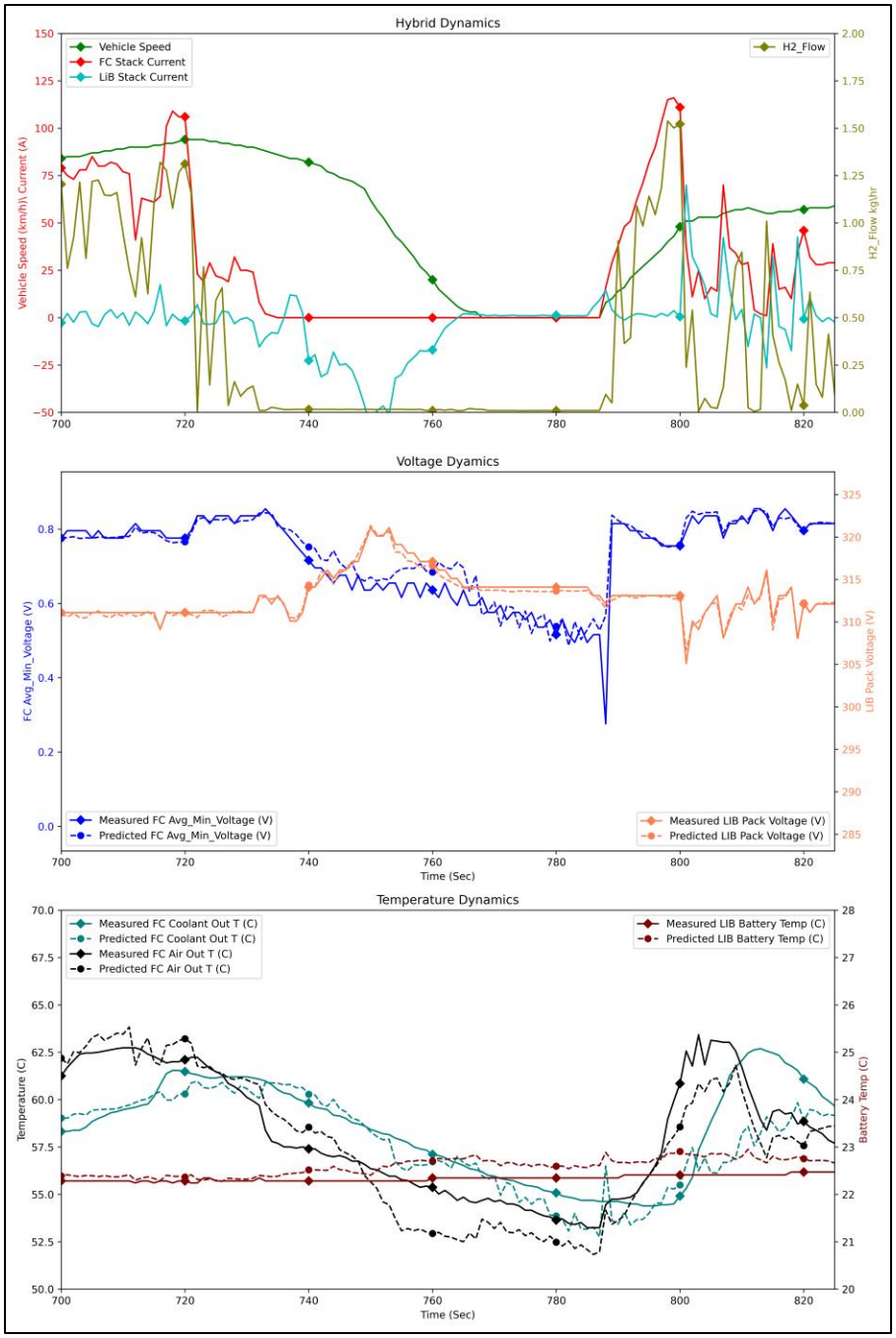


Figure 8.8 The fuel cell-battery hybrid power system dynamics and the prediction accuracy of the developed neural network model during a vehicle deceleration and acceleration event for the vehicle operating on the HwFET (Highway Fuel Economy Test) Cycle.

8.5.2 FTP Cycle (Federal Test Procedure)

The FTP cycle is a standardized driving test to evaluate emissions and overall performance of a vehicle operating under various driving conditions, which is a relatively more transient drive cycle when compared to HwFET presented earlier. The average speed throughout the cycle is around 34.1 km/h, and the maximum speed reached during the test is approximately 91.2 km/h, including a mix of idling, acceleration, deceleration, and cruising phases to simulate real-world urban and suburban driving conditions. Like the case for HwFET, the vehicle's operating parameters during the FTP cycle are used as inputs for the model to predict the hybrid power system dynamics during the transient operation. The prediction performance of the trained model is illustrated in Figure 8.9. It is evident that the model prediction accuracy in extreme transient conditions is outstanding, similar to physics-based models mentioned in the literature [231], [232]. The model can also distinguish the system noise in extreme transient conditions to a certain extent.

The extreme transient part of the FTP cycle is illustrated in Figure 8.10, where the vehicle is subjected to high-frequency acceleration and deceleration events in a short period. As observed from the first minute of the illustrated time series (between 3500 and 3550 seconds), despite the the vehicle being idle, the measured fuel cell voltage is at 0.8 V, the fuel cell stack current is around 20 A, and hydrogen flow fluctuates around 0.5 kg/hr while the measured LiB stack current is around -20A and rising LiB voltage indicates that the fuel cell is recharging the battery as determined by the supervisory controller. Here, the neural network model accurately identifies the battery regeneration event at idle during the start of the second FTP cycle and not only accurately predicts the fuel cell and battery pack voltage simultaneously, but also captures the rising temperature dynamics accurately. On the other hand, there are two more instances between 3560 and 3750 seconds where the vehicle is idle, and there is no battery regeneration; here, the model accurately distinguishes and predicts the voltage dynamics similarly.

In the second (3600-3700 seconds) and third phase (3700-3800 seconds) of the drive cycle, the high-frequency vehicle acceleration-deceleration events pushes the hybrid dynamics into another zone where the bulk of the transient power demand is fulfilled by the fuel cell, and the battery pack supplements and regenerates during the peak transient conditions. Here, the model again accurately correlates the changing transients of the vehicle speed and operating parameters, such as hydrogen flow rate and current outputs, to predict the voltage and temperature dynamics without

any time delay (lag) associated with the reactant transport and diffusion dynamics, demonstrating the potential of the developed model for real-time application.

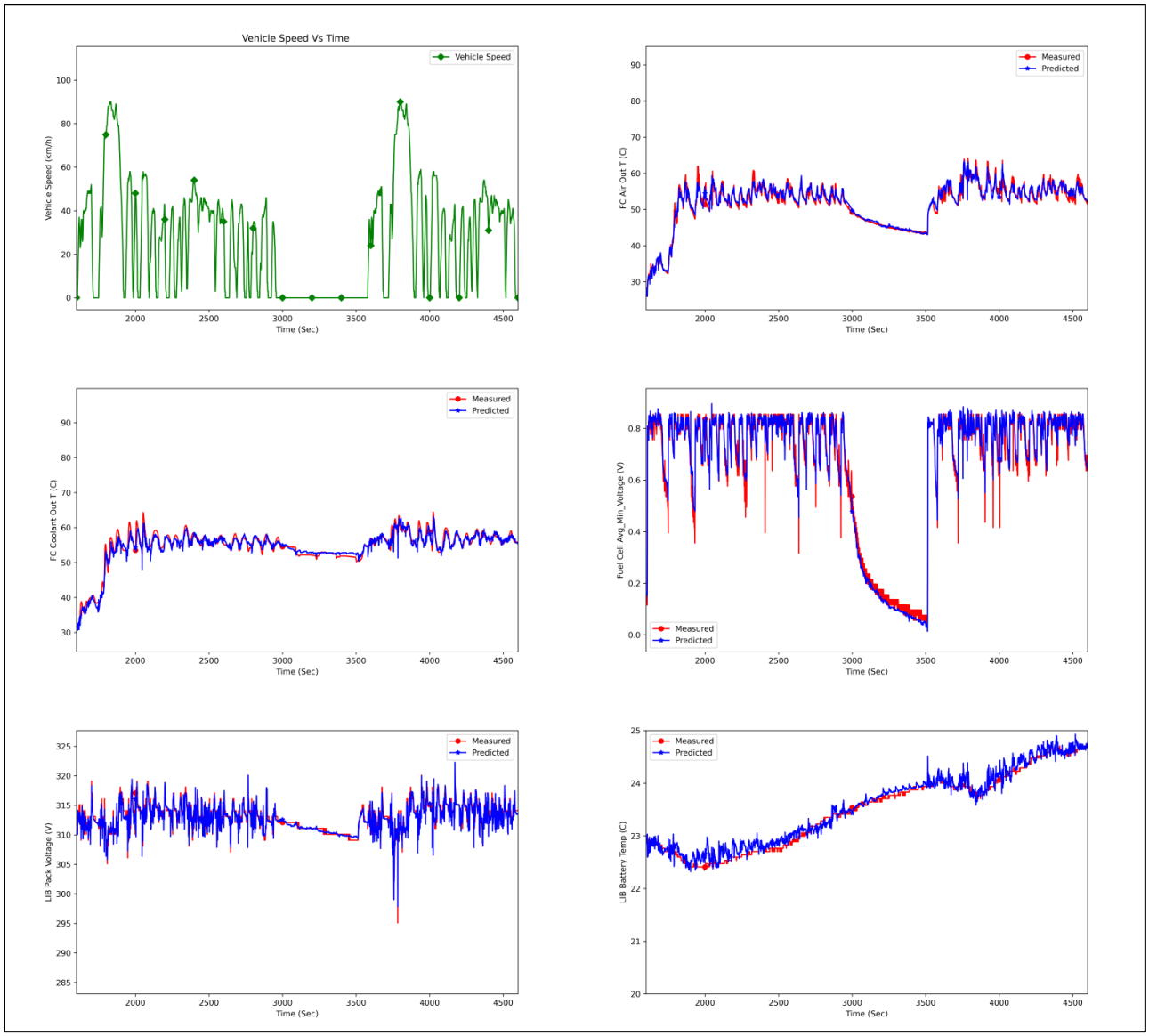


Figure 8.9 The performance of the present neural network model for the vehicle operating on the FTP (Federal Test Procedure) Cycle.

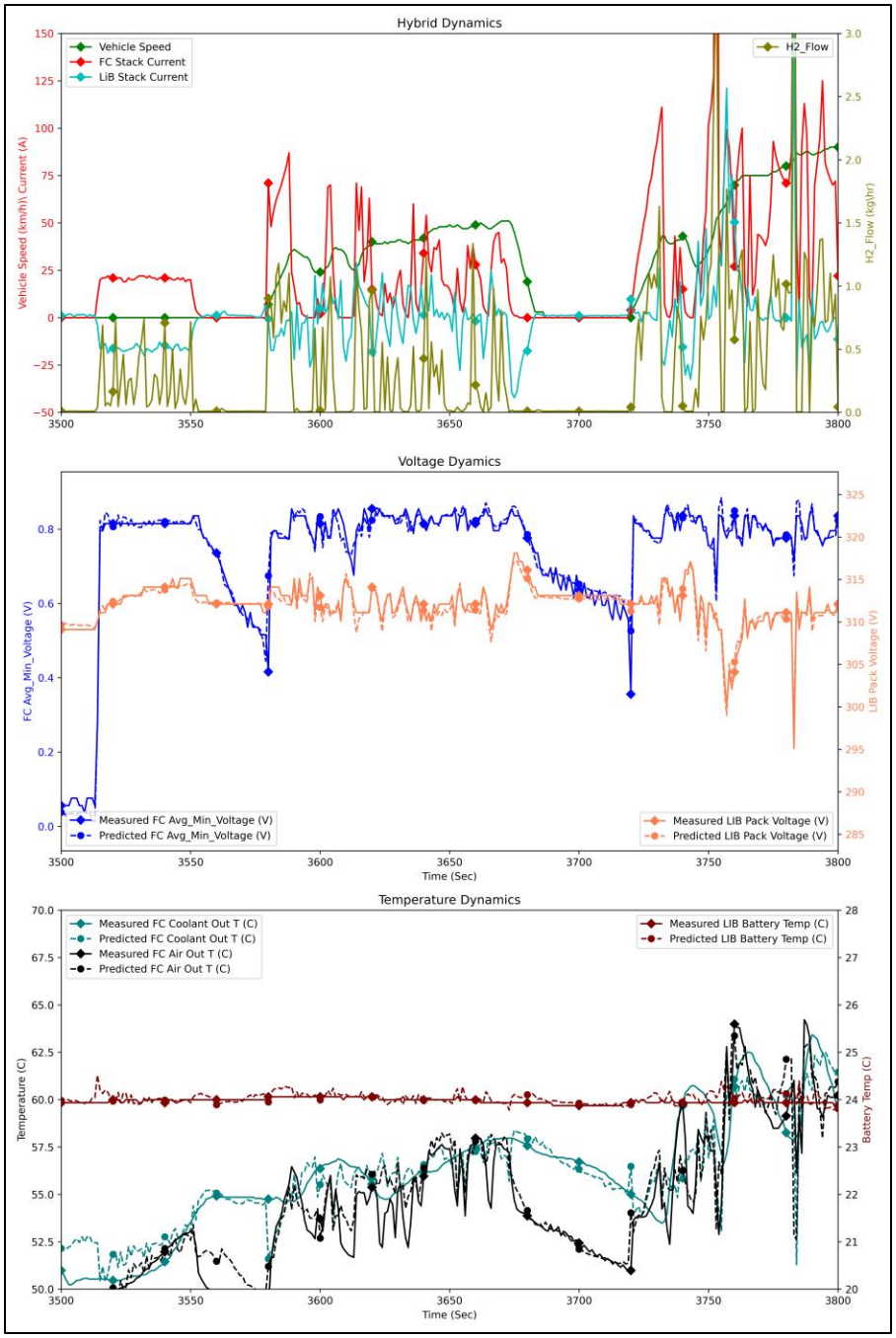


Figure 8.10 The hybrid power system dynamics and the prediction accuracy of the developed neural network model during high-frequency deceleration and acceleration events for the vehicle operating on the FTP (Federal Test Procedure) Cycle.

8.5.3 Gradient Cycle

The gradient cycle is a non-standard in-house drive cycle developed to subject the vehicle to high loads and speeds, extracting the rated power to understand the powertrain system behavior at extreme conditions, as typical automotive drive cycles do not cover the entire operating spectrum of the vehicle. Gradient cycle pushes the system performance to its design limits, as in this case, the vehicle hits the thermal derate to protect the fuel cell system from being exposed to excessive high operating temperatures. This cycle combines idle, steady-state, and transient modes where the operating parameters of the vehicle are fed as inputs to the model for the prediction of the powertrain system output attributes in extreme conditions. The measured and predicted results are illustrated in Figure 8.11, where a wide range of fluctuations in the system attributes, such as rising system temperatures and dropping voltages during acceleration, can be observed. Figure 8.11 shows that the model prediction is in good agreement with the experimental data, encompassing the entire fuel cell hybrid operational spectrum, even for extreme conditions.

Figure 8.12 illustrates the final phase, or the most challenging part of the gradient cycle, where the vehicle is subjected to transient driving conditions almost at rated power. In the first half of the illustrated timer series (between 20500 and 20800 seconds), the vehicle is subjected to quick deceleration followed by rapid acceleration at a high load in the second phase (after 20800 seconds). As observed from Figure 8.12, the vehicle is operated in extreme conditions at almost thrice the hydrogen fuel flow rate and fuel cell stack current with fuel cell temperature dynamics consistently over 85ºC to reach a vehicle speed close to 120 km/hr. Here, the neural network model identifies both the deceleration and acceleration events under these extreme operating conditions and accurately predicts the wide swings in the fuel cell and battery voltages along with temperature dynamics.

The rapid change in the fuel cell temperature dynamics can be observed at the end of the deceleration and the start of the acceleration phase (20600-20900 seconds), where both the fuel cell coolant out and air (cathode) outlet temperatures fall and rise between 65C and 95C coupled with the swings in fuel cell voltage and LiB stack voltage. Here, the model correlates the extreme operating conditions and predicts the fluctuations in temperatures and voltages across all the transient phases without any significant changes in the prediction accuracy and also avoids

replicating the measurement noise to some extent, demonstrating the robustness and applicability of such models across broad operating spectrums.

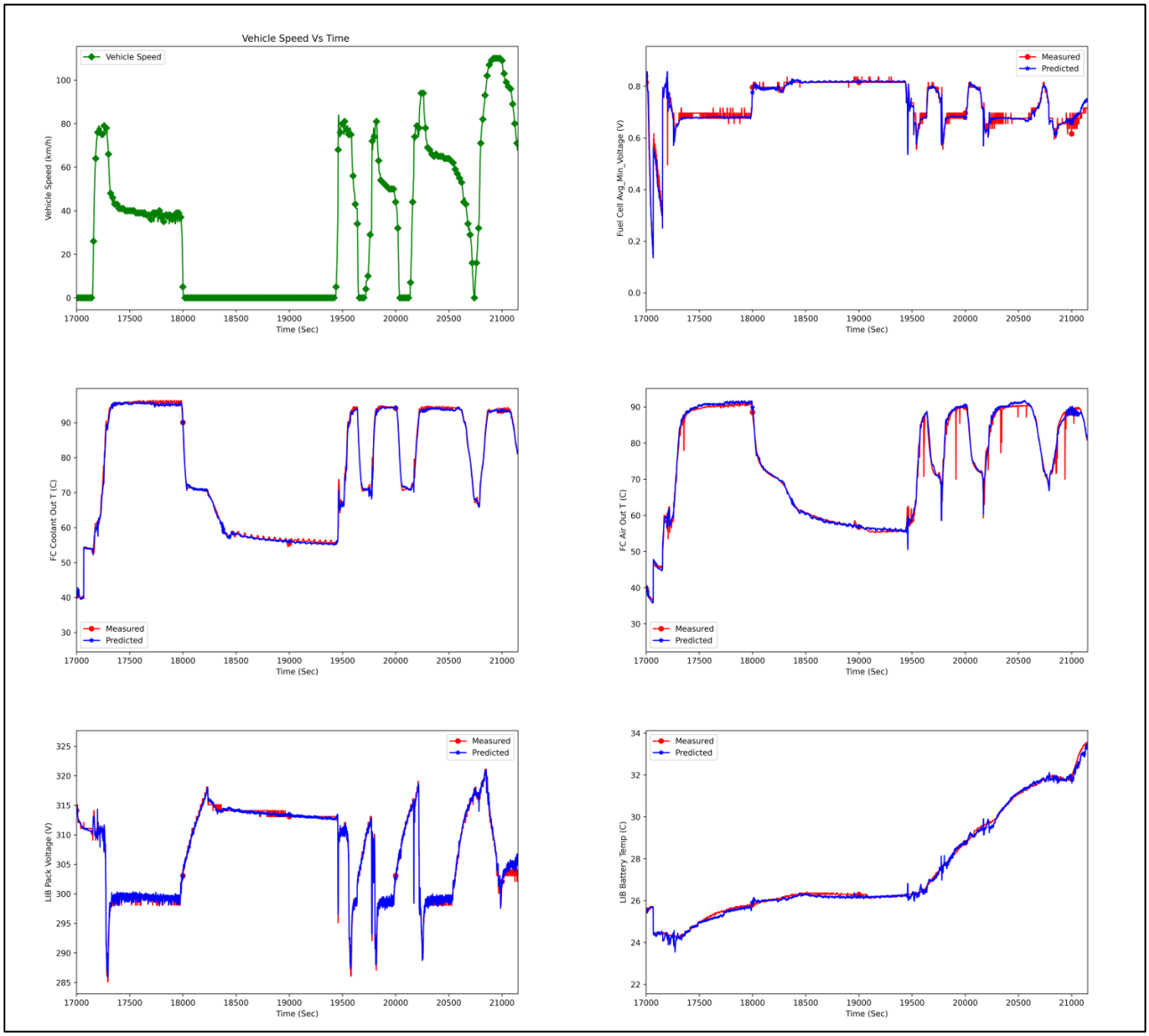


Figure 8.11 The performance of the present neural network model for the vehicle operating on the Gradient Cycle.

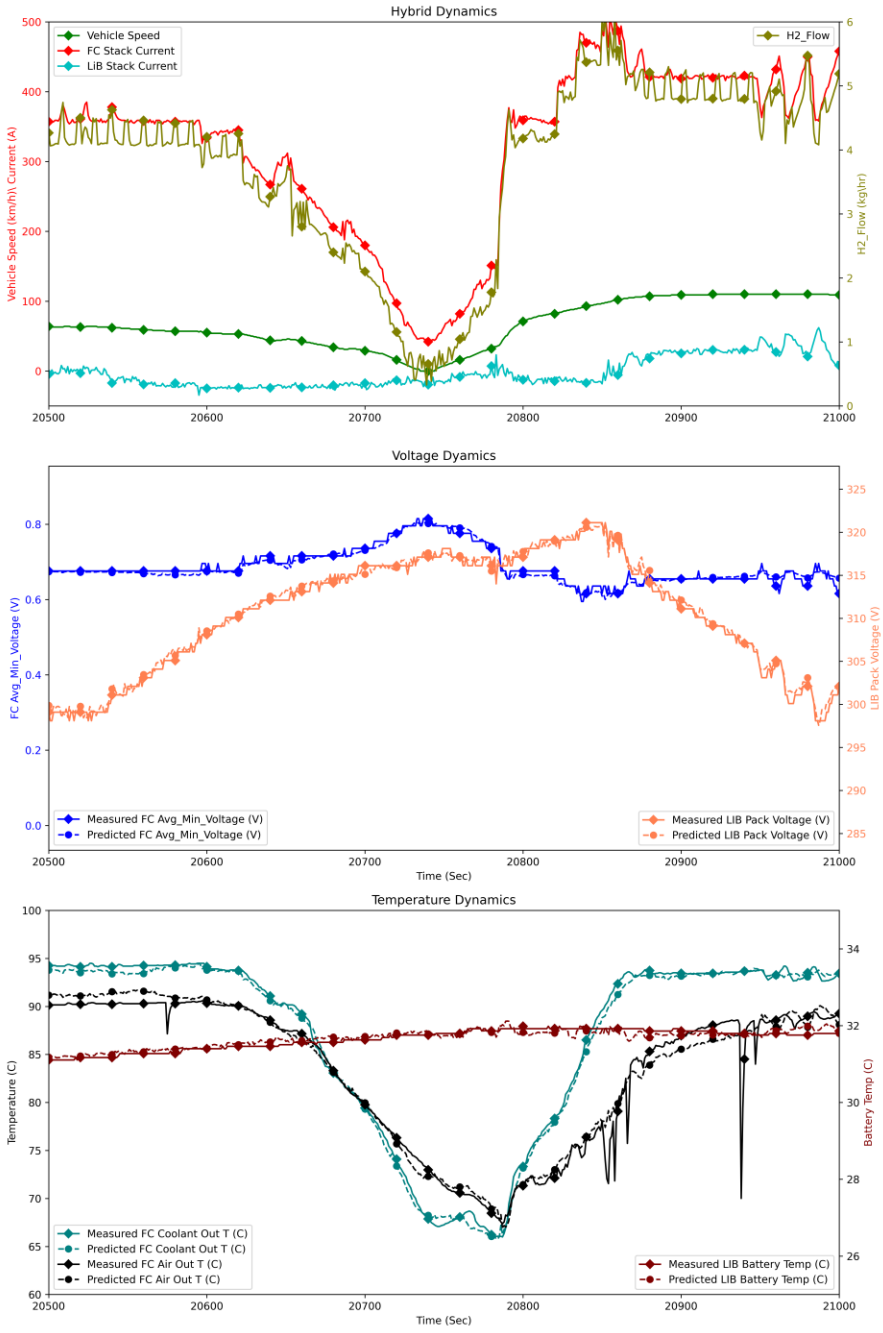


Figure 8.12 The hybrid power system dynamics and the prediction accuracy of the present neural network model during extreme driving conditions at the rated power for the vehicle operating on the Gradient Cycle.

It is crucial to consider a range of error metrics that provide a more comprehensive assessment of the model's prediction accuracy. Metrics like Mean Absolute Error (MAE), Mean Squared Error (MSE), Root Mean Squared Error (RMSE), and Mean Absolute Percentage Error (MAPE) offer valuable insights into different aspects of prediction accuracy. MAE provides a straightforward measure of average absolute errors, MSE emphasizes more significant errors due to its squaring

nature, RMSE offers a measure of error magnitude that is interpretable in the same units as the original data, and MAPE gives an understanding of the average error as a percentage of the actual values. Considering these metrics together, as shown in Table 8-4, a more nuanced and complete evaluation of a model's performance can be achieved, especially in complex, nonlinear, or transient data.

Table 8-4 Error attributes for the model predicted fuel cell-battery electric-electric hybrid power system attributes over the different drive cycles investigated.

Cycle	***Predicted Parameter***	***MSE***	***RMSE***	***MAE***	***MAPE***
HwFET	Fuel Cell Avg_Min_Voltage (V)	0.001	0.028	0.014	2.17%
	FC Coolant Out T (C)	2.802	1.674	1.004	1.92%
	FC Air Out T (C)	1.532	1.238	1.001	1.82%
	LIB Pack Voltage (V)	0.224	0.473	0.348	0.11%
	LIB Battery Temp (C)	0.021	0.146	0.113	0.50%
FTP	Fuel Cell Avg_Min_Voltage (V)	0.001	0.032	0.021	5.06%
	FC Coolant Out T (C)	1.617	1.271	0.925	1.70%
	FC Air Out T (C)	1.183	1.088	0.799	1.54%
	LIB Pack Voltage (V)	0.289	0.537	0.422	0.13%
	LIB Battery Temp (C)	0.015	0.122	0.096	0.41%
Gradient	Fuel Cell Avg_Min_Voltage (V)	0.000	0.014	0.009	1.32%
	FC Coolant Out T (C)	0.622	0.789	0.545	0.73%
	FC Air Out T (C)	1.514	1.230	0.728	1.00%
	LIB Pack Voltage (V)	0.361	0.601	0.449	0.15%
	LIB Battery Temp (C)	0.018	0.135	0.102	0.37%
MSE – Mean Squared Error; RMSE – Root Mean Squared Error; MAE – Mean Absolute Error; MAPE – Mean Absolute Percentage Error					

The above results suggest that the trained machine-learning model has accurately predicted the Mirai vehicle's critical fuel cell hybrid power system attributes, even under extreme transient operating conditions with noisy measurement and limited signal processing. The computational speed for each time step is around 740 Microseconds, or ~ 0.00074s, when operated on a computer equipped with an Nvidia Graphic Card – RTX 3070, 12th Gen Intel (R) Core (TM) i9-12900, and 32GB of RAM. Considering the model development time, computational speed, and excellent prediction performance, the developed machine learning model has great potential for use in diagnostics and product development.

8.6 Summary

In this study, a full-fledged machine-learning model based on a feed-forward neural network has been developed to model the dynamics of the fuel cell-lithium-ion battery (LIB) hybrid power system implemented in the 2021 Toyota Mirai 2nd generation fuel cell electric vehicle. The data is acquired from the vehicle in real-time during a chassis dynamometer test under various driving cycles, including the US Environmental Protection Agency's Urban Dynamometer Driving Schedule (UDDS) and the Highway Fuel Economy Driving Schedule (HFEDS), Federal Test Procedure (FTP), Highway Fuel Economy Test (HwFET), Neutral Cycle, and Grade Testing Cycle. During the training and validation phase, the model utilizes the data generated from the vehicle's onboard controller area network (CAN) bus and other data acquisition systems. Over 21,000 data points across the different driving cycles are acquired from vehicle testing to understand the dynamic characteristics and nonlinearity of the fuel cell battery hybrid powertrain system under various operating conditions. After analysis, 15 operating parameters are chosen as the feature vectors for the neural network mode to predict the average minimum cell voltage, coolant, and cathode out air outlet temperatures of the fuel cell, along with LiB voltage and temperature. The hyperparameters used for training the neural network, testing cases, and resultant data spread are analyzed, and the trained model demonstrates excellent accuracy in predicting the fuel cell-battery hybrid power system dynamics with an R-squared value greater than 0.98. The neural network model performance across the various drive cycles representing steady state and extreme transient operating conditions is outstanding and robust despite measurement noise, illustrating their applicability in system development and onboard diagnostic systems.

Chapter 9 Conclusions and Future Work

This study successfully explored the aspect of using artificial neural network (ANN) and support vector machine regressor (SVR) to develop various data-based models for electrochemical devices and thermal systems. Various data-based models are designed to predict multiple attributes of a fuel cell battery hybrid system at the component and system levels. This chapter summarizes the key conclusions derived from the research.

9.1 Conclusions

This study demonstrated the feasibility of developing a data-based model for electrochemical and thermal systems using machine learning algorithms trained on data derived from virtual simulations and laboratory experimentation.

The feasibility of building accurate data-based models by solely relying on data derived from physics-based models is proven, reducing the necessity of extensive experimentation. When developing the surrogate models (digital twins) for the PEMFC based on data derived from the CFD model, it was found that the ANN was advantageous over the SVR, especially for solving multivariable input-output regressions. ANN thereby provided a better way to replicate various feature vectors' complex nonlinearity attributes to predict multiple system outputs. In contrast, SVR was advantageous for modeling simple regressions as it dramatically reduced the level of computation without sacrificing accuracy, making it ideal for predicting a single entity of a complex system. It can be concluded that ANN is preferred for instances where a single model predicts multiple electrochemical system attributes simultaneously, and SVR is preferred for cases where the model predicts a single attribute, such as system voltage or resistance.

The electrode catalyst surface area and the total number of accelerated stress test (AST) cycles strongly correlate with electrochemical system degradation. Based on the correlation, this study demonstrated that predicting voltage degradation behavior can be formulated as a regression problem. Here, the endured accelerated stress test (AST) cycles or electrode catalyst surface area can serve as one of the inputs to the neural network to determine degradation level, providing an alternative technique for existing time series modeling. The proposed data-based model developed on ANN was accurate and robust, requiring no additional data filtration or signal conditioning to

predict system output attributes. These results validate the model's applicability for steady and transition operations to predict reactant temperatures, pressures, and electrical attributes without any computationally intensive processing, demonstrating the feasibility of real-time onboard diagnostics.

The LIB battery's heat release rate strongly correlates with its depth of discharge, and a novel hybrid data-based model, which combines Kalman Filter and ANN, is developed based on this correlation to predict the LIB's instantaneous heat release rate. The hybrid model was able to predict the cumulative heat output from the battery and control the thermal management system, demonstrating the data-based model's capability. Further, the hybrid model could compare the cumulative heat output predicted by various hybrid models and experimental/measured data to detect multiple sensor faults, demonstrating the applicability of such algorithms for onboard diagnostics.

The system’s internal state, such as soot load for a particulate filter or state of charge for a battery, and operating conditions strongly correlate with exothermic behavior and thermal gradients. This study has demonstrated that the data-based models can predict the complex thermal gradients and temperature dynamics during an exothermic with great accuracy and fast computational speed by considering the system's internal state and operating conditions. These thermal gradient prediction results demonstrate that the data-based model can be an alternative to complex CFD models during product development to determine thermal management, cooling system design, regeneration strategies, and onboard diagnostics.

This study has demonstrated the pertinency of data-based models in a real-world scenario to predict the fuel cell-battery hybrid system dynamics by using drive cycle data at a vehicle level. When the ANN is trained on the data derived from various drive cycles, the model accurately predicts the system dynamics, including the electrical and thermal attributes. The model identifies the zones of battery regeneration and fuel cell-battery power split along with thermal derate and minimum cell voltages across different operating conditions without any objective functions or manual optimizations, thereby demonstrating the viability of such models in the future for field applications.

9.2 Future Work

The modeling work presented in this thesis can further be expanded by developing advanced time series-based prediction models based on long short-term memory networks and transformers. A comparative study of improvement in accuracy, robustness, and computational time between various models can provide a unique perspective on understanding each modeling technique's pros and cons. Similarly, the data-based models can further be used to solve new challenges in the space of clean energy that aids in rapid commercialization and improves the safety of new electrochemical and thermal systems such as:

1. Develop data-based models to predict the LIB's heat release rate during fast charging (3C-5C) and optimize real-time battery fast charging and thermal management. This model would help us understand the impact of fast charging on LIB thermal behavior and provide insights into the associated thermal runaway and aging factors.

2. Development of a machine learning model to predict the internal temperature and current gradients in a PEMFC. Accurately predicting the cell's internal temperature and current distribution will help us determine the long-term aging gradients and flooding/reactant starvation zones inside the membrane electrode assembly.

3. Develop advanced hybrid data-based models such as physics-informed neural networks to solve advanced electrochemical and thermal problems. Integrating the physics-based CFD, empirical models with ANN, or other time series-based machine learning algorithms can help predict PEMFC internal states such as state of health, electrode catalyst surface area, membrane hydration, and resistance more accurately. This type of modeling can play a critical role in developing next-generation system controls as it brings the best of both worlds with the advantages of governing equations that determine the boundary conditions and the computational speed of black box modeling.

References

[1] R. Weiner *et al.*, "Climate change coverage in the United States media during the 2017 hurricane season: implications for climate change communication," *Clim Change*, vol. 164, no. 3–4, Feb. 2021, doi: 10.1007/s10584-021-03032-0.

[2] "Inventory of U.S. Greenhouse Gas Emissions and Sinks: 1990-2022 | US EPA." US EPA, 13 Aug. 2024, www.epa.gov/ghgemissions/inventory-us-greenhouse-gas-emissions-and-sinks-1990-2022.

[3] S. Wappelhorst, "The end of the road? An overview of combustion-engine car phase-out announcements across Europe," 2020. Available: https://theicct.org/wp-content/uploads/2021/06/Combustion-engine-phase-out-briefing-may11.2020.pdf

[4] UNFCCC, "The Paris Agreement," Dec. 2015. Available: https://unfccc.int/sites/default/files/resource/parisagreement_publication.pdf.

[5] M. Ewing, "Zero Emissions Vehicles At Scale: Steps To Replace Fossil Fuel Vehicles With Battery-Electric, Part 2," Forbes. https://www.forbes.com/sites/markewing/2022/01/08/zero-emissions-vehicles-at-scale-steps-to-replace-fossil-fuel-vehicles-with-battery-electric-part-2/

[6] N. R. Canada, "The Hydrogen Strategy," natural-resources.canada.ca, Oct. 20, 2020. https://natural-resources.canada.ca/climate-change/canadas-green-future/the-hydrogen-strategy/23080.

[7] "Enabling factors for alternatively powered cars and vans in the European Union Making The Transition To Zero-Emission Mobility." Available: https://www.acea.auto/files/ACEA_progress_report_2021.pdf

[8] "Press corner," European Commission - European Commission, Jul. 20, 2016. https://ec.europa.eu/commission/presscorner/detail/en/MEMO_16_2497.

[9] "State of the States: Fuel Cells in America 2017," Energy.gov, 2017. https://www.energy.gov/eere/fuelcells/articles/state-states-fuel-cells-america-2017 (accessed Oct. 13, 2024).

[10] A. Brooker *et al.*, “Vehicle Technologies and Hydrogen and Fuel Cell Technologies Research and Development Programs Benefits Assessment Report for 2020,” 2021. [Online]. Available: www.nrel.gov/publications.

[11] J. Zhao and X. Li, “A review of polymer electrolyte membrane fuel cell durability for vehicular applications: Degradation modes and experimental techniques,” *Energy Convers Manag*, vol. 199, no. September 2019, p. 112022, 2019, doi: 10.1016/j.enconman.2019.112022.

[12] Z. Zhao, T. Wang, M. Li, H. Wang, and Y. Wang, “Optimization of fuzzy control energy management strategy for fuel cell vehicle power system using a multi-islandgenetic algorithm,” *Energy Sci Eng*, vol. 9, no. 4, pp. 548–564, 2021, doi: 10.1002/ese3.835.

[13] H. Zhang, X. Li, X. Liu, and J. Yan, “Enhancing fuel cell durability for fuel cell plug-in hybrid electric vehicles through strategic power management,” *Appl Energy*, vol. 241, no. January, pp. 483–490, 2019, doi: 10.1016/j.apenergy.2019.02.040.

[14] Li, X. (2005). Principles of Fuel Cells (1st ed.). CRC Press. https://doi.org/10.1201/9780203942338

[15] J.-K. Park, Principles and Applications of Lithium Secondary Batteries. John Wiley & Sons, 2012. DOI:10.1002/9783527650408

[16] Slobodan Petrovic, Battery technology crash course: a concise introduction. Cham, Switzerland: Springer, 2021. https://doi.org/10.1007/978-3-030-57269-3

[17] X. Xue, J. Tang, A. Smirnova, R. England, and N. Sammes, “System level lumped-parameter dynamic modeling of PEM fuel cell,” *J Power Sources*, vol. 133, no. 2, pp. 188–204, 2004, doi: 10.1016/j.jpowsour.2003.12.064.

[18] A. Forrai, H. Funato, Y. Yanagita, and Y. Kato, “Fuel-cell parameter estimation and diagnostics,” *IEEE Transactions on Energy Conversion*, vol. 20, no. 3, pp. 668–675, 2005, doi: 10.1109/TEC.2005.845516.

[19] M. Rajabzadeh, S. M. T. Bathaee, and M. Aliakbar Golkar, “Dynamic modeling and nonlinear control of fuel cell vehicles with different hybrid power sources,” *Int J Hydrogen Energy*, vol. 41, no. 4, pp. 3185–3198, 2016, doi: 10.1016/j.ijhydene.2015.12.046.

[20] W. R. Grove, “ XLII. On a small voltaic battery of great energy; some observations on voltaic combinations and forms of arrangement; and on the inactivity of a copper positive electrode in nitro-sulphuric acid ,” *The London, Edinburgh, and Dublin Philosophical Magazine and Journal of Science*, vol. 15, no. 96, pp. 287–293, Oct. 1839, doi: 10.1080/14786443908649881.

[21] H. Wang, X.-Z. Yuan, and H. Li, PEM Fuel Cell Diagnostic Tools. CRC Press, 2011.

[22] C. Spiegel, “PEM Fuel Cell Modeling and Simulation Using Matlab,” *PEM Fuel Cell Modeling and Simulation Using Matlab*, pp. 1–14, 2008, doi: 10.1016/b978-012374259-9.50002-1.

[23] J. Zhao, “Catalyst Layers in Polymer Electrolyte Membrane Fuel Cells: Formation, Characterization and Performance,” 2019, [Online]. Available: https://uwspace.uwaterloo.ca/handle/10012/14425

[24] J. Wu *et al.*, “A review of PEM fuel cell durability: Degradation mechanisms and mitigation strategies,” Sep. 15, 2008. doi: 10.1016/j.jpowsour.2008.06.006.

[25] Y. Wang, K. S. Chen, J. Mishler, S. C. Cho, and X. C. Adroher, “A review of polymer electrolyte membrane fuel cells: Technology, applications, and needs on fundamental research,” 2011, *Elsevier Ltd*. doi: 10.1016/j.apenergy.2010.09.030.

[26] M. L. S. Carnevali, “Modelling and Control of PEM Fuel Cells,” no. Fuel Cell Control, p. 183, 2017, [Online]. Available: https://mat-web.upc.edu/people/carles.batlle/fitxers/thesis_MLSC.pdf

[27] J. T. Pukrushpan and Jay Tawee Pukrushpan, “Modeling and control of fuel cell systems and fuel processors,” 2003. [Online]. Available: http://www-personal.umich.edu/~annastef/FuelCellPdf/pukrushpan_thesis.pdf

[28] T. Sasaki, Y. Ukyo, and P. Novák, “Memory effect in a lithium-ion battery,” *Nat Mater*, vol. 12, no. 6, pp. 569–575, 2013, doi: 10.1038/nmat3623.

[29] David. Linden and T. B. Reddy, *Handbook of batteries*. McGraw-Hill, 2002.

[30] S. Sepasi, “Adaptive state of charge estimation for battery packs”, doi: 10.13140/RG.2.1.4737.5209.

[31] G. Gauthier, “Experimental and modeling investigation of thermal behaviour and performance of lithium ion prismatic cells at cold-start temperatures,” 2017.

[32] J. van Amerongen and P. Breedveld, “Modelling of physical systems for the design and control of mechatronic systems,” *Annu Rev Control*, vol. 27 I, no. 1, pp. 87–117, 2003, doi: 10.1016/S1367-5788(03)00010-5.

[33] F. Segura and J. M. Andújar, “Step by step development of a real fuel cell system. Design, implementation, control and monitoring,” *Int J Hydrogen Energy*, vol. 40, no. 15, pp. 5496–5508, 2015, doi: 10.1016/j.ijhydene.2015.01.178.

[34] K. Belmokhtar, M. Hammoudi, M. L. Doumbia, and K. Agbossou, “Modelling and fuel flow dynamic control of proton exchange membrane fuel cell,” *International Conference on Power Engineering, Energy and Electrical Drives*, no. May, pp. 415–420, 2013, doi: 10.1109/PowerEng.2013.6635643.

[35] S. C. Page, A. H. Anbuky, S. P. Krumdieck, and J. Brouwer, “Test method and equivalent circuit modeling of a PEM fuel cell in a passive state,” *IEEE Transactions on Energy Conversion*, vol. 22, no. 3, pp. 764–773, 2007, doi: 10.1109/TEC.2007.895857.

[36] T. Lan and K. Strunz, “Modeling of multi-physics transients in PEM fuel cells using equivalent circuits for consistent representation of electric, pneumatic, and thermal quantities,” *International Journal of Electrical Power and Energy Systems*, vol. 119, no. December 2019, p. 105803, 2020, doi: 10.1016/j.ijepes.2019.105803.

[37] B. J. T. Pukrushpan, A. G. Stefanopoulou, and H. Peng, “Avoid fuel cell oxygen starvation with air flow controllers.,” *IEEE Control Systems Magazine*, no. April, pp. 30–46, 2004.

[38] C. Bao, M. Ouyang, and B. Yi, “Modeling and control of air stream and hydrogen flow with recirculation in a PEM fuel cell system-I. Control-oriented modeling,” *Int J Hydrogen Energy*, vol. 31, no. 13, pp. 1879–1896, 2006, doi: 10.1016/j.ijhydene.2006.02.031.

[39] W. R. W. Daud, R. E. Rosli, E. H. Majlan, S. A. A. Hamid, R. Mohamed, and T. Husaini, “PEM fuel cell system control: A review,” *Renew Energy*, vol. 113, pp. 620–638, 2017, doi: 10.1016/j.renene.2017.06.027.

[40] N. Zamel and X. Li, “Effective transport properties for polymer electrolyte membrane fuel cells - With a focus on the gas diffusion layer,” *Prog Energy Combust Sci*, vol. 39, no. 1, pp. 111–146, 2013, doi: 10.1016/j.pecs.2012.07.002.

[41] A. Abbaspour, A. Khalilnejad, and Z. Chen, “Robust adaptive neural network control for PEM fuel cell,” *Int J Hydrogen Energy*, vol. 41, no. 44, pp. 20385–20395, 2016, doi: 10.1016/j.ijhydene.2016.09.075.

[42] J. Jia, J. Liang, Y. Shi, J. Wen, X. Pang, and J. Zeng, “SOH and RUL prediction of lithium-ion batteries based on Gaussian process regression with indirect health indicators,” *Energies (Basel)*, vol. 13, no. 2, 2020, doi: 10.3390/en13020375.

[43] B. Wang, B. Xie, J. Xuan, and K. Jiao, “AI-based optimization of PEM fuel cell catalyst layers for maximum power density via data-driven surrogate modeling,” *Energy Convers Manag*, vol. 205, no. January, 2020, doi: 10.1016/j.enconman.2019.112460.

[44] K. Sun, I. Esnaola, O. Okorie, F. Charnley, M. Moreno, and A. Tiwari, “Data-driven modeling and monitoring of fuel cell performance,” *Int J Hydrogen Energy*, vol. 46, no. 66, pp. 33206–33217, 2021, doi: 10.1016/j.ijhydene.2021.05.210.

[45] A. Legala, J. Zhao, and X. Li, “Machine learning modeling for proton exchange membrane fuel cell performance,” *Energy and AI*, vol. 10, p. 100183, Nov. 2022, doi: 10.1016/j.egyai.2022.100183.

[46] W Melek, ME780: Computational Intelligence, lecture notes, University of Waterloo, 2018.

[47] B. Chen, “7 popular activation functions you should know in Deep Learning and how to use them with Keras and…,” Medium, Jan. 04, 2021. https://towardsdatascience.com/7-popular-activation-functions-you-should-know-in-deep-learning-and-how-to-use-them-with-keras-and-27b4d838dfe6

[48] Andriy Burkov, The Hundred-Page Machine Learning Book. 2019.

[49] R. Chanklan, N. Kaoungku, K. Suksut, K. Kerdprasop, and N. Kerdprasop, “Runoff prediction with a combined artificial neural network and support vector regression,” *Int J Mach Learn Comput*, vol. 8, no. 1, pp. 39–43, Feb. 2018, doi: 10.18178/ijmlc.2018.8.1.660.

[50] Y. Wang, B. Seo, B. Wang, N. Zamel, K. Jiao, and X. C. Adroher, “Fundamentals, materials, and machine learning of polymer electrolyte membrane fuel cell technology,” *Energy and AI*, vol. 1, p. 100014, 2020, doi: 10.1016/j.egyai.2020.100014.

[51] A. Kheirandish, N. Shafiabady, M. Dahari, M. S. Kazemi, and D. Isa, “Modeling of commercial proton exchange membrane fuel cell using support vector machine,” *Int J Hydrogen Energy*, vol. 41, no. 26, pp. 11351–11358, 2016, doi: 10.1016/j.ijhydene.2016.04.043.

[52] M. Mehrpooya, B. Ghorbani, B. Jafari, M. Aghbashlo, and M. Pouriman, “Modeling of a single cell micro proton exchange membrane fuel cell by a new hybrid neural network method,” *Thermal Science and Engineering Progress*, vol. 7, no. October 2017, pp. 8–19, 2018, doi: 10.1016/j.tsep.2018.04.012.

[53] I. S. Han and C. B. Chung, “A hybrid model combining a support vector machine with an empirical equation for predicting polarization curves of PEM fuel cells,” *Int J Hydrogen Energy*, vol. 42, no. 10, pp. 7023–7028, 2017, doi: 10.1016/j.ijhydene.2017.01.131.

[54] I. S. Han and C. B. Chung, “Performance prediction and analysis of a PEM fuel cell operating on pure oxygen using data-driven models: A comparison of artificial neural network and support vector machine,” *Int J Hydrogen Energy*, vol. 41, no. 24, pp. 10202–10211, 2016, doi: 10.1016/j.ijhydene.2016.04.247.

[55] Z. Deng, Q. Chen, L. Zhang, Y. Zong, K. Zhou, and Z. Fu, “Control oriented data driven linear parameter varying model for proton exchange membrane fuel cell systems,” *Appl Energy*, vol. 277, no. July, 2020, doi: 10.1016/j.apenergy.2020.115540.

[56] N. Khajeh-Hosseini-Dalasm, S. Ahadian, K. Fushinobu, K. Okazaki, and Y. Kawazoe, “Prediction and analysis of the cathode catalyst layer performance of proton exchange membrane fuel cells using artificial neural network and statistical methods,” *J Power Sources*, vol. 196, no. 8, pp. 3750–3756, 2011, doi: 10.1016/j.jpowsour.2010.12.061.

[57] L. Mao and L. Jackson, “Comparative study on prediction of fuel cell performance using machine learning approaches,” *Lecture Notes in Engineering and Computer Science*, vol. 1, pp. 52–57, 2016.

[58] M. Wang, W. Hu, Y. Jiang, F. Su, and Z. Fang, “Internal temperature prediction of ternary polymer lithium-ion battery pack based on CNN and virtual thermal sensor technology,” *Int J Energy Res*, vol. 45, no. 9, pp. 13681–13691, Jul. 2021, doi: 10.1002/er.6699.

[59] S. Arora, W. Shen, and A. Kapoor, “Neural network based computational model for estimation of heat generation in LiFePO4 pouch cells of different nominal capacities,” *Comput Chem Eng*, vol. 101, pp. 81–94, 2017, doi: 10.1016/j.compchemeng.2017.02.044.

[60] X. Qian, D. Xuan, X. Zhao, and Z. Shi, “Heat dissipation optimization of lithium-ion battery pack based on neural networks,” *Appl Therm Eng*, vol. 162, Nov. 2019, doi: 10.1016/j.applthermaleng.2019.114289.

[61] W. He, N. Williard, C. Chen, and M. Pecht, “State of charge estimation for Li-ion batteries using neural network modeling and unscented Kalman filter-based error cancellation,” *International Journal of Electrical Power and Energy Systems*, vol. 62, pp. 783–791, 2014, doi: 10.1016/j.ijepes.2014.04.059.

[62] Z. Chen, S. Qiu, M. A. Masrur, and Y. L. Murphey, “Battery state of charge estimation based on a combined model of extended kalman filter and neural networks,” in *Proceedings of the International Joint Conference on Neural Networks*, 2011, pp. 2156–2163. doi: 10.1109/IJCNN.2011.6033495.

[63] V. Q. Dao *et al.*, “Design of an effective state of charge estimation method for a lithium-ion battery pack using extended kalman filter and artificial neural network,” *Energies (Basel)*, vol. 14, no. 9, May 2021, doi: 10.3390/en14092634.

[64] H. Tao, S. Hua, K. Wu, S. Wu, Q. Liu, and K. Jiao, “Two-Dimensional simulation of purge processes for dead-ended H2/O2 proton exchange membrane fuel cell,” *Int J Green Energy*, 2022, doi: 10.1080/15435075.2022.2040508.

[65] X. G. Yang, Y. Wang, and C. Y. Wang, “Ultra-high fuel utilization in polymer electrolyte fuel cells part I: An experimental study,” *Int J Green Energy*, vol. 19, no. 2, pp. 159–165, 2022, doi: 10.1080/15435075.2021.1941041.

[66] M. Pan, P. Hu, R. Gao, and K. Liang, “Multistep prediction of remaining useful life of proton exchange membrane fuel cell based on temporal convolutional network,” *Int J Green Energy*, pp. 1–15, Mar. 2022, doi: 10.1080/15435075.2022.2050377.

[67] C. le Quéré *et al.*, “Temporary reduction in daily global CO2 emissions during the COVID-19 forced confinement,” *Nat Clim Chang*, vol. 10, no. 7, pp. 647–653, Jul. 2020, doi: 10.1038/s41558-020-0797-x.

[68] C. C. Yañez, F. M. Hopkins, X. Xu, J. F. Tavares, A. Welch, and C. I. Czimczik, “Reductions in California’s Urban Fossil Fuel CO2 Emissions During the COVID-19 Pandemic,” *AGU Advances*, vol. 3, no. 6, Dec. 2022, doi: 10.1029/2022AV000732.

[69] Unfccc, “ADOPTION OF THE PARIS AGREEMENT - Paris Agreement text English.” Accessed: May 14, 2022. [Online]. Available: https://unfccc.int/sites/default/files/english_paris_agreement.pdf

[70] R. Lempert et al., “CLIMATE INNOVATION,” 2019. Available: https://www.ourenergypolicy.org/wp-content/uploads/2019/05/pathways-to-2050-scenarios-for-decarbonizing-the-us-economy-final.pdf.

[71] N. Sazali, W. N. W. Salleh, A. S. Jamaludin, and M. N. M. Razali, “New perspectives on fuel cell technology: A brief review,” May 01, 2020, *MDPI AG*. doi: 10.3390/membranes10050099.

[72] L. Vichard, N. Y. Steiner, N. Zerhouni, and D. Hissel, “Hybrid fuel cell system degradation modeling methods: A comprehensive review,” Sep. 15, 2021, *Elsevier B.V.* doi: 10.1016/j.jpowsour.2021.230071.

[73] T. Jahnke *et al.*, “Performance and degradation of Proton Exchange Membrane Fuel Cells: State of the art in modeling from atomistic to system scale,” Feb. 01, 2016, *Elsevier*. doi: 10.1016/j.jpowsour.2015.11.041.

[74] M. Whiteley, S. Dunnett, and L. Jackson, “Failure Mode and Effect Analysis, and Fault Tree Analysis of Polymer Electrolyte Membrane Fuel Cells,” *Int J Hydrogen Energy*, vol. 41, no. 2, pp. 1187–1202, Jan. 2016, doi: 10.1016/j.ijhydene.2015.11.007.

[75] G. H. Mousa, “Fuel Cell Diagnostics using Electrochemical Impedance Spectroscopy,” Summit.sfu.ca, Sep. 02, 2014. https://summit.sfu.ca/item/14545

[76] R. Petrone *et al.*, “A review on model-based diagnosis methodologies for PEMFCs,” Jun. 10, 2013. doi: 10.1016/j.ijhydene.2013.03.106.

[77] S. Asghari, A. Mokmeli, and M. Samavati, “Study of PEM fuel cell performance by electrochemical impedance spectroscopy,” in *International Journal of Hydrogen Energy*, Sep. 2010, pp. 9283–9290. doi: 10.1016/j.ijhydene.2010.03.069.

[78] A. A. S. Lazarou, K. Karavotas, E. Pyrgioti, “PEM Fuel Cell Equivalent Circuit Models, A Review,” *Power and Energy Systems (EuroPES 2008),* no. July, pp. 22–26, 2008.

[79] Zhang, Xian & Pisu, Pierluigi. (2012). An Unscented Kalman Filter Based Approach for the HealthMonitoring and Prognostics of a Polymer Electrolyte Membrane Fuel Cel. Proceedings of the Annual Conference of the Prognostics and Health Management Society 2012, PHM 2012. 4. 353-361. 10.36001/phmconf.2012.v4i1.2167.

[80] J. Zhao, X. Li, C. Shum, and J. McPhee, “A Review of physics-based and data-driven models for real-time control of polymer electrolyte membrane fuel cells,” *Energy and AI,* vol. 6, p. 100114, 2021, doi: 10.1016/j.egyai.2021.100114.

[81] L. Mao and L. Jackson, “Comparative study on prediction of fuel cell performance using machine learning approaches”. Loughborough University, 18-Mar-2016..

[82] R. Petrone *et al.*, “A review on model-based diagnosis methodologies for PEMFCs,” Jun. 10, 2013. doi: 10.1016/j.ijhydene.2013.03.106.

[83] T. J. Chang, S. J. Cheng, C. H. Hsu, J. M. Miao, and S. F. Chen, “Prognostics for remaining useful life estimation in proton exchange membrane fuel cell by dynamic recurrent neural networks,” *Energy Reports*, vol. 8, pp. 9441–9452, Nov. 2022, doi: 10.1016/j.egyr.2022.07.032.

[84] B. Zuo, J. Cheng, and Z. Zhang, “Degradation prediction model for proton exchange membrane fuel cells based on long short-term memory neural network and Savitzky-Golay filter,” *Int J Hydrogen Energy*, vol. 46, no. 29, pp. 15928–15937, Apr. 2021, doi: 10.1016/j.ijhydene.2021.02.069.

[85] R. Ma, T. Yang, E. Breaz, Z. Li, P. Briois, and F. Gao, “Data-driven proton exchange membrane fuel cell degradation predication through deep learning method,” *Appl Energy*, vol. 231, pp. 102–115, Dec. 2018, doi: 10.1016/j.apenergy.2018.09.111.

[86] R. E. Silva *et al.*, “Proton exchange membrane fuel cell degradation prediction based on Adaptive Neuro-Fuzzy Inference Systems,” *Int J Hydrogen Energy*, vol. 39, no. 21, pp. 11128–11144, Jul. 2014, doi: 10.1016/J.IJHYDENE.2014.05.005.

[87] S. Morando, S. Jemei, D. Hissel, R. Gouriveau, and N. Zerhouni, “Proton exchange membrane fuel cell ageing forecasting algorithm based on Echo State Network,” *Int J Hydrogen Energy*, vol. 42, no. 2, pp. 1472–1480, Jan. 2017, doi: 10.1016/j.ijhydene.2016.05.286.

[88] L. Vichard, F. Harel, A. Ravey, P. Venet, and D. Hissel, “Degradation prediction of PEM fuel cell based on artificial intelligence,” *Int J Hydrogen Energy*, vol. 45, no. 29, pp. 14953–14963, May 2020, doi: 10.1016/j.ijhydene.2020.03.209.

[89] E. Pahon, D. Hissel, S. Jemei, and N. Y. Steiner, “Signal-based diagnostic approach to enhance fuel cell durability,” *J Power Sources*, vol. 506, Sep. 2021, doi: 10.1016/j.jpowsour.2021.230223.

[90] K. Chen, S. Laghrouche, and A. Djerdir, “Degradation prediction of proton exchange membrane fuel cell based on grey neural network model and particle swarm optimization,” *Energy Convers Manag*, vol. 195, pp. 810–818, Sep. 2019, doi: 10.1016/j.enconman.2019.05.045.

[91] J. Zhao, S. Shahgaldi, A. Ozden, I. E. Alaefour, X. Li, and F. Hamdullahpur, “Effect of catalyst deposition on electrode structure, mass transport and performance of polymer electrolyte membrane fuel cells,” *Appl Energy*, vol. 255, Dec. 2019, doi: 10.1016/j.apenergy.2019.113802.

[92] S. Shahgaldi, I. Alaefour, J. Zhao, and X. Li, “Impact of ionomer in the catalyst layers on proton exchange membrane fuel cell performance under different reactant flows and pressures,” *Fuel*, vol. 227, pp. 35–41, Sep. 2018, doi: 10.1016/j.fuel.2018.04.076.

[93] S. Shahgaldi, A. Ozden, X. Li, and F. Hamdullahpur, “A scaled-up proton exchange membrane fuel cell with enhanced performance and durability,” *Appl Energy*, vol. 268, Jun. 2020, doi: 10.1016/j.apenergy.2020.114956.

[94] “DOE CELL COMPONENT ACCELERATED STRESS TEST PROTOCOLS FOR PEM FUEL CELLS,” 2007. [Online]. Available: http://www1.eere.energy.gov/hydrogenandfuelcells/mypp/

[95] M. Dougherty, “A review of neural networks applied to transport,” Transportation Research Part C: Emerging Technologies, vol. 3, no. 4, pp. 247–260, Aug. 1995, doi: https://doi.org/10.1016/0968-090x(95)00009-8.

[96] J. J. Hopfield, “Artificial Neural Networks,” *IEEE Circuits and Devices Magazine*, vol. 4, no. 5, pp. 3–10, 1988, doi: 10.1109/101.8118.

[97] D. Hammerstrom, “Working with neural networks,” *IEEE Spectr*, vol. 30, no. 7, pp. 46–53, 1993, doi: 10.1109/6.222230.

[98] A. S. Eesa and W. Kh. Arabo, “A Normalization Methods for Backpropagation: A Comparative Study,” *Science Journal of University of Zakho*, vol. 5, no. 4, p. 319, Dec. 2017, doi: 10.25271/2017.5.4.381.

[99] T. Jayalakshmi and A. Santhakumaran, “Statistical Normalization and Back Propagationfor Classification,” *International Journal of Computer Theory and Engineering*, pp. 89–93, 2011, doi: 10.7763/ijcte.2011.v3.288.

[100] D. Kim, “Normalization methods for input and output vectors in Backpropagation neural networks,” *Int J Comput Math*, vol. 71, no. 1–2, pp. 161–171, 1999, doi: 10.1080/00207169908804800.

[101] G. Aksu, C. O. Güzeller, and M. T. Eser, “The Effect of the Normalization Method Used in Different Sample Sizes on the Success of Artificial Neural Network Model,” *International Journal of Assessment Tools in Education*, pp. 170–192, Apr. 2019, doi: 10.21449/ijate.479404.

[102] S. Technická univerzita (Košice, IEEE Hungary Section, M. IEEE Systems, and Institute of Electrical and Electronics Engineers, *SAMI 2020 : IEEE 18th World Symposium on Applied Machine Intelligence and Informatics : proceedings : January 23-25, 2020, Herl’any, Slovakia*.

[103] B. Ding, H. Qian, and J. Zhou, “Activation functions and their characteristics in deep neural networks,” in *Proceedings of the 30th Chinese Control and Decision Conference, CCDC 2018*, Institute of Electrical and Electronics Engineers Inc., Jul. 2018, pp. 1836–1841. doi: 10.1109/CCDC.2018.8407425.

[104] A. Apicella, F. Donnarumma, F. Isgrò, and R. Prevete, “A survey on modern trainable activation functions,” Jun. 01, 2021, *Elsevier Ltd*. doi: 10.1016/j.neunet.2021.01.026.

[105] T. Szandała, “Review and comparison of commonly used activation functions for deep neural networks,” in *Studies in Computational Intelligence*, vol. 903, Springer, 2021, pp. 203–224. doi: 10.1007/978-981-15-5495-7_11.

[106] M. H. Saleem, J. Potgieter, and K. M. Arif, “Plant disease classification: A comparative evaluation of convolutional neural networks and deep learning optimizers,” *Plants*, vol. 9, no. 10, pp. 1–17, Oct. 2020, doi: 10.3390/plants9101319.

[107] Vani, S. and Dr. T. V. Madhusudhana Rao. “An Experimental Approach towards the Performance Assessment of Various Optimizers on Convolutional Neural Network.” 2019 3rd International Conference on Trends in Electronics and Informatics (ICOEI) (2019): 331-336.

[108] S. K. Niranjan, K.L.S. Gogte Institute of Technology, Institute of Electrical and Electronics Engineers. Bangalore Section., and Institute of Electrical and Electronics Engineers, *Proceedings of the International Conference on Computational Techniques, Electronics and Mechanical Systems (CTEMS-2018) : 21 -23 December 2018, Belagavi, India*.

[109] Z. Runxuan, “Efficient Sequential and Batch Learning Artificial Neural Network Methods for Classification Problems,” 2005.

[110] J. Lin and D. X. Zhou, “Online Learning Algorithms Can Converge Comparably Fast as Batch Learning,” *IEEE Trans Neural Netw Learn Syst*, vol. 29, no. 6, pp. 2367–2378, Jun. 2018, doi: 10.1109/TNNLS.2017.2677970.

[111] S. Z. Qin, H. te Su, and T. J. McAvoy, “Comparison of Four Neural Net Learning Methods for Dynamic System Identification,” *IEEE Trans Neural Netw*, vol. 3, no. 1, pp. 122–130, 1992, doi: 10.1109/72.105425.

[112] F. M. Collette, C. Lorentz, G. Gebel, and F. Thominette, “Hygrothermal aging of Nafion®,” *J Memb Sci*, vol. 330, no. 1–2, pp. 21–29, Mar. 2009, doi: 10.1016/j.memsci.2008.11.048.

[113] K. Chen, “Heat Generation Measurements of Prismatic Lithium Ion Batteries.”

[114] K. Chen, G. Unsworth, and X. Li, “Measurements of heat generation in prismatic Li-ion batteries,” *J Power Sources*, vol. 261, pp. 28–37, 2014, doi: 10.1016/j.jpowsour.2014.03.037.

[115] U. Epa and C. Change Division, “Inventory of U.S. Greenhouse Gas Emissions and Sinks: 1990-2019 – Executive Summary,” 1990. [Online]. Available: http://unfccc.int

[116] David. Linden and T. B. Reddy, *Handbook of batteries*. McGraw-Hill, 2002.

[117] R. M. Spotnitz, J. Weaver, G. Yeduvaka, D. H. Doughty, and E. P. Roth, “Simulation of abuse tolerance of lithium-ion battery packs,” *J Power Sources*, vol. 163, no. 2, pp. 1080–1086, Jan. 2007, doi: 10.1016/j.jpowsour.2006.10.013.

[118] P. G. Balakrishnan, R. Ramesh, and T. Prem Kumar, “Safety mechanisms in lithium-ion batteries,” Apr. 21, 2006. doi: 10.1016/j.jpowsour.2005.12.002.

[119] B. K. Mandal, A. K. Padhi, Z. Shi, S. Chakraborty, and R. Filler, “Thermal runaway inhibitors for lithium battery electrolytes,” *J Power Sources*, vol. 161, no. 2, pp. 1341–1345, Oct. 2006, doi: 10.1016/j.jpowsour.2006.06.008.

[120] Q. Wang, P. Ping, X. Zhao, G. Chu, J. Sun, and C. Chen, “Thermal runaway caused fire and explosion of lithium ion battery,” Jun. 15, 2012. doi: 10.1016/j.jpowsour.2012.02.038.

[121] X. Feng, D. Ren, X. He, and M. Ouyang, “Mitigating Thermal Runaway of Lithium-Ion Batteries,” Apr. 15, 2020, *Cell Press*. doi: 10.1016/j.joule.2020.02.010.

[122] X. Feng *et al.*, “Thermal runaway features of large format prismatic lithium ion battery using extended volume accelerating rate calorimetry,” *J Power Sources*, vol. 255, pp. 294–301, Jun. 2014, doi: 10.1016/j.jpowsour.2014.01.005.

[123] W. Allafi *et al.*, “A lumped thermal model of lithium-ion battery cells considering radiative heat transfer,” 2018, doi: 10.1016/j.applthermaleng.2018.07.105.

[124] W. Zhang, W. Wan, W. Wu, Z. Zhang, and X. Qi, “Internal temperature prediction model of the cylindrical lithium-ion battery under different cooling modes,” *Appl Therm Eng*, vol. 212, p. 118562, Jul. 2022, doi: 10.1016/J.APPLTHERMALENG.2022.118562.

[125] Y. Xie *et al.*, “An improved resistance-based thermal model for a pouch lithium-ion battery considering heat generation of posts,” 2019, doi: 10.1016/j.applthermaleng.2019.114455.

[126] D. Kong, G. Wang, and J. Wen, “A coupled conjugate heat transfer and CFD model for the thermal runaway evolution and jet fire of 18650 lithium-ion battery under thermal abuse,” 2022, doi: 10.1016/j.etran.2022.100157.

[127] J. Tian, R. Xiong, W. Shen, J. Lu, and X. G. Yang, “Deep neural network battery charging curve prediction using 30 points collected in 10 min,” *Joule*, vol. 5, no. 6, pp. 1521–1534, Jun. 2021, doi: 10.1016/j.joule.2021.05.012.

[128] S. Jin, X. Sui, X. Huang, S. Wang, R. Teodorescu, and D. I. Stroe, “Overview of machine learning methods for lithium-ion battery remaining useful lifetime prediction,” *Electronics (Switzerland)*, vol. 10, no. 24, Dec. 2021, doi: 10.3390/electronics10243126.

[129] Y. Kato, Zempachi Ogumi, and M. Perlado, Lithium-Ion Batteries. CRC Press, 2019.

[130] K. Chen, “Heat Generation Measurements of Prismatic Lithium Ion Batteries,” pp. 1–98, 2013, [Online]. Available: https://uwspace.uwaterloo.ca/bitstream/handle/10012/7936/Chen_Kaiwei.pdf?sequence=1

[131] W. Waag and D. U. Sauer, “SECONDARY BATTERIES – LEAD– ACID SYSTEMS | State-of-Charge/Health,” Encyclopedia of Electrochemical Power Sources, pp. 793–804, 2009, doi: https://doi.org/10.1016/b978-044452745-5.00149-0.

[132] W.-Y. Chang, “The State of Charge Estimating Methods for Battery: A Review,” *ISRN Applied Mathematics*, vol. 2013, pp. 1–7, Jul. 2013, doi: 10.1155/2013/953792.

[133] J. Wang, B. Cao, Q. Chen, and F. Wang, “Combined state of charge estimator for electric vehicle battery pack,” *Control Eng Pract*, vol. 15, no. 12, pp. 1569–1576, Dec. 2007, doi: 10.1016/j.conengprac.2007.03.004.

[134] C. Jiang, A. Taylor, C. Duan, and K. Bai, “Extended Kalman Filter based battery state of charge(SOC) estimation for electric vehicles,” in *2013 IEEE Transportation Electrification Conference and Expo: Components, Systems, and Power Electronics - From Technology to Business and Public Policy, ITEC 2013*, 2013. doi: 10.1109/ITEC.2013.6573477.

[135] M. J. Kim and H. Peng, “Power management and design optimization of fuel cell/battery hybrid vehicles,” *J Power Sources*, vol. 165, no. 2, pp. 819–832, Mar. 2007, doi: 10.1016/j.jpowsour.2006.12.038.

[136] K. Wu, M. Milacic, A. Albousefi, M. Kuang, and J. Sun, “An optimization-oriented supervisory controller design for hybrid fuel cell electrified vehicles,” in *ASME 2018 Dynamic Systems and Control Conference, DSCC 2018*, American Society of Mechanical Engineers (ASME), 2018. doi: 10.1115/DSCC2018-8995.

[137] S. Panchal, I. Dincer, M. Agelin-Chaab, R. Fraser, and M. Fowler, “Experimental and theoretical investigation of temperature distributions in a prismatic lithium-ion battery,” *International Journal of Thermal Sciences*, vol. 99, pp. 204–212, Jan. 2016, doi: 10.1016/j.ijthermalsci.2015.08.016.

[138] S. Panchal, I. Dincer, M. Agelin-Chaab, R. Fraser, and M. Fowler, “Thermal modeling and validation of temperature distributions in a prismatic lithium-ion battery at different discharge rates and varying boundary conditions,” *Appl Therm Eng*, vol. 96, pp. 190–199, Mar. 2016, doi: 10.1016/j.applthermaleng.2015.11.019.

[139] R. Schneider and C. Georgakis, “How to NOT make the extended kalman filter fail,” *Ind Eng Chem Res*, vol. 52, no. 9, pp. 3354–3362, 2013, doi: 10.1021/ie300415d.

[140] F. Leach, G. Kalghatgi, R. Stone, and P. Miles, “The scope for improving the efficiency and environmental impact of internal combustion engines,” Jun. 01, 2020, *Elsevier Ltd*. doi: 10.1016/j.treng.2020.100005.

[141] R. D. Reitz *et al.*, “IJER editorial: The future of the internal combustion engine,” Jan. 01, 2020, *SAGE Publications Ltd*. doi: 10.1177/1468087419877990.

[142] I. A. Reşitoɨlu, K. Altinişik, and A. Keskin, “The pollutant emissions from diesel-engine vehicles and exhaust aftertreatment systems,” Jan. 04, 2015, *Springer Verlag*. doi: 10.1007/s10098-014-0793-9.

[143] D. R. Gentner *et al.*, “Review of Urban Secondary Organic Aerosol Formation from Gasoline and Diesel Motor Vehicle Emissions,” Feb. 07, 2017, *American Chemical Society*. doi: 10.1021/acs.est.6b04509.

[144] A. A. May *et al.*, “Gas- and particle-phase primary emissions from in-use, on-road gasoline and diesel vehicles,” *Atmos Environ*, vol. 88, pp. 247–260, 2014, doi: 10.1016/j.atmosenv.2014.01.046.

[145] A. Das, G. Singh, G. Habib, and A. Kumar, “Non-carcinogenic and Carcinogenic Risk Assessment of Trace Elements of PM2.5 During Winter and Pre-monsoon Seasons in Delhi: A Case Study,” *Expo Health*, vol. 12, no. 1, pp. 63–77, Mar. 2020, doi: 10.1007/s12403-018-0285-y.

[146] J. Xi and B. J. Zhong, “Soot in diesel combustion systems,” Jun. 2006. doi: 10.1002/ceat.200600016.

[147] C. A. Idicheria and L. M. Pickett, “Ignition, soot formation, and end-of-combustion transients in diesel combustion under high-EGR conditions,” *International Journal of Engine Research*, vol. 12, no. 4, pp. 376–392, Aug. 2011, doi: 10.1177/1468087411399505.

[148] V. A. Likhanov and O. P. Lopatin, “Dynamics of soot formation and burnout in a gas diesel cylinder,” in *IOP Conference Series: Materials Science and Engineering*, Institute of Physics Publishing, May 2020. doi: 10.1088/1757-899X/862/6/062033.

[149] M. K. Khair, “A Review of Diesel Particulate Filter Technologies.”

[150] M. P. Walsh, “Global Trends in Diesel Emissions Regulation-A 2001 Update Reprinted From: Diesel Exhaust Emissions Control: Developments in Regulation and Catalytic Systems (SP-1581),” 2001.

[151] A. A. Abdel-Rahman, “On the emissions from internal-combustion engines: A review,” *Int J Energy Res*, vol. 22, no. 6, pp. 483–513, 1998, doi: 10.1002/(SICI)1099-114X(199805)22:6<483::AID-ER377>3.0.CO;2-Z.

[152] B. Giechaskiel, A. Joshi, L. Ntziachristos, and P. Dilara, “European regulatory framework and particulate matter emissions of gasoline light-duty vehicles: A review,” Jul. 01, 2019, *MDPI*. doi: 10.3390/catal9070586.

[153] S. Gautam, A. Yadav, C. J. Tsai, and P. Kumar, “A review on recent progress in observations, sources, classification and regulations of PM2.5 in Asian environments,” *Environmental Science and Pollution Research*, vol. 23, no. 21, pp. 21165–21175, Nov. 2016, doi: 10.1007/s11356-016-7515-2.

[154] S. L. Winkler, J. E. Anderson, L. Garza, W. C. Ruona, R. Vogt, and T. J. Wallington, “Vehicle criteria pollutant (PM, NOx, CO, HCs) emissions: how low should we go?,” *NPJ Clim Atmos Sci*, vol. 1, no. 1, Dec. 2018, doi: 10.1038/s41612-018-0037-5.

[155] J. M. Seo, W. S. Park, and M. J. Lee, “The best choice of gasoline/diesel particulate filter to meet future particulate matter regulation,” in *SAE Technical Papers*, SAE International, 2012. doi: 10.4271/2012-01-1255.

[156] Y. Kurimoto *et al.*, “Next Generation Diesel Particulate Filter for Future Tighter HDV/NRMM Emission Regulations,” in *SAE Technical Papers*, SAE International, 2022. doi: 10.4271/2022-01-0545.

[157] B. A. A. L. Van Setten, M. Makkee, and J. A. Moulijn, “Science and technology of catalytic diesel particulate filters,” Nov. 2001. doi: 10.1081/CR-120001810.

[158] D. Fino, “Diesel emission control: Catalytic filters for particulate removal,” *Sci Technol Adv Mater*, vol. 8, no. 1–2, pp. 93–100, Jan. 2007, doi: 10.1016/j.stam.2006.11.012.

[159] J. Adler, “Ceramic diesel particulate filters,” 2005. doi: 10.1111/j.1744-7402.2005.02044.x.

[160] A. Legala, V. Premnath, M. Chadwell, P. Weber, and I. Khalek, “Impact of Selective Catalytic Reduction Process on Nonvolatile Particle Emissions,” in *SAE Technical Papers*, SAE International, 2021. doi: 10.4271/2021-01-0624.

[161] V. Di Sarli and A. Di Benedetto, “Combined effects of soot load and catalyst activity on the regeneration dynamics of catalytic diesel particulate filters,” *AIChE Journal*, vol. 64, no. 5, pp. 1714–1722, May 2018, doi: 10.1002/aic.16047.

[162] A. G. Konstandopoulos, M. Kostoglou, E. Skaperdas, E. Papaioannou, D. Zarvalis, and E. Kladopoulou, “Fundamental Studies of Diesel Particulate Filters: Transient Loading, Regeneration and Aging,” 2000.

[163] R. Feng, X. Hu, G. Li, Z. Sun, M. Ye, and B. Deng, “Exploration on the emissions and catalytic reactors interactions of a non-road diesel engine through experiment and system level simulation,” *Fuel*, vol. 342, Jun. 2023, doi: 10.1016/j.fuel.2023.127746.

[164] T. Boger, D. Rose, I.-C. Tilgner, and A. K. Heibel, “Regeneration Strategies for an Enhanced Thermal Management of Oxide Diesel Particulate Filters,” 2008.

[165] M. Bouchez and J. B. Dementhon, “Strategies for the Control of Particulate Trap Regeneration,” 2000.

[166] G. A. Merkel, W. A. Cutler, and C. J. Warren, “Thermal Durability of Wall-Flow Ceramic Diesel Particulate Filters,” 2001.

[167] K. Yang, J. T. Fox, and R. Hunsicker, “Characterizing Diesel Particulate Filter Failure During Commercial Fleet Use due to Pinholes, Melting, Cracking, and Fouling,” *Emission Control Science and Technology*, vol. 2, no. 3, pp. 145–155, Jul. 2016, doi: 10.1007/s40825-016-0036-0.

[168] I. J. Kim and L. G. Gauckler, “Formation, decomposition and thermal stability of Al2TiO 5 ceramics,” 2012. doi: 10.4416/JCST2011-00049.

[169] O. Haralampous and G. C. Koltsakis, “Intra-layer temperature gradients during regeneration of diesel particulate ÿlters,” 2002. [Online]. Available: www.elsevier.com/locate/ces

[170] R. H. Dabhoiwala, J. H. Johnson, and J. D. Naber, “Experimental Study Comparing Particle Size and Mass Concentration Data for a Cracked and Un-Cracked Diesel Particulate Filter,” 2009, [Online]. Available: http://www.sae.org

[171] Y. Deng *et al.*, “Investigations on the temperature distribution of the diesel particulate filter in the thermal regeneration process and its field synergy analysis,” *Appl Therm Eng*, vol. 123, pp. 92–102, 2017, doi: 10.1016/j.applthermaleng.2017.05.072.

[172] T. Kuki, Y. Miyairi, Y. Kasai, M. Miyazaki, and S. Miwa, “Study on Reliability of Wall-Flow Type Diesel Particulate Filter.”

[173] D. yuan Wang *et al.*, “Full course evolution characteristics of DPF active regeneration under different inlet HC concentrations,” *Fuel*, vol. 310, Feb. 2022, doi: 10.1016/j.fuel.2021.122452.

[174] V. Seiler, E. Boeckmann, and P. Eilts, “Performance of Undamaged and Damaged Diesel Particulate Filters,” 2008.

[175] T. Chittipotula, “Numerical Prediction of Particulate Matter (PM) Collection Efficiency, Loading, and Flow Characteristics in Partially Damaged Particulate Filters with Different PM

Size Classes," *Emission Control Science and Technology*, vol. 7, no. 4, pp. 302–320, Dec. 2021, doi: 10.1007/s40825-021-00195-1.

[176] R. H. Dabhoiwala, J. H. Johnson, J. D. Naber, and S. T. Bagley, "A Methodology to Estimate the Mass of Particulate Matter Retained in a Catalyzed Particulate Filter as Applied to Active Regeneration and On-Board Diagnostics to Detect Filter Failures," 2008.

[177] A. Sappok *et al.*, "On-Board Particulate Filter Failure Prevention and Failure Diagnostics Using Radio Frequency Sensing," *SAE Int J Engines*, vol. 10, no. 4, pp. 1667–1682, Mar. 2017, doi: 10.4271/2017-01-0950.

[178] E. J. Bissett, "MATHEMATICAL MODEL OF THE THERMAL REGENERATION OF A WALL-FLOW MONOLITH DIESEL PARTICULATE FILTER," 1984.

[179] H. Lee and C. J. Rutland, "Modeling uncontrolled regeneration of diesel particulate filters, taking into account hydrocarbon slip," *Proceedings of the Institution of Mechanical Engineers, Part D: Journal of Automobile Engineering*, vol. 227, no. 2, pp. 281–296, 2013, doi: 10.1177/0954407012450837.

[180] B. S. Mahadevan, J. H. Johnson, and M. Shahbakhti, "Development of a Catalyzed Diesel Particulate Filter Multi-zone Model for Simulation of Axial and Radial Substrate Temperature and Particulate Matter Distribution," *Emission Control Science and Technology*, vol. 1, no. 2, pp. 183–202, May 2015, doi: 10.1007/s40825-015-0015-x.

[181] V. Di Sarli and A. Di Benedetto, "Modeling and simulation of soot combustion dynamics in a catalytic diesel particulate filter," *Chem Eng Sci*, vol. 137, pp. 69–78, Dec. 2015, doi: 10.1016/j.ces.2015.06.011.

[182] A. Abdalla, G. Wang, J. Zhang, and S. J. Shuai, "Simulation of Catalyzed Diesel Particulate Filter for Active Regeneration Process Using Secondary Fuel Injection," in *SAE Technical Papers*, SAE International, 2017. doi: 10.4271/2017-01-2287.

[183] X. Zhao, J. E, G. Liao, F. Zhang, J. Chen, and Y. Deng, "Numerical simulation study on soot continuous regeneration combustion model of diesel particulate filter under exhaust gas heavy load," *Fuel*, vol. 290, Apr. 2021, doi: 10.1016/j.fuel.2020.119795.

[184] M. Farsodia, S. Pandey, and G. Ganguly, “Advance Data Analytics Methodologies to Solve Diesel Engine Exhaust Aftertreatment System Challenges,” in *SAE Technical Papers*, SAE International, Jan. 2019. doi: 10.4271/2019-01-5035.

[185] J. Wang, Y. Li, R. X. Gao, and F. Zhang, “Hybrid physics-based and data-driven models for smart manufacturing: Modelling, simulation, and explainability,” *J Manuf Syst*, vol. 63, pp. 381–391, Apr. 2022, doi: 10.1016/j.jmsy.2022.04.004.

[186] J. Lin, W. Lin, W. Lin, J. Wang, and H. Jiang, “Thermal prediction for Air-cooled data center using data Driven-based model,” *Appl Therm Eng*, vol. 217, Nov. 2022, doi: 10.1016/j.applthermaleng.2022.119207.

[187] O. Erge and E. van Oort, “Combining physics-based and data-driven modeling in well construction: Hybrid fluid dynamics modeling,” *J Nat Gas Sci Eng*, vol. 97, Jan. 2022, doi: 10.1016/j.jngse.2021.104348.

[188] H. Ban, Y. Zhang, and S. Feng, “A data-driven approach for real-time prediction of thermal gradient in engineered structures,” *Journal of Mechanical Science and Technology*, vol. 36, no. 3, pp. 1243–1249, Mar. 2022, doi: 10.1007/s12206-022-0215-6.

[189] G. E. Karniadakis, I. G. Kevrekidis, L. Lu, P. Perdikaris, S. Wang, and L. Yang, “Physics-informed machine learning,” Jun. 01, 2021, *Springer Nature*. doi: 10.1038/s42254-021-00314-5.

[190] D. An, N. H. Kim, and J. H. Choi, “Practical options for selecting data-driven or physics-based prognostics algorithms with reviews,” 2015, *Elsevier Ltd*. doi: 10.1016/j.ress.2014.09.014.

[191] D. Hammerstrom, “Working with neural networks,” *IEEE Spectr*, vol. 30, no. 7, pp. 46–53, 1993, doi: 10.1109/6.222230.

[192] J. J. Hopfield, “Artificial Neural Networks,” *IEEE Circuits and Devices Magazine*, vol. 4, no. 5, pp. 3–10, 1988, doi: 10.1109/101.8118.

[193] S.-H. Han, K. W. Kim, S. Kim, and Y. C. Youn, “Artificial Neural Network: Understanding the Basic Concepts without Mathematics,” *Dement Neurocogn Disord*, vol. 17, no. 3, p. 83, 2018, doi: 10.12779/dnd.2018.17.3.83.

[194] A. Canziani, A. Paszke, and E. Culurciello, “An Analysis of Deep Neural Network Models for Practical Applications,” May 2016, [Online]. Available: http://arxiv.org/abs/1605.07678

[195] G. Montavon, W. Samek, and K. R. Müller, “Methods for interpreting and understanding deep neural networks,” Feb. 01, 2018, *Elsevier Inc.* doi: 10.1016/j.dsp.2017.10.011.

[196] D. Kim, “Normalization methods for input and output vectors in Backpropagation neural networks,” *Int J Comput Math*, vol. 71, no. 1–2, pp. 161–171, 1999, doi: 10.1080/00207169908804800.

[197] T. Jayalakshmi and A. Santhakumaran, “Statistical Normalization and Back Propagationfor Classification,” *International Journal of Computer Theory and Engineering*, pp. 89–93, 2011, doi: 10.7763/ijcte.2011.v3.288.

[198] M. H. Saleem, J. Potgieter, and K. M. Arif, “Plant disease classification: A comparative evaluation of convolutional neural networks and deep learning optimizers,” *Plants*, vol. 9, no. 10, pp. 1–17, Oct. 2020, doi: 10.3390/plants9101319.

[199] Y. Shen, J. Wang, and S. Navlakha, “A correspondence between normalization strategies in artificial and biological neural networks,” *Neural Comput*, vol. 33, no. 12, pp. 3179–3203, Nov. 2021, doi: 10.1162/neco_a_01439.

[200] J. Sola and J. Sevilla, “Importance of Input Data Normalization for the Application of Neural Networks to Complex Industrial Problems,” 1997.

[201] A. Apicella, F. Donnarumma, F. Isgrò, and R. Prevete, “A survey on modern trainable activation functions,” Jun. 01, 2021, *Elsevier Ltd*. doi: 10.1016/j.neunet.2021.01.026.

[202] T. Szandała, “Review and comparison of commonly used activation functions for deep neural networks,” in *Studies in Computational Intelligence*, vol. 903, Springer, 2021, pp. 203–224. doi: 10.1007/978-981-15-5495-7_11.

[203] I. Energy Agency, “World Energy Outlook 2016,” 2040.

[204] R. Kumar *et al.*, “Transforming the transportation sector: Mitigating greenhouse gas emissions through electric vehicles (EVs) and exploring sustainable pathways,” *AIP Adv*, vol. 14, no. 3, Mar. 2024, doi: 10.1063/5.0193506.

[205] F. Liu, F. Zhao, Z. Liu, and H. Hao, “The impact of fuel cell vehicle deployment on road transport greenhouse gas emissions: The China case,” *Int J Hydrogen Energy*, vol. 43, no. 50, pp. 22604–22621, Dec. 2018, doi: 10.1016/j.ijhydene.2018.10.088.

[206] K. Bekel and S. Pauliuk, “Prospective cost and environmental impact assessment of battery and fuel cell electric vehicles in Germany,” *International Journal of Life Cycle Assessment*, vol. 24, no. 12, pp. 2220–2237, Dec. 2019, doi: 10.1007/s11367-019-01640-8.

[207] J. Li *et al.*, “Liquid pump-enabled hydrogen refueling system for heavy duty fuel cell vehicles: Fuel cell bus refueling demonstration at Stark Area Regional Transit Authority (SARTA),” *Int J Hydrogen Energy*, vol. 46, no. 78, pp. 38575–38587, Nov. 2021, doi: 10.1016/j.ijhydene.2021.09.112.

[208] A. Maity and S. Sarkar, “Data-driven probabilistic energy consumption estimation for battery electric vehicles with model uncertainty,” *Int J Green Energy*, 2023, doi: 10.1080/15435075.2023.2276174.

[209] Y. Sun, C. Xia, B. Yin, H. Gao, J. Han, and J. Liu, “Energy management strategy for FCEV considering degradation of fuel cell,” *Int J Green Energy*, vol. 20, no. 1, pp. 28–39, 2023, doi: 10.1080/15435075.2021.2023546.

[210] *Cost, effectiveness, and deployment of fuel economy technologies for light-duty vehicles*. National Academies Press, 2015. doi: 10.17226/21744.

[211] M. Gallo and M. Marinelli, “The Impact of Fuel Cell Electric Freight Vehicles on Fuel Consumption and CO2 Emissions: The Case of Italy,” *Sustainability (Switzerland)*, vol. 14, no. 20, Oct. 2022, doi: 10.3390/su142013455.

[212] T. Yoshizumi, H. Kubo, and M. Okumura, “Development of High-Performance FC Stack for the New MIRAI,” in *SAE Technical Papers*, SAE International, Apr. 2021. doi: 10.4271/2021-01-0740.

[213] T. Hasegawa, H. Imanishi, M. Nada, and Y. Ikogi, “Development of the Fuel Cell System in the Mirai FCV,” in *SAE Technical Papers*, SAE International, Apr. 2016. doi: 10.4271/2016-01-1185.

[214] L. Bartolucci *et al.*, “Fuel Cell Hybrid Electric Vehicles: Fuel Cell experimental characterization and modeling towards the development of a Hardware-in-the-Loop platform for advanced powertrain design,” in *Journal of Physics: Conference Series*, Institute of Physics, 2023. doi: 10.1088/1742-6596/2648/1/012063.

[215] J. H. Ryu, H. J. Lee, and M. H. Sunwoo, “An electric powertrain modelling of a fuel cell hybrid electric vehicle and development of a power distribution algorithm using h∞control,” in *Proceedings of the Institution of Mechanical Engineers, Part D: Journal of Automobile Engineering*, Professional Engineering Publishing, Aug. 2010, pp. 1021–1039. doi: 10.1243/09544070JAUTO1269.

[216] C. C. Chan, A. Bouscayrol, and K. Chen, “Electric, hybrid, and fuel-cell vehicles: Architectures and modeling,” *IEEE Trans Veh Technol*, vol. 59, no. 2, pp. 589–598, Feb. 2010, doi: 10.1109/TVT.2009.2033605.

[217] S. Hasegawa, Y. Ikogi, S. Kim, M. Kageyama, and M. Kawase, “Modeling of the dynamic behavior of an integrated fuel cell system including fuel cell stack, air system, hydrogen system, and cooling system,” *ECS Trans*, vol. 109, no. 9, pp. 15–70, Sep. 2022, doi: 10.1149/10909.0015ecst.

[218] C. Mizutani, M. Shiozawa, T. Maruo, and S. Aso, “On-Board Control System of Water Content inside FCV Stack by Electrochemical Impedance Spectroscopy,” *ECS Trans*, vol. 80, no. 8, pp. 357–365, Aug. 2017, doi: 10.1149/08008.0357ecst.

[219] A. A. Kulikovsky, “Analytical modeling of fuel cells,” 2019. doi: 10.1016/C2018-0-01182-2.

[220] A. Legala, S. Shahgaldi, and X. Li, “Data-based modelling of proton exchange membrane fuel cell performance and degradation dynamics,” *Energy Convers Manag*, vol. 296, p. 117668, Nov. 2023, doi: 10.1016/j.enconman.2023.117668.

[221] M. Carignano and R. Costa-Castelló, "Toyota Mirai: Powertrain Model and Assessment of the Energy Management," in IEEE Transactions on Vehicular Technology, vol. 72, no. 6, pp. 7000-7010, June 2023, doi: 10.1109/TVT.2023.3237173.

[222] V. KoteswaraRao.K and G. Naga Srinivasulu, “Modeling, downsizing, and performance comparison of a fuel cell hybrid mid-size car with FCEV for urban and hill road driving cycles,”

Int J Green Energy, vol. 16, no. 2, pp. 115–124, Jan. 2019, doi: 10.1080/15435075.2018.1549996.

[223] M. Meindl, R. Öchsner, J. Geiling and M. März, "Reverse engineering of the hydrogen system of a commercial fuel cell vehicle," 2023 IEEE 32nd International Symposium on Industrial Electronics (ISIE), Helsinki, Finland, 2023, pp. 1-6, doi: 10.1109/ISIE51358.2023.10227998.

[224] T. Maruo *et al.*, "Development of Fuel Cell System Control for Sub-Zero Ambient Conditions," in *SAE Technical Papers*, SAE International, Mar. 2017. doi: 10.4271/2017-01-1189.

[225] SAE International Recommended Practice, Chassis Dynamometer Simulation of Road Load Using Coastdown Techniques, SAE Standard J2264_202301, Revised January 2023, Issued April 1995, https://doi.org/10.4271/J2264_202301.

[226] SAE International Recommended Practice, Recommended Practice for Measuring Fuel Consumption and Range of Fuel Cell and Hybrid Fuel Cell Vehicles Fueled by Compressed Gaseous Hydrogen, SAE Standard J2572_201410, Revised October 2014, Issued August 2006, https://doi.org/10.4271/J2572_201410.

[227] "Dynamometer Drive Schedules | US EPA." US EPA, 17 May 2024, www.epa.gov/vehicle-and-fuel-emissions-testing/dynamometer-drive-schedules

[228] R. Caponetto, N. Guarnera, F. Matera, E. Privitera, and M. G. Xibilia, "Application of electrochemical impedance spectroscopy for prediction of fuel cell degradation by LSTM neural networks," in *2021 29th Mediterranean Conference on Control and Automation, MED 2021*, Institute of Electrical and Electronics Engineers Inc., Jun. 2021, pp. 1064–1069. doi: 10.1109/MED51440.2021.9480253.

[229] A. Legala, V. LakkiReddy, P. Weber, and X. Li, "Modeling of diesel particulate filter temperature dynamics during exotherm using neural networks," *Frontiers in Thermal Engineering*, vol. 3, Oct. 2023, doi: 10.3389/fther.2023.1265490.

[230] M. Jiao and D. Wang, "The Savitzky-Golay filter based bidirectional long short-term memory network for SOC estimation," *Int J Energy Res*, vol. 45, no. 13, pp. 19467–19480, Oct. 2021, doi: 10.1002/er.7055.

[231] W. He *et al.*, “A novel high-dimensional and multi-physics modeling approach of proton exchange membrane fuel cell for real-time simulation,” *Energy Convers Manag*, vol. 286, Jun. 2023, doi: 10.1016/j.enconman.2023.116988.

[232] D. Ritzberger, C. Hametner, and S. Jakubek, “A real-time dynamic fuel cell system simulation for model-based diagnostics and control: Validation on real driving data,” *Energies (Basel)*, vol. 13, no. 12, Jun. 2020, doi: 10.3390/en13123148.

Appendices

Appendix A

Numerical example:

Consider a network with input layer $(k-1)$ with two neurons, hidden layer (k) with two neurons and sigmoid activation and output layer $(k+1)$ with 1 neuron and sigmoid activation.

Numerical example:

Consider a network with input layer $(k-1)$ with two neurons, hidden layer (k) with two neurons and sigmoid activation and output layer $(k+1)$ with 1 neuron and sigmoid activation. Initially, the weights and biases for the neurons in the hidden and output layers are chosen at random.

Network Input:

$$\mathbf{a}^{(k-1)} = [0.6, 0.8]$$

Network desired value (Target): $y = 1.0$

For hidden layer (k):

$$W^{(k)} = \begin{bmatrix} 0.1 & -0.2 \\ 0.3 & 0.4 \end{bmatrix}$$

$$b^{(k)} = \begin{bmatrix} 0.05 \\ -0.05 \end{bmatrix}$$

For output layer $(k+1)$:

$$W^{(k+1)} = [0.5, -0.6]$$

$$b^{(k+1)} = 0.1.$$

Sigmoid function (σ) : $f(x) = \frac{1}{e^{-x}+1}$

Sigmoid function derivative (σ'): $f'(x) = \frac{e^{-x}}{(e^{-x}+1)^2}$

$$f'(x) = \frac{1}{e^{-x}+1}\left(1 - \frac{1}{e^{-x}+1}\right)$$

$$f'(x) = \sigma(1 - \sigma)$$

Forward Propagation:

Hidden Layer Pre-Activation $\left(z^{(k)}\right)$*:*

Compute the pre-activation for the hidden layer:

$$z^{(k)} = W^{(k)} \cdot a^{(k-1)} + b^{(k)}$$

$$z^{(k)} = \begin{bmatrix} 0.1 & -0.2 \\ 0.3 & 0.4 \end{bmatrix} \cdot \begin{bmatrix} 0.6 \\ 0.8 \end{bmatrix} + \begin{bmatrix} 0.05 \\ -0.05 \end{bmatrix}$$

Calculating the dot product:

$$\begin{bmatrix} (0.1)(0.6) + (-0.2)(0.8) \\ (0.3)(0.6) + (0.4)(0.8) \end{bmatrix} = \begin{bmatrix} 0.06 - 0.16 \\ 0.18 + 0.32 \end{bmatrix} = \begin{bmatrix} -0.1 \\ 0.5 \end{bmatrix}$$

Add biases:

$$z^{(k)} = \begin{bmatrix} -0.1 \\ 0.5 \end{bmatrix} + \begin{bmatrix} 0.05 \\ -0.05 \end{bmatrix} = \begin{bmatrix} -0.05 \\ 0.45 \end{bmatrix}$$

Hidden Layer Activation ($a^{(k)}$ *) :*

Apply the sigmoid activation function:

$$a^{(k)} = \sigma\left(z^{(k)}\right) = \frac{1}{1 + e^{-z^{(k)}}}$$

Compute for each element:

$$a_1^{(k)} = \frac{1}{1 + e^{0.05}} = 0.4875, a_2^{(k)} = \frac{1}{1 + e^{-0.45}} = 0.6106$$

Thus:

$$a^{(k)} = \begin{bmatrix} 0.4875 \\ 0.6106 \end{bmatrix}$$

Output Layer Pre-Activation $\left(z^{(k+1)}\right)$ *:*

Calculate the pre-activation output for the output layer:

$$z^{(k+1)} = W^{(k+1)} \cdot a^{(k)} + b^{(k+1)}$$

$$z^{(k+1)} = [0.5 \quad -0.6] \cdot \begin{bmatrix} 0.4875 \\ 0.6106 \end{bmatrix} + 0.1$$

Calculate the dot product:

$$z^{(k+1)} = (0.5)(0.4875) + (-0.6)(0.6106) + 0.1$$

$$z^{(k+1)} = 0.2438 - 0.3664 + 0.1 = -0.0226$$

Output Layer Activation ($a^{(k+1)}$ *):*

Apply the sigmoid activation:

$$a^{(k+1)} = \sigma\left(z^{(k+1)}\right) = \frac{1}{1 + e^{-z^{(k+1)}}}$$

$$a^{(k+1)} = \frac{1}{1 + e^{0.0226}} \approx 0.4943$$

The predicted output is:

$$\hat{y} = 0.4943$$

Error Calculation:

The error is calculated using squared error loss:

$$E = \frac{1}{2}(y - \hat{y})^2$$

$$E = \frac{1}{2}(1.0 - 0.4943)^2 \approx \frac{1}{2}(0.5057)^2 \approx 0.1278$$

Error Signal calculation for output layer ($\delta^{(k+1)}$) :

$$\delta^{(k+1)} = \left(a^{(k+1)} - y\right) \cdot \sigma'\left(z^{(k+1)}\right)$$

The derivative of sigmoid:

$$\sigma'\left(z^{(k+1)}\right) = a^{(k+1)}\left(1 - a^{(k+1)}\right)$$

$$\sigma'\left(z^{(k+1)}\right) = 0.4943(1 - 0.4943) = 0.24997$$

Calculating the output layer error signal ($\delta^{(k+1)}$) :

$$\delta^{(k+1)} = (0.4943 - 1.0) \cdot 0.24997 = -0.1264$$

Hidden Layer Error Signal ($\delta^{(k)}$):

$$\delta^{(k)} = \sigma'\left(z^{(k)}\right) \cdot \left(W^{(k+1)}\right)^T \delta^{(k+1)}$$

Calculate $\sigma'\left(z^{(k)}\right)$:

$$\sigma'\left(z^{(k)}\right) = a^{(k)} \cdot \left(1 - a^{(k)}\right)$$

$$\sigma'\left(z^{(k)}\right) = \begin{bmatrix} 0.4875(1 - 0.4875) \\ 0.6106(1 - 0.6106) \end{bmatrix} = \begin{bmatrix} 0.24985 \\ 0.23776 \end{bmatrix}$$

Calculate $\left(W^{(k+1)}\right)^T \delta^{(k+1)}$;

$$\left(W^{(k+1)}\right)^T \delta^{(k+1)} = \begin{bmatrix} 0.5 \\ -0.6 \end{bmatrix} \cdot (-0.1264) = \begin{bmatrix} -0.0632 \\ 0.0758 \end{bmatrix}$$

Calculate dot product:

$$\delta^{(k)} = \begin{bmatrix} 0.24985 \\ 0.23776 \end{bmatrix} \cdot \begin{bmatrix} -0.0632 \\ 0.0758 \end{bmatrix} = \begin{bmatrix} -0.0158 \\ 0.0180 \end{bmatrix}$$

Determine new weight $\boldsymbol{W}^{(k+1)}$:

$$W^{(k+1)} = W^{(k+1)} - \eta \frac{\partial E}{\partial W^{(k+1)}}$$

$$\eta \frac{\partial E}{\partial W^{(k+1)}} = \eta \delta^{(k+1)} \cdot \left(a^{(k)}\right)^T$$

For $\eta = 0.1$:

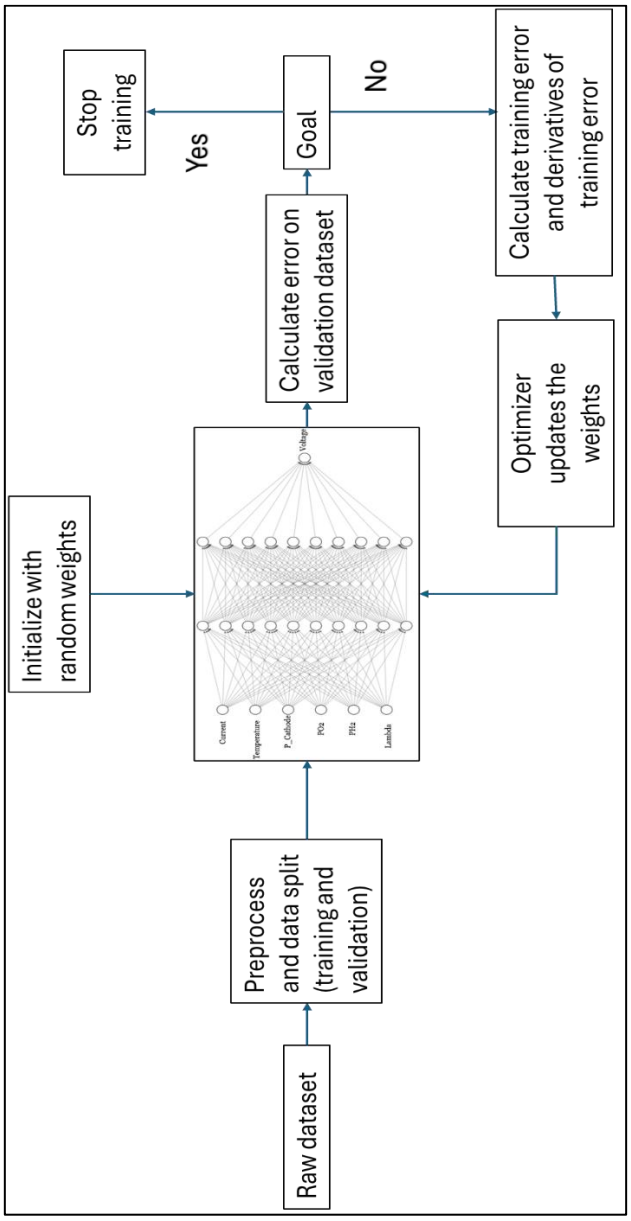
$$\eta \frac{\partial E}{\partial W^{(k+1)}} = 0.1 \cdot (-0.1264) \cdot [0.4875 \quad 0.6106] = [-0.0062 \quad -0.0077]$$

Updated weights:

$$W^{(k+1)} = [0.5 - 0.6] - [-0.0062 - 0.0077]$$

$$W^{(k+1)} = [0.4938 \quad -0.6077]$$

Flow chart: Working of a shallow neural network:



Optimizers for neural networks

1. SGD (Stochastic Gradient Descent)

The weight update rule for SGD is:

$$W = W - \eta \cdot \nabla J(W)$$

Where:

- W is the weight vector.
- η is the learning rate.
- $\nabla J(W)$ is the gradient of the loss function $J(W)$ with respect to the weights.

Momentum: To accelerate convergence, Momentum adds a fraction of the previous update to the current update:

$$v_t = \beta v_{t-1} + (1 - \beta)\nabla J(W)$$

$$W = W - \eta v_t$$

Where:

- β is the momentum factor (typically 0.9).
- v_t is the velocity (momentum term).

Preferable for small or moderate-size datasets requiring a simple, classical optimization technique, the Momentum can also help accelerate convergence.It is preferable for deep networks or when the loss landscape is complex with lots of local minima.

2. RMSprop (Root Mean Squared Propagation)

RMSprop adjusts the learning rate based on the recent magnitudes of the gradients for each weight, where it divides the learning rate by the moving average of the recent squared gradients:

$$v_t = \beta v_{t-1} + (1-\beta)\nabla J(W)^2$$

$$W = W - \frac{\eta}{\sqrt{v_t + \epsilon}}\nabla J(W)$$

Where:

- v_t is the moving average of squared gradients.
- η is the learning rate.
- β is the decay factor (usually 0.9 or 0.99).
- ϵ is a small constant (e.g., 10^{-8}).

RMSprop is suitable for maintaining stability in the optimization process when the dataset has noisy gradients and works well for recurrent neural networks (RNNs) with high variance in the gradients (e.g., time-series analysis).

3. *Adam (Adaptive Moment Estimation)*

Adam combines the benefits of RMSProp and Momentum as it adjusts the learning rate for each parameter based on the gradients' first moment (mean) and second moment (variance).

1. First Moment (mean of gradients):

$$m_t = \beta_1 m_{t-1} + (1-\beta_1)\nabla J(W)$$

2. Second Moment (variance of gradients):

$$v_t = \beta_2 v_{t-1} + (1-\beta_2)\nabla J(W)^2$$

3. Bias Correction:

$$\hat{m}_t = \frac{m_t}{1-\beta_1^t}, \hat{v}_t = \frac{v_t}{1-\beta_2^t}$$

4. Weight Update:

$$W = W - \eta \frac{\hat{m}_t}{\sqrt{\hat{v}_t} + \epsilon}$$

Where:

- η is the learning rate.
- ϵ is a small constant (e.g., 10^{-8}) to prevent division by zero.
- β_1 and β_2 are the decay rates for the first and second moment estimates (typically 0.9 and 0.999).

When the dataset is significant, Adam is recommended to avoid manually tuning the learning rate, which is very efficient and generally requires less hyperparameter tuning, especially for deep networks, complex loss landscapes, and tasks like NLP, computer vision, and reinforcement learning.

Appendix B

Physics-based semi-empirical PEMFC equations were used to generate Dataset1:

1. $v_{fc} = E - v_{act} - v_{ohm} - v_{conc}$ $(B1.1)$

2. $E = 1.229 - 0.85 \times 10^{-3}(T_{fc} - 298.15) + 4.3085 \times 10^{-5} T_{fc}\left[\ln\left(p_{H_2}\right) + \frac{1}{2}\ln\left(p_{O_2}\right)\right]$ $(B1.2)$

3. $v_{ohm} = i \cdot R_{ohm};\quad v_{act} = v_0 + v_a(1 - e^{-c_1 i});\ v_{conc} = i\left(c_2 \frac{i}{i_{max}}\right)^{c_3}$ $(B1.3)$

4. $v_0 = 0.279 - 8.5 \times 10^{-4}(T_{fc} - 298.15) + 4.308 \times 10^{-5} T_{fc}\left[\ln\left(\frac{p_{ca} - p_{sat}}{1.01325}\right) + \frac{1}{2}\ln\left(\frac{0.1173(p_{ca} - p_{sat})}{1.01325}\right)\right]$ $(B1.4)$

5. $v_a = \left(-1.618 \times 10^{-5} T_{fc} + 1.618 \times 10^{-2}\right)\left(\frac{p_{O_2}}{0.1173} + p_{sat}\right)^2 + \left(1.8 \times 10^{-4} T_{fc} - 0.166\right)\left(\frac{p_{O_2}}{0.1173} + p_{sat}\right) + \left(-5.8 \times 10^{-4} T_{fc} + 0.5736\right)$ $(B1.5)$

6. $$\begin{aligned} v_{fc} &= E - v_{act} - v_{ohm} - v_{conc} \\ &= E - \left[v_0 + v_a(1 - e^{-c_1 i})\right] - [iR_{ohm}] - \left[i\left(c_2 \frac{i}{i_{\max}}\right)^{c3}\right] \end{aligned}$$ $(B1.6)$

where v_{fc} is the final fuel cell output voltage, E is the fuel cell, v_{act}, v_{ohm} , v_{conc} refers to the fuel cell activation overpotential, ohmic overpotential, and concentration overpotential, respectively. i is the fuel cell output current, R_{ohm} is the membrane ohmic resistance, T_{fc} is the temperature of the fuel cell, $p_{H_2}, p_{O_2},$ and p_{sat} represents the partial pressures of water vapor's hydrogen, oxygen, and saturation pressure. $c_1, c_2,$ and c_3 are the empirical coefficients. Further, the equations given above are described below:

1. The net output of the fuel cell or terminal voltage is defined as the sum of reversible voltage, activation overpotential, ohmic overpotential, and concentration overpotential potentials;

2. Reversible voltage E is calculated by using the Nerst equation, adapting the thermodynamic values of the standard entropy change;

3. All the relevant overpotentials are defined by correlating operational current, resistance, and empirical constants which are determined by regressions based on the experimental data;

4 and 5. v_0 and v_a are dependent on the partial pressure of oxygen (slow cathode ORR rate), cathode operating pressure, saturation pressure, and fuel cell temperature. Saturation pressure is determined as a function of temperature

6. Equation B1.6 is achieved by substituting equations B1.2, B1.3,B1.4, B1.5, into B1.1

Dataset 1 (physics-based semi-empirical data):

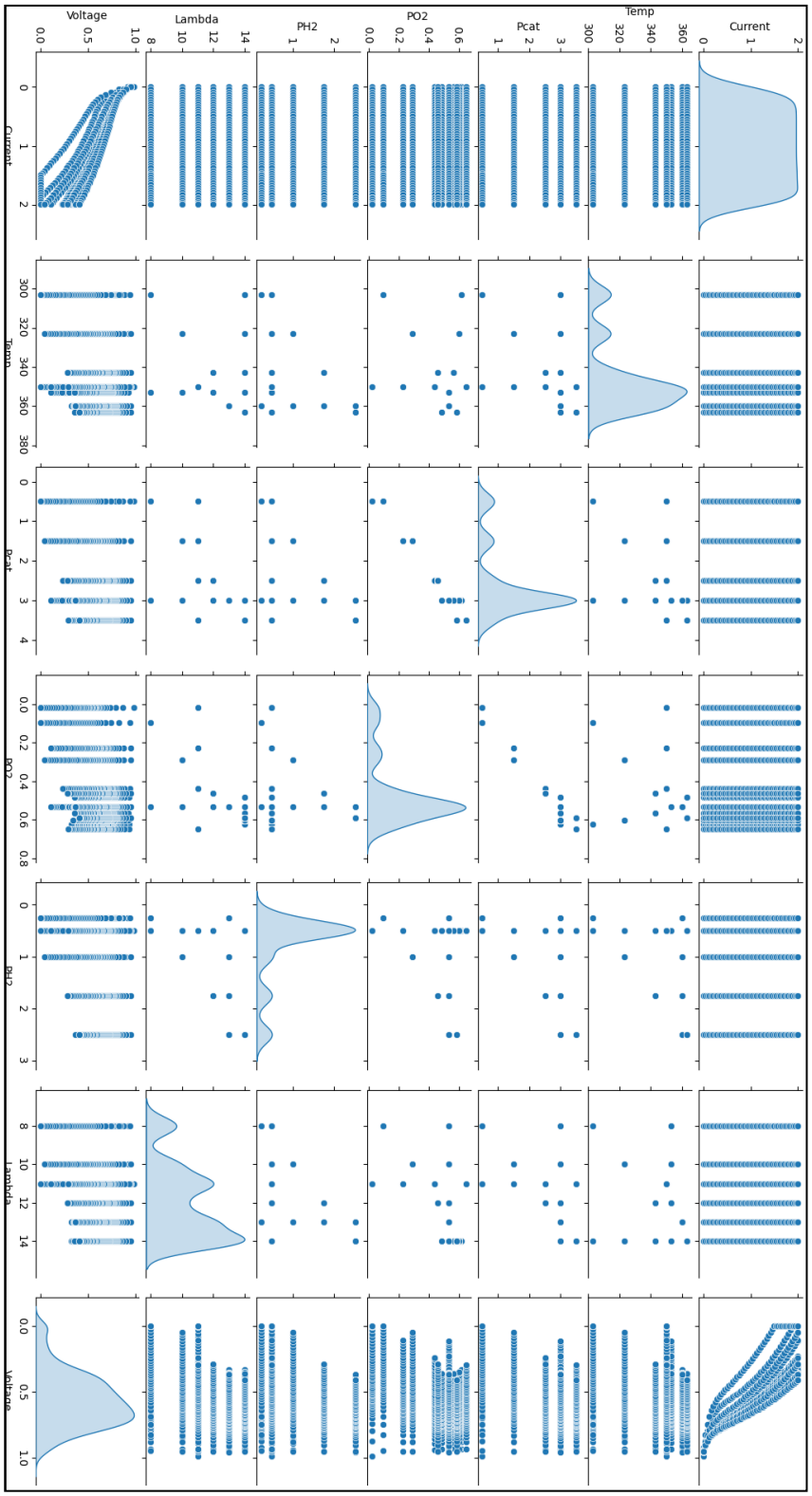


Figure B.1: Raw data distribution and cross plots of Dataset 1

Dataset 2 (1-D CFD data) [31]:

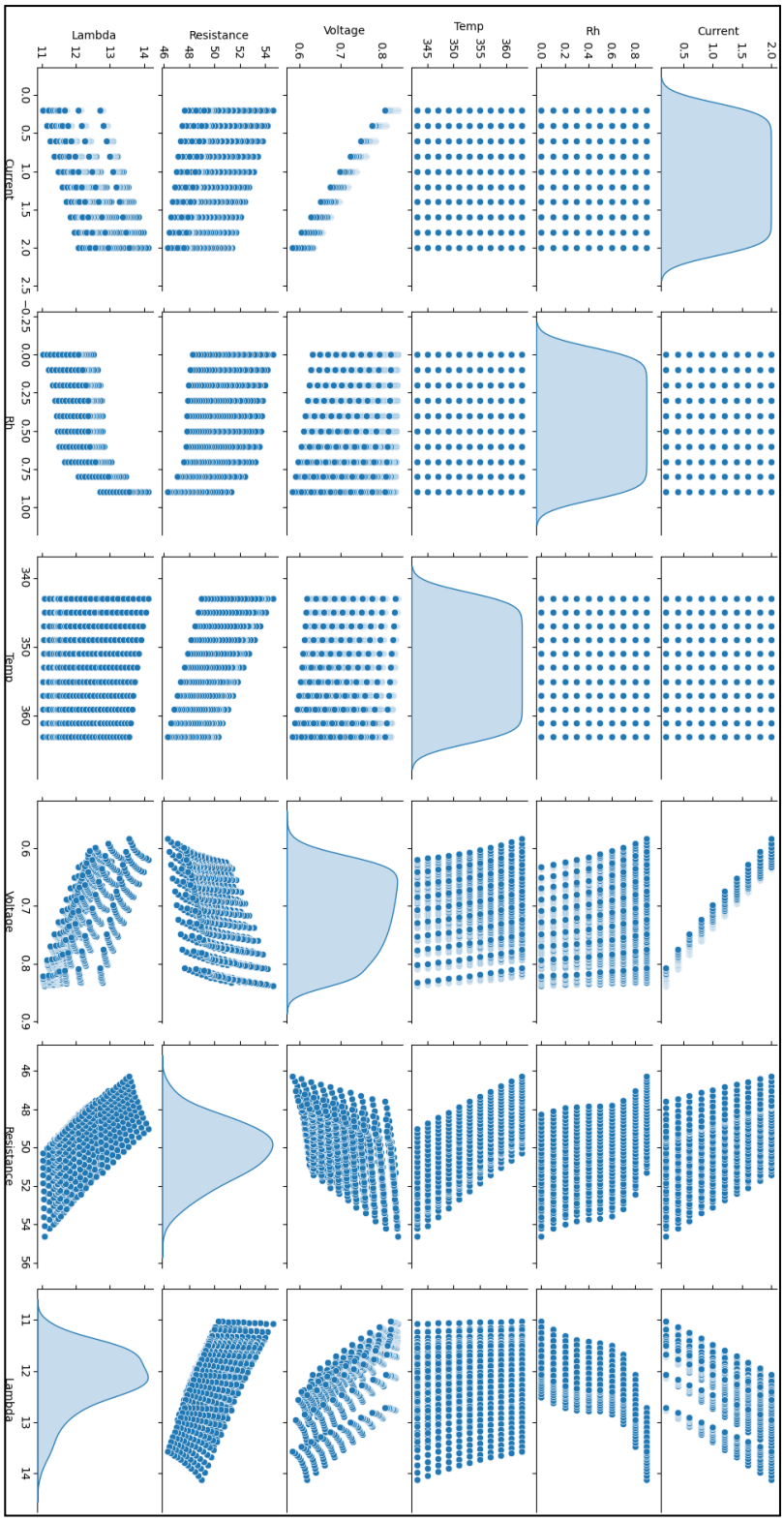


Figure B.1: Raw data distribution and cross plots of Dataset 2